Fluid transport and hygroscopicity

Elisa Julien

Harvard
School of Engineering
and Applied Sciences

FLUID TRANSPORT AND HYGROSCOPICITY

Thesis presented by

Elisa JULIEN

In fulfillment of the title of

Doctor of Philosophy in Physics

from

École des Ponts ParisTech

Thesis defended on February 9^{th}, 2023

Elise LORENCEAU	Directrice de recherche, CNRS	*Reviewer*
François BOULOGNE	Chargé de recherche, CNRS	*Reviewer*
Stefano AIME	Maître de conférences, ESPCI	*Examiner*
Olivier PITOIS	Directeur de recherche, UGE	*Examiner, President*
Rahima SIDI-BOULENOUAR	Chargée de recherche, UGE	*Examiner*
Philippe COUSSOT	Professeur, UGE	*Director*
Shmuel RUBINSTEIN	Senior Lectuer, HUJI	*Co-director*
David WEITZ	Professeur, Harvard University	*Co-director*

Abstract (english version)

Wood is a popular choice for construction due to its versatility and its mechanical properties. It is also a good thermal insulator and humidity regulator. However, its ability to absorb water from its environment, in particular in the form of bound water inside the cell walls thanks to hydrogen bonds, can also be a limiting factor for its use. Here we study, either with wood or model materials, a series of physical questions related to the presence or transport of this bound water in the system: its impact on the wettability, the diffusion of bound water, the propagation of cracks in such a wet system.

We first show that the apparent angle of contact of a liquid drop deposited on a wood surface progressively decreases over time, from a large to low value, before absorption. Reproducing the phenomenon with a model material (hydrogel) we demonstrate that this effect results from the deformation of the solid surface at larger distance as the water diffuses farther from the drop, through the gel.

With usual techniques for studying bound water a coupling with vapor and free water transport can exist, which precludes a relevant appreciation of the diffusion properties of bound water alone. Here, we prevent vapor and free water transport by filling wood with oil and we follow the bound water transport with the help of Nuclear Magnetic Resonance, diffusion coefficient was thus obtained in all three directions of the wood. The diffusion coefficient in the three directions of the wood can be thus determined unequivocally. We also show that fibers can be subsequently filled from bound water transport.

Through microscopic observation of cracks in soft colloidal gels during drying, we relate the particular shape of the crack tip to the rheological characteristics of the material. In addition to the cracking gel and the invading air-filled crack, we observe a third, wedge-shaped region filled with pure water, ahead of the crack tip. We show that in these gels, the fracture energy is determined by the water-air interface, while the mechanical properties of the gel determine the morphology of the water phase.

Abstract (version française)

Le bois est un matériau de choix pour la construction en raison de sa polyvalence et de ses propriétés mécaniques. C'est également un bon isolant thermique et un régulateur d'humidité. Cependant, sa capacité à absorber l'eau de son environnement, notamment sous forme d'eau liée à l'intérieur des parois cellulaires grâce à des liaisons hydrogène, peut également être un facteur limitant pour son utilisation. Nous étudions ici, avec du bois ou des matériaux modèles, une série de questions physiques liées à la présence ou au transport de cette eau liée dans le système : son impact sur la mouillabilité, la diffusion de l'eau liée, la propagation des fissures dans un tel système humide.

Nous montrons d'abord que l'angle de contact apparent d'une goutte de liquide déposée sur une surface de bois diminue progressivement au cours du temps, d'une grande à une faible valeur, avant absorption. En reproduisant le phénomène à l'aide d'un matériau modèle (hydrogel), nous démontrons que cet effet résulte de la déformation de la surface solide à une distance plus grande lorsque l'eau diffuse plus loin de la goutte, à travers le gel.

Avec les techniques habituelles d'étude de l'eau liée, un couplage avec le transport de vapeur et d'eau libre peut exister, ce qui empêche une appréciation pertinente des propriétés de diffusion de l'eau liée seule. Ici, nous empêchons le transport de vapeur et d'eau libre en remplissant le bois d'huile et nous suivons le transport de l'eau liée à l'aide de la résonance magnétique nucléaire, le coefficient de diffusion a ainsi été obtenu dans les trois directions du bois. Le coefficient de diffusion dans les trois directions du bois peut ainsi être déterminé sans équivoque. Nous montrons également que les fibres peuvent être remplies ultérieurement par le transport d'eau liée.

Grâce à l'observation microscopique de fissures dans des gels colloïdaux mous pendant le séchage, nous établissons un lien entre la forme particulière de la pointe de la fissure et les caractéristiques rhéologiques du matériau. En plus du gel qui se fissure et de la fissure remplie d'air qui l'envahit, nous observons une troisième région remplie d'eau pure, en avant de la pointe de la fissure. Nous montrons que dans ces gels, l'énergie de rupture est déterminée par l'interface eau-air, tandis que les propriétés mécaniques du gel déterminent la morphologie de la phase remplie d'eau.

Acknowledgements

Durant ma thèse, j'ai eu la chance de partager mon temps entre deux pays : en France dans le laboratoire Navier à l'école des Ponts ParisTech et aux États-Unis dans le laboratoire de David Weitz à l'université d'Harvard. Ces échanges m'ont permis d'évoluer scientifiquement et personnellement grâce aux nombreuses personnes qui m'ont accompagnées dans cette expérience. Je tiens donc à leur exprimer toute ma gratitude pour leur contribution.

En France,

Je remercie mon directeur de thèse, Philippe Coussot, pour ses conseils éclairés, sa patience et son soutien constant tout au long de cette aventure scientifique. Il a été pour moi un incroyable directeur de thèse sur qui j'ai toujours pu compter. Il m'a permis d'aller au bout du projet grâce à sa pédagogie et sa rigueur.

Merci à Gaétan et Thomas de m'avoir initiée au monde de la recherche et de m'avoir guidée pour appréhender les difficultés d'un doctorat. Merci aussi à Jules de m'avoir conseillée lors de ma recherche de thèse.

Je suis également reconnaissante envers les membres de mon comité de thèse, Elise Lorenceau et François Boulogne pour leurs commentaires constructifs et leur expertise.

Je tiens à exprimer ma profonde reconnaissance aux participants de cette étude, qui ont généreusement donné de leur temps pour partager leur expérience et leur expertise : la team RMN avec Rahima et Benjamin ; Sabine pour ses compétences sur le bois et Laurent pour le projet sur les gels.

Merci à tous les permanents de Navier pour leur bienveillance, les discussions constructives, les séances de course à pied et leur aide au cours de ces trois années : Brice, Emmanuel, Florence, François, Julie, Laurent, Olivier, Xavier, Yacine. Merci à l'équipe technique qui nous accompagne dans la réalisation de nos expériences : Cédric, Jaime, David et Patrick. Et enfin, merci à l'équipe administrative : Marie-Françoise, Ninon et Virginia qui ont été d'une grande gentillesse.

Je voudrais remercier chaleureusement mes collègues de laboratoire, Margaux, Nabil, Antoine, Hicham, Yuliang ; mes anciens colocs de bureau, Franck, Ahmad, Jovialy ; mes anciens collègues,

Leila, Elie, Julia, Vierajihta, Nihal, Florian, Thibault ; mes nouveaux colocs de bureau, Valentine, Kassem, Laura, Xiaohan. Leur aide fut précieuse ainsi que leur collaboration et leur amitié. Une mention particulière pour Anatole, mon frère Coussot pour son amitié si importante pour moi durant ces années.

Merci à tous les stagiaires avec qui j'ai passé de très bons moments : Julien, Adèle, Marion, Mateo et Asmaa.

Un grand merci à mes amis qui ont montré de l'intérêt pour mon travail, m'ont soutenue, m'ont accompagnée lors des confinements et m'ont permis de maintenir un équilibre entre ma vie professionnelle et ma vie privée. Et là aussi une mention spéciale à Juliette : merci pour ta bonne humeur, ta joie de vivre et d'avoir traversé la France pour me soutenir jusqu'au bout.

Enfin, je tiens à exprimer ma profonde reconnaissance envers ma famille et particulièrement mes parents pour leur soutien moral (et intestinal), leur patience et leur encouragement tout au long de ce projet.

In the U.S.,

I would like to warmly thank Dave and Shmuel for all the inspiring discussions we had. They have challenged me and share with me a constructive expertise in the research field.

Thank you, Stefano, for trusting me to help you with your project. It was wonderful to work with you.

I would like to express my gratitude to all the people who contributed to this thesis: Sijie for his guidance, Ilya for his expertise on fractures, Max for his advice and Will for all the work he does in the lab.

I would like to thank my laboratory colleagues and the volleyball and running teams: Anqi, Arka, Ben, Brendan, Bob, Bobby, Diana, Hong, Iris, JC, John, Kamar, Karla, Larissa, Mathilde, Rob, Rohan, Thomas, Tina, Wentao, Wenyun, Yinan. The Weitz Group has been invaluable helpful and thank you for your friendship during my time in Boston.

Thank you to all the other great people who made my time in the Boston area a real pleasure: Maria, Kiana, Caro, Stefan, Rob and Jessica.

Contents

Introduction

Wood has always been used in construction. Its use has taken a new momentum in recent years because it meets the current environmental challenges and presents an asset in terms of innovative structures. The development and marketing of high-performance products derived from wood offer new possibilities. Wood, a natural and porous material, differs from other construction materials by its excellent mechanical properties such as thermal insulator, humidity regulator.

However, the hygroscopicity of wood, that is to say its capacity to absorb or restore water from its environment can be a limiting factor for its use in construction. Indeed, this characteristic implies that its properties can be modified, even altered in condition of use. This can lead to performance losses in construction. The understanding of moisture transfer mechanisms in wood is therefore an important issue for a better evaluation of its hygromechanical properties in conditions of use, and for the development of preservation or finishing methods that can balance insufficient natural durability. However, water transfers and water-wood interactions are still poorly understood, either because they are reproduced by models that do not allow the physics of the phenomena involved to be properly taken into account, or because the description of the mechanisms at the various scales is incomplete.

Some research in this field has been carried out in Laboratoire Navier. The study of liquid transfer in wood has led to the demonstration of an original physical phenomenon occurring in hygroscopic porous materials: the dramatic impact of adsorption on wettability, leading to virtually stop the capillary imbibition compared to that expected given the structure of the medium. This suggests that fluid transfers in wood involve complex physical processes coupling the impact of the transport of free water, bound water, or vapor, in the vessels, cell walls, fibers (for hardwoods), or tracheids (for softwoods), and the exchanges between these different regions. This is the motivation of the present work. One essential practical issue is to master the mechanisms associated with the treatment or drying of wood, as well as the durability of wood constructions, and to develop models that are more in line with physical reality than the current models.

In this manuscript, we focus on the impact of hygroscopicity on fluid transport in wood under soaking and drying conditions. Four issues are chosen in this work: direct measurement of the diffusion coefficient of bound water, and analysis of fluid transfer in wood, the impact of water concentration on wettability, impact of the wood deformation under drying condition, understand the mechanism behind crack formation pattern during flaking. In order to answer these problems

found in wood, the work will be based on the study of different wood species as well as on model materials. The different works use a variety of methodologies that allow measurements and observations at different scales. This thesis is organized into six distinct chapters:

1. In the chapter 1, we briefly review the current state of the art on the wood structure and its hygroscopic nature.

2. In the chapter 2, we present the materials used in this work with the different wood species, as well as the model materials chosen. The methods of analysis and characterization of the materials used are also presented. We will detail in particular the principle of Nuclear Magnetic Resonance (NMR), Confocal laser scanning microscopy and the principle of rheometry.

3. In the chapter 3, we will study wood imbibition by NMR. A method that will allow us to directly analyze the evolution of water populations (bound water in the cell wall and free water in the pores) in a wood sample. We will study in particular the diffusion of bound water and the transport of water in the fibers.

4. In the chapter 4, we will study the wetting phenomena of hygroscopic materials as a function of their water concentrations. For this we will use the Sessile drop method and a gravimetric method to control the moisture content of our samples.

5. In the chapter 5, we will study the drying of deformable porous media. We will use a NMR integrated drying set-up to study the drying dynamics of colloidal gels.

6. In the chapter 6, we will study the flaking paint phenomenon using model materials (colloidal gels). The objective will be to understand the formation of crack patterns by the microscopic analysis of the drying fracture thanks to confocal microscopy.

Chapter 1

State of the art

In this chapter, we will review the current state of the art on fluid interaction in wood. First, we will tackle the complex structure of wood. Then, we will briefly review the wood hygroscopic nature and its impact on fluid transport and on its macroscopic deformation.

This chapter aims to introduce essentially general notions on the hygroscopicity of wood. We will detail a more extensive literature on the four topics studied at the beginning of each chapter.

1.1 Structure of wood

Wood is a natural material that presents a large structural variability at all scales (macrostructure, microstructure, and ultrastructure). Its physical characteristics make it a complex material to study and understand. Here, we will briefly review the general knowledge of the wood structure (see the reference [Trouy n.d.] for more details).

1.1.1 Wood macroscopic structure

Wood is plant tissue found in the trunks of trees, branches, and roots. Trees growth in height and in width in the form of concentric rings. Each ring, called annual ring contains the earlywood and the latewood formed according to the growing season. The width of the rings can play a role in the wood density.

The macroscopic structure of the tree consists of several layers (see on Fig 1.1). The bark, outer covering which has protection functions and biomechanical functions. The phloem is a conductive tissue of elaborated sap from the branches towards the roots. The cambium forms the conductive tissues of the tree which ensures growth in width. The sapwood is the newly formed wood, in which the parenchyma (vegetal tissue) cells are alive, and the raw sap is carried from the roots to the branches. The duramen (or heartwood, or perfect wood) is the older wood, in which the parenchyma cells are no longer alive. The pith (or medulla) is the central part of a trunk with a soft structure made of spongy tissue.

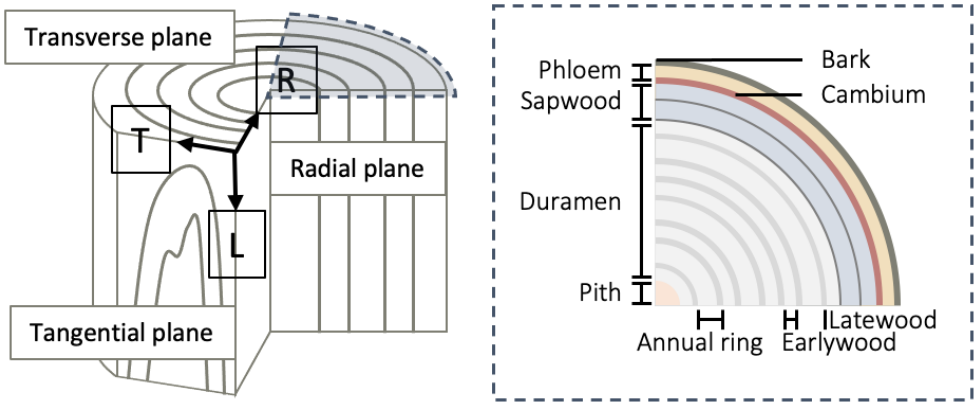

Figure 1.1: A schematic of the wood orientation with a zoom on different layer of the wood macrostructure in the TR plane.

Wood is an anisotropic material. The development of the tree is based on the ability of the initial cells to form new specialized cells (longitudinally or vertically). The arrangement of its constituent cells defines the ligneous plan of the wood. The three orthogonal directions create three reference planes (see Fig 1.1): the longitudinal direction (L) in the length of the trunk, the radial direction (R) which is perpendicular to the growth rings of the tree and the tangential direction (T) which is tangent to the rings.

1.1.2 Wood microscopique structure

Trees are divided into two main categories: softwoods and hardwoods which differ in their cellular compositions as shown on Fig 1.2. We can find in their microstructures different types of cells:

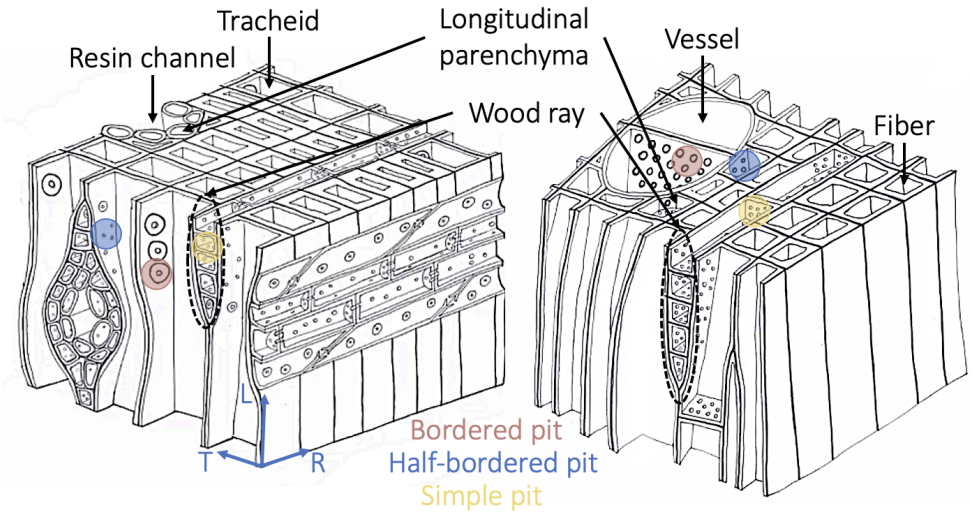

Figure 1.2: Schematic representation of microscopic structures of softwood (left) and hardwood (right) [Passas 2012].

- Tracheids are unspecialized cells that fulfill a dual function: conduction and mechanical support of the tree. They constitute over 90 % of the cells of the softwood tree and can sometimes be present in hardwoods in small quantities. Tracheids are aligned in the longitudinal direction of the tree and are 15 to 50 μm large and 2 to 9 mm long (width and thickness vary depending on the growing season of the tree).

- Vessels are dead cells specialized in sap conduction. They are only present in hardwood (on average between 10 and 20 % of the cells). Vessels are stacks of cells connected end to end in the longitudinal direction and can reach up to 10 m in length. The diameter varies between 25 and 400 μm depending on the species and their location in the annual ring. Whether they have a diameter that varies between the earlywood and latewood, the tree is qualified as diffuse pores or not.

- Fibers are dead cells specialized in mechanical support. They are present only in hardwood (on average between 50 and 60 % of the cells). Fibers are longitudinal cells with reduced sections (between 20 and 40 μm), thick walls and a length up to 2.5 mm.

- Wood rays are radial laminae consisting in radial parenchyma cells, which are living cells that ensure the storage of reserves and the radial transport of nutrients. In softwood, radial tracheids can be found associated with the radial parenchyma.

- Parenchyma cells can also be found aligned longitudinally. In softwood, they are nearly present (0 to 2 %) and in softwood, they are found in two ways, either independently of the

vessels or associated with them.

- Resin channels are tubular cavity lined with resin-producing parenchyma cells. Resin channels can only be found in softwood (longitudinally or radially) normally or traumatically (in reaction to injury or insect attack).

In order to fulfill its physical properties as a conductive porous media, each cell is connected through different communication channels as shown on Fig 1.2:

- pits are communication holes between two neighboring cells. According to the cell, there exist different kinds: bordered pits are between conductive elements (tracheids or vessels), simple pits between two parenchyma cells and semi-areal pits between parenchyma cells and conductive element. Unlike the other ones, bordered pits have an interior space (chamber) with a torus that plays a role in case of embolism by closing the pit.
- The vessel elements are connected to each other by inter vessel pits at the extremities where the terminal septum between two vessel elements has been perforated. There are two types: simple perforations (unique circular opening) and scalariform perforations (in the form of rungs ladder).
- The fibers have a reduced number of pit [Vazquez-Cooz and Meyer 2006], often present in the RL plane.

1.1.3 Wood ultrastructure

At the cell wall scale, there is several constituent layers organized concentrically around the lumen and produced at different periods during cell differentiation. Three major components are found in each layer of the cell wall: cellulose microfibrils, hemicelluloses and lignin. Lignins and hemicelluloses glue microfibrils together, make them waterproof and create stiff cell walls. There are other substances present in small amounts called extractive because they can be easily extracted with solvents.

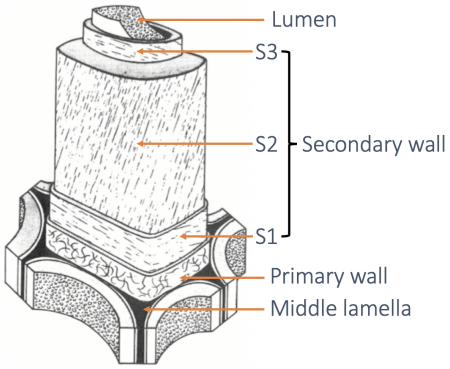

Figure 1.3: Schematic representation of the constituent layers of the wall of a wood cell.

The joint lamella, called intercellular cement allows the cells to be welded together. The primary wall is a thin wall ($0.1\ \mu m$) produced at the beginning of the cell differentiation. The secondary wall, composed of three sub-layers S1, S2 and S3, is the most important layer for the cell in terms of mechanical properties. Each layer is distinguished by the orientation of the helical microfibrils relative to the longitudinal axis of the cell. The orientation of the cellulose microfibrils with respect to the cell axis is at the origin of the anisotropy phenomenon of wood shrinkage or swelling [Siau 1984]. The most important being S2 from a mechanical properties point of view (represents $75 - 85\ \%$ of the cell wall thickness).

1.2 Hygroscopy of the wood

In this work we focus our interest on the hygroscopic characteristic of wood. This ability to absorb water allows humidity regulation but can also create structural disorders. We want here to define the water composition and its impact on the hydrodynamic and mechanical properties of wood.

1.2.1 States of water in wood

In wood, we can distinguish three different states of water:

1. Free water: corresponds to water in the liquid state. It is found in the cell cavities (lumens) of the wood and can circulate freely within the structure of the wood by capillary effect.
2. Bound water: corresponds to the water absorbed into the cell walls of wood by hydrogen bonds. It is responsible for the hydromechanical deformations (swelling or shrinkage) of the wood. It can be present in the absence of free water in the hygroscopic domain.
3. Water vapor: corresponds to water in the vapor state that is found in the air-filled spaces of cell cavities.

Moisture content (MC) is a quantity representing the amount of water present in the material. It is expressed by the ratio (in percentage) between the quantity of water present m_{wet} and the mass of anhydrous wood m_{dry}:

$$MC(\%) = \frac{m_{wet}}{m_{dry}} \times 100 = \frac{m_{wood} - m_{dry}}{m_{dry}} \times 100$$

1.2.2 Water content and composition

Wood can be found at different concentrations with water in different states (free water, bound water and vapor):

- When the tree is standing in the ground, its water content for hardwoods is estimated at about $140 - 220\ \%$.
- Green wood is cut wood with a moisture content above the fiber saturation point (FSP) [Tiemann 1906]. It therefore still contains the three states of water.

- Fiber saturation point is the point in the drying process at which only bound water remains. The value of the FSP varies between $25 - 30$ %.
- Below the FSP, only bound water and vapor are present in the wood, this is called the hygroscopic range.
- Anhydrous wood, which no longer contains water can be obtain by drying in the oven at $103°C$ until a constant mass is obtained. This method is the most common but can alter the sample. Another method would be to use silica gel [Rostom, Caré, and Courtier-Murias 2020].

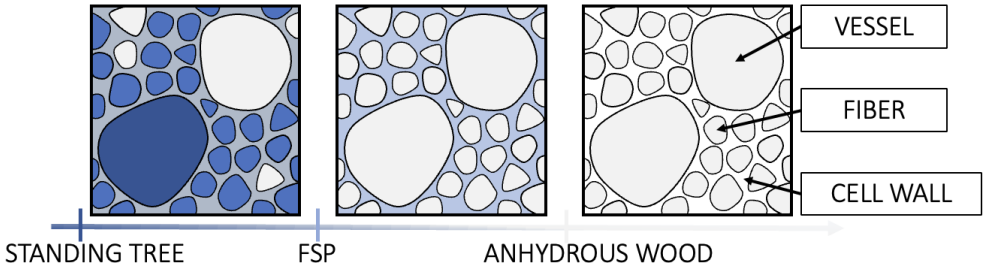

Figure 1.4: Scheme of the hardwood at different state of water concentration.

1.2.3 Sorption isotherm

Wood is a hygroscopic material, it interacts with air humidity and tends towards a balance according to external conditions by absorbing moisture (absorption) from the air or by restoring it (desorption). Its behavior can be represented by a sorption isotherm which defines the relationship between the water content in wood (MC) and the surrounding relative humidity at a given temperature (see Fig 1.5).

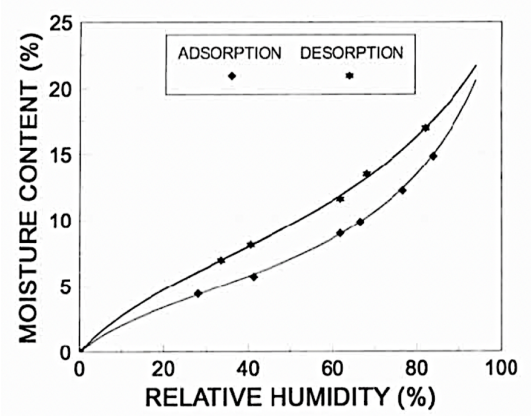

Figure 1.5: Adsorption and desorption isotherms at $30°C$ for yellow poplar wood samples[Peralta 1994].

The curve has a sigmoid shape typical of hygroscopic materials. As for many porous materials,

a hysteresis phenomenon is observed when an absorption-desorption cycle is performed [Skaar 2012, P. Navi 2005].

1.2.4 Water transport

As wood is composed of different types of water and a complex structure with several pore sizes, we can find very different fluid transport dynamics:

- Water vapor can circulate through the pores of the wood and the pits that connect them. The speed of vapor diffusion depends on the path's tortuosity, which varies according to the wood direction.
- Bound water is an essential element for the circulation of fluids in wood, whether it is during drying [Penvern et al. 2020, Cocusse et al. 2022] or soaking [Zhou, Caré, A.King, et al. 2019]. Its presence or not in the sample can imply very different dynamics of water circulation. The diffusion rate of bound water in cell walls is controversial particularly since studies are carried out in the hygroscopic domain and the vapor diffusion can impacts the results.
- The free water in the vessels or tracheids penetrates by capillarity and is therefore controlled by the wettability of the cell walls. In particular, it has been shown that water in contact with wood behaves in an unexpected way in the case of dry wood (not saturated with bound water) [Zhou, Caré, A.King, et al. 2019]. The capillary imbibition proceeds at a speed several orders of magnitude slower than expected (Washburn's model) given the structure of the medium. This observation is consistent with the flat menisci observed in the capillaries despite the very good wettability of wood by water.
- Observations by Zhou, Caré, A.King, et al. 2019 have shown that the penetration of free water into fibers occurs radially around a vessel. A question regarding fiber filling remains: does free water arrive through the pits connecting the fibers to the vessels or is it transported as bound water in the cell wall network.

During the drying or soaking of wood, the dynamics of each water population comes into play. In particular, exchanges between the populations occur, which makes the understanding of the hydraulic system of the wood quite complex.

1.2.5 Hygromechanical deformations

Bound water is responsible for the macroscopic deformation of wood. Wood swells when it absorbs bound water into its walls, and contracts when it loses bound water. The total shrinkage is the percentage of dimensional change of wood, in a given direction, between the fiber saturation point and the anhydrous state:

$$\epsilon = \frac{L - L_a}{L_a} \times 100$$

With ϵ the deformation rate (in $\%$), L_a the anhydrous length and L the measured length.

The hygromechanical properties of wood are not the same for the three reference directions. The Table 1.1 gives average values of total shrinkage for some hardwood and softwood species:

Species	Total tangential deformation (%)	Total radial deformation (%)
Poplar	9	5
Oak	10	5
Ash	8	6
Fir	8	4
Douglas	7	4

Table 1.1: Order of magnitude of the total shrinkage of some species in the tangential and radial directions [Leboucher n.d.].

Note that for all species, the shrinkage of wood is strongly anisotropic: it is in the tangential direction that the shrinkage is most important. The wood is also subject to longitudinal shrinkage but about $0.2 - 0.3$ % and therefore negligible.

Scope of study

We have seen in this first chapter that wood is a complex material which presents an asset in terms of innovative structures and environmental issues. Its structure today is well known but it involves water transfers still poorly understood. In particular, it is a hygroscopic material, and its properties can be modified, even altered in conditions of use, a phenomenon that can lead to disorders in structures. This sensitivity to moisture can be an obstacle to the use of wood in construction. The understanding of moisture transfer mechanisms in wood is therefore an important issue for a better evaluation of its hydromechanical properties, and for the development of preservation or finishing methods that can balance its insufficient natural durability. In this work, we are interested in four issues related to the hygroscopicity of wood:

1. Although the dynamics of wood imbibition has been the subject of numerous research studies, the individual behavior of each water population (bound water, free water (in tracheids, vessels, or fibers) or water vapor) is still poorly understood. Indeed, the diffusion of bound water is often associated with that of water vapor and no direct monitoring experiments have been performed. In chapter 3, we propose a new method that allows us to follow the rise of bound water in wood. A second axis of study will be the understanding of the water and air flows in wood to answer the question of the origin of the fiber filling.

2. The capillary rise in vessels is now better understood but original phenomena have been observed such as the influence of the bound water concentration on the wetting properties of wood. Chapter 4 is focused on understanding the influence of water concentration on the wettability of a hygroscopic material and its impact on the advance of a free waterfront in a capillary.

3. The hygroscopicity of wood is also responsible for its hygromechanical behavior. During drying, this tendency to shrink is often not taken into account. In chapter 5, we have then taken interest in a more global problem to understand the drying of a deformable porous medium composed of different pore sizes.

4. Finally, in construction the use of paint or surface treatments is often used on wood. However, the soaking and drying cycles of wood can cause fractures. The paint, similar to a viscoelastic material, flakes off creating regular patterns. The objective of Chapter 6 is to understand drying cracks in viscoelastic materials and the mechanisms that drive patterns formation.

Now that the scope of our studies is set, let us detail the materials used as well as the most adapted techniques to answer these different questions.

Chapter 2

Materials & Methods

In this chapter, we will introduce the different materials used in this work. Then, we will review the different set-ups implemented. Finally, we will present the principles of the measurement techniques used: nuclear magnetic resonance (NMR), confocal laser scanning microscopy and rheometry. These techniques were used to both characterize and analyze our systems at different macroscopic and microscopic scales.

2.1 Materials

This section includes the different materials and fluids used in this work. We focused this thesis project on hygroscopic materials in which water is a central element with respect to their physical and mechanical behavior: wood with its ability to absorb water into the cell walls and its different scales of porosity; hydrogel, a model material allowing us to mimic and isolate certain properties of wood such as its hygroscopicity. We will also present the different fluids used in this work.

2.1.1 Wood

2.1.1.1 Studied species

Wood is our central material in this work, a material that has challenged scientists by its complex structure and its hygroscopic nature. We have seen in section 1.1.2 that there are two main categories of wood. In this work, we analyze several species: softwood (fir) and hardwood (poplar, oak, and ash wood). Fig 2.1 shows the microscopic structure of the different studied species. They exhibit different characteristics:

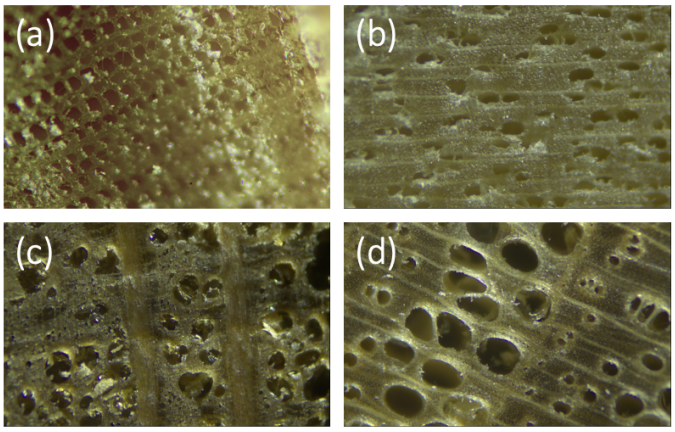

Figure 2.1: Images of the microscopic structure of the transverse plane of different species: (a) fir, (b) poplar, (c) oak and (d) ash wood samples.

- Softwood: Fir is a non-porous wood made up of structured tracheids. The average radius of the tracheids is different for earlywood and latewood ($10 - 25\ \mu m$) [Cocusse et al. 2022].
- Hardwood: Poplar is a diffuse-porous wood made of a homogeneous distribution of medium pores (solitary, multiples, and small cluster). The average radius of the fibers is $8\ \mu m$ and that of the vessels is $55\ \mu m$ [Zhou, Caré, A.King, et al. 2019]. Oak is a ring-porous wood made of a up to four rows of solitary large pore in earlywood. Ash is also a ring-porous wood made of large solitary or clustered vessels in small and scattered groups.

Observations of the internal structure of the poplar samples were made by Meng Zhou and Sabine Caré by optical microscopy (see Fig 2.2). Their analysis allowed the quantification of the

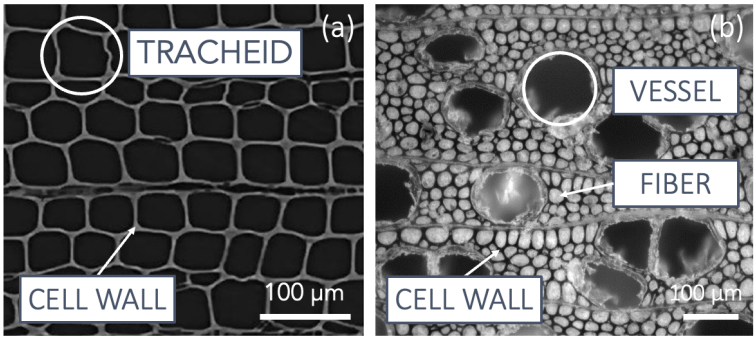

Figure 2.2: Image in the transverse plane of (a) a fir and (b) a poplar sample from optical microscopy from Meng Zhou showing the different elements of a hardwood and a softwood: tracheid, vessel, fiber, and cell wall.

pore volume distribution in the sample (Table 2.1). In the poplar sample, we obtain $70\ \%$ of the total volume composed of pores with $44\ \%$ of vessels and $26\ \%$ of fibers.

	Vessel (%)	Fiber (%)	Porosity (%)	Cell wall (%)
Poplar	43.5 ± 0.2	26.4 ± 0.6	70.3 ± 0.4	30 ± 0.4

Table 2.1: Porosity of the poplar sample presented in % volume.

Table 2.2 provides us with information on the physical and mechanical properties of wood extracted from [Gérard et al. 2016]. In particular, we note the mean density, the total shrinkage, the fiber saturation point, and the tangential elastic modulus.

Characteristics	Fir	Poplar	Oak	Ash
Mean density ($kg.m^{-3}$)	490	450	740	680
Total shrinkage (TR)	4.0	4.8	4.5	5.7
Fiber saturation point ($\%$)	29	30	31	32
E (MPa)	14300	9800	13300	12900

Table 2.2: Physical and mechanical properties of the different species used at $15\ \%rH$ [Gérard et al. 2016].

2.1.1.2 Wood preparation

Fir, oak, and ash wood samples were collected in Seine-et-Marne region (France). Poplar samples were collected in the commune of Marigny-en-Orxois (France). The wood was stored in the ambient air of the laboratory at $20°C$. They are sawn along the general anisotropic directions of wood (longitudinal L, radial R, and tangential T) and come from the inner part of the trunk (heartwood). Samples were cut with a band saw along the general anisotropic directions of the wood to obtain samples of either $10 \times 10 \times 10\ mm^3$ or $5 \times 5 \times 10\ mm^3$ which correspond to the dimensions of the two NMR tubes at our disposal. The wood is shaved to minimize its roughness. Sanding the surface can drastically change the surface condition as the pores are then full of sawdust.

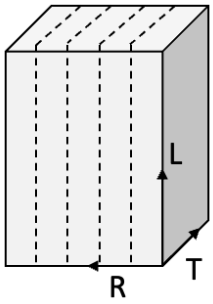

2.1.2 Hydrogel

2.1.2.1 PEG hydrogel as a model material for wood

To mimic the hygroscopic character of the wood and eliminate its porosity, we used a PEG hydrogel (polyethylene glycol) as a model material. This material has previously been used to study wood imbibition [Zhou, Caré, A.King, et al. 2019]. Moreover, using PEG polymers allows us to reproduce the hydrophilic nature of wood. Its advantage is its transparency which allows us to use other analysis tools such as confocal microscope. The properties of the material can be varied by changing its water concentration (maintained at different humidities) or by changing the polymer ratio.

Hydrogels were formed from a solution of poly(ethylene glycol) methacrylate (PEG-MA: $H_2C = C(CH_3)CO(OCH_2CH_2)_nOH$) average molecular mass number (Mn) 500, and poly(ethylene glycol) diacrylate average Mn 700 (PEG-DA: $C_3H_3O(OCH_2CH_2)_nC_3H_3O_2$) in demineralized water with a radical initiator, Ammonium persulfate (APS: $(NH_4)_2S_2O_8$ at $5\ wt\%$ in water) and a catalyst, N,N,N',N'- Tetramethylethylenediamine (TEMED: $C_6H_{16}N_2$ at $10\ wt\%$ in water). All chemicals were purchased from Sigma-Aldrich, USA. The composition of the hydrogel used in most of the experiments is summarized in table 2.3. For some experiments the ratio of PEG-MA and PEG-DA varies but the total amount of polymers ($25\ \%$) does not change (see annex 7.1).

FORMULATION	MASS PERCENTAGE (wt %)	QUANTITY	DENSITY (g/mL at 25°C)
dH2O	72.3	6.18 g	1
PEG methacrylate	23.4	2.00 g	1.10
PEG diacrylate	2	0.17 g	1.12
APS	1.15	100 μL	1.9
TEMED	1.15	100 μL	0.775

Table 2.3: Hydrogel components and quantities with corresponding densities.

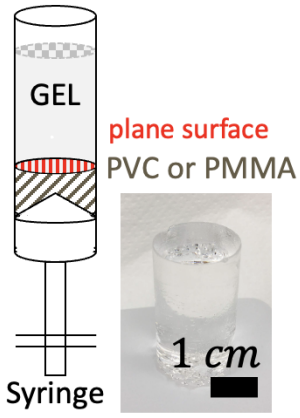

The protocol for preparing the gels is as follows: we first mix together the water and the two polymers until we obtain a homogeneous solution. We can use a vacuum pump to get rid of air bubbles in the solution. We then add the APS and finally the TEMED. These last two solutions will react to create a radical initiator to form the polymeric network by a cross-linking process. The solution is poured in a cylindrical mold with a polyvinyl chloride (PVC) or a poly(methyl methacrylate) (PMMA) bottom to obtain a smooth surface. The polymerization starts after 15 minutes and is finished after 30 minutes where the hydrogel can be easily unmolded. From images obtained with an optical profilometer, we observe that the roughness the hydrogel surface is less than $1\mu m$.

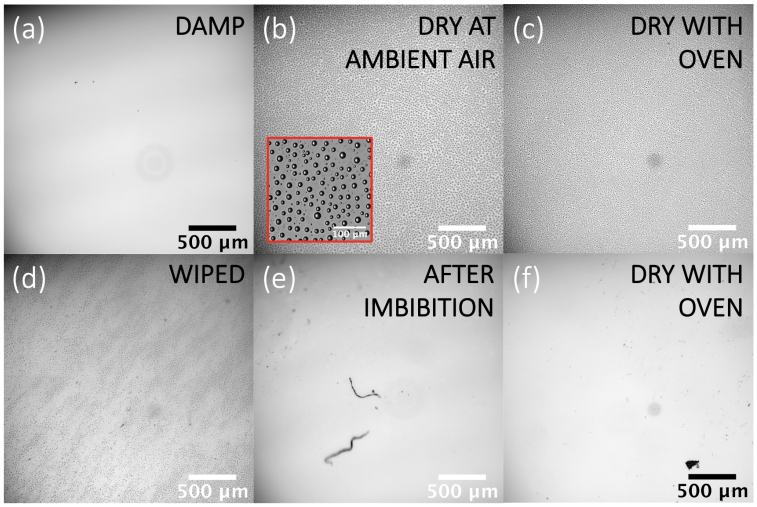

Figure 2.3: Aspect of the gel surface through microscope at different conditions: (a) damp gel after unmolding, (b) dry gel at ambient air (the inset shows a zoom of the surface), (c) dry gel with an oven at $60°$, (d) gel after wiping the surface, (e) damp gel after imbibition and (f) after further rinsing and dry again in the oven at $60°$.

Fig 2.3, we observe the aspect of the gel surface in different conditions. After unmolding the gel, we obtain a smooth surface without asperities. After drying this surface at ambient air, we observe the surface of the gel is filled with small droplets with a diameter smaller than $20\ \mu m$. Even after leaving the sample several days in the oven, the drops do not disappear. This is our belief that these droplets are made up of residual solution. Wiping the surface with a tissue is not a solution to get rid of them and it can also alter the surface. For some tests, the hydrogel is immersed in a water bath for several days until reaching a saturated state, the final water concentration is 89%. In this case, we observe that the gel regains a smooth surface. However, as seen in Fig 2.3-e, dust contaminated the surface. In fact, our gel is quite sticky and can quickly catch dust if not kept in an enclosed environment. Finally, if the hydrogel is immersed or rinsed in water and dry again in the oven at $60°$, we can obtain a dried surface free of droplets.

Hydrogels can undergo extremely large and reversible volume changes during swelling. Swelling is a volumetric growth process in which a porous material expands by spontaneous imbibition of additional interstitial fluid. The swelling properties of hydrogels are dependent on the degree of cross-linking, the chemical structure of the network and the affinity of the gel with the solvent. The degree of swelling is an equilibrium property of a given gel in a given environment and is now relatively well understood. Quantitatively, the most commonly used formula to calculate the degree of swelling in a hydrogel is the comparison of a sample volume in its driest state to its most soaked state:

$$\alpha = \frac{V_{sg}}{V_{dg}} = \frac{\frac{m_s}{d_s} + \frac{m_n}{d_n}}{\frac{m_n}{d_n}} \tag{2.1}$$

With α the swelling ratio, V_{sg} the volume of the saturated gel, V_{dg} the volume of the dry gel, m_s and d_s the mass and density of the solvent contained in the gel, m_n the mass of the swollen network and d_n the density of the network. In our case, we assume that if the sample is shrinking, it is because it is losing water mass (with m_{sg} the mass of the saturated gel and m_{dg} the mass of the dry gel). Experimentally, we calculated the mass of a gel in its driest state (kept at $60°C$ in an oven) and compared it with its mass in its most soaked state (soaking for one week in a water bath) and we obtained the following swelling ratio:

$$\alpha = \frac{m_{sg}}{m_{dg}} = \frac{13.23}{1.40} = 9.45$$

When varying the polymer ratio in the gel (see annex 7.1 for the different compositions used), we change the gel properties including the swelling ratio and the elastic modulus of the gel. The percentage of PEG-MA is the ratio of the mass introduced to the total mass (PEG-MA and PEG-DA):

$$C_p = \frac{m_{PEG-MA}}{m_{PEG-MA} + m_{PEG-DA}} \times 100$$

With C_p the polymer concentration (in $\%$), m_{PEG-MA} the mass of poly(ethylene glycol) methacrylate and m_{PEG-DA} the mass of poly(ethylene glycol) diacrylate.

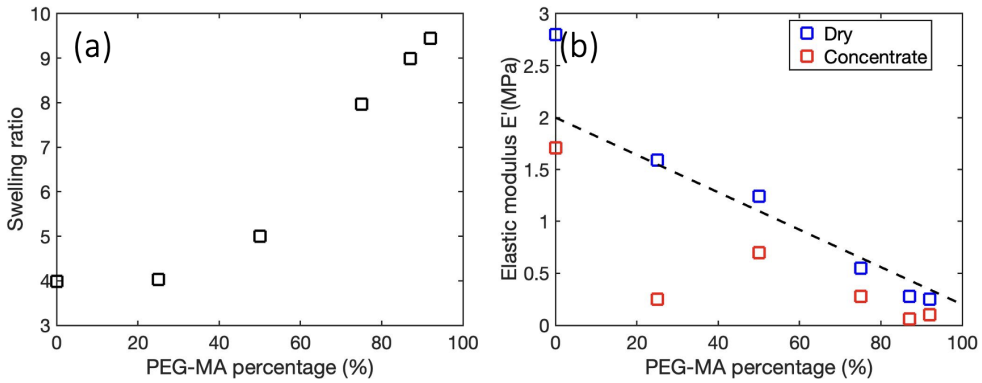

Figure 2.4: Elastic modulus according to (a) the percentage of PEG-MA for hydrogel prepared at $50\ \%rH$ and to (b) the water concentration for hydrogel at 92% PEG-MA). The dotted black line as a slope of one.

Fig 2.4, we observe that the swelling ratio increases as the PEG-MA concentration increase. This is expected as the cross-link degree is decreasing with PEG-MA $\%$ increasing.

From the measure made on the DMA (see section 2.5.2.2), the Fig 2.4 shows that the elastic modulus increase as the concentration of PEG-DA increase. This is due to the fact that the presence of this polymer allows us to obtain a polymer network with more connections. Moreover, it is well known that by increasing the degree of cross linking, the elastic modulus increases. For small deformations, the elastic modulus follows [Coussot 2012]:

$$G = nk_BT$$

With n the cross-linking number, k_B the Boltzmann constant and $T = 20°C$ the temperature. It is then not surprising that we obtain the same evolution by decreasing the water concentration. The less concentrate is the gel, the stiffer it is.

2.1.2.2 Silica colloidal gel

To mimic the deformable character of wood due to its hygroscopicity, we used a viscoelastic materials. For a better understanding of drying in deformable porous media we will use silica colloidal gel as a model material. Using different particle sizes ($d_{TM\ 50} = 22\ nm$, $d_{HS\ 40} = 12\ nm$ and $d_{SM\ 30} = 6\ nm$, see Fig 2.6) at different concentrations (from $\phi = 1.875\ \%$ to $\phi = 11.25\ \%$) allows us to explore a wide range of structures.

Colloidal silica is prepared as monodisperse suspension in an aqueous phase stabilized electrostatically [Coussot 2012]. Silica particles are small enough for gravity force to be negligible compared to the Brownian agitation. They are subjected to two dominant forces:

- Van der Waals interaction: short-range attractive force. The interaction potential scales as $U_{vdW} \propto -\frac{1}{h^2}$ with h the distance between two particles.
- Electrostatic interaction : repulsive force. The interaction potential scales as $U_{elec} \propto \exp(-kr)$, with k^{-1} the Debye length representing the double layer thickness where the electrostatic effect persists.

The DLVO theory ([B.Derjaguin and Landau 1941], [Verwey and G.Overbeek 1949]) establish that colloidal stability is a competition between van der Waals and electrostatic forces. In Fig 2.5, the DLVO interaction potential show that the behavior of the colloidal suspension depends on the relative strength of these two interactions: $U_{DLVO} = U_{vdW} + U_{elec}$. At short and long distances, the overall interaction remains attractive. At intermediate range, electrostatic forces dominate which create a repulsive barrier. This prevents particle aggregation and ensures the suspension stability.

The behavior of the charges follows the basic Stern model: the silica particles carry a negative charge (from the deprotonation of silanol groups), and its magnitude gradually increases with

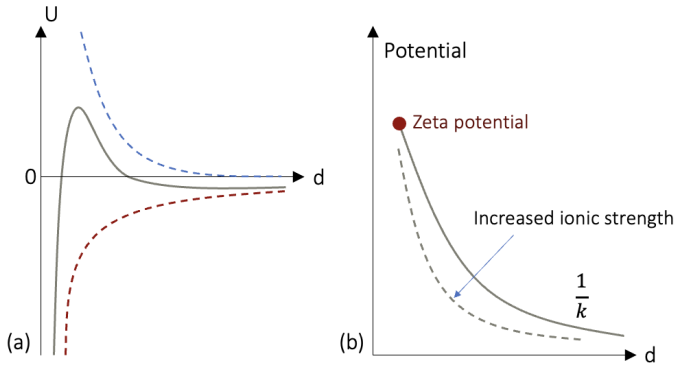

Figure 2.5: (a)The DLVO interaction potential (grey line) between two particles with separation d is the sum of the attractive van der Waals potential (red line) and a repulsive electrostatic contribution (blue line). (b) The Debye length variation according to the pH evolution.

increasing pH and ionic strength [Kobayashi et al. 2005]. Silica is an amorphous material of chemical formula SiO_2. In water, silica can either absorb proton or release one. The surface charge of silica depends on the pH of the suspension:

- for pH $<$ 2, the concentration of dissociated silanol groups is too low to allow aggregation, and the suspension is stable.
- for 2 $<$ pH $<$ 7, there are more dissociated groups, which allows particle aggregation; thus silica suspensions are instable in this pH range.
- or pH $>$ 7, there are enough dissociated silanol groups to create electrostatic repulsion between the particles, ensuring the stability of the suspension. The limit value pH = 7 is dependent on the ion concentration of the suspension, as adding salt to the suspension decreases the Debye length.

As the ion concentration increases in the liquid phase, the Debye length decreases, shortening the range of the repulsive interactions between particles. This results in a decrease of the repulsive maximum, and ultimately in the destabilization of the suspension, as the particle interaction becomes attractive at all distances.

Colloidal gels were formed from a solution of Ludox (solution 1: silica colloidal suspension stabilized by Na_2O) with Urea (solution 2: 8 moles solution in water) and a catalyst Urease (3 times of the total volume in mass) and water (solution 3). All chemicals were purchased from Sigma-Aldrich, USA. Studies presented in this manuscript involved three different types of Ludox suspensions: TM, HS and SM described in the table 2.4. In our solution, we use Urea that react with Urease creating ammonium leading to the decrease of the electrostatic repulsive force: $(NH_2)_2CO + 2\ 2\ H_2O \xrightarrow{Urease} 2\ NH_4^+ + CO_3^{2-}$.

Ludox	Mass fraction % w/w (% v/v)	Bead diameter (nm)	pH (at 25°C)	Ratio of SiO_2/Na_2O
TM 50	50 (30)	21	8.5 - 9.5	200 - 250
HS 40	40 (22)	10	9.2 - 9.9	89 - 101
SM 30	30 (14.6)	5.5	9.7 - 10.3	45 - 56

Table 2.4: Different silica solutions with the mass fraction of colloid, the diameter of the particles, the pH and the ratio of SiO_2/Na_2O.

The amount of the different solution is calculated to obtain a range of colloidal volume fraction from low to high concentration ($\phi = 1.875$ % to $\phi = 11.25$ %) with the following equations with details of each solution in the appendix:

$$V_{sol1} = \frac{100}{\%v,v}\phi V_{TOT}$$

$$V_{sol2} = \frac{V_{TOT}}{8}$$

$$V_{sol3} = (\frac{7}{8} - \frac{100}{\%v,v}\phi)V_{TOT},\ M_{Urease} = 3V_{TOT}\frac{mg}{ml}$$

We dissolved the desired quantity of salt into a volume of water and do the same for the Urease mixed with the solution 3. All the solutions are then added together. The gelation time depends on the amount of Urease: the higher the quantity introduced, the faster the catalytic reaction. However, note that the preservation of this product is poor, and its efficiency decrease over days. This is why we obtain discrepancies of the gelation time between each experiment.

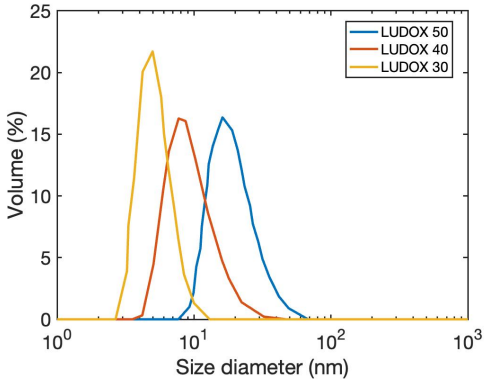

Figure 2.6: Size distribution by volume of the different Ludox solution in diameter (nm) made with particle size analyzers (MALVERN).

We analyze the bead size of our different Ludox solutions with a particle size analyzer - MALVERN (see Fig 2.6). The measurement is based on dynamic light scattering. The mean value for each solution is: $d_{TM\ 50} = 22\ nm$, $d_{HS\ 40} = 12\ nm$ and $d_{SM\ 30} = 6\ nm$. We observe that the distribution is quite scattered. Colloidal silica particles can aggregate over time. Even if Ludox solutions are stabilize, it is not surprising to obtain dispersed values.However, literature indicates particle sizes similar to those obtained with our method [Lesaine et al. 2020].

2.1.3 Conditioning method

Using the gravimetric method, we can control the moisture content of our samples. This method consists in placing the sample in an enclosure (desiccator), maintained at a fixed temperature ($20°C$) and a constant relative humidity of the air. To fix the relative humidity ($\%rH$) of the air, concentrated saline solutions (summarized in Table 2.5) are used and the sample is left to reach equilibrium.

PRODUCT	Relative humidity ($\%rH$ at 20°C)
Potassium sulphate	97
Baryum chlorure	90.4
Potassium chlorure	86
Ammonium sulphate	80.1
Strontium chlorure	71.5
Ammonium nitrate	65
Magnesium nitrate	53.5
Potassium carbonate	44
Potassium acetate	22.8
Silica gel	2

Table 2.5: Summary of saline solution used to control the relative humidity of our environment from 2 $\%rH$ to 97 $\%rH$.

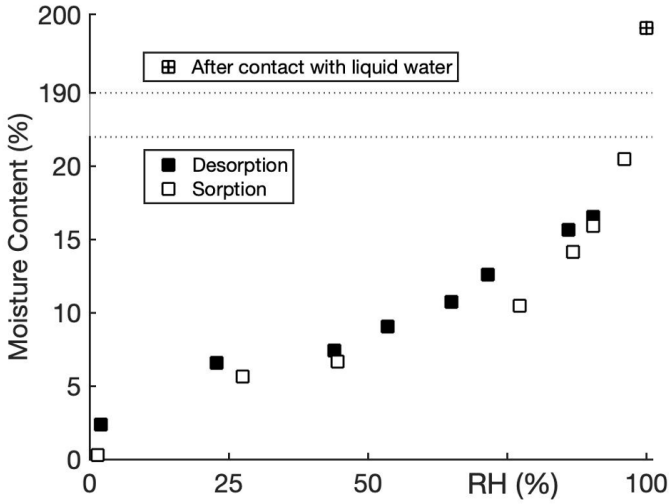

Figure 2.7: Sorption (blank square) and desorption (black square) curves for fir sample. The cross-square symbol corresponds to a fully saturated sample.

With the gravimetric method, we were able to obtain the sorption curve allowing us to compute the moisture content corresponding to a conservation humidity of our samples (Fig 2.7). As a reminder, the moisture content (MC) is the ratio between the quantity of water present in the sample and the mass of anhydrous wood: $MC(\%) = (m_{wood} - m_{dry})/m_{dry} \times 100$. The sorption

experiment was made on fir sample in sorption (blank square) and desorption (black square). The mass of anhydrous wood is obtained at the end of the sorption curve by putting the sample in the oven at $60°C$ during one week.

The water concentration of the hydrogel significantly varies with the relative humidity. After its preparation, each sample is placed in a desiccator in which the air is maintained at a fixed temperature ($20°C$) and a constant relative humidity imposed by a saturated salt solution (see table 2.5). The sample is used when equilibrium is reached (usually after a week). Measuring the mass fraction of water at equilibrium for the different $\%rH$ makes it possible to obtain the sorption isotherm of the material $C(\%) = m_{wet}/m_{tot} \times 100$. Corresponding data are shown in Fig 2.8. With such a material, we thus qualitatively reproduce the hygroscopicity of natural materials such as wood with in the case of hydrogels an important increase of the water content.

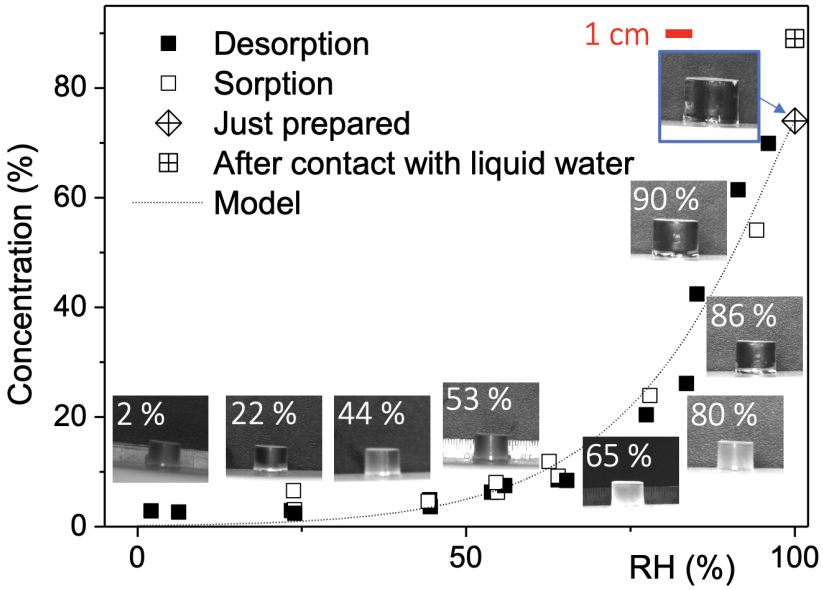

Figure 2.8: Sorption and desorption curves for the gel: water concentration according to relative humidity. A model is fitted to data. The cross-diamond symbol corresponds to a gel just prepared. The image corresponding to this stage is shown circled in blue. We then showed the volume evolution of the sample by images taken at different humidities. The cross-square symbol corresponds to a gel at equilibrium in contact with a liquid bath (fully saturated).

To obtain an approximation of the dry mass of our samples, we put the hydrogel in an oven at $60°C$ for a few days in order to remove as much water as possible. From our results in Fig 2.8, we observe that at ambient humidity ($\approx 50\ \%rH$), our samples are close to null saturation less than $5\ \%$ of water. Also, the dimensions of the gel evolve very little. Here we could verify that the evolution in volume of the sample corresponds to a loss of water in mass. From a humidity of about $70\ \%rH$, the curve rises sharply. Even at $98\ \%rH$, the hydrogel is not fully saturated. Indeed, for some tests, the hydrogel is immersed in a water bath for several days until reaching a saturated state (cross square), the final water concentration is then 89%.

2.1.4 Fluids

In this work we use different fluids to study our hygroscopic materials: water, dodecane, silicone oils and neutral cooking oil. This last fluid was studied mainly during the lockdown and the properties are not well known. For other fluids, the physical properties are described in the table 2.6.

FLUIDS	Viscosity ($mPa.s$ at 25°C)	Density ($g.cm^{-3}$ at 25°C)	Surface tension ($mN.m-1$)
Water	1	1	72
Dodecane	1.324	0.746	25.35
Silicon 20	20	0.950	20.6
Silicon 50	50	0.959	20.7
Silicon 550	125	1.065	24.5
Silicon 1000	1000	0.970	21.1

Table 2.6: Physical properties of the studied liquids.

The advantage of dodecane is that it has a viscosity similar to water. Silicone oils comes from Chimie Plus Laboratoire and are a useful tool as we can play with the viscosity parameter.

Some oils were used to filled the pores of wood in order to isolate the diffusion phenomenon of water in the cell wall. In Fig 2.9, we see that all the oils used have an NMR spectrum with a T_2 in the range on the T_2 of water in the vessels, fibers, or tracheids of the wood (see section 2.3 for more details on NMR techniques). This allows us to study the bound water in the cell wall without losing any information.

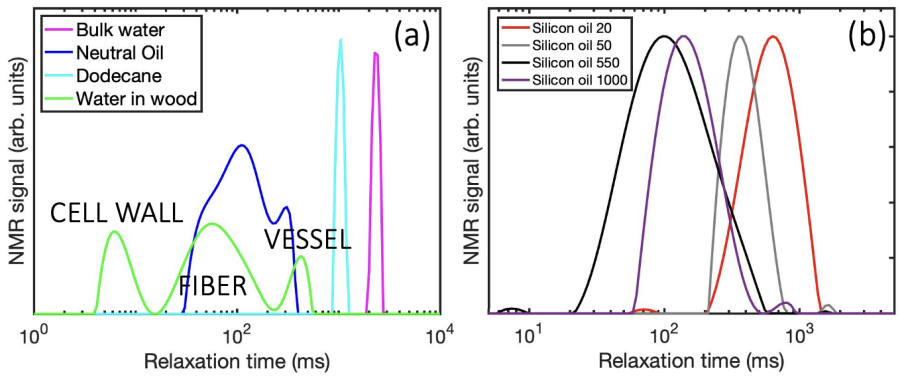

Figure 2.9: (a) Distribution of the relaxation time of the different fluids: water (pink), neutral oil (dark blue) and dodecane (light blue) compared to the water present in wood structure (green). (b) Distribution of the relaxation time of the different silicon oil.

2.2 Set-up

2.2.1 Sessile drop method

The dynamic of droplets is reported using the sessile drop method. This method is used to characterize the surface energy of a material but is adapted mostly for large contact angle. Indeed, by placing a droplet of liquid with a known surface energy, we can obtain from the shape of the drop (its contact angle θ_E on the material surface) the surface energy of the solid sample from the Young-Dupré equation (see Fig 2.10):

$$\gamma_{LV} \cos\theta_E = \gamma_{SV} - \gamma_{SL}$$

With V the vapor phase, L the liquid phase and S the solid phase.

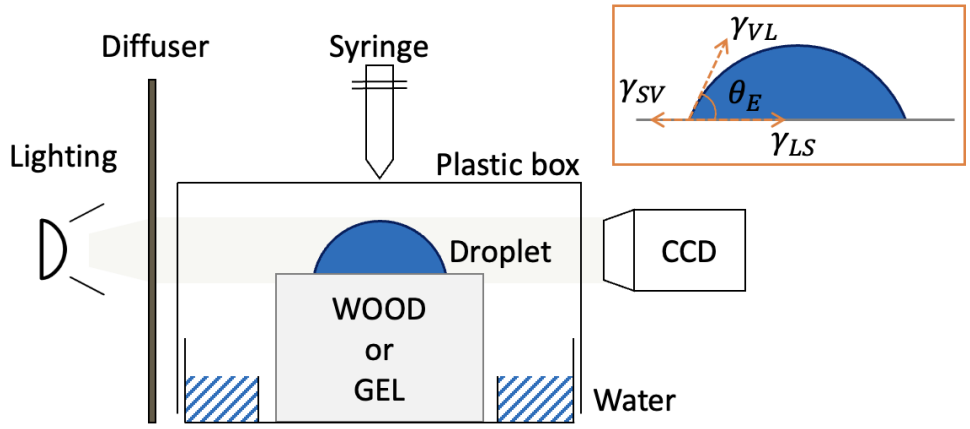

Figure 2.10: A schematic of the experimental set-up contact angle analysis. The insert represents an illustration of the sessile drop technique with a liquid droplet partially wetting a solid substrate with θ_C the contact angle and γ_{SV} the solid–vapor, γ_{LS} the liquid–solid and γ_{VL} vapor–liquid interfaces.

Fig 2.10 shows a schematic of the experimental set-up. A drop of liquid is deposited on top of the gel with a syringe and is filmed sideways with a Pike F-421 camera (2048×2048 $pixel$ resolution and 7.4×7.4 $\mu m/pixel$ spatial resolution). We are amongst others interested in the spreading and absorption dynamics of the drop. Thus, to restrain the effect of water evaporation from the droplet and from the sample (wood or gel), the experiment is sealed by a small plastic box in which air was saturated with water vapor (by adding a water bath). Note that, in contact with high humidity, hygroscopic material can absorb water and change its water concentration. However, our experiments follow timing too short for a sample to undergo a significant change. Note that we did not use a closed environment for all our experiments. Indeed, when we were only interested in the beginning of the dynamics or when we used the Goniometer method (evolution of liquid volume in time), the evaporation rate is negligible relative to the experiment time.

2.2.2 Imbibition experiment

A long cylindrical piece of hydrogel is immersed in a water bath at initial time. We then follow the apparent volume of the sample through its apparent diameter in time and the advancing front. Due to the large aspect ratio of the sample (length to diameter ratio larger than 10) we expect the water penetration to be essentially in the radial direction.

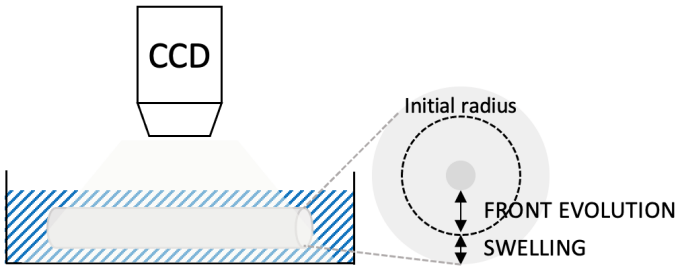

Figure 2.11: A schematic of the experimental set-up for imbibition.

The origin of the swelling phenomenon is due to an osmotic pressure gradient and the kinetics of water absorption by the gel is characterized by diffusion phenomena in the network. The solvent diffuses towards the interior of the network which leads to the swelling of the gel and the expansion of the polymer chains. The equilibrium state is reached when the pressure inside the network (due to the elastic retractive forces induced to the chains by the cross-linking nodes) is equal to the osmotic pressure [Bertrand et al. 2016].

When a gel is immersed in solution, water molecule first penetrates the surface of the sample and then diffuse towards the center of the gel, inducing a concentration gradient. The measurement of the amount of water absorbed by the hydrogel over the immersion time depends on the relaxation rate of the polymer chains V_{relax} relative to the diffusion rate of the solvent V_{diff} [Bajpai et al. 2008, Wadsö 1992]:

- $V_{diff} < V_{relax}$: the diffusion follows Fick's law.
- $V_{diff} > V_{relax}$: the diffusion follows a non-Fickian law.
- $V_{diff} = V_{relax}$: the diffusion is abnormal.

Ritger and Peppas 1987 have taken into account the geometry of the gel to predict the type of diffusion mechanism. The law is valid at short time with a water mass gain lower than 60 %:

$$\frac{M_t}{M_\infty} = kt^n$$

With M_t and M_∞ (in g) are respectively the water mass gains at time t and at the swelling equilibrium, k the diffusion constant and n the diffusion exhibitor depending on the geometry (see Table 2.7).

Diffusion exhibitor n			Diffusion mechanism
PLATE	CYLINDER	SPHERE	
0.50	0.45	0.43	Fick diffusion
$0.50 < n < 1.00$	$0.45 < n < 0.89$	$0.43 < n < 0.85$	Abnormal diffusion
1.00	0.89	0.85	non-Fickian diffusion

Table 2.7: General diffusion mechanisms for variable geometry systems.

2.2.3 Drying experiment

Drying experiment were conducted to observe the macroscopic deformation of colloidal gels. The gel is dried inside a $10\ mm$ diameter NMR tube with a constant air flux imposed on the free surface. The sample is a cylinder of $10\ mm$ diameter and $10\ mm$ height. The drying dynamic is filmed sideways with a camera at $0.01\ fps$.

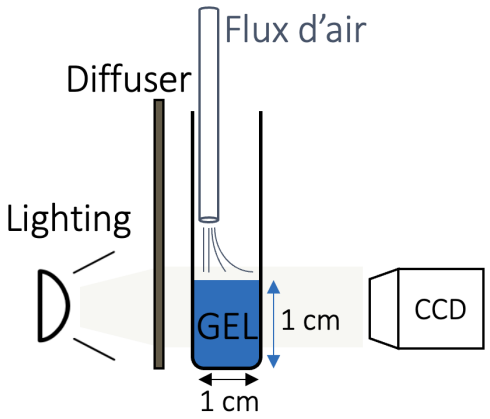

Figure 2.12: A schematic of the experimental set-up for drying.

2.3 Nuclear Magnetic Resonance - NMR

Nuclear Magnetic Resonance (NMR) is a non-destructive and non-invasive technique. It is most known for its applications in chemistry and medicine, but it has also wildly been used to study porous media. However, this instrument has his limits and using it can be challenging. First, it is not suited to every material as no metallic part can be used around the magnetic field of the apparatus. Also, NMR is a compromise between the time scale of the analyzed phenomenon and the minimum time machine needed to obtain accurate (or exploitable) data. However, it is a very powerful instrument, optimal for the study of wood and porous media targeting ^{1}H and following water present in the structure. We can obtain various information about the structure of materials and the processes occurring in them (porosity, pore size distribution, permeability, wettability, water saturation) [Hore 2015]. This technique allows to discern quantitatively, qualitatively, and locally liquid water in all its states. On the other hand, it is unable to detect solid and gaseous protons.

2.3.1 Principle of NMR

NMR works in 3 steps: polarization of the nucleus (equilibrium state), tilting of the magnetization in another plane with magnetic resonance (excitation) and signal acquisition with relaxation time (return to the equilibrium state).

2.3.1.1 Nuclear spin to nuclear magnetism

NMR exploits the magnetic properties of certain atomic nuclei which have a nuclear spin ($I = 1/2$) using a magnetic field to act on specific isotopes (most common used are ^{1}H, ^{13}C and ^{19}F).

The atomic nucleus can be assimilated to a sphere rotating around its axis characterized by its magnetic moment $\vec{\mu}$. Without any external magnetic field, the orientation of the nucleus is random, and the global magnetization of these protons is zero. However, if we apply a magnetic field $\vec{B_0}$, the magnetic moments can take two different orientations: aligned with the applied magnetic field ($m_s = +1/2$, spin quantum number) or aligned against the applied magnetic field ($m_s = -1/2$).

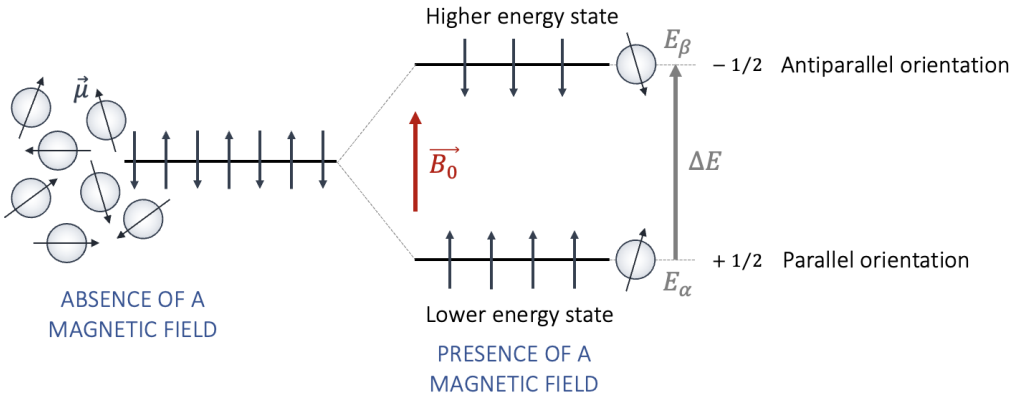

Figure 2.13: The different spin states of a nucleus ($I = 1/2$) from the absence of a magnetic field to the magnetization.

The presence of the magnetic field tends to lower the energy E_α (parallel orientation) but the thermal agitation provides them the energy to pass in the excited state E_β (antiparallel orientation) and thus tries to equalize the populations of two levels ($\Delta E = \mu \bar{h} B_0$). But the resulting equilibrium leads to a higher alpha level. This sum is called nuclear magnetization $\vec{M_0}$ and is different from 0. This is the value calculated in NMR and is proportional to the number of nuclei in the system:

$$M_0 = \frac{N B_0 \gamma^2 \bar{h}^2}{4 k_B T}$$

With N the number of protons oriented along $\vec{B_0}$, γ the gyromagnetic ratio specific to each isotope, $\bar{h}$ Planck's constant, k_B the Boltzmann constant and T the temperature.

The magnetic moments of the spins of the nuclei μ do not align exactly with B_0, but have a rotational movement around the field axis (precession motion) with an angular velocity w_0 described by the Larmor relation:

$$w_0 = \gamma B_0 = 2\pi\nu_0$$

With ν_0 the magnetic resonance frequency specific to each isotope.

2.3.1.2 Relaxation time to signal acquisition

We introduce a second electromagnetic field $\vec{B_1}$, perpendicular to $\vec{B_0}$. The time of the $\vec{B_1}$ pulse allows to control the orientation of the dipoles before letting the precession-relaxation take place. The magnetic moments will then reorient along B_0 in their thermodynamic equilibrium state, and their component in the xOy plane is measured. In certain experimental sequences (see section 2.3.2.2-IR or CPMG), the relaxation can then be described by two distinct processes (see Fig 2.14):

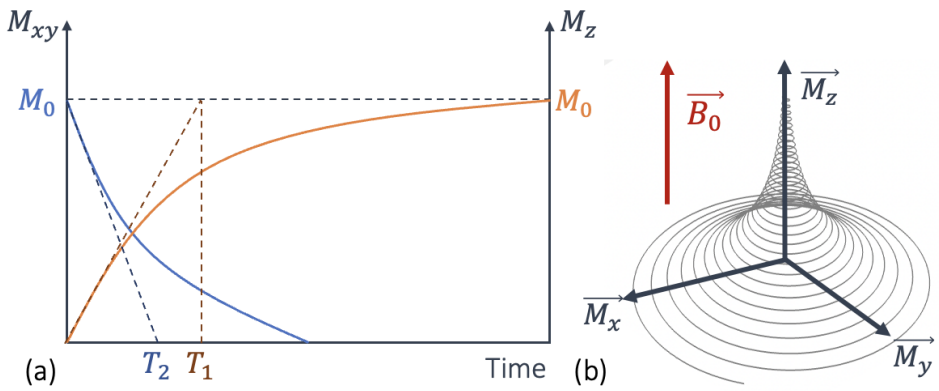

Figure 2.14: (a) Evolution of the amplitudes of the M_z and M_{xy} components of the magnetization during the relaxation. (b) Representation of the proton spin during relaxation in the plan (xyz).

- Longitudinal relaxation: it corresponds to the recovery of the longitudinal magnetization M_z

which is characterized by a relaxation time noted T_1 and follow an exponential law:

$$M_z(t) = M_0 - 2M_0 \exp^{-t/T_1}$$

- Transversal relaxation: it corresponds to the decay of the transverse magnetization M_{xy} which is characterized by a decrease of a relaxation time noted T_2 and follow a mono-exponential law:

$$M_{xy}(t) = M_0 \exp^{-t/T_2}$$

2.3.1.3 1D profile

We can obtain a 1D profile of the sample over the z axis by introducing a third magnetic field (gradient field). The resulting profile is an average value that can be measured in each section of a sample along the z axis. The 1D NMR profiles are obtained with Spin Echo sequence.

2.3.2 Protocol and sequence

2.3.2.1 Apparatus

We use a relaxometer that target the ^{1}H isotope by Bruker Minispec MQ20 with a $0.5\ Tesla$ permanent magnetic field corresponding to a frequency of $20\ MHz$. The maximum and optimal dimensions of a sample are $10\ mm$ or $18\ mm$ in diameter for $10\ mm$ in height according to the relaxometer used. Note that 1D profile experiment can only be done on the $10\ mm$ which is equipped with a $4\ T.m^{-1}$ vertical pulsed gradient unit. The samples in the relaxometer is controlled at a constant temperature of $20°C$.

2.3.2.2 Sequence

There are different sequences to recover the data needed for the experiment: Free Induction Decay (FID) to obtain a quick NMR signal, Inverse Recovery(IR) to obtain T_1, Carr and Purcell 1954, Meiboom and Gill 1958 (CPMG) to obtain T_2 or 2D sequences to obtain a correlation spectrum $T_1 - T_2$ or $T_2 - T_2$. In general, these sequences are composed of three steps and is usually repeated several times to increase the signal to noise ratio:

- Perturbation of the magnetic field by the application of magnetic field $\vec{B_1}$ at $90°$ (maximum signal) or $180°$ (no signal) pulse depending on sequence.
- Time to return to equilibrium (TR): the minimum time for the magnetization to reach its equilibrium state is $5\ \times T_1$.
- Acquisition of the NMR signal.

The measure of T_1 is not sensitive to inhomogeneity of the magnetic field. But the measure of T_2 can be faster and is more suitable for our samples. For the CPMG sequence (see Fig 2.15) a $90°$ pulse is applied in order to tilt the magnetization in the transverse plane (O_{xy}), then a series of n

$180°$ pulses spaced by an echo time (TE) allows to get rid of the inhomogeneity of the magnetic field.

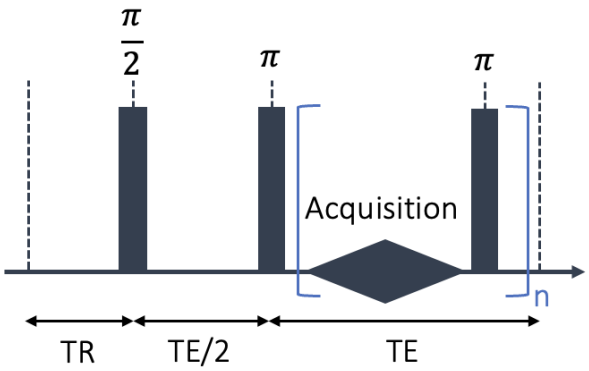

Figure 2.15: Description of the CPMG sequence for measuring the transversal relaxation T_2.

Unidimensional profiles can be obtained by coupling previous sequencing techniques with a spatial encoding method.

2.3.3 Interpretation

2.3.3.1 Interpretation of the NMR signal

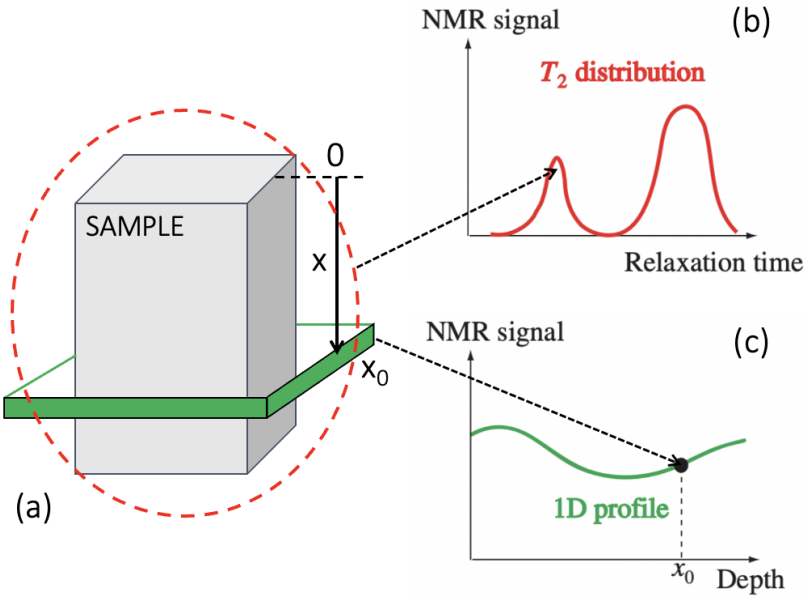

Figure 2.16: (a) Scheme of the experimental setup with the sample inside the magnet and (b) main NMR (T2 distribution) and (c) 1D profile sequences used to explore the water content [Cocusse et al. 2022].

NMR allows us to target hydrogen at the liquid state highly present in water (not the ones in the solid matrix and not the water vapor). We measure the transverse relaxation time T_2 using

a Carr-Purcell-Meiboom-Gill (CPMG) sequence. After a Laplace transform of the NMR signal ([Provencher 1982]), we can directly access the relaxation time distribution (see Fig 2.16-b). The representative T_2 is not the T_2 at the maximum value of the peak but the weighted mean of the peak. The amplitude of the signal is proportional to the magnetization and thus to the number of nuclei. It is reflected in the spectrum by the sub-peak air. This amplitude can be converted to a known quantity and applied to the whole experiment (transformed in water content for example).

The 1D profiles obtained by Fourier Transform represent the spatial distribution of water along the sample axis, each data point corresponding to the water content in a cross-sectional layer of thickness equal to the spatial resolution (see Fig 2.16-c). We thus obtain the total quantity of water distributed along the z axis. This can be used to follow a capillary rise or to observe dry fronts.

2.3.3.2 Relaxometry in porous media

We can investigate a liquid inside a porous media thanks to NMR described by the Fast Exchange Theory [Brownstein and Tarr 1976]. The water contained in a pore is then divided into two categories: surface water present as a thin layer near the surface of the pore and bulk water present in the rest of the pore. The experimentally measured relaxation time is described by the percentage of these two quantities:

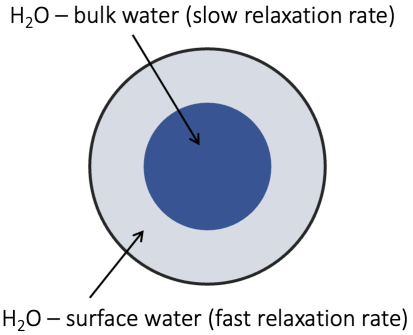

$$\frac{1}{T_{1,2}} = \frac{\eta_{surface}}{T_{1,2\ surface}} + \frac{\eta_{bulk}}{T_{1,2\ bulk}}$$

With $\eta_{surface} + \eta_{bulk} = 1$, the relaxivity in $m.s^{-1}$.

Considering a pore of diameter a, volume V and surface S filled with liquid, the molecules diffuse (D, the coefficient of diffusion) in the pore with a Brownian motion. The interpretation is the results of the difference between the exploration time of the pore and the diffusion time:

- Surface limited relaxation: the diffusion is fast between the two populations ($(\rho a)/D << 1$), the molecules have been able to explore the whole pore and the average relaxation time is influenced by the surface paramagnetism. This is the case in small pores.

$$\frac{1}{T_{1,2}} = \frac{1}{T_{1,2\ bulk}} + \eta_{1,2}\frac{S}{V} \tag{2.2}$$

  With $\eta_{1,2}$, the relaxivity in $m.s^{-1}$ characteristic of the pore, 1 and 2 are two possible cases of longitudinal relaxation or transversal relaxation and $S/V = 6/a$ for a sphere.

- Diffusion limited relaxation: the pore size is too large compared to the characteristic diffusion

time ($(\rho a)/D >> 1$), the magnetization is no longer homogeneous in the pore.

$$\frac{1}{T_{1,2}} = \frac{1}{T_{1,2\ bulk}} + \alpha\frac{D}{a^2}$$

With α an adimentionnal coefficient depending only on the shape of the pore.

These models allow us to approximate the pore size of a material in the analyze of the relaxation time $T2$ [Maillet, Sidi-Boulenouar, and Coussot 2022]. They allow us to understand that the relaxation time is proportional to the radius of a pore. Thus, in a porous medium, the greater the relaxation time, the larger the pores.

2.3.3.3 Interpretation of the relaxation time evolution

In the resolution of CONTIN [Provencher 1982], the parsimony factor (λ) is a free parameter allowing us to optimize the noise sensitivity of the inverse Laplace transform. The criterion for a precise choice always remains arbitrary [Faure and Rodts 2008]. Changing the value can alter the peak distribution: either by refining the peaks (even dividing them) or by thickening a peak (even merging them). Note that whatever the value of the lambda, for the same peak, its amplitude and its representative $T2$ will not change. Choosing the right lambda is a matter of finding the right compromise between a distribution bearing physical content or an artifact while keeping a maximum resolution.

The advantage of fixing the lambda is that we can compare each distribution during a dynamic. One analysis is interesting in our study: the shift or not of the representative $T2$. This information is all the more interesting in the case of porous media, physically interpreted by [Maillet, Sidi-Boulenouar, and Coussot 2022].

2.4 Confocal laser scanning microscopy

Confocal microscopy or confocal laser scanning microscopy is an optical imaging technique designed to increase the optical contrast and resolution of a sample by focusing on a certain depth of the sample and blocking out any out-of focus light. This instrument is widely used in life sciences and materials science. Gels are a well-suited material for confocal microscopy as it is transparent, but the limitation is the acquisition time which makes it challenging to observe fast dynamic phenomenon.

2.4.1 Principle of confocal microscopy

Confocal microscopy relies on the presence of a fluorophore in the sample that can be excited with a specific light source with a given wavelength and then emits light at a higher wavelength.

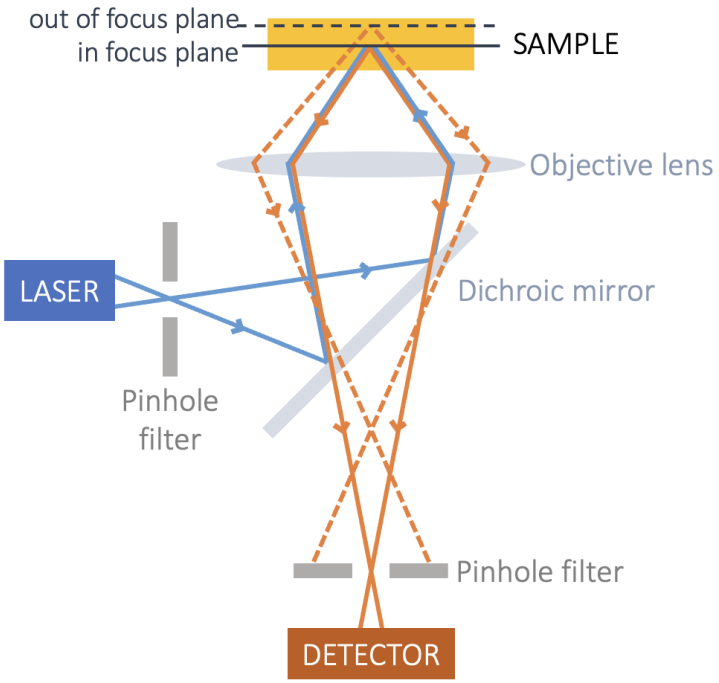

Figure 2.17: Scheme of the principle of confocal microscopy showing the excited light path (blue), the emit light path (orange) and the rejected light path (orange dotted).

A schematic of a typical confocal microscope is given in Fig 2.17. Instead of white light, the confocal microscope uses a laser light which is more focus to excite the sample. The laser beam (blue line) passes through a first pinhole filter that prevent any background noise. The light is then reflected by a dichroic mirror, passes through the objective lens, and reaches the sample. The fluorophore is excited by the light source and emits light in response. The light (orange line) is then able to pass through the specific dichroic mirror. The dichroic mirror allows one type of wavelength to be reflected and one type to pass through. The light finally passes by a last pinhole designed to cut out any unwanted emission light before being detected. Indeed, light from other locations in the sample goes through the objective and the dichroic mirror, but is rejected by the pinhole

(orange dotted line).

From this principle of capturing one single point in space, we are able to construct 2D or 3D images by moving the laser beam relative to a fixed sample (rotating the mirrors) or translating the sample relative to a fixed laser beam (Z-stack or tile-scans).

2.4.2 Main features

We use a Leica SP5 confocal microscope with a 10X objective, a $488\ nm$ laser (the most powerful and best configured for our objective) and a pinhole at $71\ \mu m$. Image format is $512 \times 512\ pixels$. We can also play with a lot of features to improve the results of our experiments:

- Objective lens: the magnification of the objective can be changed (typically ranges from 10x to 100x) according to sample scale we want to look at. Changing the index of refraction can also improve the resolution of the image and increase the magnification, the highest the better (air 1.003, water 1.33, oil 1.51).
- Laser: changing the light can improve the resolution, the smallest wavelength the better the resolution. Our confocal microscopes are built with an optimal wavelength of $488\ nm$ which gives the strongest signal.
- Mirrors: the correct dichroic mirror as to be chosen according to the excitation/emission spectrum of the fluorophore being used in the experiment. The two wavelengths (excited and emitted) must be large enough to allow separation of illumination and detection beams by the mirror.
- Gain: the gain corresponds to the amplification applied to the detection system. Higher gain results in brighter images but also in higher amount of background noise. The gain must be adjusted with the laser power strength to obtain the best image. Increasing too much the laser power can also result in bleaching.
- Pinhole: the pinhole can be adjusted in order to obtain the best signal to noise ratio. Increasing the pinhole diameter leads to enhance the amount of light detected and decreasing it leads to study a thinner section of the sample.
- Time: the confocal microscope is limited in time by the displacement frequency of the mirrors to reconstruct a 2D or 3D image. Conventional mirrors have a line scanning frequency of $500\ Hz$. Resonant scanners are mounted on piezoelectric and can go up to $8\ Hz$. Both confocal microscopes are used in this work.

2.4.3 Applications

2.4.3.1 Specific features for colloidal gel

In the case of colloidal silica gel, we use a conventional confocal at $0.01\ fps$ with a specific mirror, beam splitters 30/70 that allows to reflect 30% and transmit 70% of the light. The emission bands

should be on the same wavelength as the exited band. This system will allow us to detect speckle patterns in the sample due to the diffraction of the light by colloidal particles. The magnitude of the transmitted beam depends on the thickness and the refractive index of the substrate. Therefore, this assembly is suitable for materials with very different refractive index (see Fig 2.18-a and b).

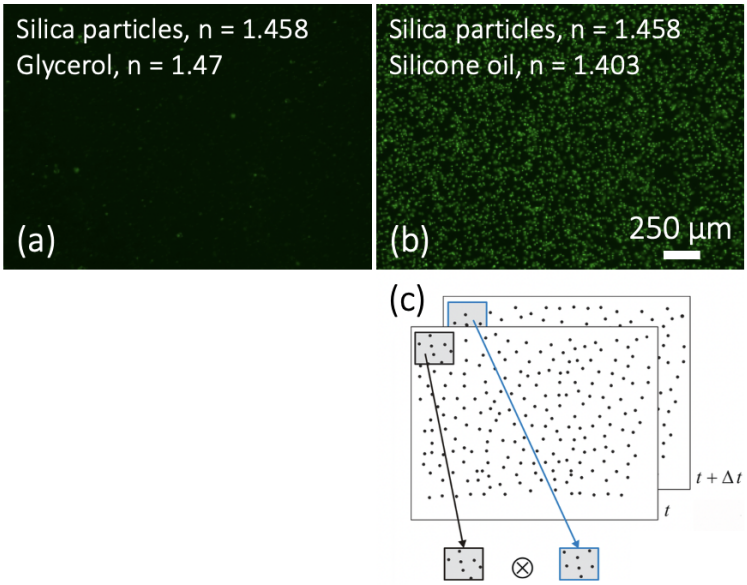

Figure 2.18: Fluorescent images of a colloidal suspension in (a) glycerol and (b) silicone oil. Note that all colors are artificial: the detected signal is an intensity unrelated to the color of the excitation or emission lights. (c) Scheme of the PIV technique comparing two images at different timing [H. Kim 2022].

Moreover, tracking the speckles, we can analyze the deformation of the sample [Aime et al. 2016] with PIV (particle image velocimetry) (see Fig 2.18-c). It also allows us to correlate the raw image with fluorescent signal and distinguish the different phases present in the system.

2.4.3.2 Specific features for polymeric hydrogel

In the case of the PEG hydrogel, as we are looking at a fast dynamic, we used the resonant confocal that allows us to reach $15\ fps$. We used the fluorophore detection of the confocal in different ways: adding fluorescent particles or using a fluorescent dye in the fluid (fluorescein).

As we do not need such sharp images, we also use fluorescent microscopy that relies on the same principles without using pinholes and with the use of the white light and an exciting filter. We then have more noise but a larger field of view and a better frame rate.

2.5 Rheometer

2.5.1 Principle of rheometry

2.5.1.1 Simple materials in rheology

Mechanical properties of material are defined by their constitutive equations which describe the force undergone during their deformations. Let us review some basic laws for solid materials:

- In tension or compression, in the linear elastic region of a material, the stress-strain relation is described by Hooke's law: $E = \sigma/\epsilon$ where E, the Young modulus is express in Pa, the stress $\sigma = F/A$ in Pa with F, shear force (N) and A, shear area (m^2), the strain $\epsilon = \Delta L/L$ in $m/m(\%)$.
- In simple shear, the shear modulus is described by: $G = \tau/\gamma$ in Pa with the shear stress $\tau = F/A$ in Pa and the shear strain $\gamma = s/h$ in $m/m(\%)$ with s, the transverse displacement (m) and h, shear gap (m).

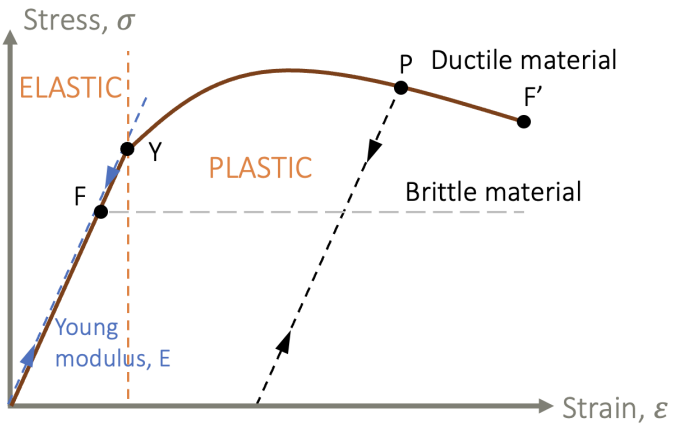

Figure 2.19: Stress-strain diagram showing the elastic and plastic regime for ductile and brittle materials [Coussot 2012].

The mechanical strength depends on the type of material (see Fig 2.19):

- Ductile materials: can undergo large deformation before failure (F'). The deformation increases linearly with the stress and is reversible until a critical deformation (Y defined as the yield strength). We are in the elastic regime. From point Y, all deformations are partly irreversible (as shown at point P). We are then in the ductile (or plastic) regime. .
- Brittle materials: deforms elastically up to a critical value (F) where the material fractures defined as the yield stress in rheology.

2.5.1.2 Apparatus

A rheometer works simply by relating a materials property from how hard it is being pushed, to how far it moves by. They are two main categories, stress controlled (TA instrument) or strain

controlled (Ares G2). Strain controlled rheometers are considered better defined and can probe higher frequency. They are well suited for diluted or semi-diluted systems like gels. Stress controlled rheometers have a better torque sensitivity and are well suited for medium and large particle materials such as cement or pasty materials. Nowadays, feedback loops are fast enough that most rheometers can operate in both modes. The main geometries used under shearing conditions are:

- Couette cell made of concentric cylinder with bob radius R_i and cup radius R_e and internal angle α at the tip of the bob. This geometry has a good sensitivity for low-viscosity fluids.
- Plate-plate with radius R and a distance between plates h. This geometry has a non-uniform strain along the sample, but we can adjust the gap height so is good for testing boundary effects like slip.
- Cone-plate with radius R and a cone angle α. This geometry has a uniform strain/strain-rate along the sample but have a fixed gap height.

2.5.1.3 Oscillation tests

Most material exhibit a viscoeslastic behavior. To analyze this type of material, we use the rheometer in rotational oscillation. Oscillation experiments (see Fig 2.20) are based on dynamic stress or strain applied sinusoidally with defined amplitude and frequency (input deformation). And then the material response in strain or stress is measured (output response). Strain and stress are described with $\gamma(t) = \gamma_0 \sin(wt)$ and $\tau(t) = \tau_0 \sin(wt + \delta)$. The phase angle δ between the deformation and response is measured:

- $\delta = 0°$: ideally elastic deformation behavior (Hookean Solid).
- $\delta = 90°$: ideally viscous flow behavior (Newtonian Liquid).
- $0° < \delta < 90°$: viscoelastic material.

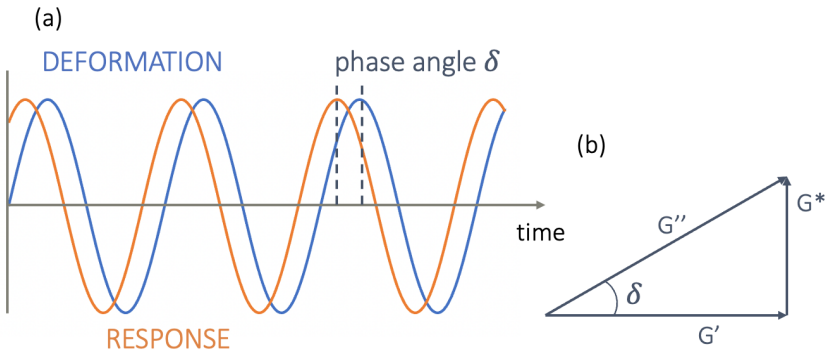

Figure 2.20: (a) Comparison between the preset and response sine curves of strain and stress with the phase-shift angle δ. (b) Vector diagram illustrating the relationship between complex shear modulus G^*, storage modulus G' and loss modulus G'' using the phase-shift angle δ.

The viscoelastic parameters are then defined by:

- Complex shear modulus: $G^* = \frac{\tau_0}{\gamma_0}$ in Pa with τ_0, shear stress amplitude in Pa and γ_0, strain amplitude $(\%)$. Measure of materials overall resistance to deformation.
- Storage modulus: $G' = G^* \cos\delta$ in Pa represents the elastic portion of the material, its ability to store energy.
- Loss modulus: $G'' = G^* \sin\delta$ in Pa characterizes the viscous portion of the material, its ability to dissipate energy (energy lost as heat).
- Loss factor: $tan\delta = G''/G'$ is dimensionless. This factor describes the ratio of the two portions of the viscoelastic behavior.

2.5.2 Applications

2.5.2.1 Protocol for colloidal gel

The objective here is to follow both the gelation process of the colloidal gels and its rheological properties until failure. For this, we used both types of rheometers because of unavailability of devices. We have verified later on that both rheometers exhibit similar results. The rheometers are used in oscillation mode with a cone plate geometry of $50\ mm$ diameter and $0.02\ rad$ angle corresponding to a $500\ \mu m$.

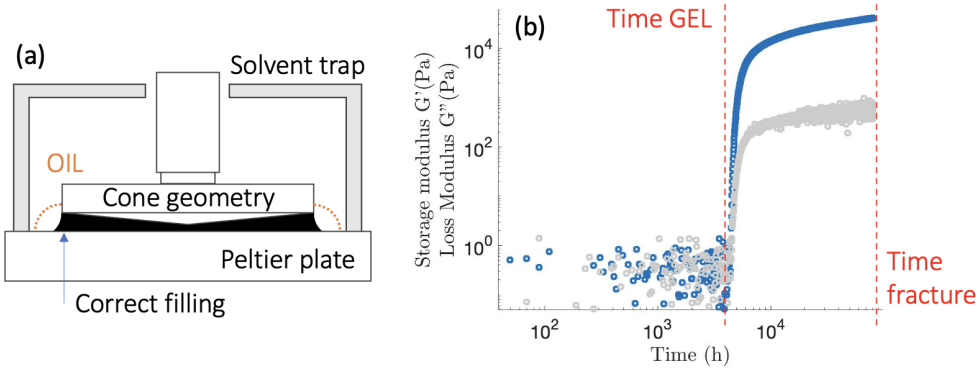

Figure 2.21: (a) Scheme of the rheometer set-up. (b) Evolution of the storage (blue square) and loss (grey square) modulus with time during aggregation of $12\ nm$ silica particles with initial volume fraction of $7.5\ \%$.

First, to look at the gelation process of our system over time, we realize a time sweep: the material is monitored at a constant frequency ($w = 1\ Hz$), amplitude (strain $\gamma_0 = 0.05\ \%$) and temperature ($25°C$). The experiment starts by loading the sample as it is still liquid without introducing air bubbles (see Fig 2.21). To restrain the effect of evaporation, the edge of the sample (in contact with air) is covered with silicon oil (insoluble in water) and the all system is closed in a chamber (solvent trap cover). The gelation process is followed during $22\ h$. The gel then follows different behavior (see Fig 2.21-b): the diluted regime (the storage modulus is equal to zero), the

network formation (the storage modulus increase rapidly) and the ageing (the storage modulus increase slowly). This point will be detailed furthermore in this thesis but note that we defined the change between the diluted regime and the network formation regime but a time noted t_{GEL}. As the gel can age, we impose the same experiment time to be consistent between each gel. Thus, the fracture experiment will start at time $t_{FRAC} = 22\ h$.

To determine the linear viscoelastic regime of our system, we realize a strain sweep from $0.03\ \%$ to $1000\ \%$ until the failure of the material. The material response to increasing strain deformation amplitude is monitored at a constant frequency ($w = 1\ Hz$) and temperature ($25°C$). We then record the evolution of storage modulus, the loss modulus, the yield stress, and the normal force according to the yield strain.

2.5.2.2 Protocol for hydrogel - DMA

We are interested in the young modulus of our hydrogels, and we want to know its evolution as a function of their water concentration. The use of a rheometer was not adapted here. Indeed, the torsion experiment was not suitable as we observed a slip of the geometry on the surface of the gel (more important when the sample was concentrated in water). We have therefore performed tests with a Dynamic Mechanical Analysis (DMA) which allows us to perform tests in compression. DMA measurements are performed in oscillation using two parallel plates. The viscoelastic properties of materials are determined as functions of frequency from $1\ Hz$ to $300\ Hz$ with a constant applied force ($0.1\ N$), displacement ($10\ \mu m$) and temperature ($25°C$). We used square samples with variable dimensions (less than $1\ cm^2$). The dimensions are directly recorded in the machine and are taken into account for the evaluation of rheological properties. It is however important to obtain smooth and parallel surfaces. The samples are either dried in an oven at $60°C$, or used at the unmold time, or soaked for a few days in a water bath to obtain different water concentrations. The sample is then placed between two planes and the instrument oscillates the top plane in compression to determine the rheological properties of our materials. Thanks to this technique, we avoid any slip of the gel with the geometry.

Chapter 3

Water transport in wood

Wood material has remarkable mechanical, thermal, and hygroscopic properties but water transfers inside wood as vapor or liquid can alter the material with time. The physical mechanisms governing water transfers are still not fully understood. Indeed, the complex structure of wood implies a subtle hydraulic system involving exchanges between the three water phases: vapor, bound water and free water. We therefore want to understand the different flows involved in the imbibition and drying process.

1. During imbibition process, due to the porous structure of wood, the penetration of a liquid can be considered analogous to a capillary rise in a porous medium with well-defined pore radii. Laplace's law shows that a liquid will rise in a dry capillary if the tube has a surface energy γ_{SV} greater than the surface energy γ_{SL}, with S relating to the solid phase, V the vapor phase and L the liquid phase. From the spreading parameter (measure of the tendency of a liquid phase to spread on the solid phase), we can define an imbibition parameter: $I = \gamma_{SV} - \gamma_{SL}$.

   - In the case of the rise of the liquid ($I > 0$), the system energy is lower for a wet surface.
   - In the case of the drop of the liquid ($I < 0$), the system energy is lower for a dry surface.

   The hydrostatic equilibrium is described by Jurin's law. The equilibrium of the pressure field is reached when gravity compensates the Laplace pressure in the tube at atmospheric pressure:

$$H = \frac{2\gamma \cos\theta}{\rho g R}$$

   With H the maximum height reached by the water(in m), γ the surface tension of the liquid and ρ its density, θ the contact angle between the liquid and the solid wall of the tube of radius R and g the acceleration of gravity.

   Darcy's law is an equation that describes the flow of an incompressible fluid in steady state through a porous medium:

$$\nabla P = \frac{\mu Q}{kS}$$

Where ∇P is the pressure gradient between two points separated by a unit distance (in Pa/m), μ is the viscosity of the fluid (in $Pa.s$), Q is the flow rate of the fluid through the medium (in m^3/s), S is the cross-sectional area of the medium (in m^2) and k is the permeability (in m^2). The permeability of an interconnected porous material of uniform pores can be written in a simple form as: $k = (\varepsilon R^2)/8$ with $\varepsilon = V_{pores}/V_{total}$ the porosity of a porous medium defined as the ratio between the volume of pores and the total volume of the medium. We expect the permeability to increase with the square of the pore size ($k \propto R^2$). However, the coefficient depends on the exact structure of the medium (including connectivity and tortuosity). For a porous sample of length L, the effective average length for a flow line through the sample is $L_e > L$, the ratio of these two values defines the dimensionless tortuosity τ of the porous medium: $\tau = L_e/L > 1$.

Spontaneous imbibition in the pores is created by the pressure gradient at the interface causing the fluid to flow.

$$\nabla P = \frac{2\gamma \cos\theta}{hR} = \frac{\mu V}{k}$$

Where $V = \delta h/\delta t$ and h is the position of the imbibition front. By neglecting the gravity and setting the initial condition $h(t = 0) = 0$, we can solve this differential equation and obtain the Washburn model in the absence of gravity effects:

$$h(t) = \sqrt{\frac{\gamma R \cos\theta}{2\mu} t}$$

In the case of wood, it has been shown experimentally for hardwood [Johansson and Salin 2011] and softwood [Sedighi-Gilani et al. 2014] that the evolution of the mass of water absorbed evolves as a square root of time. These results suggest typical Washburn behavior. However, taking into account the capillary rise via vessels of radius R, Zhou, Caré, Courtier-Murias, et al. 2018 have shown that spontaneous water imbibition in dry wood is several orders of magnitude slower than expected from standard Washburn capillary imbibition. Mainly, it was demonstrated that below the FSP (saturation of the wood in bound water), some interplay between bound and free water could affect the imbibition process. The same observation was made with both wood types (hardwood and softwood) [Gezici-Koç et al. 2017] showing that the imbibition is internally limited by the transport of water in the form of bound water at larger distance than free water, suggesting that this bound water could control the free water advance. In contrast, oil imbibition is much faster, and its dynamic is well described by the standard Washburn theory [D. Nguyen et al. 2020, Zhou, Caré, A.King, et al. 2019].

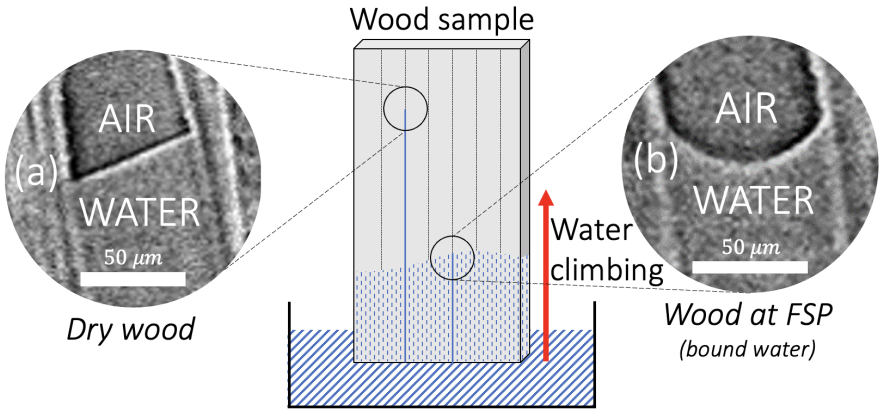

Figure 3.1: Air-liquid interfaces inside vessels in tangential-longitudinal (TL) cross-sectional images taken in different conditions: (a) dry sample and (b) saturated in bound water [Zhou, Caré, A.King, et al. 2019].

Zhou, Caré, A.King, et al. 2019 explained the origin of the effect of the slowed dynamics by comparing microscopic images of the capillary rise in a dry sample with a saturated sample (see Fig 3.1). Note that at FSP, it was shown that the imbibition process is fast and corresponds to Washburn model. Looking at the interface of air-water in the vessels, the slowed dynamics can be explained by a strong change in the wetting properties. Similar results were obtained using a model material, hydrogel.

It should be noted that hardwood has different pore sizes including vessels and fibers. The fibers are closed pores connected by small pits. Their filling process is poorly understood. It seems that pits connecting fibers together or with vessels are too small to allow water to pass through [Zhou, Caré, A.King, et al. 2019]. Indeed, using oil with same viscosity as water, it seems that the sample is filled with liquid only in vessels (see Fig 3.2-b). Although the process by which water fills the fibers is poorly understood, assumptions about the involvement of bound water in this process have already been made by 3.2. Indeed, it seems that the fibers fill homogeneously in all the directions of the wood which goes against a filling by the pits which are more or less present according to the directions of the wood. Furthermore, it has been observed that the fibers gradually fill up around a vessel by layers from one to the next (starting from the closest to the vessel) (see Fig 3.2-a).

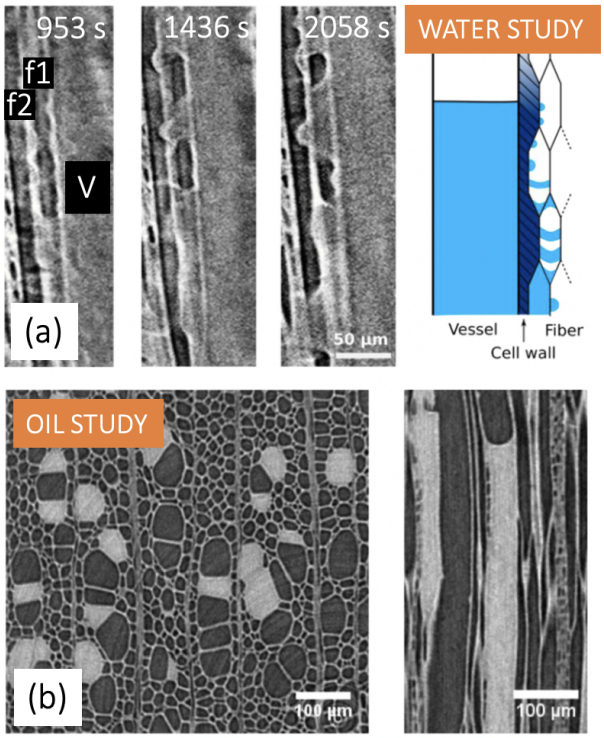

Figure 3.2: (a) Image sequence at different times during imbibition, showing how water invades the fibers around a vessel (V: vessel filled with water, f1: fiber close to vessel V, f2: fiber farther from vessel V) with a schematic of the proposed mechanism of water penetration in wood. (b) XRμCT images of a hornbeam sample put in contact with oil (RT slice and TL slice of the sample) [Zhou, Caré, A.King, et al. 2019].

2. In drying, it has also been shown that bound water is a central element for the circulation of free water. Indeed, in softwood and hardwood, for slow drying, the bound water is the last to be extracted [Penvern et al. 2020, Cocusse et al. 2022]. The drying is controlled by water diffusion through solid cell-walls, which transports free water from cell lumens to the free surface (see Fig 3.3). Note that in hardwood, the water in vessels is extracted before the water in fibers. In softwood, for fast drying, the water extraction relies on two mechanisms of diffusion of bound water where bound water concentration gradient develops from the free surface, in a region without free water, and extends in depth in the sample [Cocusse et al. 2022].

Finally, bound water seems to be the central element that governs the flow transport processes in wood. Obtaining the diffusion coefficient of bound water in the wood cell wall is therefore an important task. Diffusion is the process by which matter is transported from one part of a system to another as a result of random molecular motions [Crank 1975].

A number of works have been done to obtain a diffusion coefficient for various species in the different directions of the wood with methods such as weight tracking or monitoring of wood deformations. Table 3.1 shows some examples of diffusion coefficients obtained in the hygroscopic

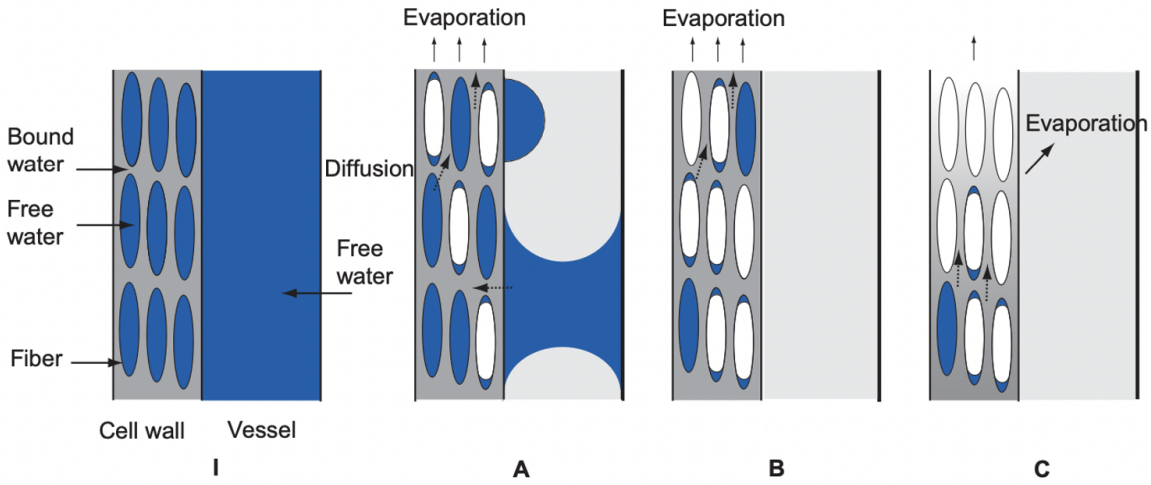

Figure 3.3: Scheme of principle of water transport at the different stages of longitudinal drying of wood. (I) initial stage. (A) Free water extraction from fiber and vessel towards cell walls, then diffusion towards free surface. (B) Vessels are empty. Extraction of free water from fibers then diffusion. (C) Vessels and fibers are empty over some distance below the free surface. Extraction of bound water leading to the formation of a concentration gradient in this region. Main evaporation from around the upper boundary of free water. [Penvern et al. 2020].

domain for different species. The diffusion coefficient depends on different parameters:

Diffusion coefficient ($m^2.s^{-1}$)	**Longitudinal direction (L)**	**Tangential direction (T)**	**Radial direction (R)**
Beech [Agoua, Zohoun, and Perré 2001, T. Nguyen 2014]	1.54×10^{-9} 5.24×10^{-10}	9.9×10^{-11} 8.96×10^{-11}	1.92×10^{-10} 1.79×10^{-11}
Scots pine [Agoua, Zohoun, and Perré 2001]	1.8×10^{-9}	4.29×10^{-11}	2.87×10^{-10}
Fir [T. Nguyen 2014]	1.04×10^{-9}	2.47×10^{-11}	1.24×10^{-11}
Douglas [Jamaaoui 2017]	1.92×10^{-10}	4.36×10^{-11}	9.29×10^{-11}

Table 3.1: Bibliographic synthesis of diffusion coefficient values (in $m^2.s^{-1}$).

- The permeability of wood: the porosity of wood allows water to circulate in the form of vapor. Therefore, the diffusion coefficient can only be considered as an apparent diffusion coefficient (where the diffusion of vapor interferes with the measurement of the diffusion coefficient of bound water). The vapor is adsorbed on one side of the cell wall and then desorbed on the other. The porosity can therefore involve different paths of water by considering the cell walls as obstacles where exchanges take place between bound water and water vapor.
- The anisotropy of wood: we have seen in the section 1.2.5 that bound water implies more deformation in the tangential direction than in the longitudinal direction. It is therefore not

surprising to obtain diffusion coefficients that differ depending on the directions. Moreover, it has been shown that the permeability of wood implies different diffusion paths for the three directions. Indeed, the connectivity between the pores is not identical. In particular, it is known that there is little connection in the tangential direction for hardwoods. According to Siau 1984, the longitudinal diffusion coefficient is about three times that of tangential direction and two times that of radial direction. This difference should be lower for softwoods due to the strong presence of areolated pits allowing a greater migration of water in the transverse and radial planes.

- The humidity of the environment: the diffusion coefficient seems to increase with the increase of the surrounding humidity, especially in the radial and tangential directions. Rosen 1976 proposed a law of exponential form to represent the influence of the water content on the diffusion coefficient:

$$D = D_0 e^{\alpha n}$$

  With n the moisture content of the wood, α a factor that takes into account the direction (positive in the radial and tangential directions, and negative in the longitudinal direction) and D_0 the diffusion coefficient in anhydrous state.

- The temperature of the environment: it has also been noticed that the diffusion coefficient increases with temperature.

Nowadays, there are two main methods to evaluate the diffusion coefficient of water:

- The cup method uses data from the steady-state experiments of bound water transfer [Olek 2003]. The diffusion flux $\overrightarrow{j}$ is described by Fick's law (in $m^{-2}.s^{-1}$):

$$\overrightarrow{j} = -D\frac{\partial \phi}{\partial x}$$

  Where D is the diffusion coefficient (in $m^2.s^{-1}$), ϕ is the concentration (in m^{-3}) and x the position (in m).

- The method based on the unsteady-state experiments and Fick's second law of diffusion [Olek, Perre, and Weres 2005, Mannes et al. 2009]:

$$\frac{\partial \phi}{\partial t} = \frac{\partial}{\partial x}(D\frac{\partial \phi}{\partial x})$$

The literature has shown that the diffusion of bound water depends on many parameters including the humidity of the environment. However, nowadays the studies of bound water diffusion are mainly carried out in the hygroscopic domain, with methods such as weight tracking or wood deformation. Zhou, Caré, A.King, et al. 2019 obtained an approximation of the diffusion coefficient during the imbibition of a poplar sample with MRI ($D = 5.8 \times 10^{-9}\ m.s^{-1}$), which corresponds to physical model [Siau 1984]. However, in this case, the penetration of free water impacts the

dynamics of bound water since it provides a new source of diffusion. Indeed, the imbibition in wood is a complex phenomenon which involves both the penetration of free water and the diffusion of bound water. The use of NMR, a non-invasive and non-destructive method, allows us to differentiate the water populations in the wood. Using this last method, we have in this chapter two main objectives:

1. Obtain a direct measurement of the diffusion coefficient when limiting the penetration of free water, thus isolating the dynamics of bound water during imbibition. And then compare the coefficients obtained in the three directions of the wood.

2. Understand the origin of the filling of the fibers thanks to the understanding of the exchanges between water populations and the circuit which evacuates air from the pores.

3.1 Imbibition of wood by NMR

The NMR technique is a powerful nondestructive method for the investigation of water-solid interactions in wood. NMR spectrum provides a clear distribution of the different populations of water present in the solid matrix that we will analyze for poplar sample (hardwood). It should be noted that preliminary studies have been carried out on softwoods and are detailed in the appendix 7.3. Our experiment includes the imbibition process dynamic that we follow over time with the relaxation time T_2 using the CPMG sequence since its measurement is faster than T_1. Imbibition can be a fast process, we therefore adjust the number of applied pulses to obtain a compromise between a good resolution and a small experiment time.

3.1.1 Water in wood

As we saw in section 1.1.2, the different microstructures encountered in wood give different NMR distributions of water that we can interpret thanks to the literature [Menon et al. 1987, Araujo et al. 1992, Dvinskikh et al. 2011, Bonnet et al. 2017].

3.1.1.1 Water distribution in hardwood

Fig 3.4 shows the relaxation time distribution (T_2) of a poplar sample after imbibition. A $10 \times 10 \times 10\ mm^3$ sample is immersed in a water bath (around $1\ g$ of water) for several days. At the end of the imbibition, three peaks are observed. They correspond to water in different states or in different structures that we analyze according to the literature and the fact that the relaxation time increases with the pore size:

- Bound water present in the cell wall of the wood via hydrogen bonds. This population relaxes the fastest at T_2 smaller than $10\ ms$. Bound water has a reduced mobility and is located in nanometric pores. Note that the initial step in the experiment is set to $1\ ms$ which prevents us from observing a T_2 lower than this value. The hydrogen atoms of polymers are therefore not measurable as they relax too fast.

- Free water in the fibers (smallest pores of the wood with a diameter around $20\ \mu m$) at a representative $T_2 = 50\ ms$. Free water can circulate more or less freely depending on the pore size. Note that this peak could also correspond to free water in other pores, such as the wood rays, but this does not affect subsequent interpretations.

- Free water in the vessels (largest pores of the wood with a diameter around $100\ \mu m$) at a representative $T_2 = 400\ ms$.

The NMR signal is proportional to the number of protons, so the area under a peak is proportional to the amount of the corresponding component. The signal is in arbitrary units since it depends on resolution parameters but can be linked to the actual quantity of water by calibration. In our case, the calibration is made by identifying the amount of initial bulk water incorporated in the NMR tube to imbibe the wood sample.

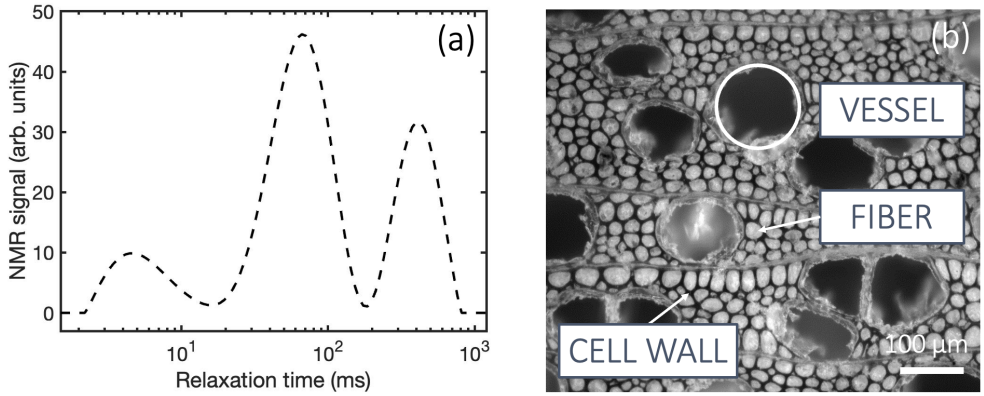

Figure 3.4: (a) T_2 relaxation time distribution of a poplar sample saturated with water. (b) Representation of the microstructure of a hardwood sample in TR section from an optical microscope.

Finally, it should be noted that the ratio of the areas of the two peaks for free water does not correspond to the volume ratio between fibers and vessels (see Table 3.2). Although we do not currently have an explanation, we can simply interpret them as free water in the small and large pores. This will not influence our analysis of the results later.

	Vessel (%)	**Fiber (%)**	**Cell wall (%)**
Microscopic imaging	43.5 ± 0.2	26.4 ± 0.6	30 ± 0.4
NMR analysis	25.75 ± 10	61.75 ± 12.25	23.75 ± 11

Table 3.2: Volume distribution between the pores and the cell walls of poplar (in $\%$ volume) from microscopic imaging [Zhou, Caré, A.King, et al. 2019] compared with the maximum water content (in $\%$ mass) from final state of imbibition in NMR.

3.1.1.2 Water evolution in hardwood

During the imbibition process, the NMR signal changes, reflecting the amount of water in the pores of the sample and their change in size and shape. We can analyze the evolution of the different peaks in terms of amplitudes, positions, and shapes. In this part we will focus on the evolution of the amplitude in time.

We follow the evolution of the different water populations during the imbibition process. Here we plunge a wood sample of $10 \times 10 \times 10\ mm^3$ in the NMR tube where we incorporated $1\ g$ of water, and we close the tube with a cap to avoid evaporation. To obtain the maximum temporal resolution during the experiment, we minimize the experiment time (about $2\ min$ between two points) while keeping an acceptable resolution (number of scans is between 4 and 16).

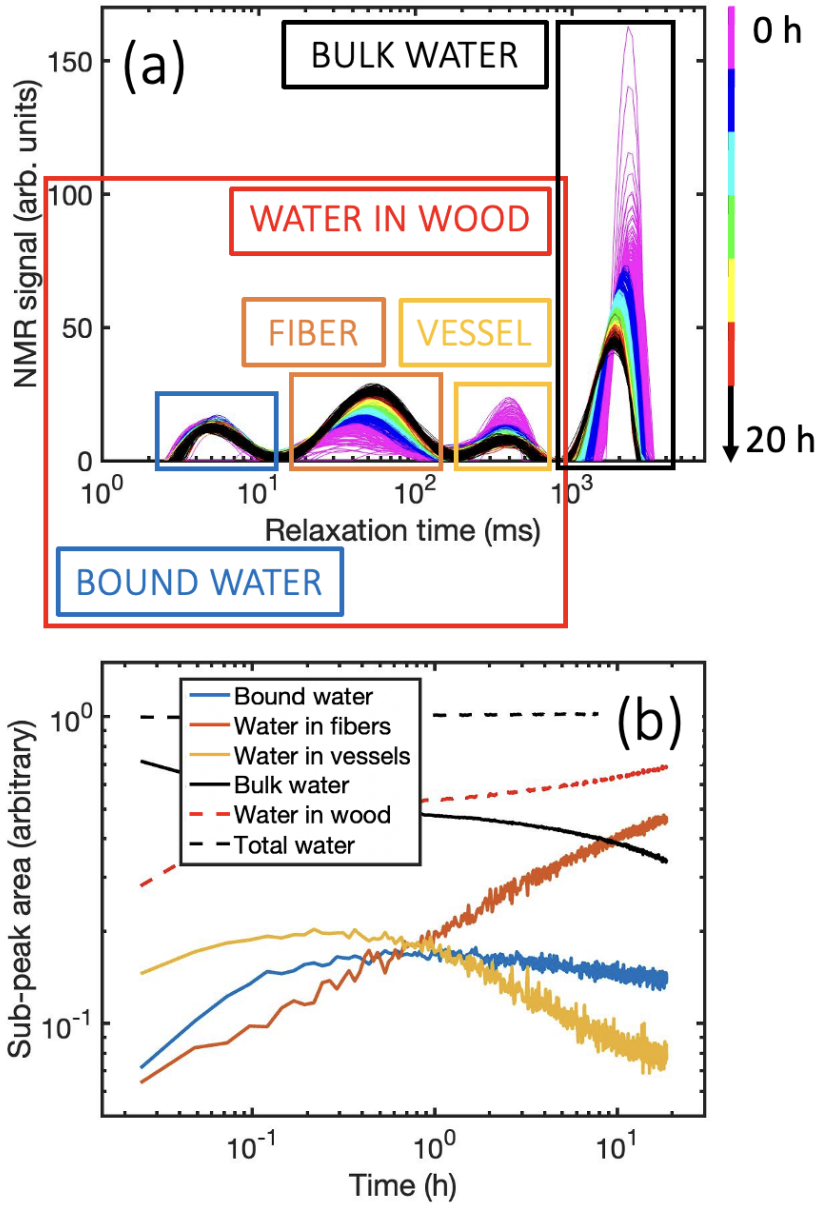

Figure 3.5: (a) Evolution of the T_2 relaxation time distribution over time from $0\ h$ in pink to $20\ h$ in black for a poplar sample. Each peak corresponds to a different water population: bound water (blue), water in fibers (orange), water in vessels (yellow) and bulk water (black). (b) Representation of the sub-peak area as a function of the time for the different populations and for the total water in wood (red dotted line) and the total water (black dotted line).

In Fig 3.5-a, we observe the appearance of a fourth peak at $T_2 = 2300\ ms$. This population corresponds to the bulk water present in the NMR tube to soak the wood sample. We overlaid the NMR signals taken at each time of the experiment (from the pink curve at the beginning to the black curve at the end). Note that the amplitude of the signal is comparable over time because we apply the same parsimony factor (lambda) [Faure and Rodts 2008]. The parsimony factor allows to optimize the noise sensitivity of the inverse Laplace resolution. Moreover, from the NMR signal, we can calculate the sub-peak area of each population and look at its evolution in time (see Fig 3.5-b):

- The total water (black dotted line) represents the sum of all water populations in the system. The total signal is constant throughout the experiment since the system is confined and evaporation is avoided. This also proves that we observe all the water in our sample, and we are not losing any information in the low T_2. Note that it is possible to notice some fluctuations of the total signal at the beginning of the experiment. This is due to temperature control between the sample and the device.

- The amount of water from the bath or bulk water (black line) is decreasing over time while the amount of water in wood (dotted red line) is increasing in time. This reflects the fact that bulk water penetrates the wood sample.

- Free water in the sample is represented by the evolution of water in vessels (yellow line) and the evolution of water in fibers (orange line). We observe that the vessels fill up very quickly. However, after reaching a maximum, the water in vessels starts decreasing. This is thought to be due to water exchange between populations and will be discussed later. Also, we observe a progressive increase of water in the small pores.

- Bound water (blue line) increases rapidly and diffuses faster than free water in the vessels or fibers at the beginning of the imbibition dynamic.

We also followed the macroscopic deformations of wood before and after imbibition. We measured with a caliper the lengths of a sample in the three different directions (longitudinal, radial, and tangential). From the literature (see Table 3.3), we know that wood has preferential directions of deformation, and the withdrawal rate depends on the species.

	Longitudinal direction (L)	**Radial direction (R)**	**Tangential direction (T)**
Literature	low/negligible	$5\ \%$	$9\ \%$
Experiment	$2.5 \pm 0.1\ \%$	$3 \pm 1.5\ \%$	$9.6 \pm 1.4\ \%$

Table 3.3: Deformation rate in poplar from literature [Leboucher n.d.] compared to our experiment data for square samples.

3.1.2 Towards the limits

Thanks to NMR, we can observe the dynamics of water penetration in wood: total water, water in the pores and bound water. We observe in particular that water penetrates very quickly in the form of bound water. In parallel we observe the rise of water in the pores by filling first the big pores. However, it is difficult to isolate the different dynamics. Indeed, if free water can enter, it will necessarily influence the penetration speed of bound water as it will provide another source of diffusion. We will try in the next section to decouple the different dynamics to obtain the diffusion process of bound water.

3.2 Diffusion process

3.2.1 Isolation of bound water dynamic

In order to obtain an approximation of the diffusion coefficient of bound water, our objective is to control the boundary conditions: we want to limit the diffusion to one direction (unidirectional diffusion) and limit the sources of diffusion by preventing free water from entering.

3.2.1.1 Insulation of imbibition plan

Our first solution is to use Baufix paint to prevent water from penetrating the side surfaces, so we have only one imbibition surface. This wood paint is a highly weather-resistant acrylic paint with a high polyurethane content. Its advantage is that it gives no NMR signal. However, the paint can penetrate a little into the wood sample through the pores. We have noticed that this can impact the maximum water content, which decreases by up to $2\ \%$ after the addition of paint. This loss will be neglected hereafter. We also tried to use Teflon tape, which would prevent damage to the sample, but the water could get between the wood and the tape.

Due to its high elasticity and tear resistance, this paint should not flake. However, we tested its efficiency by increasing the number of layers applied. We wanted on the one hand to obtain a very homogeneous layer of paint (which can be difficult to do because of the roughness of the wood) and on the other hand, we feared that the paint would crack under the deformation of the sample. Fig 3.6 shows the evolution of the moisture content over time for experiments obtained by varying the number of paint layers applied on the side surfaces: images a, d and g represent the dynamics without paint, images b, e and h the dynamics with two layers of paint, images c, f and i the dynamics with six layers of paint. Each graph line corresponds to a different imbibition surface (TR, RL, and LT), the four side surfaces are painted and the top surface is left as it is. Note that the sample is dried in the oven at $60°C$ during at least $24\ h$ before each experiment. A sample tends to degrade after many drying and soaking cycles. One consequence is that the sample water capacity can increase, but these variations are negligible compared to the total amount of water in the sample. The imbibition experiment lasts about $20\ h$, we can note that in each case, the sample does not seem to have reached its maximum water capacity since the fibers continue to fill (red curve). However, as we are only interested in the dynamics of bound water (blue curve), we consider the experiment finished when this curve has reached a plateau. We compare the effectiveness of the paint used in the different experiments:

- Experiments without paint (first column - a, d, and g) exhibit the same dynamics at comparable times. This is not surprising since water can in fact enter through all planes. However, we can note that water in the vessels reach a higher maximum value when the sample is oriented in the transverse direction (a). This might be due to Laplace pressure which accompanies the capillary rise.
- Experiments with two layers of paint (second column - b, e, and h) exhibit a change of

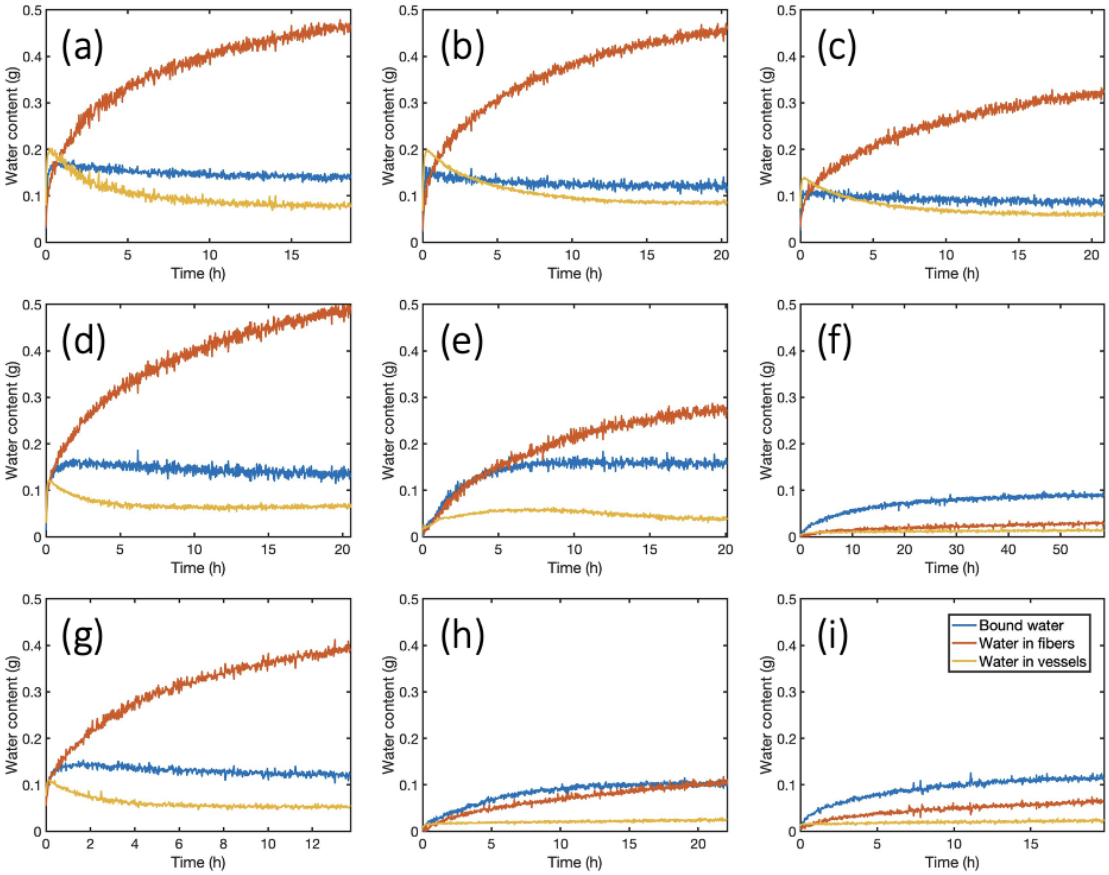

Figure 3.6: Evolution of the moisture content (in g) for the three different water populations: bound water (blue), water in fibers (red) and water in vessels (yellow) over time for the same poplar sample. The different graph corresponds to the variation of the imbibition surface with the increase of apply paint layers: transverse plane (a- without paint, b- two layers, and c- six layers), radial plane (d- without paint, e- two layers, and f- six layers) and tangential plane (g- without paint, h- two layers, and i- six layers).

dynamics for the two RL and LT planes of imbibition. In particular, there is a limitation of water penetration into the vessels. This also leads to a slower dynamic for the bound water and the water in the fibers. Note that for the TR plane, we obtained a result identical to the imbibition without paint (see Fig a and b).

- Experiments with six layers of paint (third column - c, f, and i) show an even slower dynamic for the two RL and LT planes of imbibition, which shows that a minimum of six coats is required for the paint to be effective. Note that the dynamic also decreases for the TR plane. Whatever the dynamics in the different directions, we consider that we have limited it to a unidirectional imbibition.

We have determined that it takes a minimum of six coatings of paint to become effective in insulating a soaking plane. One can argue on the fact that the paint could prevent the deformation of the wood sample and therefore prevent bound water from entering the sample. However, it is known that the penetration of bound water can exert pressure up to $1\ MPa$ which is much greater than the compression imposed by the paint [Wells and Moon 2015].

By using the paint, we manage to limit the penetration of free water in the RL and LT planes since respectively only $7\ \%$ and $12\ \%$ of the free water capacity was reached. We have repeated the experiment with different samples, and we have plotted the evolution of the height reached by the bound water as a function of time (see Fig 3.7). This height is obtained by following the evolution of the bound water content Amp evolution over time. We can approximate this value from the hypothesis that at the end of the experiment, the bound water has reached the maximum height of the sample (at $t = t_x$, $h = h_x$ and $Amp = Amp_x$). Thus: $h = (Amp \times h_x)/Amp_x$.

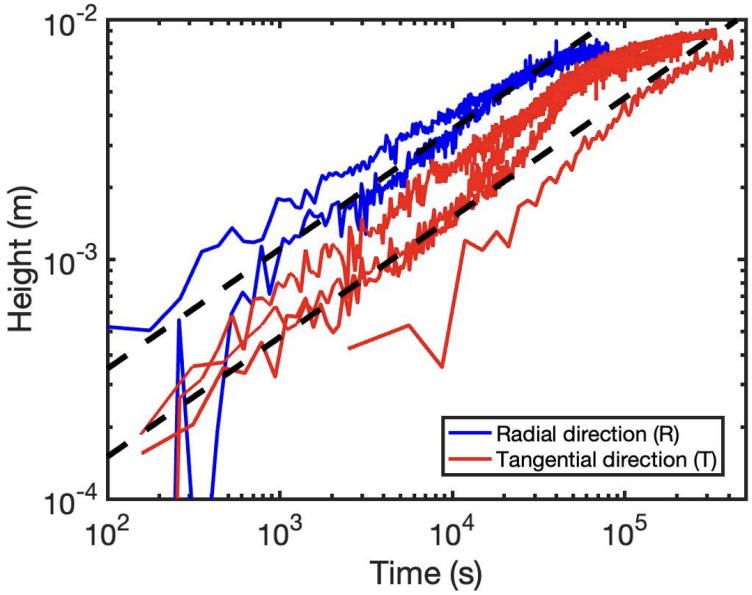

Figure 3.7: Evolution of the height (in m) reached by the bound water over time (in s) for the two wood directions: radial direction (blue line) and tangential direction (red line). The dotted lines have a slope in $1/2$.

In Fig 3.7, we observe that the curves follow a dynamic in square root of time (dotted curves) which corresponds to a diffusion mechanism. The dotted curves represent the average dynamic for the bound water in the radial and tangential directions.

In the TR plane, the free water filled up to $68\ \%$ of its maximum capacity (see 3.6 comparison between a and c). Thus, the paint had almost no effect on limiting the penetration of free water, and we still cannot distinguish the different dynamics. We need to find another way to keep the water out.

3.2.1.2 Limitation of air evacuation

In Fig 3.8-a, we observe that for the transverse imbibition plane (TR), the six layers of paint do not prevent the infiltration of free water. We want to prevent air from leaving the sample. Thus, if the pores are filled with air and air is blocked inside, water will not be able to penetrate. To do so, we painted the top surface. In Fig 3.8, we compare the filling dynamics of the different populations in the cases with and without paint on the top surface. Both experiments are performed with the same sample and in the TR plane.

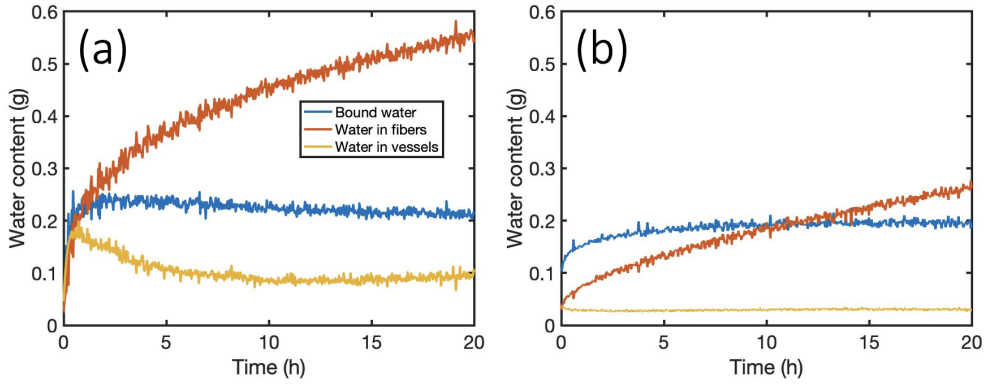

Figure 3.8: Evolution of the water content (in g) over time for a poplar sample in the TR plane of imbibition with six layers of paint (a) on the four side surfaces and (b) on the five surfaces.

We notice that the filling of the free water is less important when we paint the top surface. Indeed, the vessels are almost not filled, and the dynamics of fiber filling is slower (see Fig 3.8-b). By painting the top surface, the air initially filling the pores is not able to evacuate through this plane. Therefore, the capillary rise is prevented. However, we observe the presence of air bubble in the bulk water at the end of the experiment. Thus, some air was able to exit the sample through the imbibition plane: there is still an evacuation path for the air. This explains why the water still continues to fill the pores. We must therefore find another solution to prevent free water from entering through the transverse plane.

3.2.1.3 Limitation of water penetration

Our last solution is to limit water penetration by filling the pores with oil. We looked for a compromise for the oil viscosity so that it could both enter the pores and not be ejected by air or water. We tested oil viscosities ranging from $20\ mPa.s$ to $1000\ mPa.s$. The use of oil also allows us to avoid the diffusion of bound water by the water vapor in the lumens.

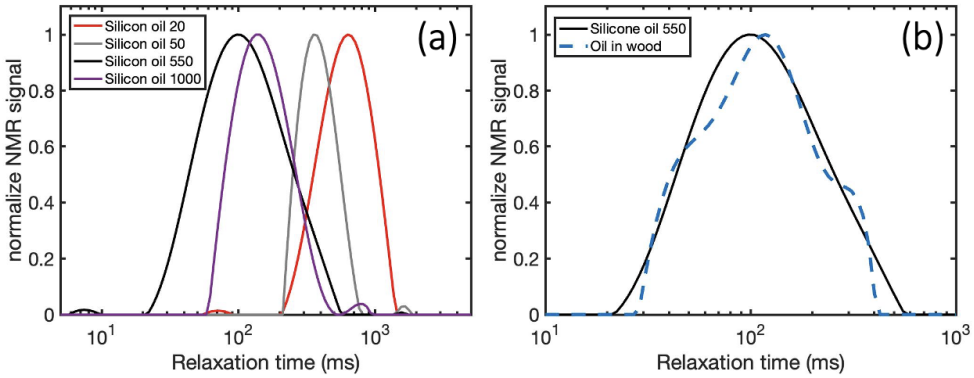

Figure 3.9: (a) Relaxation time distribution T_2 for the different silicon oil at different viscosity. (b) Comparison of the NMR signal for the silicon oil (black line) and a wood sample after imbibition with the same silicone oil (blue dotted line).

In Fig 3.9, we look at the NMR signal of various oils with different viscosities to make sure their representative T_2 will not impact the visualization of the bound water peak in wood. On the Fig 3.9-a, we observe that for each signal, the relaxation is larger than $10\ ms$ so it should not overlap the peak of the bound water (smaller than $10\ ms$). Moreover, we observe that after the imbibition of wood in oil (see Fig 3.9-b), the same relaxation time is obtained for pure oil (black plain curve) and oil in wood (blue dotted curve) (the relaxivity tends to 0 in the case of oil in wood). This shows that there is no interaction between wood surface and oil. It will therefore be impossible for us to identify where the oil is in the sample. However, Meng Zhou made microscopic images to observe the distribution of silicone oil in poplar [Zhou, Caré, A.King, et al. 2019]. In particular, she observed that the oil penetrates mainly into the vessels and cannot penetrate the fibers via pits [McCully et al. 2014]. We have also tried to use dodecane, but this fluid is easily ejected by water as it has almost the same viscosity ($1.3\ mPa.s$) and seems to interact with the wood pores which makes it difficult to differentiate the water populations in wood.

The wood sample is first soaked in oil. In Table 3.4, we have calculated the minimum time to reach its maximum oil concentration. In the case of silicone oil with a viscosity of $1000\ mPa.s$ (noted silicone 1000 in the following), the imbibition time is $18\ h$ for a sample of $7 \times 7 \times 7\ mm^3$. This time can fluctuate according to the viscosity, the sample size, and the sample porosity. After the imbibition in oil, we applied the six layers of paint on the desired faces. As between each layer, we leave the paint to dry (usually in the oven at $60°C$), we need to immerse the sample again in oil for $4\ h$. Before performing the imbibition test in the NMR tube with water, we wiped the

imbibition surface to remove the excess of oil. Indeed, one fear was that the oil contained by the wood could end up on the imbibition surface, which could create a thin layer that would prevent water from entering the sample.

Imbibition time (h)	0	1	2	17	17.5	18	18.5	19
Weight (g)	0.125	0.144	0.147	0.155	0.156	0.157	0.157	0.157

Table 3.4: Evolution of the mass of a $7 \times 7 \times 7\ mm^3$ poplar sample soaked in silicone oil 1000.

In Fig 3.10, we show the results for four different water imbibition experiments with four samples filled with oil at variable viscosity ($0.02\ Pa.s$, $0.05\ Pa.s$, $0.125\ Pa.s$ and $1\ Pa.s$). We observe the apparition of peaks at different representative relaxation times ($T2$) during the imbibition dynamics depending on the oil used. This was expected since the oils used have different relaxation time distributions (see 3.9) and therefore influence the water peaks differently (there is an average on the relaxation time of water and oil). For example, in the sample filled with oil 50, the peak of the bound water is found at $15\ ms$ while the peak of the pure oil 50 had been found at $360\ ms$, and for oil 1000, the peak of the bound water is at $10\ ms$ while in pure oil it was at $170\ ms$. Note that we did not represent the bulk water peak for the sake of clarity. But as expected, it decreases over time. We now analyze the different peaks obtained:

- In the four cases, we differentiate the evolution of the bound water peak (blue line) which relaxes at less than $20\ ms$ from the other peaks. Note that the case with oil 20 is a critical case since the bound water is barely differentiable.
- It is more or less easy to differentiate the fibers peak (red line).
- In all cases, the peak of the vessels does not appear because it is hidden by the oil peak. However, the increase of this peak is attributed to free water penetration in vessels.
- We calculated the total amount of free water (black dotted line) that penetrated the sample. This value is the addition of the water in fibers with the value of the oil peak increase. In all four cases, it is obvious that the infiltration of the wood by free water is clearly slowed down even if it is not prevented.

To analyze furthermore those experiments, we compared them with a control sample (see Table 3.5). This sample is obtained without any paint or any oil but with the same dimensions of the tested sample. After imbibition for one day in a water bath, we can obtain the maximum water content that the control sample can contain. In this case, the sample contained $0.162\ g$ of total water at the end of the experiment with $0.037\ g$ of bound water and $0.125\ g$ of free water (with a distribution of $0.103\ g$ in the fibers and $0.022\ g$ in the vessels). Naturally, it must be considered that from one sample to another the total water capacity may vary. Having chosen samples of the same wood in comparable locations, we can assume that the difference is negligible.

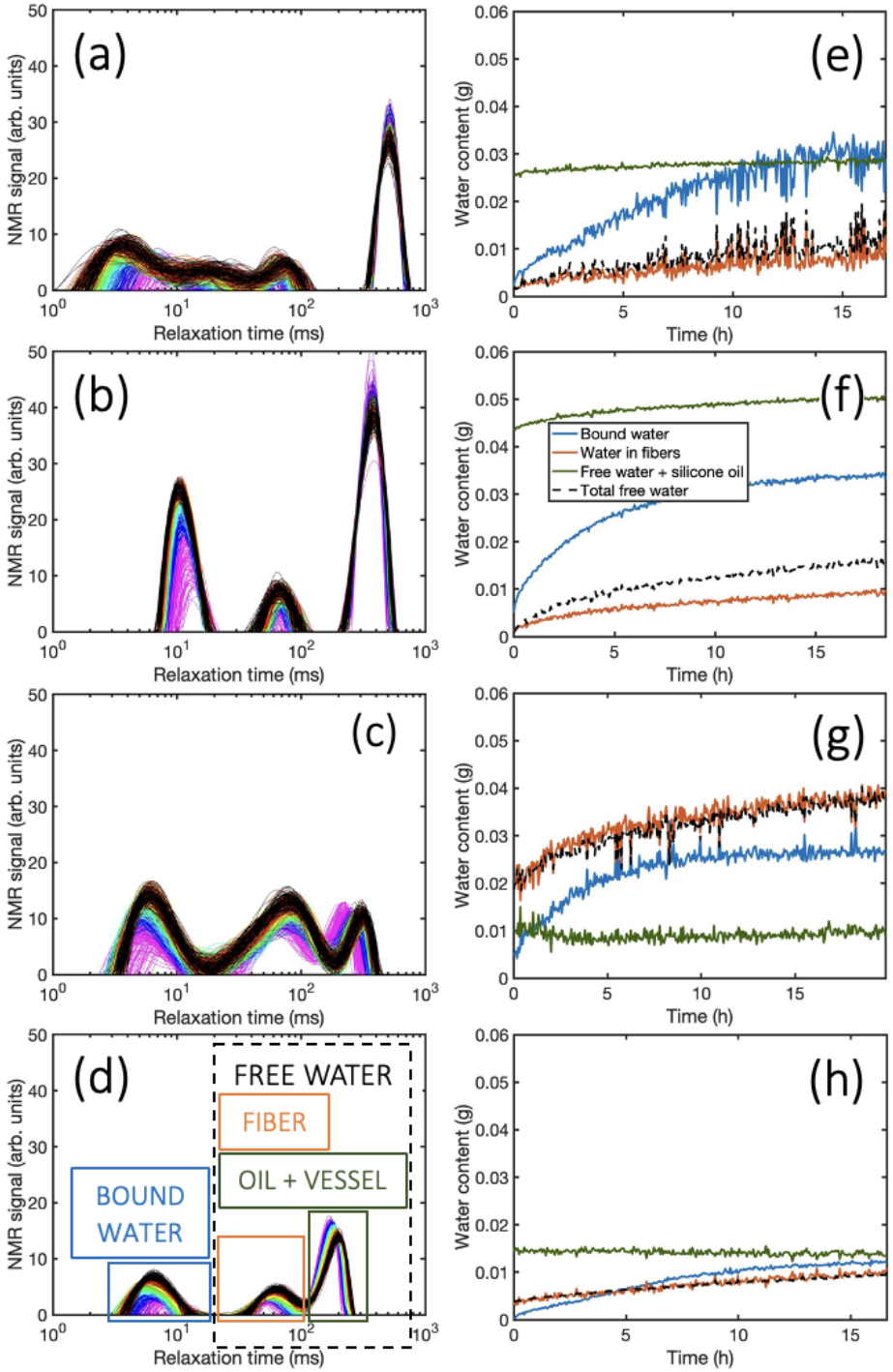

Figure 3.10: Evolution of the relaxation time distribution over time (first column) and the corresponding water content (in g) evolution (second column): bound water (blue), water in fibers (red) and free water and oil (dark green). The dotted black lines represent the total free water which correspond to the addition of water in fibers and the increase of the green curve. Each experiment is made with poplar samples filled with oil at variable viscosity: silicone 20 (a and e), silicone 50 (b and f), silicone 550 (c and g) and silicone 1000 (d and h).

		Silicone 20		Silicone 50		Silicone 550		Silicone 1000	
Bound water (%)		79		91		71		32	
Free water (%)		9		13		30		7	
Water in fibers (g)	Water in vessels (g)	0.010	0.007	0.009	0.003	0.037	0.001	0.009	0

Table 3.5: . Percentage of filling of the different populations compared to the control sample for the experiments using oil at various viscosity after $20\ h$.

First, we observe that after about $15\ h$, we have reached more than $70\ \%$ of the total amount of bound water for the first three experiments. The fact that only $32\ \%$ was filled for the case of the silicon oil 1000 can be explained either by the fact that the control sample is not representative of this experiment or that the dynamic is much slower, and it would take twice as long to reach $80\ \%$. Secondly, we observe that silicone oils 20 and 1000 are the most efficient in preventing free water from entering the sample since only $9\ \%$ and $7\ \%$ of the total free water managed to penetrate. It should be noted that oil 550 is the least efficient with $30\ \%$. Silicone oil 50 is acceptable since only $13\ \%$ has infiltrate the system. Moreover, we can observe that it was mainly the water in the fibers that filled up since we observe an increase of $0.01\ g$ against up to $0.009\ g$ for the water in vessels. In the case of oil 550, we observe that the fluid was efficient to prevent water from entering the sample ($0.001\ g$ of water in vessels) but poorly efficient to keep water from entering the fibers ($0.037\ g$). We find that the use of oil is a good way to prevent free water from penetrating. Note that for the experiment using only paint, the free water filled to $68\ \%$ of its maximum capacity.

In addition, we carry out a drying experiment of a wood sample filled with oil and water after imbibition. The objective is to verify that the increase of the green curve (water and oil inside the pores) corresponds to an increase of free water. To realize the experiment, we apply a constant air flux in the NMR tube, and we use the sample filled with silicone 550.

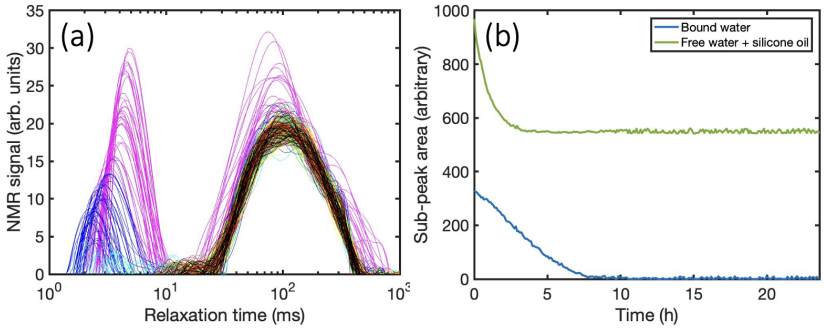

Figure 3.11: (a) Evolution of the $T2$ relaxation time distribution over time for a fir sample during drying.(b) Representation of the sub-peak area according to time for the bound water (blue line), water and silicone 550 oil in the wood pores (green line).

In Fig 3.11, we can observe the evolution of the two populations during drying: water in the cell

walls (blue curve) corresponding to the pic at low $T2$ and water and oil in the pores (green curve) corresponding to the pic at high $T2$. The curve of the bound water decreases until all the water disappears at $7-8\ h$. The green curve also decreases until reaching a plateau at $4\ h$. This plateau would therefore correspond to the amount of oil remaining in the sample. We therefore have an increase of water in the pores during the imbibition. This experiment shows also that even if the water infiltrates the wood pores, oil still remains and is not ejected by the water. In the imbibition experiments, we can withdraw the initial amount of oil that remains identical along the experiment to obtain the water content in the pores (black dotted line in Fig 3.10).

In the longitudinal direction we have demonstrated that coupling the paint method with the oil method allows us to isolate the bound water dynamic. We can obtain the evolution of the height reached by the bound water as a function of time (see Fig 3.12).

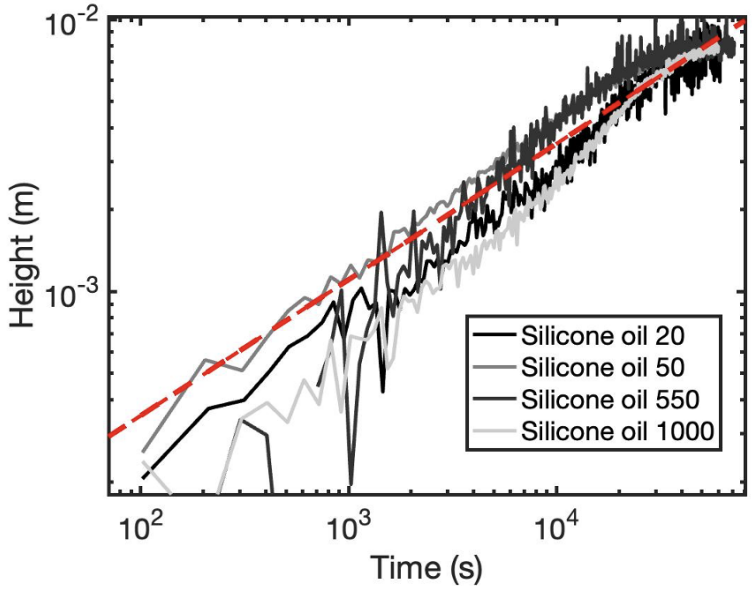

Figure 3.12: Evolution of the height (in m) reached by the bound water over time (in s) in the longitudinal direction using oils with different viscosities: silicone oil 20, silicone oil 50, silicone oil 550 and silicone oil 1000. The dotted line has a slope in $1/2$.

In the same way as for the radial and tangential directions, we obtain in all cases a square root of time dynamic (dotted curve).

3.2.2 Diffusion coefficient

After defining the most suitable protocol and using Crank's resolution of the Fick's equation, we can obtain the diffusion coefficients for each direction in each species of wood and compare them with the current literature.

3.2.2.1 Modeling of the diffusion

The bound water diffusion in cell walls is due to concentration differences described unidirectionally by Fick's second law:

$$\frac{\partial C}{\partial t} = \frac{\partial}{\partial x}(D\frac{\partial C}{\partial x}) \tag{3.1}$$

With C, the ratio between the amount of bound water and the maximum number of water molecules that can be adsorbed and D, the diffusion coefficient of bound water in the walls, considered here to be constant.

To solve this equation (3.1), we use the boundary conditions of a semi-infinite medium:

$$at\ t = 0 \begin{cases} C = C_1\ for\ x = 0 \\ C = C_0\ for\ x > 0 \end{cases}$$

Where, C_0 is the initial concentration inside the sample set at zero and C_1 is the maximum concentration. The solution can be found in the works of Crank 1975:

$$M_t = 2\ C_0 \left(\frac{Dt}{\pi}\right)^{\frac{1}{2}} \tag{3.2}$$

The total amount taken up by the medium in time t can be obtained with 3.2 at $C_0 = C_1$. In our case, as the sample is not infinite, we take a corresponding height where at $x = h_x$, $C = C_1$. This concentration is defined with an initial test where the sample is left for several days in a water bath. We then obtain the maximum water content of each population. We can therefore approximate the maximum value M_t/C_1 by an equivalent height h:

$$h = \sqrt{\frac{4}{\pi}Dt} \tag{3.3}$$

From NMR experiments, we can obtain the bound water content evolution over time. We can approximate this value from the hypothesis that at the end of the experiment, the bound water has reached the maximum height of the sample (at $t = t_x$, $h = h_x$ and $Amp = Amp_x$). Thus:

$$h = \frac{Amp \times h_x}{Amp_x}$$

With Amp the sub-peak air from the NMR signal (in $arb.\ units$). The representation of the height according to time is shown for the three directions on Fig 3.7 and Fig 3.12. The diffusion coefficient from equation 3.3 is approximated with the directing coefficient of the line (a) which follows a square root dynamic:

$$D = \frac{a^2 \times \pi}{4}$$

3.2.2.2 Diffusion of bound water in hardwood

From the evolution of the height of the bound waterfront as a function of time, we can use the Crank solution 3.3 of the Fick's second law to obtain the diffusion coefficient. In Table 3.6, we have collected the experiments obtained with paint for the radial and tangential directions (see Fig 3.7) and obtained with paint and oil for the longitudinal direction (see Fig 3.12). The diffusion coefficient is obtained by plotting a curve passing through the set of experimental curves representing the evolution of the height of the bound waterfront over time. In Fig 3.7 and 3.12, we have drawn this curve in dotted line which follows a law in square root of the time. The diffusion coefficient obtained through the value of the slope of this line is represented in the Table 3.6 with an error bar calculated with respect to the experiments with the lowest and highest coefficient.

Diffusion coefficient ($m^2.s^{-1}$)	**Radial direction (R)**	**Tangential direction (T)**	**Longitudinal direction (L)**
NMR experiment	$(9.6 \pm 0.5) \times 10^{-10}$	$(3.1 \pm 1.8) \times 10^{-10}$	$(1.2 \pm 0.3) \times 10^{-9}$

Table 3.6: Diffusion coefficient in the three wood direction for poplar samples obtain with NMR experiment.

Different diffusion coefficients are obtained depending on the imbibition direction. The longitudinal diffusion coefficient is about 1.5 times that in radial direction and 4 times that in tangential direction. It is common to observe a dependence of the wood orientation on the diffusion coefficient [Olek, Perre, and Weres 2005, Siau 1984]. In the literature these differences are often explained by a variable tortuosity which would accelerate more or less the diffusion of bound water by vapor. However, in the longitudinal direction, where vapor diffusion is not negligible, we used oil in the vessels to prevent vapor from circulating. In the other two directions, the tortuosity implies that the diffusion of vapor is slower than that of bound water and can therefore be neglected. The difference in coefficient would rather be explained by the orientation of the microfibrils. And this is in agreement with the preferred directions of swelling of wood.

The advantage of using the NMR technique was that we were able to directly follow the evolution of the bound water. We are then free from the lack of knowledge of the boundary conditions and the impact of all other populations of water, which is a limitation for the techniques currently used. Indeed, the current techniques are essentially done in the hygroscopic domain and often in a macroscopic way.

3.3 Transfer of water

Our goal here is to identify the source of water for fiber filling as well as the pathway for air removal from the fibers. We will complement what we already know on wood structure and water transfer with NMR imbibition studies to answer these questions.

3.3.1 Current state of knowledge

3.3.1.1 Wood structure

Hardwood is composed of two pore sizes: the vessels which are large channels oriented in the longitudinal direction of the wood and the fibers which are smaller closed pores (see Fig 3.13-a). The vessels are often surrounded by several layers of fibers.

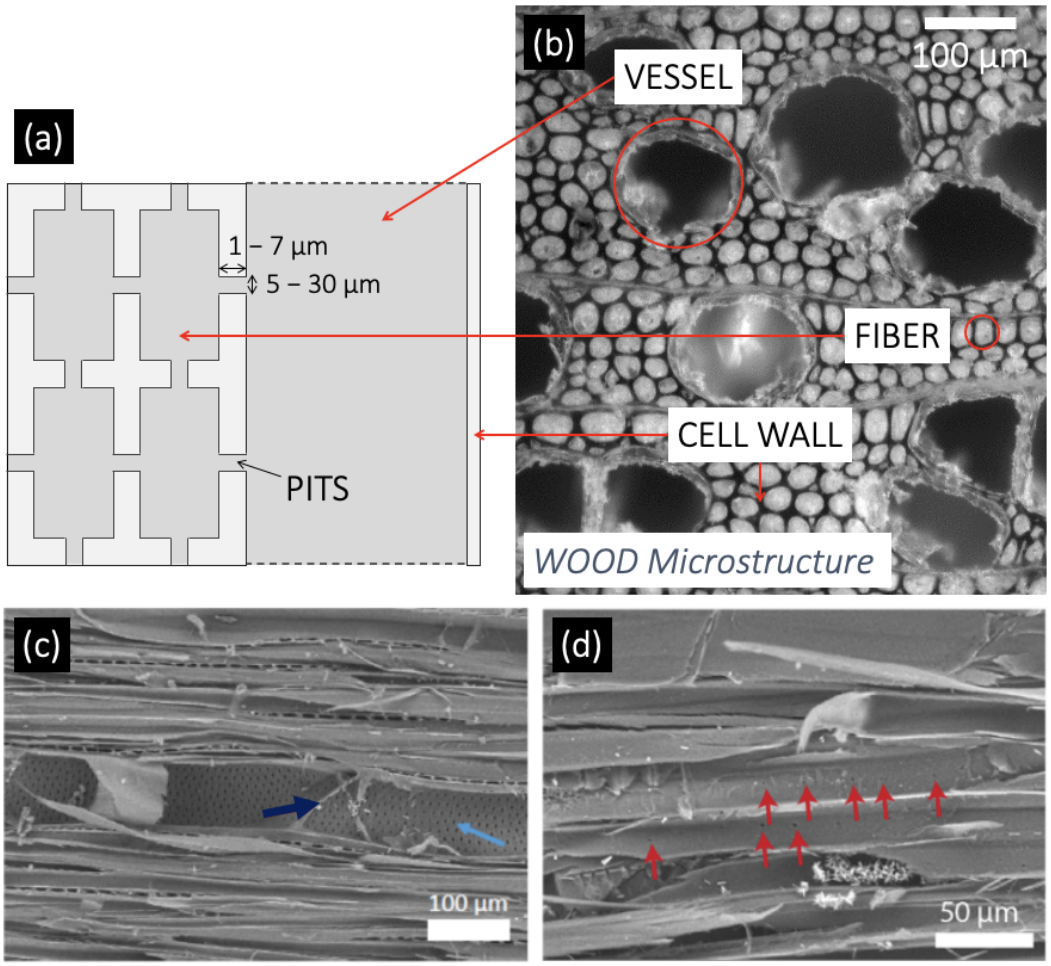

Figure 3.13: (a) Simplified diagram of the wood structure - section in the TL plane. (b) Representation of the microstructure of a hardwood sample in TR plane from an optical microscope. SEM images showing the structure of poplar in the RL plane: (c) within vessels and (d) within fibers. Dark blue arrow: a single perforation between two vessels. Light blue arrow: intervascular pits. Red arrows: pits in the fibers. Images by Sabine Caré.

Wood has pits that connect its different pores (see Fig 3.13-c-d). The pits are more or less present depending on the plane of the wood. The wood has therefore a very different tortuosity in each plane. The vessels connect a large number of pits to each other with a homogeneous distribution on the whole wall. On the contrary, there are few pits in the fibers (with a size of about $1-2\ \mu m$). Little information on the operation of pits in fibers is available in the literature. It is simply known that fiber pits are mostly found in the radial plane, which eventually allows transfers in the tangential direction.

3.3.1.2 Water circulation in wood

The complex structure of wood makes the analysis of fluid transfer challenging. However, the current literature provides many insights into fluid exchange in wood, which we present in a summary diagram in Fig 3.14.

When putting a sample of wood in contact with water, water will diffuse into the cell walls and advance by capillary rise (in the longitudinal direction) into the vessels. We also demonstrated that bound water could penetrate from all directions in the wood but with different speeds depending on the orientation of the microfibril (see section 3.2.2). Bound water can also diffuse using free water in the tracheids or water vapor in the pores as a water source. Indeed, in Fig 3.6, we could observe that the presence of free water accelerated the dynamics of diffusion. However, the origin and the mechanism of the filling of the fibers is still not well understood.

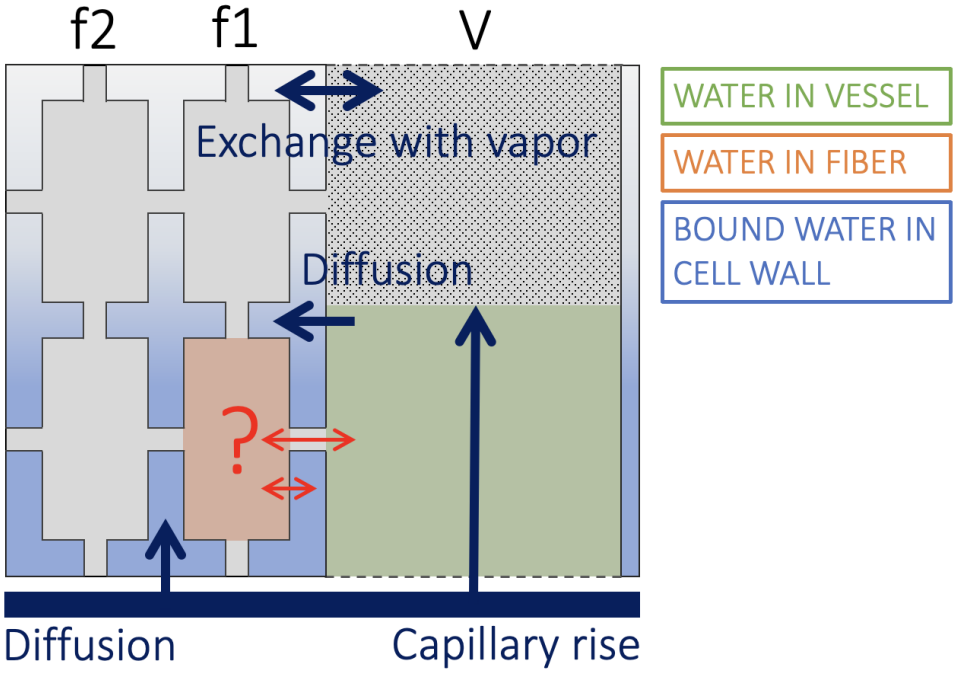

Figure 3.14: Summary diagram of known exchanges between different water populations within a hardwood sample. V: vessel, f1: fibers close to vessel V, and f2: second layer of fibers.

Concerning the fibers, Meng Zhou demonstrated that fibers fill up gradually (from the closest to the farthest from the vessel) around a vessel (see Fig 3.2). Moreover, using oil, it was observed that the fluid filled only the vessels by capillary rise. This shows that the oil cannot pass through the pits to fill the fibers. This is not necessarily extended to water.

3.3.2 Water filling of the fibers

Now that we have recalled the current knowledge on the filling of wood, we use NMR experiments to gain a better understanding on the filling of fibers. We will first try to understand how they fill with water, then how they empty with air.

3.3.2.1 Source of water for fiber filling

Two hypotheses exist regarding the source of fiber filling: free water passes through the pits that connect the vessels to the fibers (see Fig 3.13-c) or the fibers are filled by bound water that recondenses into free water in the fibers.

In order to identify the correct hypothesis, we will try to prevent the water from entering the vessels. We will then see if without this water source, the fibers are still filling up. To avoid vessel filling, we painted five sides of the wood sample, keeping a transverse plane as a soaking plane. This method allows to block the air in the vessels during the imbibition: the air cannot be evacuated at the top of the sample and therefore the water cannot rise by capillary action.

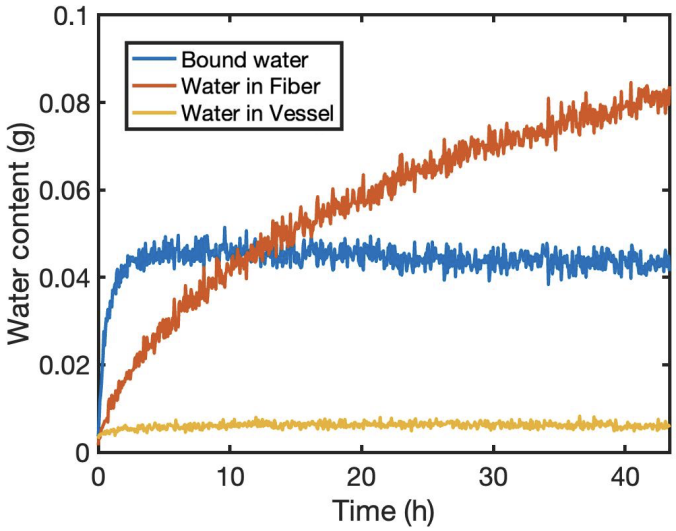

Figure 3.15: Evolution of the water content (in g) showing the increase of water in fibers (red curve) while it has barely penetrated the vessels (yellow curve) for a poplar sample in the TR plane of imbibition with paint on the five other sides.

In Fig 3.15 we show an experiment where we measure water content inside a sample as a function of time. We remark that water fails to enter the vessels (yellow curve). The small increase corresponds essentially to residual water present at the bottom of the sample. Indeed, only 3% of

the total water capacity in the vessels was able to penetrate. Despite the inability of the vessels to fill, we observe that water is still infiltrating the fibers (red curve). This observation shows that only bound water remains a possible source for the imbibition of fibers. It therefore seems that bound water condenses into free water in the fibers. We can note that in the experiment shown in Fig 3.15, the air circulation is not totally blocked since the air of the fibers is evacuated by the imbibition plane. Indeed, we observed the presence of air bubbles in the bulk water at the end of the experiment.

This shows that the whole imbibition dynamics is dominated by the diffusion of bound water in the cell walls. The fibers must therefore be able to be filled from all directions. This will be discussed in the next section.

3.3.2.2 Emptying the air from the fibers

In this section we want to identify if the filling dynamics of the fibers depends only on the diffusion dynamics of the bound water. Previously, we have seen that the diffusion rate of bound water depends on the imbibition direction (see section 3.2.2). We would now like to observe the impact that the change in imbibition direction has on fiber filling. We use the same experiments as before (see Fig 3.6-c-f-i and Fig 3.8-b) where we varied the plane of imbibition (isolated with the use of paint on the 4 sides surfaces). In Fig 3.16, we compare the mass of water in the fibers to the mass of bound water over time in the three planes of the wood (transverse in black, radial in red and tangential in blue). We have also represented this dynamic in the case where the upper surface is also painted (grey curve). We recall that the paint prevents the water from entering but also prevents the air from leaving the sample.

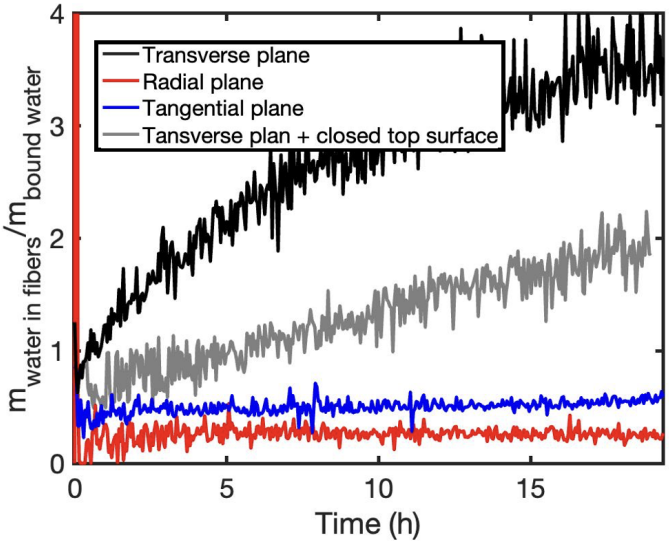

Figure 3.16: Evolution over time of the ratio of water in the fibers to the amount of bound water for different imbibition plane: transverse plane (black), radial plane (red), tangential plane (blue) and transverse plane with use of paint on the top surface (grey).

Normalizing by the mass of bound water, one would expect to obtain the same slope for each direction if the filling dynamics depend only on the diffusion of bound water. However, we notice that the water seems to transfer more easily from bound water to filling the fibers in the case of imbibition by the transverse plane (black curve - longitudinal direction). Moreover, the transfer is slightly slower when removing an air evacuation plane (grey curve). Finally, in radial and tangential planes, the fibers have much more difficulty in filling up (blue and red curves). Thus, the rate of fiber filling does not appear to be simply related to the diffusion rate of bound water.

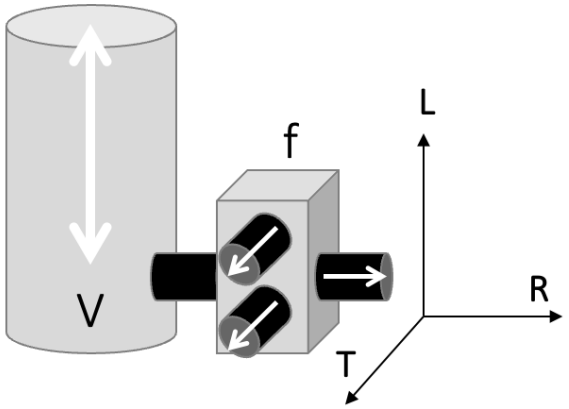

Figure 3.17: Scheme of the different air paths (white arrows) in hardwood from the fiber to the outside of the sample in the three wood directions (V: vessel, f: fiber). The pits are represented in black.

We suggest that these differences in dynamics are due to the tortuosity of the wood, which differs depending on the wood direction. Indeed, in the longitudinal direction, the vessels allow an efficient evacuation of the air. We note that if we block one of the two evacuation planes, the path becomes more tortuous. In the other two directions (tangential and radial), it is the pits that allow the evacuation of the air towards the exit of the sample. Moreover, it has been observed that the wood has less pits in the radial plane which also explains the difference between the red and the blue curves in Fig 3.16. Therefore, in order for water to fill the fibers, it must first be able to evacuate the air contained in it. Depending on the direction of imbibition, the path to evacuate the air from the fibers to the outside of the sample is more or less tortuous (see Fig 3.17).

The filling of the fibers is achieved by the recondensation of the bound water. However, the dynamics of filling also depends on the tortuosity of the wood, which allows a more or less efficient evacuation of air from the fibers.

3.3.3 Fiber filling process

Now that we have understood the different flows of air and water occurring in wood, we can propose a mechanism explaining the filling of the fibers (see Fig 3.18). We simplify the wood structure by presenting only one vessel (V) with three rows of fibers ($f1$, $f2$ and $f3$). The cell walls are

represented in light grey, and the red represents the bound water inside the cell walls. The blue represents the presence of free water, and the white arrows represent the air path. The filling of the fibers during an imbibition in the longitudinal direction is presented in three stages:

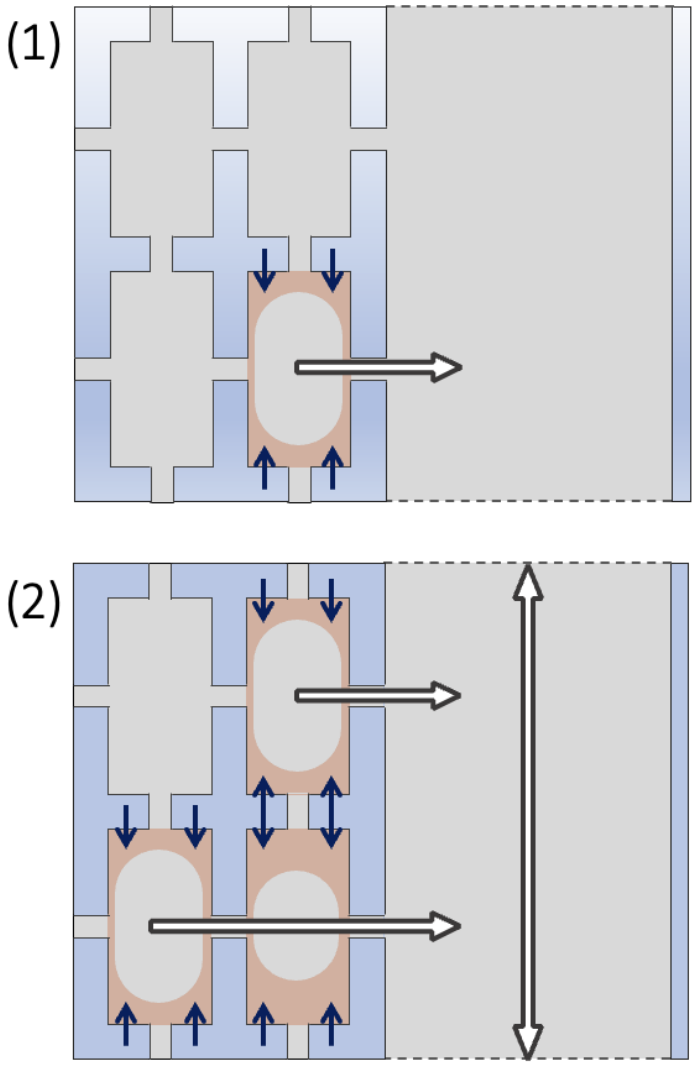

Figure 3.18: Scheme of the different air (white arrows) and water flux in hardwood during imbibition (V: vessel, f1: fibers close to vessel V, and f2: second layer of fibers).

1. Bound water penetration is followed by the capillary rise of the water in the vessels (V). The bound water has reached a certain height, saturating the first fiber line with bound water. Thus, the fibers start to fill up. According to Zhou, Caré, A.King, et al. 2019 (see Fig 3.2), it is the fiber closest to the vessel which fills up first. Indeed, the closest evacuation path is the simplest. Thus, the fiber empties its air via the pits towards the vessel. And the vessel will quickly expel this air outside the sample.

2. After filling the fiber closest to the vessel, the second fiber fills. The air in the second fiber

empties into the first fiber and into the vessel. Note that the first fiber $f1$ is never completely filled because it keeps an evacuation path for the other fibers. As the bound water diffuses upstream, a second row of fibers can begin to be filled.

3. Finally, the process is repeated all around the vessel. Up to $7-8$ layers of fibers can be found around a vessel in poplar. But this varies according to the species.

3.4 Conclusion

In this chapter, we studied the phenomenon of imbibition in hardwood. Thanks to NMR, we were able to isolate the dynamic of bound water and obtain a direct measurement of the diffusion coefficient. In the radial and tangential directions, we used paint to isolate the imbibition plane which prevent free water from entering the wood pores. In the longitudinal direction we also added a step where we pre-soaked the sample with oil, which prevented water from entering by capillarity. Furthermore, we suggest here that the difference in diffusion coefficient in the three directions of the wood is explained by the orientation of the cell layers (microfibril angle) suggesting an acceleration of the diffusion rate in a preferential direction (longitudinal direction).

Then, NMR measurements allowed us to study the transfer and exchange of fluids during imbibition. We were able to identify the bound water as the source of water filling the fibers as well as the air evacuation pathway connecting the fibers to the vessels through the pit. We were thus able to propose a model describing the dynamics of fiber filling.

For a deeper understanding of these exchanges, the laboratory is currently working on the development of $T_2 - T_2$ maps that provide access to information on the typical exchange time between two water populations. In particular, this study will highlight the recondensation of bound water into free water in the fibers. Another axis could also be developed on the impact of the initial concentration of bound water of the samples on the diffusion coefficient. For this, the laboratory has at its disposal desiccators that can be controlled in humidity thanks to different salts. Finally, we provide preliminary results on the investigation of the diffusion coefficient in softwood in Appendix 7.3.

Chapter 4

Wetting on hygroscopic materials

Surfaces like wood, with a heterogeneous, hygroscopic, porous, and rough nature have challenged scientists to identify its surface wettability. Wettability refers to the process through which a liquid spreads over a solid surface. It is an important parameter describing the ability of fluids to wet, flow and penetrate on wood surfaces. The book of [Gennes, Brochard-Wyart, and Quéré 2004] is a good introduction to this subject.

Let's us defined first, the phenomena involve at the interface of the different phases: gas, liquid or solid. In a condensed phase (liquid or solid), due to cohesive forces, atoms, or molecules are subjected to attractive interactions with their neighbors. Therefore, creating an interface between different phases amounts to losing part of this cohesion energy (see Fig 4.1). Surface tension is then defined by the energy shortfall per unit of surface. Let a be the size of the atom or molecule (a^2 its exposed surface) and U the cohesion energy between two atoms or two molecules (cohesive forces can be hydrogen bonds, electrostatic forces, or Van der Waals forces):

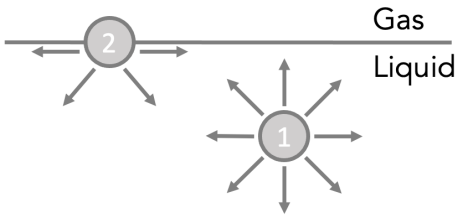

Figure 4.1: Representation of the attractive interactions involved for a molecule in the midst of a liquid phase (1) and a molecule at the interface liquid/gas (2).

$$\gamma = \frac{U}{2a^2}(J.m^{-2})$$

For mineral oil, the molecular interactions are of the Van Der Waals type and its surface tension is around $20\ mJ/m^2$. Water is more cohesive due to hydrogen interactions ($\gamma = 72\ mJ/m^2$). In liquid metals, the cohesion energies are much greater (for mercury $\gamma = 500\ mJ/m^2$). An interface is then a tense membrane that seeks to minimize its energy. Therefore, surface tension can also be seen as a force that keeps the system in this configuration. Thus, to create a surface, it is necessary to supply energy represented by a work proportional to the number of molecules that must be brought up to the surface:

$$\gamma = \frac{F}{2L}(N/m)$$

Measuring surface tension is not an easy task. There are many methods, and each have their own complexity [Adamson and Gast 1997]. In particular, liquid surfaces can be easily contaminated and solid surfaces are rarely ideal either physically or chemically.

Wetting is the study of the deposition and the spreading of a liquid over a solid or another liquid [Berg 1993]. It therefore included the study of the contact between three phases. There exist two regimes of wetting distinguished by the spreading parameter S, which compares the surface energies of the dry solid and the wet solid (with S is the solid phase, V the vapor phase, and L the liquid phase):

$$S = [E_{substrate}]_{dry} - [E_{substrate}]_{wet}$$
$$S = \gamma_{SV} - (\gamma_{SL} + \gamma_{LV}) \tag{4.1}$$

- Total wetting, when $S > 0$ the liquid spreads completely in order to lower its surface energy $\theta = 0$. If the liquid is water, we can characterise the surface as hydrophilic.
- Partial wetting, when $S < 0$ the drop does not spread but forms a spherical cap with a contact angle $\theta > 0$. When $\theta \leq \frac{\pi}{2}$, the liquid is said "mostly wetting" and when $\theta \geq \frac{\pi}{2}$, the liquid is "mostly non-wetting". In this case, for water, the surface is hydrophobic.

At the basis of contact angle theory is the equilibrium at a three phase boundary. Young equation (4.2) determines an equilibrium angle of a free-phase contact line by a balance of liquid-vapor, solid-vapor, and solid-liquid surface tension:

$$\gamma_{LV} \cos\theta_E = \gamma_{SV} - \gamma_{SL} \tag{4.2}$$

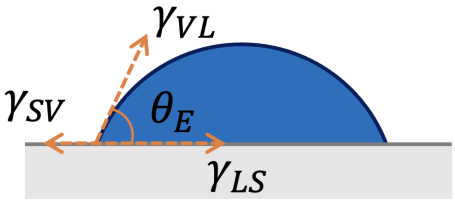

Young's equation has been discussed since its validity only applies to smooth, homogeneous, isotropic, and non-deformable surfaces. Real surfaces often do not meet the above restrictions, we will then see the contribution of many scientists to the development of new models to explain wetting phenomenon [Neumann 1974, Morra, Occhiello, and F.Garbassi 1990]. Many works attempted to determine the contact angle of water on wood, but some original effects were observed due to its complex characteristics not always taken into account: surface roughness, wood porosity, chemical composition and wood hygroscopicity.

1. Indeed, a surface is never ideal, and some chemical defect or physical defect can alter the surface and therefore the contact angle. The contact angle has a range of possible values between the advancing and the receding angle:
    - The advancing angle θ_A is the largest angle obtained by inflating the drop without the contact line moving.
    - The receding angle θ_R is the angle obtained by deflating a drop when the contact line start decreasing.

Some important causes of hysteresis have been summarized by Andrade et al. 1979 and Good 2012 on any type of surface: surface roughness, surface heterogeneity, reorientation of molecules and functional groups, penetration, adsorption and swelling. More specifically on the wood surface, a significant hysteresis has been observed, considered to be due to the surface roughness [Wålinder and Ström 2001]. Note that during drying, the liquid water apparently dewets the cell-walls which are absorbing water and various contact angles are then observed [Penvern et al. 2020]. In 1936, [Wenzel 1936] is the first to recognize that Young's equation may not be a universal equilibrium condition. He developed a model for rough surface but chemically homogeneous by introducing a roughness factor r (4.3). Its basic idea is that the interfacial surface energies should not be referred to the geometric area, but to the actual surface area:

$$r = \frac{actual\ surface}{geometric\ surface} \tag{4.3}$$

$$r\ (\gamma_{SV} - \gamma_{SL}) = \gamma_{LV}\ \cos\theta_W \tag{4.4}$$

$$\cos\theta_W = r\ \cos\theta_E$$

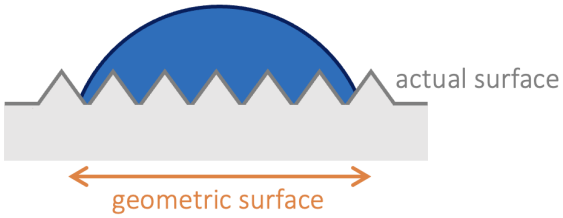

Wenzel equation (4.4) shows that surface roughness amplifies its apparent hydrophilic or hydrophobic character. The same type of reasoning was applied to chemically heterogeneous surfaces on both smooth and rough surfaces. For example, wood is composed of cellulose, hemicelluloses, lignin, and extractives and can be viewed as a heterogeneous composite. Indeed, wood can undergo surface changes such as the migration of hydrophobic extractives during drying (resin acids, fats) affecting the contact angle [Piao, Winandy, and Shupe 2010, Wang et al. 2014]. For this type of material composed of different species, Cassie's law (4.5) defines from each surface fraction f_1 and f_2, each characterized by its own contact angle θ_1 and θ_2, the expected angle:

$$\cos\theta_C = \sigma_1 \cos\theta_1 + \sigma_2 \cos\theta_2 \tag{4.5}$$

$$\sigma_1 + \sigma_2 = 1$$

Also, there is a general agreement that hysteresis will be negligible when roughness is below $0.5 - 0.1\mu m$, or when the heterogeneous phase is smaller than $0.1\mu m$ [Morra, Occhiello, and F.Garbassi 1990].

2. Moreover, a progressive decrease of the contact angle in time can be observe [Boehem and

Hora 1996, Scheikl and Dunky 1998 and Liptáková and Kúdela 1994] due to the porous structure of wood. Cassie and Baxter extended the notion of roughness to porous mediums where liquid does not penetrate but leaves air gaps with f_1 and f_2 respectively the fractional surface area of the material and the fractional surface area of pores:

$$\cos\theta_{CB} = \sigma_1 \cos\theta_1 - \sigma_2$$
$$\sigma_2 = 1 - \sigma_1$$

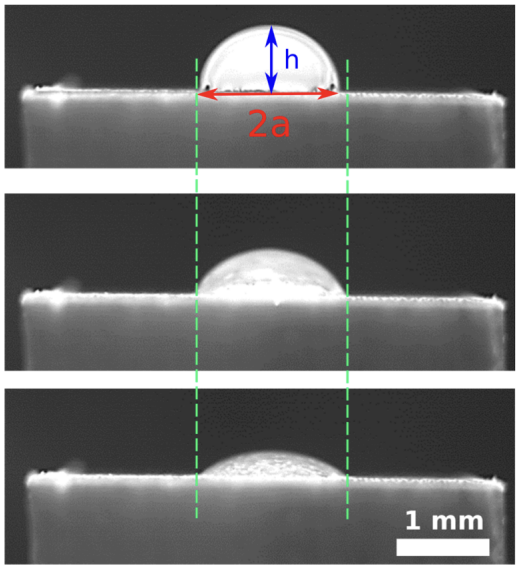

Figure 4.2: Successive images showing the penetration of a drop of water in a poplar sample on the TR plane. The vertical lines show the contact diameter of the drop [Zhou, Caré, A.King, et al. 2019].

If a liquid contacts a porous media such as wood, and the contact angle formed on the material is less then $90°$, then spontaneous penetration of the liquid into the porous medium will occur and can cause the transport of liquid along the surface by capillary forces (see Fig 4.2). Thus, we can observe contact angles that differ depending on the wood plane studied [Laskowska and Kozakiewicz 2017].

3. The chemical composition (cellulose and hemicellulose) of wood involves the hydrophibicity of wood [Piao, Winandy, and Shupe 2010] and therefore the total wetting by water on his surface. For a dynamic of total wetting, L.Tanner proposes a model presenting that the contact angle θ_D depends on the spreading time t. When surfaces are smooth and clean, and for non-volatile liquids, the Tanner's law is remarkably universal:

$$\theta_D(t) \propto t^{-3/10}$$

4. The hygroscopicity of wood can also alter the contact angle. Indeed, Zhou, Caré, A.King, et al. 2019 has demonstrated that the contact angle measured from the droplet shape at

the vessel scale, appears to strongly vary depending on whether the wood cell walls are saturated (contact angle around $30°$) or partially saturated (contact angle around $90°$) with bound water. This effect was also observed with a model wood in terms of hygroscopicity (a hydrogel). A consequence of surface tension is the pressure jump that occurs upon traversing the boundary between two phases. In his work, Laplace 1805 describes the shape of the fluid interface. The Laplace equation (4.6) relates the hydrostatic pressure ΔP to the surface tension γ and the curvature of the surface:

$$\Delta P = \gamma_{LV} \left(\frac{1}{R_1} + \frac{1}{R_2} \right) \tag{4.6}$$

Where R_1 and R_2 are the radii of curvature of the surface.

When liquids are brought into contact with the hygroscopic wood substance, diffusion, and penetration of the liquid into the bulk substance will occur. As the bound water is responsible for the deformation of the wood, we must also take into consideration the local deformation that can impact the contact angle. This has been demonstrated with gels [Anderson 2004, Kajiya, Daerr, et al. 2011, Kajiya, Brunet, et al. 2014, Boulogne, Ingremeau, et al. 2016].

Thus, the purpose of this work is to achieve a better understanding of wetting phenomena on wood and distinguish the main effects among the various factors possibly playing a role (porosity, bound water absorption (hygroscopicity), roughness, species in solution). We will first study wood with the sessile drop method. Then, we will extend the study to hydrogel material (use as a model material). Understanding the contact angle of a drop and its evolution when it is brought in contact with a hygroscopic material will allow us to identify the mechanisms that leads the capillary rise in this type of material.

4.1 Global evolution

4.1.1 Behavior on wood surface

4.1.1.1 Critical wood orientation

In this work, we want to understand the impact of the hygroscopic nature of wood on the contact angle. However, wood is also a porous media and can absorb water by capillary forces in his transverse plane (TR) which can impact the deposition of a drop of water on the wood surface [Zhou, Caré, Courtier-Murias, et al. 2018].

We are interested here in the angle in direct contact with the wood cell wall. However, depending on the direction of study, we can observe differences explained by the fast absorption of the drop in the TR plane and the roughness of the wood leading to scattered values. To minimize this disadvantage, the surface is prepared with a wood planer to obtain a surface as smooth as possible. In this experiment, sanding the wood is not an option because residual sawdust will alter the contact angle. Further in the chapter, we will focus on the radial plane of the sample (RL).

4.1.1.2 Evolution in time

First, we analyze the dynamic of a water drop in time on a partially dry fir wood sample (see Fig 4.3) using the Sessile drop method describe in section 2.2.1. From the side view (Fig 4.3-a), we observe a large initial contact angle and then a spontaneous spreading of the drop with a decrease of the contact angle until the total disappearance of the drop. From the top view (Fig 4.3-b), we notice that the spreading mainly develops along the longitudinal (L) direction and remains much more limited in the perpendicular (R) direction. In softwood, the filling of water in the tracheids accompanies and accelerates the spreading in the longitudinal direction. The same phenomenon is expected in softwood as vessels and fibers are also oriented in this direction.

Further, the analyze of the evolution in time of the contact angle, the spreading length (increase of the diameter from its initial value along the longitudinal direction), and the relative volume (calculated as if the drop keep a spherical cap shape, see equation 4.7), reveals two main regimes:

- In the first regime (1 to 2'), we record a large initial contact angle. The initial image is defined as the first image after the deposit of the drop. Then, the drop spontaneously spreads during a few hundreds of seconds (empty blue square) and the contact angle significantly decreases (empty grey triangle). The spreading seems too slow to correspond to a total wetting dynamic described by Tanner [Gennes, Brochard-Wyart, and Quéré 2004]. Note that the spreading velocity follows a $1/2$ slope. During this time, the liquid volume (filled red circle) remains approximately constant.

- In the second regime (2' to 3), the spreading slows down and finally stops corresponding to the plateau of the spreading curve. The volume also starts decreasing, either due to evaporation, absorption in the solid or flow through the porous structure. Note that we limit

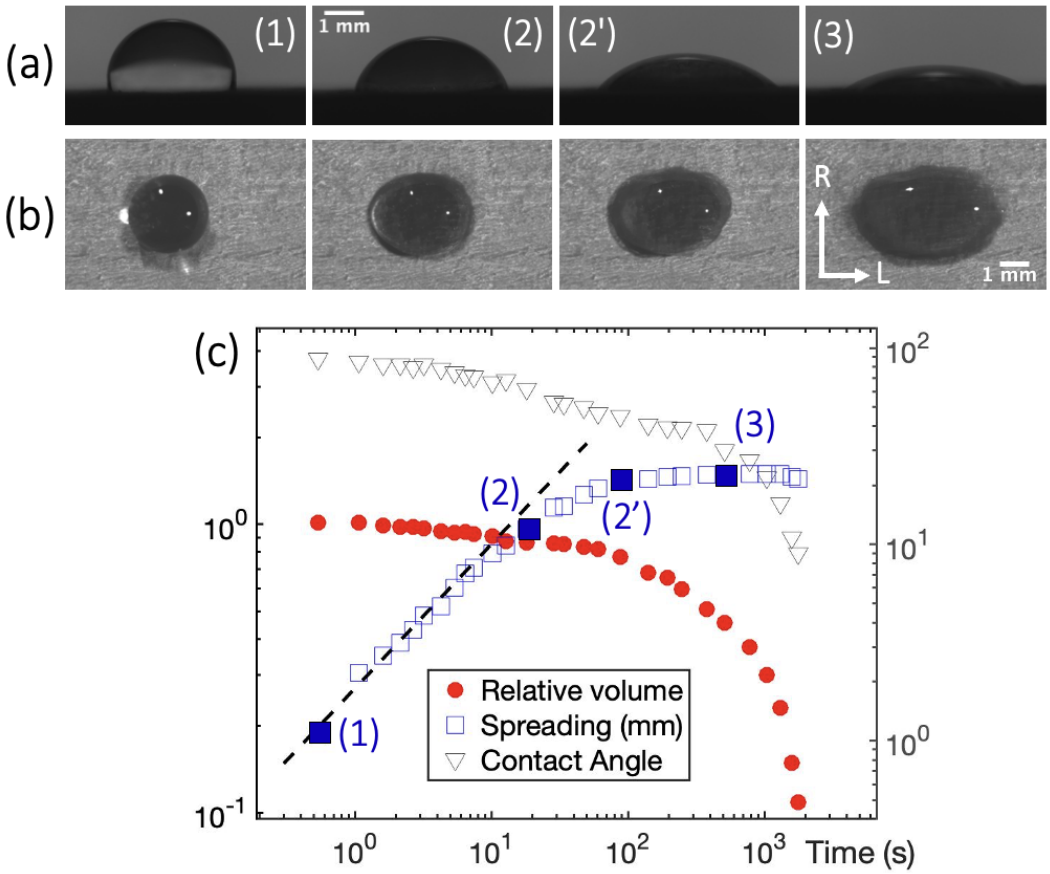

Figure 4.3: Images of the aspect of a drop over a horizontal wood (fir) surface (prepared at $50\ \%rH$) at different times (a) in the front view and (b) in the top view showing the spreading along the longitudinal (L) direction. (c) Evolution of liquid drop characteristics in time: spreading length (diameter increase from initial value), relative volume (current to initial volume ratio) and contact angle. The dotted line has a slope $1/2$. The timing of the images is reported by numbers in the graph.

the evaporation of the drop by enclosing the set-up in a humid environment. We also notice a stronger decrease of the contact angle. As the angle decreases, it become harder to obtain the precise value. In fact, the sessile drop method is more suitable for large angles.

The large initial contact angle is unexpected considering the hydrophilic character of wood. Let's analyze furthermore this initial angle.

4.1.1.3 Initial contact angle

The first observation of a drop put in contact with a horizontal surface of a fir wood (RL plane) shows remarkable dependency on the sample water concentration (see Fig 4.4). For wood with a moisture content at or above the fiber saturation point (FSP), we obtain a small initial contact angle. We recall that at this concentration the wood is saturated with bound water. However, for wood with a moisture content bellow the FSP (partially saturated with bound water), we obtain an angle larger than $90°$. This angle is unexpected since this material is considered hydrophilic. Here, to obtain the wood sample above the FSP, we immerse it for several days in water and the surface was then cleaned of its excess water with a tissue. For the partially saturated wood, we left it dry for several days in an oven at $60°C$.

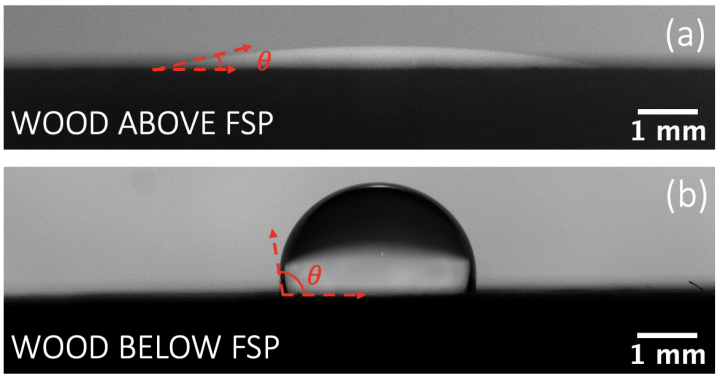

Figure 4.4: Images of the initial contact angle over a horizontal wood (fir) surface (a) at high water concentration and (b) low water concentration.

This dependency on the water concentration is consistent with the wetting properties tested from imbibition tests by Zhou, Caré, A.King, et al. 2019. It has been shown that the contact angle measured during liquid penetration through the structure with capillary effects as the driving force varies greatly depending on whether the wood cell walls are saturated (contact angle around $30°$) or partially saturated (contact angle around $90°$) with bound water.

4.1.1.4 Generalization to various types of wood

We now challenge our results by using different wood species: hardwood (oak, ash, and poplar) and softwood (fir). We notice the same qualitative features for each species with a dry surface: a large initial contact angle (see Table 4.1) followed by the slow spreading of the drop (see Fig 4.5).

Considering the roughness of wood surface, we repeated the experiment at different locations on the same sample surface and obtained an error of $\pm 8°$.

Wood species	Oak	Ash	Poplar	Fir
Initial contact angle (°)	96	81	100	120

Table 4.1: Average value of the initial angle of a drop put in contact with different wood species on the RL plane.

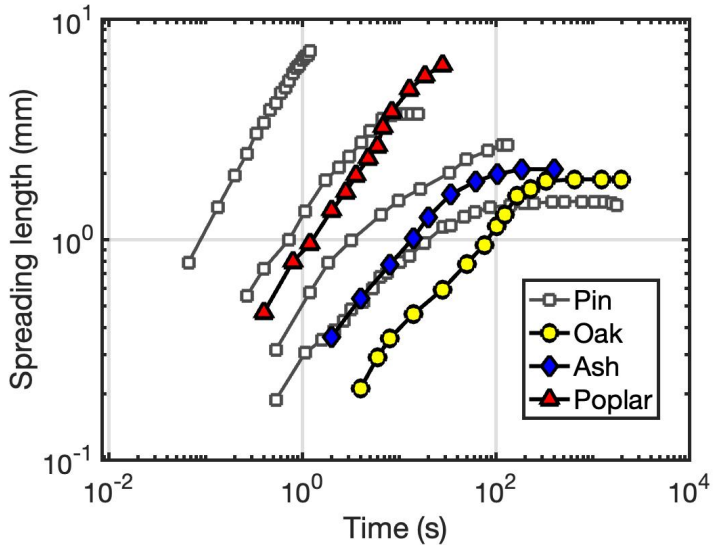

Figure 4.5: Water drop spreading along the direction L over horizontal different wood species (prepared at $50\ \%rH$): spreading distance (diameter increase from initial value) as a function of time.

The spreading length correspond to diameter increase from its initial value along the longitudinal direction. The results obtained for the spreading dynamics for a given wood are somehow scattered. For example, for fir samples, the final spreading distance varied by a factor 3 depending on the different points where we deposited the drop on the wood sample surface. We believe that this is due to the roughness variations of the surface at the scale of the droplet, which strongly affect the initial contact and spreading. However, the qualitative trends in the process are reproducible.

It is remarkable that despite the different structures, we obtain a similar phenomenon. Therefore, it seems that the large initial contact angle followed by a spontaneous spreading is intimately linked to some common characteristics of woods: its hygroscopicity. However, wood has a roughness and a heterogeneity complicated to control.

4.1.2 Behavior on hydrogel surface

We have seen that wood have unexpected wetting properties when it is not saturated with bound water. The slow spreading dynamics cannot explain a total wetting phenomenon where the initial

angle would only be an intermediate state. Moreover, we observe that this phenomenon is repeated for different wood species. The difference in angle between the saturated and unsaturated cases leads us to believe that this phenomenon is related to the hygroscopicity characteristic of wood. However, wood has a complex structure and its porosity or roughness make the analysis of the phenomena involved rather difficult. For a better understanding, we therefore considered a model system with a much simpler structure but in which water can be absorbed, leading to swelling: PEG hydrogels. The transparency of this material will make it possible to use different techniques for further studies.

4.1.2.1 Evolution in time

We analyze the dynamic of a water drop in time on a partially dry gel sample (see Fig 4.6) using the Sessile drop method. We obtain similar results on the drop dynamics as for wood with two regimes:

- In the first regime (1 to 3), we observe a large initial contact angle (around $120°$) and a slow spreading over the surface (empty blue square) with no significant change in the volume of the drop (filled red circle). At the beginning of the dynamic, the spreading follows a square root of time dynamic (see black dotted line). While the drop is spreading, we notice a progressive decrease of the contact angle (empty grey triangle).
- In the second regime (3 to 3'), the drop stops to spread and the volume decreases. At one point, the drop start receding until it disappears (a slight decrease in the contact diameter of the drop is observed). In Fig (3'), we observe a gel promontory. Indeed, on this picture, the water drop has totally disappeared and has been fully absorbed by the gel. We recall that the experiment is closed in a humid environment to avoid evaporation of the drop. The absorption of water is therefore manifested by a swelling of the gel.

From the observation of the drop, we extract different parameters like the contact angle, the height of the drop and the radius of the drop (see Fig 4.6-c). We can use those parameters to calculate the volume of the drop in time:

$$V_{drop} = \frac{\pi}{2} h_{drop} \left(r_{drop}^2 + \frac{h_{drop}^2}{3} \right) \tag{4.7}$$

The distinction between the gel height (h_{gel}) and the drop height (h_{drop}) remains complicated to define. Especially at the beginning of the dynamics. However, when the contact angle is smaller than $90°$, the change of slope between θ_{gel} and θ_{drop} allows us to make this delimitation. When this delimitation was not possible, we neglected the height of the gel.

By reproducing the hygroscopic character of wood with a model material, it seems that we obtain identical dynamics. Let's see if we obtain the same conclusions when we vary the water concentration of the material.

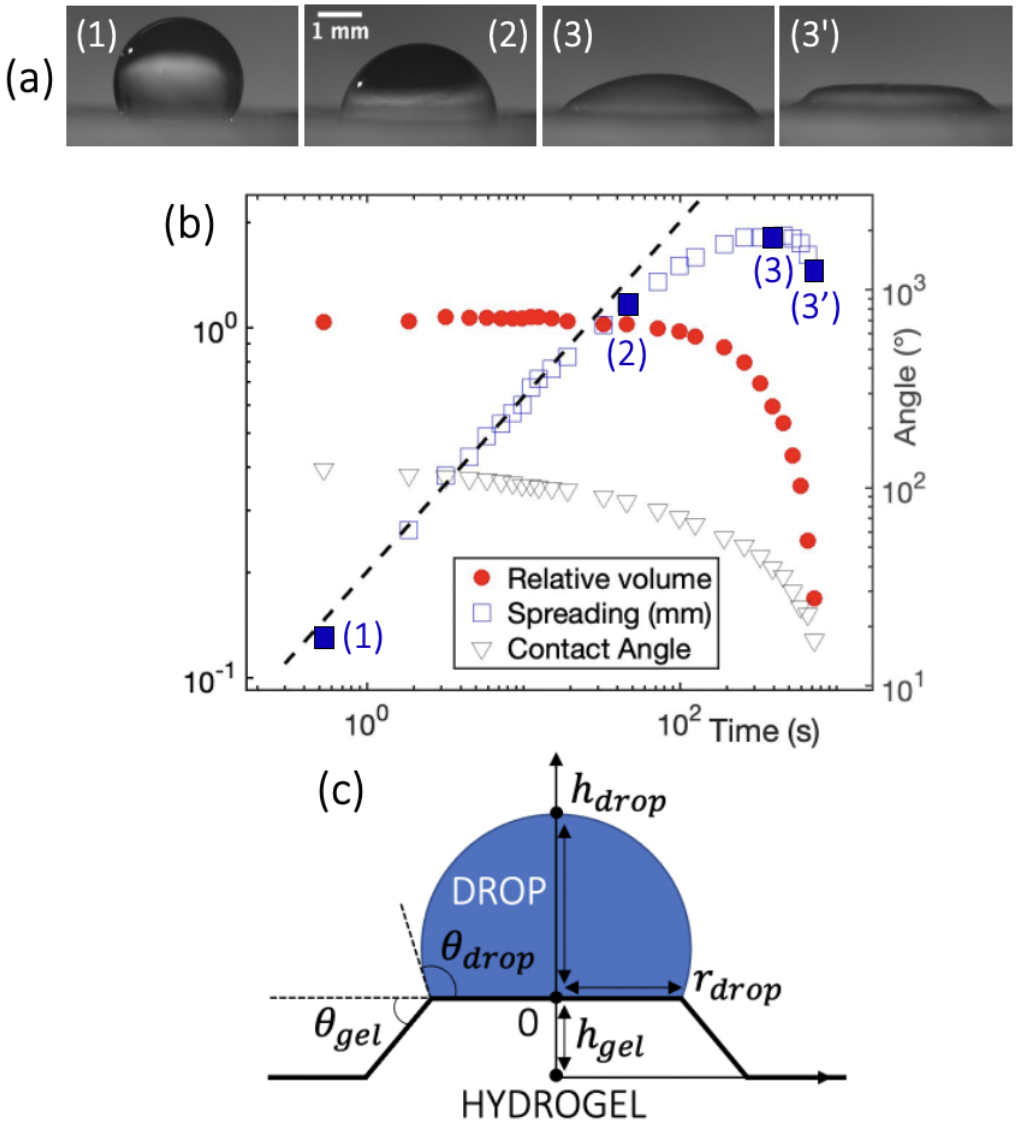

Figure 4.6: (a) Images of the aspect of the drop at different times in the front view. (b) Water drop spreading over a horizontal hydrogel surface (prepared at $50\ \%rH$). Evolution of liquid drop characteristics in time: spreading length (diameter increase from initial value), relative volume (current to initial volume ratio) and contact angle (θ_{drop}). The dotted line has a slope $1/2$. The timing of the images is reported by numbers in the graph. (c) Profile of the droplet and substrate with the definition of the different parameters.

4.1.2.2 Initial contact angle

The initial contact angle is defined in the same way as for wood with the first image obtained from the spreading dynamics of the drop. In Fig 4.7, we performed two experiments with a gel at different water concentrations. As for wood, changing the water concentration impact on the contact angle. For a saturated gel, we obtain a low contact angle (smaller than $90°$). This observation is not surprising since our hydrogel is composed of 70 % of water and of hydrophilic polymers. But as the gel is dried, we obtain the same phenomenon as in wood, a large contact angle, around $120°$.

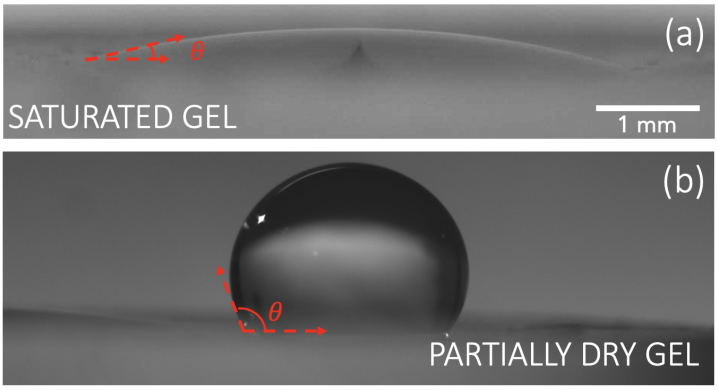

Figure 4.7: Images of the initial contact angle over a horizontal gel surface (a) at high water concentration and (b) low water concentration.

PEG hydrogel exhibits the same wetting properties as wood. But then two questions arise: what is the physical phenomenon that is at the origin of this high contact angle and why does the drop spread?

4.2 Analysis of the wetting parameters

In this section, we will investigate the wetting properties on different surfaces (variations of the water concentration or of the gel composition). First, we will study the initial contact angle and then the spreading of the drop.

4.2.1 Characterization of the contact angle

4.2.1.1 Water concentration dependency

The main characteristic of our materials is their hygroscopicity. Let us then challenge our observation by changing the water concentration. Different concentrations are obtained by varying the relative humidity of the sample environment using various saturated salt solutions (see Table 2.5).

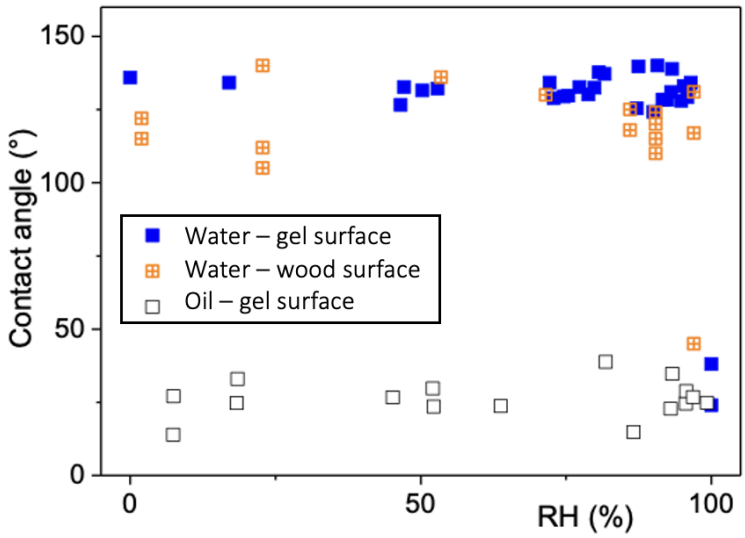

Figure 4.8: Initial contact angle of water over a hydrogel (filled blue square) or wood (fir) (crossed orange square) surfaces and oil over hydrogel surface (empty black square), as a function of the relative humidity ($\%rH$) at which the sample (gel or wood) has been prepared.

Looking at the Fig 4.8, we notice different initial contact angle for the different surfaces using various fluids:

- For the wood surface at water concentration different from its maximal value, we observe a large contact (between $105°$ and $140°$). When wood is saturated in water, the contact angle drops to value smaller than $50°$.
- For the gel surface using water drop, we observe the same phenomenon: a large contact angle at water concentration different from its maximal value and a small contact angle for the saturated case.

- Using a different fluid on hydrogel surface, here a drop of rapeseed oil, we observe for different concentrations of the hydrogel no significant impact on the initial contact angle (around $25°$). As this fluid is viscous, we waited the stabilization of the drop to obtain the equilibrium angle.

We conducted an additional experiment to validate the contact angle in the saturated state for the hydrogel surface. Indeed, the Sessile drop method is adapted for large angles but becomes less accurate for the calculation of small contact angles. Thus, we have reversed the gas phase with the liquid phase. We immerse in a water bath our gel (which is already saturated in water) and an air bubble is placed on the surface. The contact angle of a drop of water is therefore the difference between $180°$ and the angle obtained with the air bubble. This experiment inspired by the paper [Andrade et al. 1979] allows us to validate the small contact angle in the saturated state.

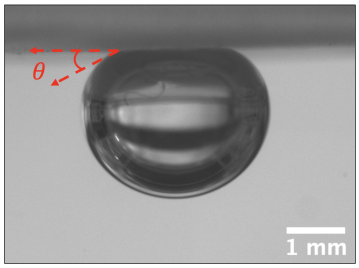

As a theoretical point of view, for the hydrogel, we can directly compute the interfacial energies between the different phases, which a priori makes it possible to predict the contact angle from Young-Dupré equation (4.9):

$$S = \gamma_{SV} - (\gamma_{SL} + \gamma_{LV}) \tag{4.8}$$

$$\gamma_{LV} \cos\theta = \gamma_{SV} - \gamma_{SL} \tag{4.9}$$

With V the vapor phase, L the liquid phase and S the solid phase corresponding to the air, the water, and the gel in our case.

Since water is the polymer solvent, as long as the gel is at equilibrium and not almost dry, the free surface of polymer chains is surrounded by water molecules. Thus, the gel-air and water-air interfacial energies should be close ($\gamma_{SV} = \gamma_{LV}$) and the gel-water interface energy should be equal to zero ($\gamma_{SL} = 0$). It follows that the spreading coefficient S (4.8) is equal to zero. This implies that a contact angle equal to zero is expected at equilibrium, whatever the gel concentration. Note that a similar analysis for oil leads to the same result, which in that case is consistent with the observations (see Fig4.8). The wettability theories do not explain in our case the existence of a high contact angle.

Wood and hydrogel are considered in the literature as hydrophilic materials. However, it is observed that when these materials are not saturated, water does not wet their surfaces. This is not due to a change in structure, since when using oil, the water concentration has no impact on the contact angle.

4.2.1.2 Hysteresis of Triple Lines

We must now verify the value of the contact angle and the potential impact of the surface condition (chemical or physical defects). To do so, we analyze the hysteresis between the advancing and the receding contact angle (see Fig4.9):

- We measure the advancing contact angle by progressively injecting water in the drop just placed on the gel surface. We observe that the advancing contact angle remains approximately constant and equal to the initial angle of contact observed after pouring the drop (see the filled dots in Fig 4.9-c). Thus, the initial contact angle may be considered as the maximum value of the contact angle.
- If we now withdraw the liquid from the drop just placed on the horizontal solid surface, we observe that the line of contact does not recede and remains pinned. The contact angle decreases to zero as the drop volume decreases to zero (see the empty dots in Fig 4.9-c).

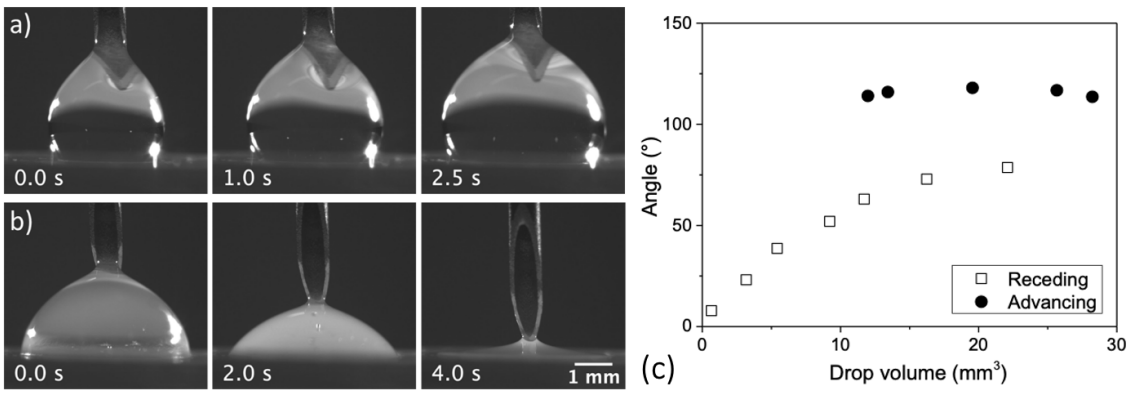

Figure 4.9: Views at successive times of (a) the progressive injection of water in a drop just placed in contact with a hydrogel surface and (b) the progressive withdrawal of water from the drop. (c) Representation of the angle according to the drop volume for the advancing and the receding contact angle. Note that the color changes of the drop are mainly due to the illumination and refraction of the light.

Same result was obtained when forcing a bigger initial diameter of the drop. In the Fig 4.10, we conducted two experiments on the same gel, but we varied the height of the syringe. In the case (a), the drop is released from a low height leading to a small initial diameter and a high initial contact angle. In the case (b), the drop is released from a higher height leading to the crashing of the drop on the gel surface. During this bounce, the drop reaches a larger diameter and the triple line do not recede to the same diameter as in case (a). Thus, we obtain a lower contact angle different from the advancing contact angle. Note that we also performed tests where we modified the initial volume of the drop to validate we were not in a case where the gravity was not negligible.

The roughness can be considered as the explanation of such a large contact angle. But according

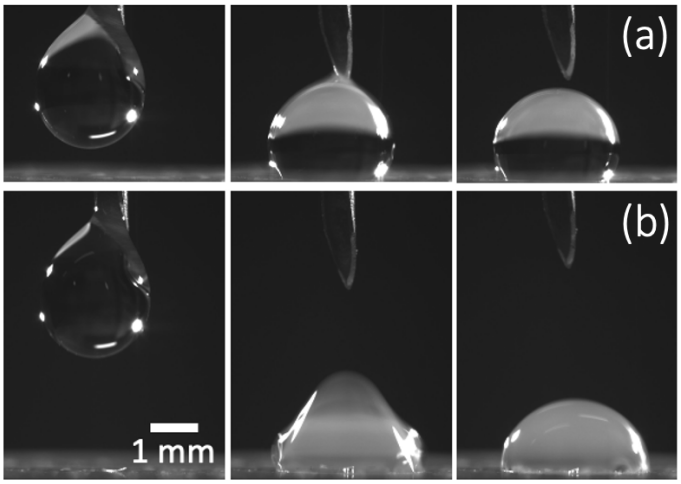

Figure 4.10: Views at successive times of (a) the release of a water drop in contact with a hydrogel surface and (b) the release from a higher height of a water drop in contact with the same hydrogel surface.

to the Wenzel's model, the effect of roughness is to magnify the wetting properties of the solid, that is the Wenzel's angle will increase with roughness if the Young's angle is greater than 90°, and will decrease if it is lower than $90°$ [Gennes, Brochard-Wyart, and Quéré 2004]. It therefore can't be the solution of such a large contact angle for a material that should be hydrophilic. The roughness of our hydrogel calculated with an optical profilometer is around $20\ nm$. It is generally accepted [Morra, Occhiello, and F.Garbassi 1990] that hysteresis will be negligible when roughness is below $0.5 - 0.1\ \mu m$.

4.2.1.3 Hydrogel composition dependency

We also challenge our result by changing the ratio of polymer that we used between PEG-MA and PEG-DA. The higher the PEG-DA concentration is, the stiffer is our hydrogel. Here we calculate the percentage of PEG-MA with the following equation:

$$C(\%) = \frac{m_{PEG-MA}}{m_{PEG-MA} + m_{PEG-DA}} \times 100$$

From Table 4.2 we note that for dry gel (dried at $60°C$ in the oven), the stiffer the hydrogel, the smaller the contact angles. Also, for all composition, if the gel is saturated (kept at relative humidity close to $100\ \%rH$), the contact angle stays very low (around $46°$). Note that we observe an uncertainty in the contact angle that can vary by $\pm 12°$ between experiments on the same gel. This dependence on the gel composition will be detailed later.

Water concentration	Polymer ratio (MA %)							
	0	**12**	**25**	**50**	**75**	**87**	**92**	**100**
Angle on dry surface (°)	65	72	75	80	82	87	100	104
Angle on wet surface (°)	52	40	42	45	48	48	41	47

Table 4.2: Initial contact angle of water over a saturated hydrogel and a dry hydrogel surface as a function of polymer PEG-MA concentration.

4.2.2 Characterization of the spreading

4.2.2.1 Spreading over a horizontal plane

We now focus on the progressive spreading of the drop. In Fig 4.11, we plotted the evolution of the diameter of the drop in time. Here we showed two main experiments: the dynamic for wood (fir) surface and for gel surface. As a reminder, we neglect evaporation as it is prevented by a very high relative humidity in the experimental chamber.

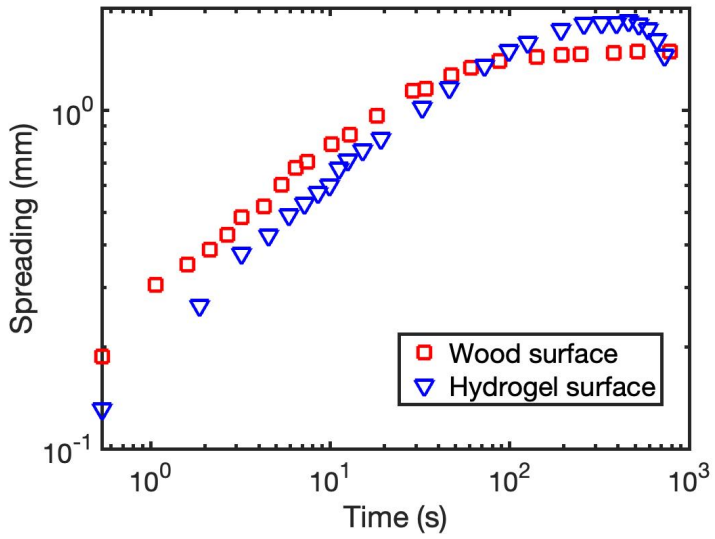

Figure 4.11: Spreading (increase of the diameter) in times of a water drop over a horizontal plane for wood (red square) and gel (blue triangle) samples.

As a theoretical point of view, in the absence of other effects, the spontaneous spreading of the drop entering in contact with the gel results from the balance between the surface energy gain per unit time and the viscous dissipation in the drop:

- For a drop of spherical cap shape of height h and initially in contact with the gel surface along a disk of radius r, we obtain the area of liquid-air interface (4.10) and the volume of

the drop (4.11).

$$A = \pi(r^2 + h^2) \tag{4.10}$$

$$\Omega = \frac{\pi h(r^2 + \frac{h^2}{3})}{2} \tag{4.11}$$

Assuming the volume remains constant in the first stage, if the radius of the disk is increased to $r+dr$, the height is decreased to $h-dh$ with $(r^2+h^2)dh = 2rhdr$. The area of liquid-air interface of the drop is then increased of $2\pi(\frac{r^2-h^2}{r^2+h^2})dr$, while the aera of the liquid-air interface around the drop is decreased of $2\pi r dr$. The total loss of area of the water-air interface is finally $\Delta A = 2\pi r h^2 \frac{dr}{r^2} + h^2$ and the surface energy gain per unit time is $\sigma \cos\theta dA/dt$.

- Considering the flow as a simple shear at a shear rate $\dot{\gamma} = dr/hdt$, the viscous dissipation is $\mu\dot{\gamma}^2\Omega$, in which $\Omega = \pi h\left(r^2 + h^2/3\right)/2$ is the drop volume.

It follows that the velocity of spontaneous spreading is $V_s = dr/dt \approx 4(\sigma/\mu)(h/r)^3$, which varies between about a value of the order of $100\ m.s^{-1}$ when $h \approx r$, to about $0.1\ m.s^{-1}$ when $h \approx r/10$. These values are strongly inconsistent with the slow spreading of the sessile drop observed for water on horizontal gel or wood surfaces (less than $10^{-4}\ m.s^{-1}$). On the other side, an oil drop of similar viscosity widely spreads with a timing shorter by several orders of magnitude. This fast spreading of the oil drop is that expected under such conditions when viscous and surface effects govern the system evolution.

4.2.2.2 Water concentration dependency

Let us first challenge these observations by varying the water concentration of the hydrogel. Fig 4.12 show two main dynamics: at high concentration (red curves), the drop is faster than at low concentration. At low concentration (dark curves), the dynamics are somehow scattered but no significant change in the dynamic is seen here. Therefore, as we have seen the initial concentration of the sample had no impact on the initial contact angle, it also has no significant impact on the spreading velocity.

4.2.2.3 Spreading on an inclined plane

In order to isolate the spreading dynamic, we want to prevent any deformation that can pinned the drop and prevent it from moving forward. Therefore, we conducted the experiment on an inclined plane.

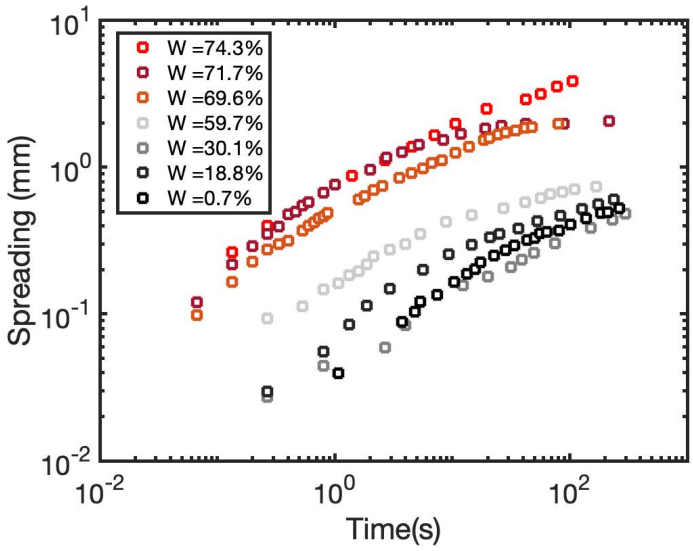

Figure 4.12: Spreading (increase of the diameter) of a water drop over a hydrogel surface at different water concentration (C in $\%$).

In Fig (see Fig 4.13), similar experiments over an inclined wood or gel surface have been made with both water or oil (dodecane) drops. Let us consider the flow of such a drop along the slope for a pinned upper line of contact. Though, it is worth noticing that, due to gravity, the downward contact angle is much larger than the upward contact angle with spreading only occurs downwards. This shows that due to a sufficiently small contact angle the upward line of contact is stable. Thus, the spreading occurs only when the apparent contact angle is larger than some critical value. Downwards, neglecting inertia and capillary effects, the spreading is governed by a balance between:

- The gravity stress, at first order $\rho g h \sin i$, where h is the typical thickness of the drop, ρ the liquid density, g the gravity and i the plane slope.
- The viscous stress, $\mu\dot{\gamma}$, in which $\dot{\gamma}$ is some gradient of velocity in the drop and μ the liquid viscosity. Here, for the sake of simplicity, we estimate $\dot{\gamma}$ by assuming a simple shear, so that $\dot{\gamma} \approx (1/h)dx/dt$, an assumption strictly valid when $h << x$, x being the position of the line of contact along the plane or equivalently the drop length.

Taking into account that the liquid volume is constant ($xLh \approx \Omega$), we get after integration $x \approx \left(\rho g \Omega^2 \sin i/\mu L^2\right)^{1/3} t^{1/3}$. Typically, for a drop size of a few millimeters, this expression predicts a displacement of the order of $1\ cm$ over the first $0.1\ s$, which is quite consistent with our observation of dodecane (oil of similar viscosity $1.3\ mPa.s$) on wood, but is several orders of magnitude shorter (of the order of $2.5\ cm$ over the first $100\ s$) than the observations for the water on wood (see Fig 4.14).

From these observations of slow spreading over horizontal and inclined surfaces we deduce that there is an effect tending to damp the spreading, by inducing a large contact angle, and an effect, possibly of similar origin, tending to induce some spreading. It is natural to assume that the surface roughness, inherent to the wood structure as cutting necessarily goes through vessels, fibers, or

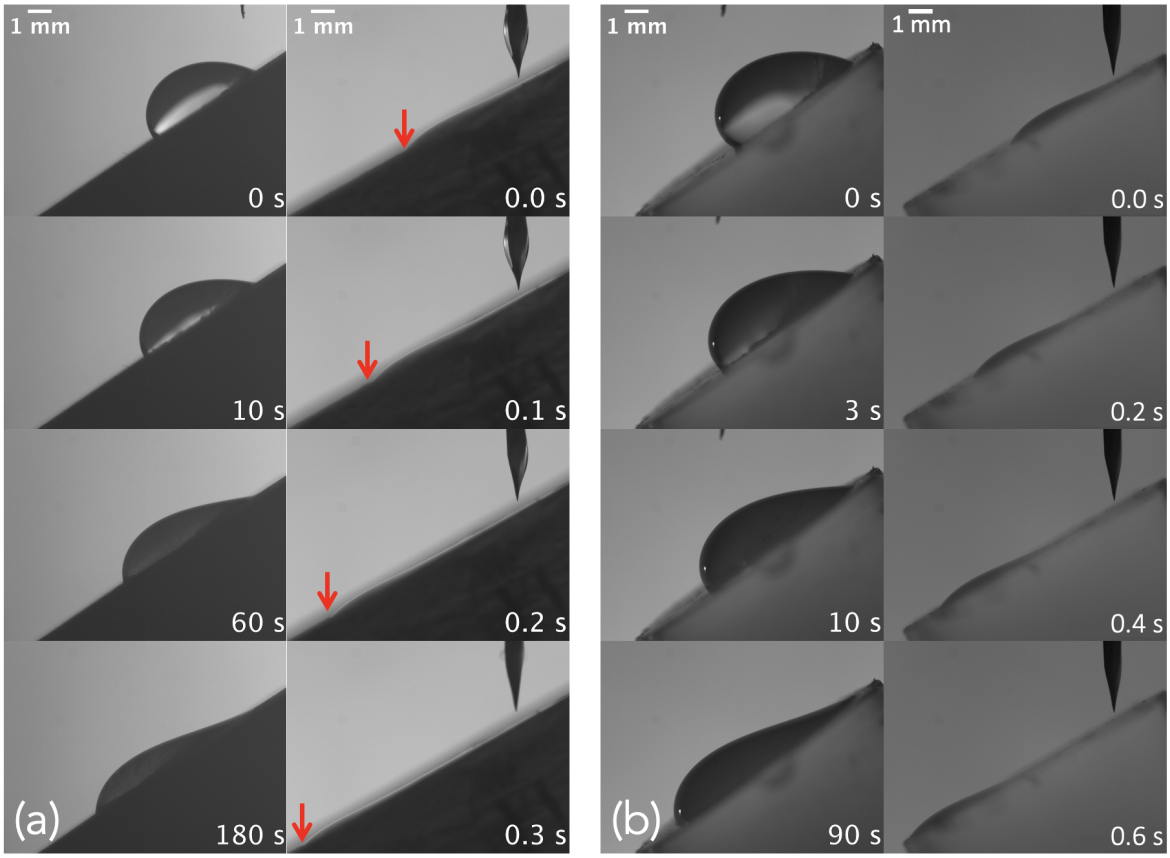

Figure 4.13: Spreading of a liquid drop poured over inclined surfaces: side views at different times on wood (a) or hydrogel (b). For both, we have water drop on the left and oil (dodecane) drop on the right. All samples were prepared at $50\ \%rH$. The red arrows indicate the front of the drop.

tracheids, plays a role in this process, by tending to pin the line of contact. However, if such an effect was at play, we would expect, after unpinning, a significant and fast advance following the above model. Instead, we observe that the fluid continuously advances over the inclined plane, without significant stick-slip effects [Kajiya, Brunet, et al. 2014] (see Fig 4.14).

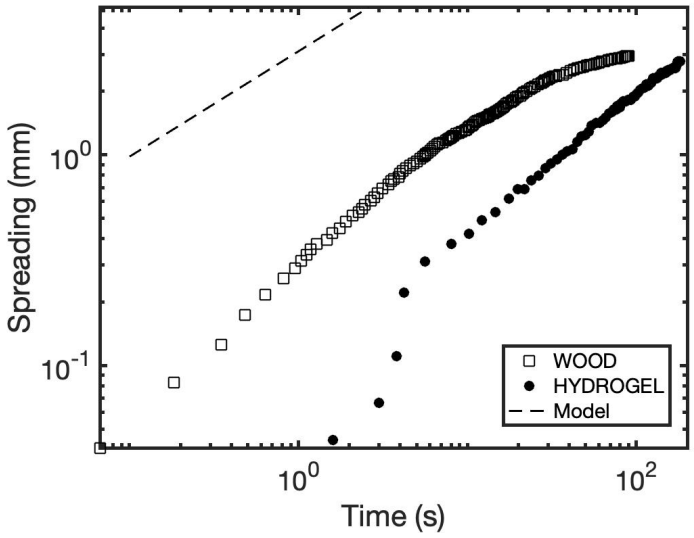

Figure 4.14: Downstream spreading evolution of the water drop in contact with the inclined plane for wood (empty square) and gel (filled circle) surfaces from Fig 4.13. The dotted line represents the expected spreading dynamic controlled by surface energy and viscosity.

4.3 Physical phenomena at the origin of the unusual wetting

In this section, we will first demonstrate the mechanisms at the origin of the apparent large contact angle using complementary studies performed with a confocal microscope. Then, we will explain the different phenomena causing the spreading of the drop.

4.3.1 Apparent contact angle

4.3.1.1 Analysis of the early stage

It is now important to introduce the fact that we obtained two different sets of experiment according to the gel preparation protocol. In Fig 4.15, we observe two surface textures:

- Surface (a) is filled with small droplets. They are not made of water since they don't evaporate, and they are not absorbed into the gel. However, they are miscible with water. It is our belief that they are made of residual solution (some extract after the chemical reaction). Whatever, their exact composition is not important here.

- Surface (b) is obtained by washing away these droplets. Rinsing the gel several times in a water bath is sufficient for the droplets to disappear. The gel is afterwards left to dry. We notice that the spreading dynamics of the drop is slowed down in the case of rinse surfaces. This will be discussed furthermore but here it allows us to look closer at the contact line.

Here, we suggest that the penetration of water into the gel starts from the very first contact, leading to the swelling of the gel. This swelling is obvious in the final stage where we notice the

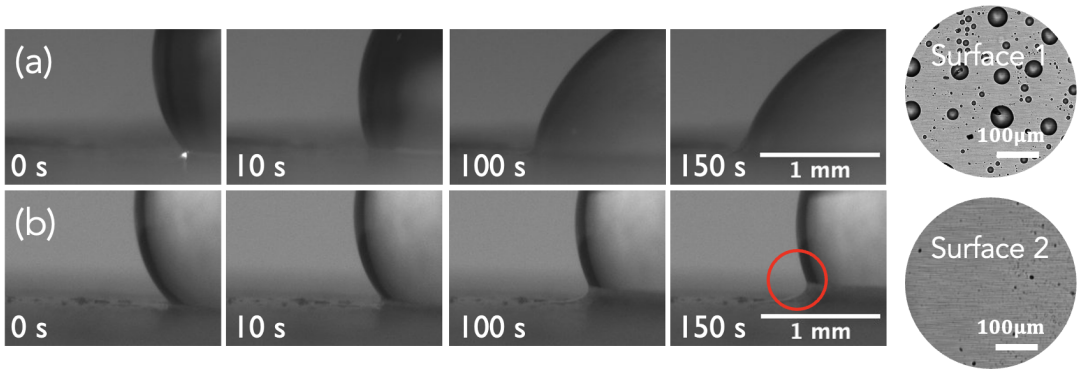

Figure 4.15: Local aspect of the foot of a droplet at different times for a gel sample prepared (a) by drying and (b) after being rinse than dried at $50\ \%rH$. Microscope images of dry hydrogel surfaces (1) filled with residual solution and (2) after being rinse with water.

yielding of a solid promontory (see Fig 4.6-3'). In Fig 4.15-b, looking closer at the triple line during its evolution in time for the rinse gel, we observe a local swelling of the gel (shown at $t = 150\ s$ by a red circle). Going back in time, this local deformation is less and less perceptible. For the raw surface, direct observation of the local deformation is difficult.

We have shown that it is possible that the gel is deformed when in contact with water. This deformation could be the cause of the high initial contact angle since it would pin the drop. As these hydrogels are transparent, it allows us to use other techniques such as confocal microscopy to further investigate this hypothesis. We have developed two methods that allow us to evaluate the swelling of the gel over time.

4.3.1.2 First method: deformation pattern

Some observations from a top view of the drop were conducted. Looking with a confocal microscope from the bottom of the gel at the interface between the droplet and the gel, we notice regular patterns (see Fig 4.16-a). These patterns appear regardless of the surface condition and are due to the deformation of the gel. As they appear from the beginning of the dynamics, their presence is a proof of the instantaneous deformation of the surface.

A hydrogel can swell significantly when in contact with water. Upon swelling in a small area, the rest of the hydrogel can play a role of rigid substrate and patterns can locally develop on the surface (see 4.16-b). This instability is due to a gradient of water concentration and appear in the case of sufficiently large stresses. The gel wants to expend due to water absorption and the dry gel exerts a resisting force [Liaw, Pereyra, and Guvendiren 2019, Trujillo, J. Kim, and Hayward 2008].

Using poly(methyl methacrylate) particles (PMMA) inside the gel, we can track the deformation of the gel. In Fig 4.16-c, we compare the position of the particles before and after the deposition of a drop of water. In the fluorescent image, we only observe the PMMA particles (in red). After the deposition of the water drop, we observe the four particles (indicated by green arrows) moving

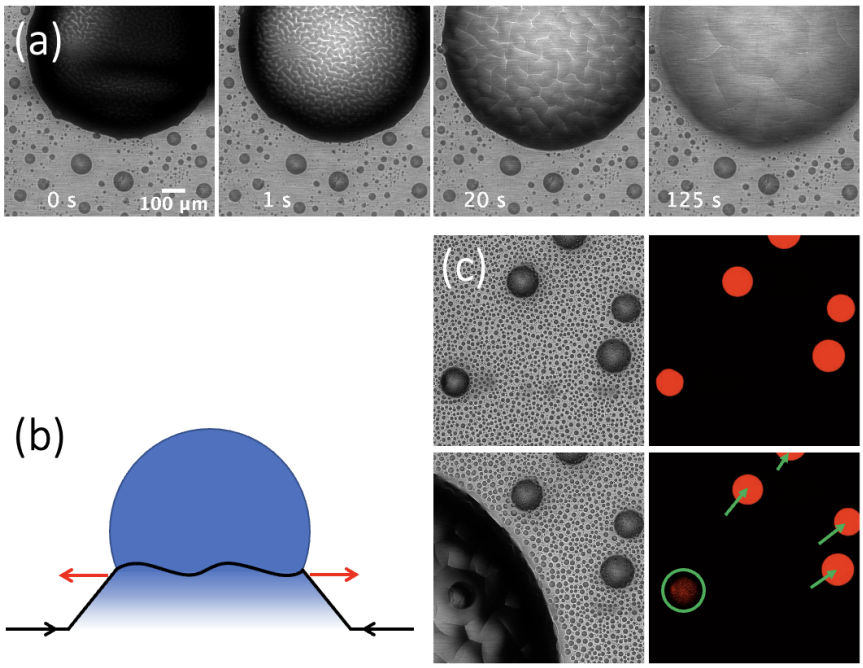

Figure 4.16: (a) Droplet seen from a top view at the interface between the gel and the droplet on a raw surface. (b) Scheme of the competition between swelling and resistant force creating patterns [J. Kim 2014]. (c) Bright-field images of the surface of the gel and fluorescent image tracking the particle layer.

away from the drop and the particle under the drop (indicated by the green circle) moving out of focus, proof of gel swelling. In the following we will only consider the uniaxial swelling of the gel.

Looking closer at the patterns over time, we observe that they are regular and evolve over time by keeping the same shape (see Fig 4.17). We can identify a junction (branching point - indicated by the green circle) always sharing three branches spaced at $120°$. We also identify the length of the branches (red arrow) and the length between two junctions (λ defined as a wavelength - blue arrow). The length of the branches is usually twice smaller than the wavelength. Note that as the gel is swelling, the interface is moving up and we lose more and more focus. This is represented by the width of the branches getting bigger.

We can characterize our deformation by a single parameter, the wavelength. This parameter follows a Fickian-type kinetics [Guvendiren, Burdick, and Yang 2010]:

$$\lambda(t) = (1 - \frac{1}{\alpha})\sqrt{Dt} \tag{4.12}$$

With $\alpha = h/h_0$, the linear extension ratio that correspond to the swelling ratio and D, the diffusion coefficient. In this case, the swelling ratio is $\alpha = 9.5$ (see equation 2.1) and the diffusion coefficient $D = 4.10^{-9}\ m^2.s^{-1}$ obtain by imbibition experiment (see Fig 4.22).

A key parameter to obtain is the amplitude of the wrinkling pattern as it represents the height

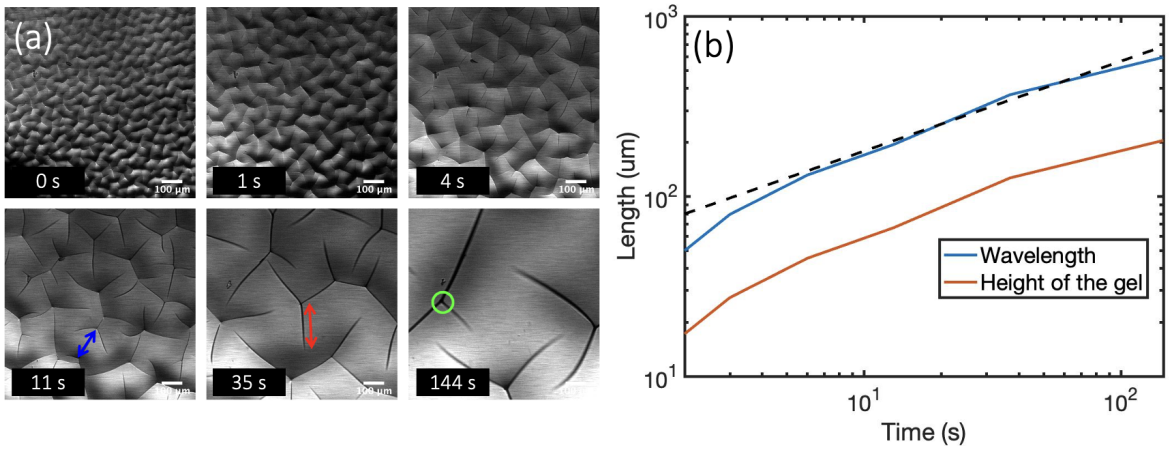

Figure 4.17: (a) Images of the evolution of the pattern in time from a confocal microscope. The blue arrow corresponds to the wavelength, the red one to the length of one branch and the green circle to the branches junction. (b) Evolution of the wavelength between two creases and the height of the gel in time. The dotted line shows the model (equation 4.12) following a Fickian-type kinetics.

of the deformation. If we considered our system as a two-layer system: the top layer is the deformed layer with a modulus E_2 corresponding to the wet gel and the bottom layer is the dry gel with a modulus E_0. From the wavelength, we can directly obtain the height of the gel in time [Guvendiren, Yang, and Burdick 2009]:

$$h \sim \frac{\lambda\sqrt{3}}{2\pi}\left(\frac{E_0}{E_2}\right)^{1/4} \tag{4.13}$$

Fig 4.17-b represent the evolution of both the wavelength and the height of the gel in time obtain experimentally with the recording of wavelength measurements. The black dotted line represents the evolution of the wavelength obtain from the model equation (4.12) which fit perfectly too our experimental data. With this technique, we were able to follow the evolution of the deformation in time and obtain a value of the swelling at the beginning of the dynamics (around $20\ \mu m$ at $2\ s$ after the drop is deposited).

4.3.1.3 Second method: droplets behavior at the contact line

In the case of the raw surface, looking with a confocal microscope from the bottom of the gel at the interface between the droplet and the gel, we can observe the small droplets progressively being included in the water drop or blocked on the contact line (see Fig 4.18). The way these droplets are included in the water drop, either by mixing (miscible liquids) or by covering the drop surface (immiscible liquids), is not critical here. Depending on their size the droplets when they reach the line of contact behave differently. This can give us an estimation of the deformation:

- Droplets are immediately included in the water drop when they reach the line of contact (see red circle in Fig 4.18-b), which means that they enter in contact with the water-air interface. If the droplet is absorbed, the deformation is smaller than the radius of the droplet.

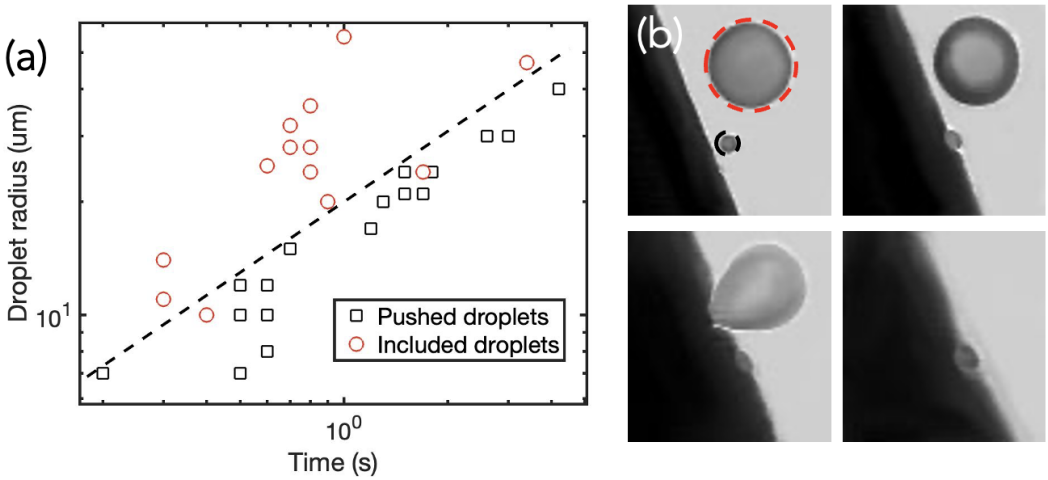

Figure 4.18: (a) Radius of the droplets of residual liquid as a function of time observed along the drop spreading in experiments with non-rinsed gel. The two types of behavior are distinguished: included (circles) or pushed (squares) droplets. (b) Successive upper views of a line of contact of a water drop (black) advancing on the surface of not rinsed gel ($50\ \%rH$) (white). We can see the behavior of two droplets (grey) of residual liquid in front of the line of contact: the largest one is immediately included in the water drop when it touches it; the smallest one is just deformed, remains in contact with the line of contact and is pushed by the drop.

- Droplets are just deformed and remain along the line of contact (see black circle in Fig 4.18-b), and they are then displaced as the line of contact goes on advancing. If the droplet is stuck in the deformation, the deformation is bigger than the radius of the droplet.

By taking images at different depth (z-stack) of the surface, we were able to estimate the height h, the radius r and the contact angle of these droplets with $\theta = 2\tan^{-1}(h/r)$. The angle obtained is greater than $90°$. However, as the droplet is deformed as it approaches the triple line, we made the simplifying assumption that the radius of the droplet is representative of the height of the droplet.

In Fig 4.18-a, we recorded the size of droplets for different experiments at the time they reach the contact line. This gives use a diagram showing the radius of deformed or included droplets. The boundary between these two regions provides an estimate of the height of deformed gel increasing in time. Note that this result overlaps with the one obtained with the patterns method.

Moreover, the presence of these droplets makes it possible to confirm that the gel is strongly deformed at the approach of the line of contact. In Fig 4.19, we see that the droplet is deformed when it entered in contact with the gel promontory. In this case, the drop is actually stuck on the edge of the deformation. The visible line on figure (c) is due to the change of curvature of the gel.

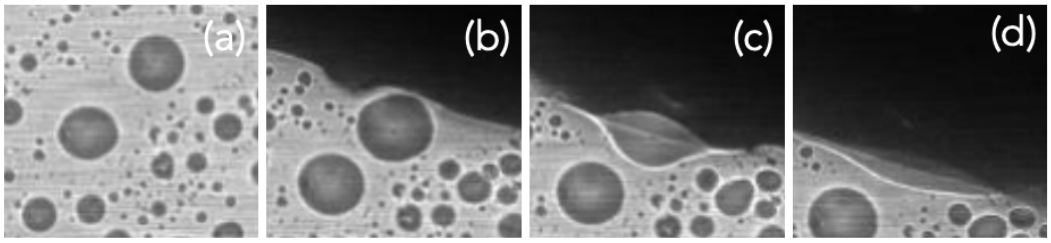

Figure 4.19: Scheme of the different behavior of the droplets entering in contact with the gel deformed.

4.3.1.4 Origin of the deformation

Let us now try to understand the origin of this deformation. Such a phenomenon does not seem to be solely explainable by the soft elastic behavior of the gel, which would then deform under the action of capillary effects [Shanahan 1987, Carré, Gastel, and Shanahan 1996, Style, Hyland, et al. 2013, Style, Boltyanskiy, et al. 2013, Style, Hyland, et al. 2017]. Indeed, such an effect is a priori negligible when $R >> \sigma/E$, in which R is the droplet size, σ the surface tension, and E the elastic modulus of the solid (here of the order of a few thousand Pascals). Here, since $R \approx 2\ mm$, we have $\sigma/ER \approx 1.4 \times 10^{-4}$. Thus, capillary effects alone cannot be at the origin of the significant deformation undergone by the gel around the line of contact.

Moreover, we conducted experiments by varying the polymer ratio to analyze the impact of the elastic modulus on the deformation of the gel. We obtained the swelling ratio α and the diffusion coefficient D with imbibition test (see section 4.3.2.2) and elastic modulus at dry and wet state with the DMA (see section 2.5.2.2). On Table 4.3 we reported the value for different polymer ratios. We notice that while the swelling ratio increases with the concentration in polymer PEG-MA, both elastic moduli for wet and dry surfaces decrease.

Water concentration	**Polymer ratio (MA %)**					
	0	**25**	**50**	**75**	**87**	**92**
Swelling ratio (α)	3.99	4.03	5	7.97	8.99	9.45
E dry (MPa)	2.8	1.59	1.24	0.55	0.28	0.25
E wet (MPa)	1.71	0.25	0.70	0.28	0.06	0.1
D ($um^2.s^{-1}$)	4000	4000	4000	4000	4000	4000

Table 4.3: Swelling ratio, elastic modulus for dry surfaces and wet surfaces and diffusion coefficient according to the percentage of PEG-MA .

We performed the same experiment used in the first method where we follow the deformation patterns in time. We reported the values of the evolution of the wavelength obtained experimentally in Fig 4.20 (represented by black plain curves). From the model 4.12, we represented the evolution of the wavelength for different gel compositions (plain curves) obtain with Table 4.3. Again, the model is coherent. From the equation 4.13, we were able to obtain the evolution of the height of the gel (dotted curves). We notice that there is no elastic dependence on the deformation as all

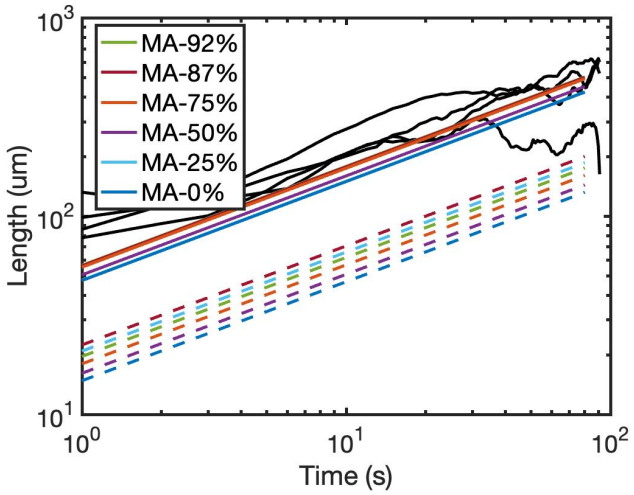

Figure 4.20: Evolution of the wavelength between two creases for different gel compositions (plain curves) and the corresponding evolution of height obtained with the model (dotted curves).

curves are more or less overlapping.

In fact, the deformation observed with these hydrogels rather finds its origin in the fast penetration of water in a thin region of the gel in contact with the drop, which induces the gel swelling.

4.3.1.5 Apparent contact angle

As shown on Fig 4.6, the observed angle (θ_{drop}) is not the angle relevant for the evaluation of the surface tension as the surface is not plane but have swellen in contact with the water. The local deformation of the gel creates an angle with the rest of the gel (θ_{gel}) and the real contact angle is the difference between the two angles:

$$\Delta\theta = \theta_{drop} - \theta_{gel}$$

The real contact angle is therefore closer to the angle obtained on the fully saturated gel. It follows that the apparent large contact angle observed here likely results from a pinning of the contact line when the liquid drop is put in contact with the surface. In this context, it is particularly surprising to observe that this line of contact slowly advances, as this is in contradiction with the assumption of pinned contact line. We will therefore try to understand this phenomenon.

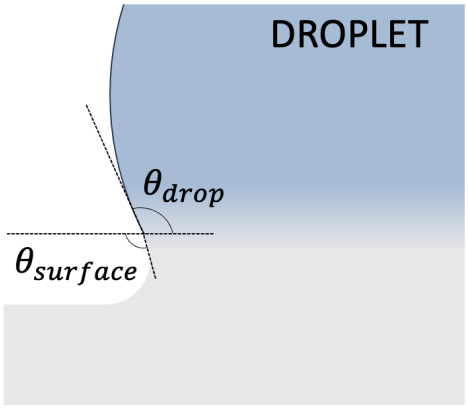

Figure 4.21: Scheme showing the angle of the surface and the angle of the drop.

4.3.2 Diffusion of the water drop

4.3.2.1 Diffusion at macroscopic scale

Here we suggest that the spreading dynamics is driven by water diffusion. We would have a continuous unpinning of the contact line by swelling of the gel. To validate this theory, we conduct imbibition experiments to approximate the diffusion coefficient with the method seen in section 2.2.2.

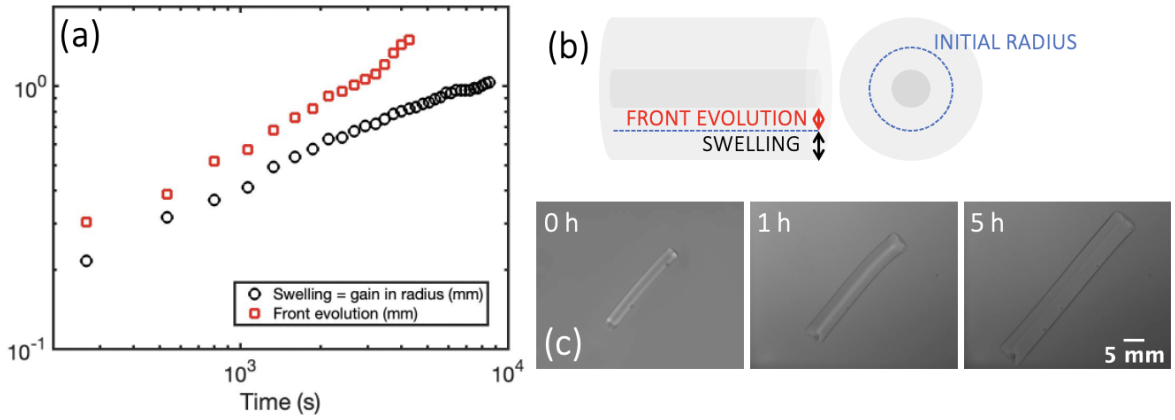

Figure 4.22: (a) Evolution of total radius of the gel (black circles) and the penetration of the water (red square). (b) Scheme of the gel parameters calculated according to the initial radius of the gel from a side view and a front view. (c) Images of the evolution of a cylinder in time.

In Fig 4.22 we follow the swelling of a dry cylinder immersed in a water bath in time. As a gel is opaque when it is dry and transparent when it is wet, we are able to distinguish an advancing front (visible inside the sample, see images 4.22 (c)) (red square). However, we assume that the increase in water in the sample is equivalent to the increase in the volume of the gel. Therefore, the swelling diameter correspond to the difference between the initial diameter and the diameter in time.

We fitted to the data, the solution for simple diffusion through a cylindrical volume at a given initial concentration. A critical assumption here is that the diameter is constant and equal to the initial one. This obviously does not correspond to our case since the diameter reaches a final value (at saturation, here a concentration of 90%). The model predicts that the entered volume of water is given by

$$\Omega(t) = \Omega_{max}\left[1 - \sum_{n=1}^{\infty} \frac{4}{a^2\alpha_n^2} \exp\left(-D\alpha_n^2 t\right)\right]$$

In which Ω_{max} is the maximum volume that can enter the gel, α_n is the n^{th} root of $J_0(a\alpha_n) = 0$, in which J_0 is the Bessel function of the first kind of order zero, and a the cylinder radius. This model remarkably fits to the data (see Fig 4.23) despite our strong assumption on the diameter value. A full description of the mechanisms should take into account the poroelasticity of the medium. However, the agreement with a simple diffusion model in a constant diameter cylinder whereas taking into account the diameter variations would lead to a significantly different prediction of the model, suggests that despite the sample swelling there is a physical analogy of the mechanisms with a simple diffusion in a constant diameter cylinder.

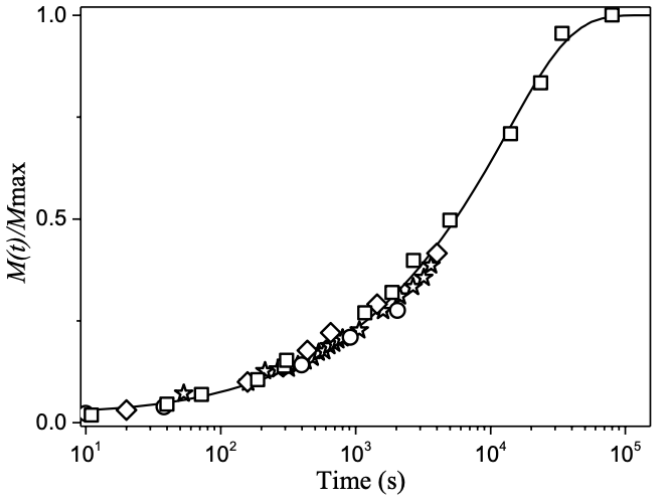

Figure 4.23: Water imbibition in a gel cylinder (initially dry) of initial diameter $2.8\ mm$. The different symbols correspond to different experiments. The continuous line is the model fitted to data by adjusting the diffusion coefficient value.

Here, we consider a standard diffusion process through a cylinder with a diffusion coefficient (D) of water in the gel. Under the (rough) assumption of a constant cylinder diameter we can

fit the diffusion coefficient value in the theoretical expression for the entered volume vs time curve expression (see Fig 4.23), which gives $D = 2.3 \times 10^{-11}\ m^2.s^{-1}$.

4.3.2.2 Diffusion according to different initial conditions

We also conducted experiment to obtain the diffusion coefficient while varying the initial water concentration (from $2\ \%$ to $60\ \%$) (see Fig 4.24-a). The samples were condition in different relative humidities. Then, we conducted some experiment by changing the polymer ratio (PEG-DA from $0\ \%$ to $100\ \%$) (see Fig 4.24-b).

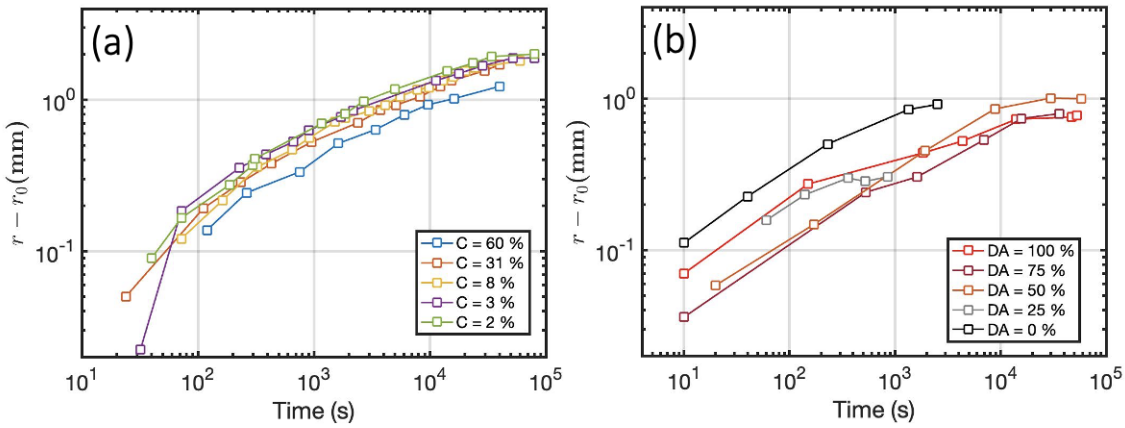

Figure 4.24: Evolution of the swelling (radius) of the gel prepared (a) at different initial water concentration and (b) at different polymer ratio as a function of time.

Fig 4.24 is a representation of the swelling (gain in radius) according to time. For both experiment sets, we do not see any significant change in the swelling dynamic. We have therefore reported for all cases the same diffusion coefficient (see Table 4.3). If diffusion is the driving force behind the advancement of the drop, it is not surprising that identical spreading dynamics are obtained when varying the concentration of water (see Fig 4.12).

4.3.2.3 Comparison of spreading and diffusion dynamics

On Fig 4.25, we compared the diffusion dynamics (black curve) with the spreading rate for raw (blue curve) and rinse (red curve) gel surfaces. In the case of raw surfaces, we observe that the spreading dynamics is ten times faster than the diffusion. As we mentioned before, the spreading dynamics is much slower in the case of rinse surfaces (almost insignificant) and follows the same rate as the diffusion.

Regarding wood, we recall that the diffusion coefficient of wood obtained in the previous chapter (see section 3.2.2.2) is even lower than that of gel (in the tangential direction, $D \approx 3.10^{-10}\ m^2.s^{-1}$).

Therefore, diffusion cannot be the only driving force. In order to get a dynamic faster by several orders of magnitude than the diffusion, the timing must be imposed by some other specific effect

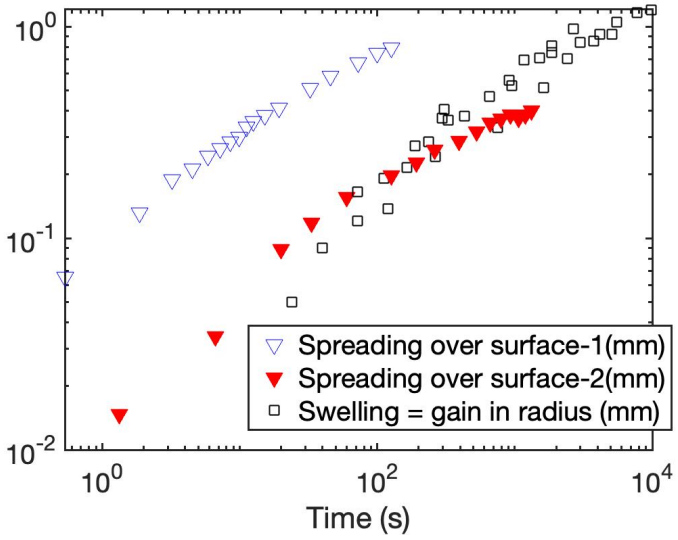

Figure 4.25: Evolution of the swelling (radius, $r - r_0$) compared to the spreading dynamic (increase of the radius) of a water drop over different gel surfaces: (empty blue triangle) raw surface filled with small droplets and (filled red triangle) rinsed surface without droplets (shown 4.15).

present on the raw surface.

4.3.3 Disruptive element

As we notice, the surface condition impacts the velocity of the spreading. To better understand we carried out experiment above the surface using a confocal microscope.

4.3.3.1 Shape of the contact line

The difference in drop behavior on the rinsed and not rinsed gel surface likely comes from the presence of the small droplets of unknown liquid in the latter case (see Fig 4.15-a). In this case, we aimed to observe the contact line according to different parameters: the drop fluid, the gel water concentration, and the surface condition. Note that in each case, we have the fluorescent signal to validate the location of the water drop. Indeed, some fluorescein was added to water to differentiate the water drop from water in the hydrogel. Different shapes of the contact line were obtained:

- (a) Using oil, the drop spreads rapidly but the contact line is perturbed on the raw surface by the small droplets. Here, as the oil is not miscible with the residual solution, the droplets play a role of roughness.
- (b) For saturated gel, the line is smooth. We have no droplets nor swelling to perturb the contact line.

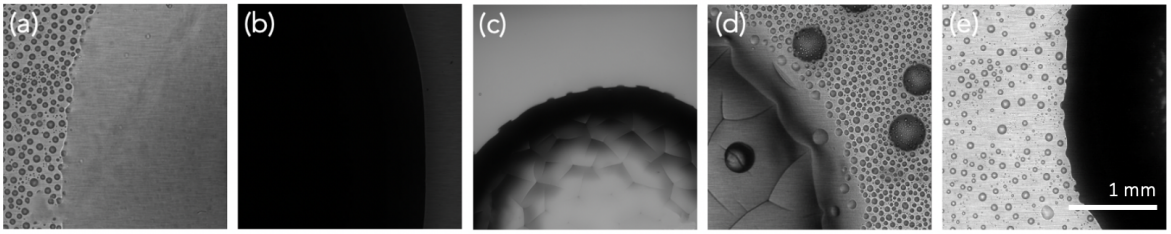

Figure 4.26: Bright-field images of a drop put in contact of the gel surface at different conditions: (a) oil drop on raw surface, (b) water drop on saturated surface, (c) water drop on rinse surface, (d) water drop receding from a raw surface and (e) Water drop on raw surface.

- (c) For the rinse surface, the shape is somehow smooth. However, we can see some deformation on the contact line due to the deformation of the gel. As we have seen above, the absorption of water leads to pattern of deformation. These patterns have an impact on the edges of the drop.
- (d) As for (c), when the drop recedes because of absorption, the contact line follows the shape of the surface that has been disturbed by the swelling of the gel.
- (e) For the raw surface, the contact line is not smooth. We see here that it is disrupt by the small droplets.

The observations show that the deformation of the gel disturbs the contact line (c and d). However, we also observe that droplets also contribute to the disruption of the contact line when they are present (e). Let's analyze in more details the spreading dynamics of the drop in the presence of these droplets.

4.3.3.2 Pinning-unpinning mechanism

Looking at the drop spreading at a smaller scale we can see that these droplets are progressively included in the water drop. The way these droplets are included in the water drop, either by mixing (miscible liquids) or by covering the drop surface (immiscible liquids), is not critical here. The critical point is that the line of contact is continuously disturbed as it advances and encounters new droplets and so on. These successive perturbations are at the origin of its advance. After each step forward the line of contact encounters a new gel region, which rapidly swells, and a new provisional equilibrium would tend to be reached, soon destabilized when the contact line encounters other droplets at other points. Fig 4.27 describes the different steps of the process: (a) The contact line encounter a disruptive element (a small droplet). (b) The contact line is deformed. (c) The contact line wants to homogenize due to Laplace pressure. (d) The contact encounters a new disruptive element. (e) The contact line wants to homogenize again.

Considering the similarity of their physical properties and the similarity of the behavior of water drops on their surface, it seems natural to consider that the explanation proposed for hydrogels applies to wood: the initial large contact angle results from the absorption of water as bound

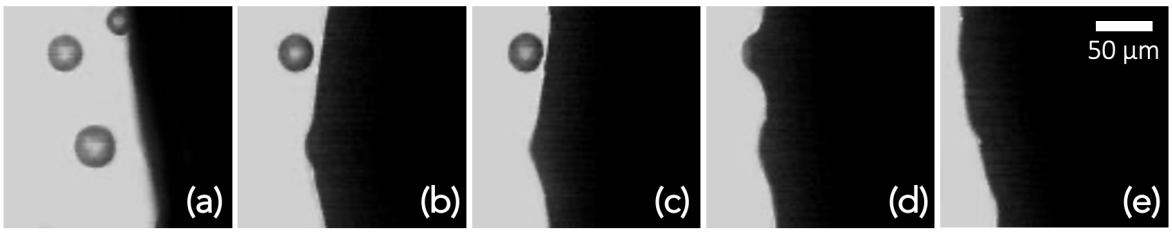

Figure 4.27: Evolution of the contact line perturbed by small droplets: (a) initial state, (b) disruption by a droplet, (c) homogenization of the contact line for pressure balance, (d) new disruption by a droplet and (e) new homogenization. The increment time between two images is $0.7\ s$.

water in the solid structure of the material which forms a soft swollen region leading to a large apparent contact angle of the drop; the line of contact is then pinned, but will unpin when the local conditions have changed. In that case we expect that the destabilization is due to the fact that the wood surface roughness somewhat evolves as bound water penetrates it, so that the line of contact must continuously adapt its shape to this new local shape of the solid surface. Finally, the diffusion of the water upstream the interface controls the drop spreading.

4.4 Conclusion

The analyze of the global evolution of a drop put in contact with a hygroscopic material allows us to identify two phenomenon: a large initial contact angle when the surface is not fully saturated with water followed by a slow spreading of the drop over the surface.

The investigations made on the contact angle showed us that the initial high contact angle is an apparent contact angle due to the local deformation of the surface at the contact line. The contact angle is actually closer to the contact angle obtained at the fully saturated stage (closer to zero). The same phenomenon can be observed during the capillary rise: the flat interface is in fact due to the local deformation of the cell wall at the triple point (see Fig 4.28).

The investigations made on the spreading showed us that in order for the drop to move forward, we have a continuous pinning-unpinning. The spreading then results from the progressive diffusion of water at farther distance and successive perturbations of the line of contact when the drop enters in contact with small liquid droplets dispersed along the surface (residues of the chemical reaction during gel preparation). A similar effect occurs for the water drop over a wood surface and explains the slow spreading: the line of contact is initially pinned thanks to a wood surface deformation resulting from wood surface swelling due to water absorption, thus leading to a large contact angle, but will unpin when the local conditions (deformation of the wood surface roughness) have changed as a result of water diffusion at further distance, allowing for a small displacement up to the next pinning point and so on.

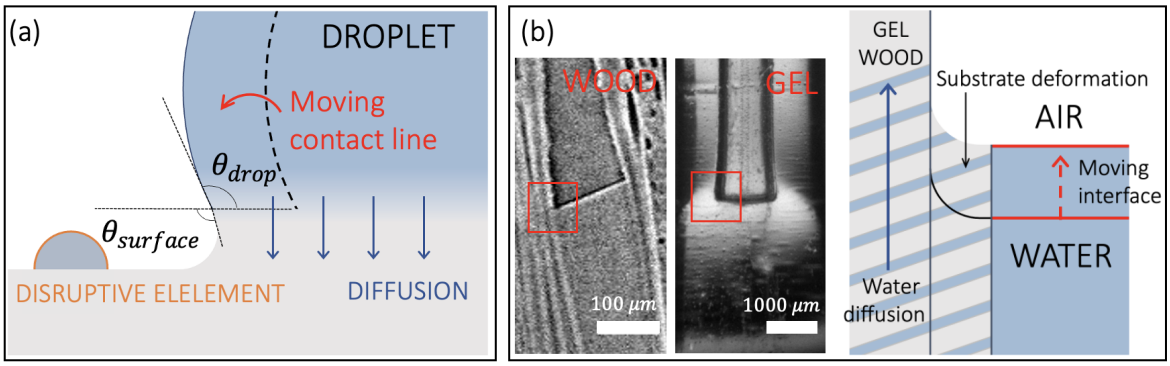

Figure 4.28: (a) Scheme of the mechanism of the contact angle and the spreading. (b) Analogy with the capillary rise.

Although the physical process of the advancing of the contact line is explain here, the process of the capillary rise is rather complex as it requires to take into account the different source of water diffusion, 3D characteristics of the water diffusion and the resulting deformability of the solid.

Chapter 5

Drying of colloidal gel

The variation of the bound water content in the cell walls leads to the macroscopic deformation of the wood. During drying, wood shrinks anisotropically (with more or less contraction depending on the directions of the wood). However, the shrinkage of this porous medium is rarely taken into account in models of water drying in wood. In this chapter, we have broadened the question to drying of a deformable porous medium composed of different pore sizes. To answer this problem, we use a model material, colloidal gels. This will allow us to control the size of the pores while keeping a rather homogeneous medium.

Let's first review the current literature on the drying of porous media. A porous media is a three-dimensional structure presenting a solid matrix and a void phase where the void phase can be connected or not. A porous medium is characterized by its structure, its pore size, accessibility, and its porosity:

$$\varepsilon = \frac{V_{void}}{V_{total}}$$

Liquid flows through a porous media are commonly described by Darcy's law, highlighting a linear relation between flow velocity (v) and the pressure gradient (∇P) throughout the porous structure. For a unidirectional pressure gradient along the z axis:

$$v = \frac{k}{\mu}.\frac{\partial P}{\partial z}$$

With μ the dynamic viscosity of the fluid and k the permeability. Here, we defined the permeability from the monodisperse packing sphere formula with radius a as a function of the density ϕ, through Kozeny-Carman's expression (5.1) [Lesaine et al. 2020]:

$$k = \frac{(1-\phi)^3}{45\phi^2}a^2 \tag{5.1}$$

Evaporation from a liquid surface will proceed until the air becomes completely saturated with water molecules ($\rho_{vap} = \rho_{sat}$). Therefore, when $n = \rho_{vap}/\rho_{sat} < 100\%$, the system is out of equilibrium and water molecules diffuse from the surface of the liquid to the air, leading to a mass

transport phenomenon toward the dryer region described by Fick's Law as:

$$\overrightarrow{j} = -D_0 \nabla \overrightarrow{\rho}$$

Where D_0 is the diffusion coefficient of vapor water through the air (at $25°$, $D_0 = 2.7 \times 10^{-5}\ m^2.s^{-1}$). When we have a controlled air flux blown over a wet surface S, a vapor gradient, considered constant is distributed on a very thin layer of thickness δ over the surface (considered constant over the thickness δ) and the rate of evaporation V_e is obtained by the following equation:

$$V_e = \frac{j}{\rho_w} = D_0 \frac{\rho_{sat}}{\rho_w} . \frac{(n-1)}{\delta}$$

Where $\rho_w = 1000\ kg.m^{-3}$ is the liquid water density and n the relative humidity of the convective air. This approximation well describes the drying rate recorded for any type of wet material put to dry when their surface exposed to the airflow remains covered by a significant layer of liquid water.

Moisture transport in porous media can mainly be describe in three main period (see Fig 5.1):

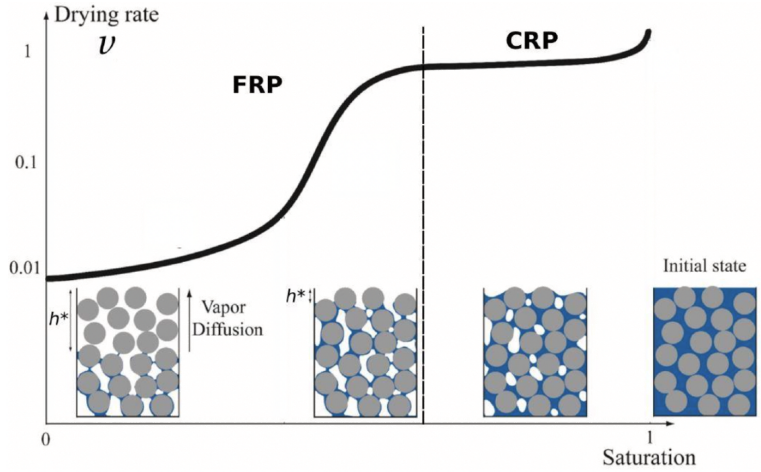

Figure 5.1: Evolution of the drying rate v matched with the evolution of the water distribution within the sample for a porous media. Air is blown parallel to the free surface of the sample at all times as pointed out on the far right scheme representing the initial state. $h*$ here represents the extent of the dry region forming from the sample free surface.

1. An induction period is observed until the heat and mass transfer processes between the material and the surrounding atmosphere approach an initial steady state and the boundary layer of thickness δ has stabilized. The duration of the induction period is usually insignificant compared to the time of the other drying periods. During this short transient regime, the material may be considered saturated.

2. CRP: Following the induction period, a constant drying rate is observed as long as the sample free surface is maintained effectively wet. Here the gas mass transfer is determined by the

thickness of the boundary layer δ. Evaporation only occurs from the free surface. Therefore, the extent of the constant rate period, depends on the material's ability to keep its surface wet enough, so to say to maintain a liquid network capable to drain enough water through the sample to the free surface for drying to remain boundary layer controlled.

3. FRP: The third stage of drying is the falling rate period. Essentially, this is the period when the removal of moisture from the solid is dictated by the material itself. The transition between the constant and falling rate drying periods appears at an average moisture content called the critical moisture content or saturation, which also corresponds to a critical capillary velocity. Note that past this point, the liquid network is assumed to become rapidly discontinuous [Coussot 2000].

If the sample is composed of different pore sizes (see Fig 5.2-a), the largest pores at the surface (where the capillary pressure is lowest) empty first and even if they are located in the bottom of the sample, the water is to be sucked by the bigger pores.

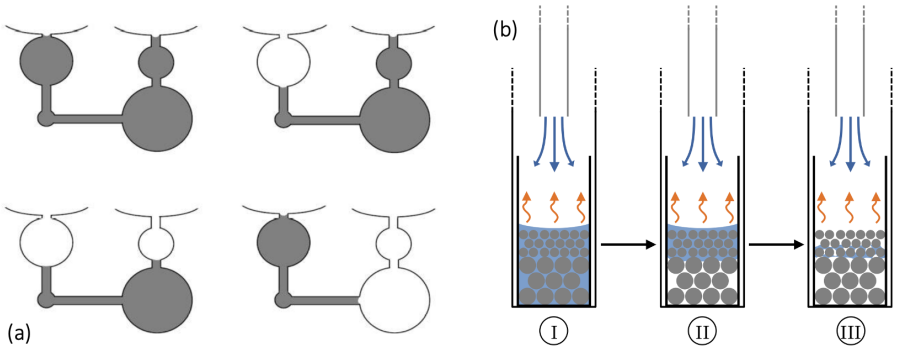

Figure 5.2: (a) Scheme for capillary equilibrium in a porous structure presenting a wide pore size distribution [Coussot 2000]. (b) Simplified diagram of the drying process of a small bi-layer on large balls [Suard 2022].

Studies have been made on drying regimes for bi-porous by modelling the material with packing beads (see Fig 5.2-b). They mainly demonstrate that whatever the position of the layers, it is the larger pores that desaturate first before the smaller pores can desaturate.

Compressible materials with double porosity were recently studied by Lerouge et al. 2020 which may be seen as model systems of wood. They showed the drying of the porous medium depends on the organization of the pores: if the large pores are not directly connected, drying induces the homogeneous emptying of the large pores first along with some compression of the small-pore matrix, if the large pores are connected, they successively empty without compression. In both cases, the small pores start or finish to empty in the next stage.

Our objective here is to apply the current knowledge of porous media drying on deformable materials. First, we want to understand the drying of a homogeneous porous medium at different pore sizes. Then, we will develop the study by overlaying the sample to obtain different concentrations (different particle densities) or different structures (different bead sizes).

5.1 Drying single layer

In this first section, we studied the drying of a single layer of colloidal silica gels. The layer is defined as a homogeneous gel composed of the same particles size (diameter of $d = 6\ nm$, $d = 12\ nm$ or $d = 22\ nm$) and at a fix particle density (between $\phi = 1.875\ \%$ and $\phi = 11.25\ \%$ volume fraction). We first characterize our system using two techniques to follow the evolution of our network structure in time: ^{1}H NMR and rheology. Then, we follow the drying dynamics with ^{1}H NMR. We also conducted experiment in parallel by filming sideways with a camera.

5.1.1 Gelation process

5.1.1.1 Evolution of the structure

After preparing the gel solution (see section 2.1.2.2), it is poured in the NMR tube. Note that at this moment, the solution is still liquid, and the gelation process has barely begun. The probability density function (PDF) of a colloidal silica gel obtained by NMR gives a distribution around one relaxation time $T2$ (one peak) (see Fig 5.3-a). This peak corresponds to the water present in the gel. The silica particles do not give any signal since it does not have any hydrogen atoms. Note that each color corresponds to a different time of gelation (from pink $t = 0\ h$ to black $t = 15\ h$). In this experiment, we have an increment of $12\ min$. As the gelation process lasts at least $5\ h$ with minimal changes on the relaxation time distribution, we prioritized measurement accuracy over temporal resolution.

From the PDF, we obtain the evolution of the amplitude in time (in h). This parameter is obtained from the integration of the distribution over the corresponding range of relaxation times and is proportional to the amount of water in the tube (blue line on Fig 5.3-b). During the gelation process, as we keep the tube closed, the evaporation is prevented and the sample does not lose any water, which is verified by the evolution of the amplitude that remains constant over time. We can also follow the evolution of the relaxation time $T2$ over time (grey line on Fig 5.3-b) informing us on the confinement of water in the system. We observe three different slopes. The difference between the first value and the last value of the representative relaxation time is small but the slope changes are consistent in all experiments.

At the same time of NMR study, we follow the gelation process with a rheometer using a cone-plan geometry (see annex 7.4 for all experiments). We follow the evolution of the storage in time (see Fig 5.3-c). We compare the evolution of the elastic modulus with that of the relaxation time. Once again, we distinguish three regimes that appear at the same time in both experiments:

- 1- Diluted regime: during a certain time $t_{GEL} = 3\ h$, the storage modulus is equal to zero and $T2$ is decreasing more and more. The gel is still in a liquid phase, but colloidal particles are starting to aggregate.
- 2- Network formation: at $t = t_{GEL}$ the storage modulus increases rapidly following a power law $G' \sim t^3$. In this time, the connectivity between the particle increases leading to the total

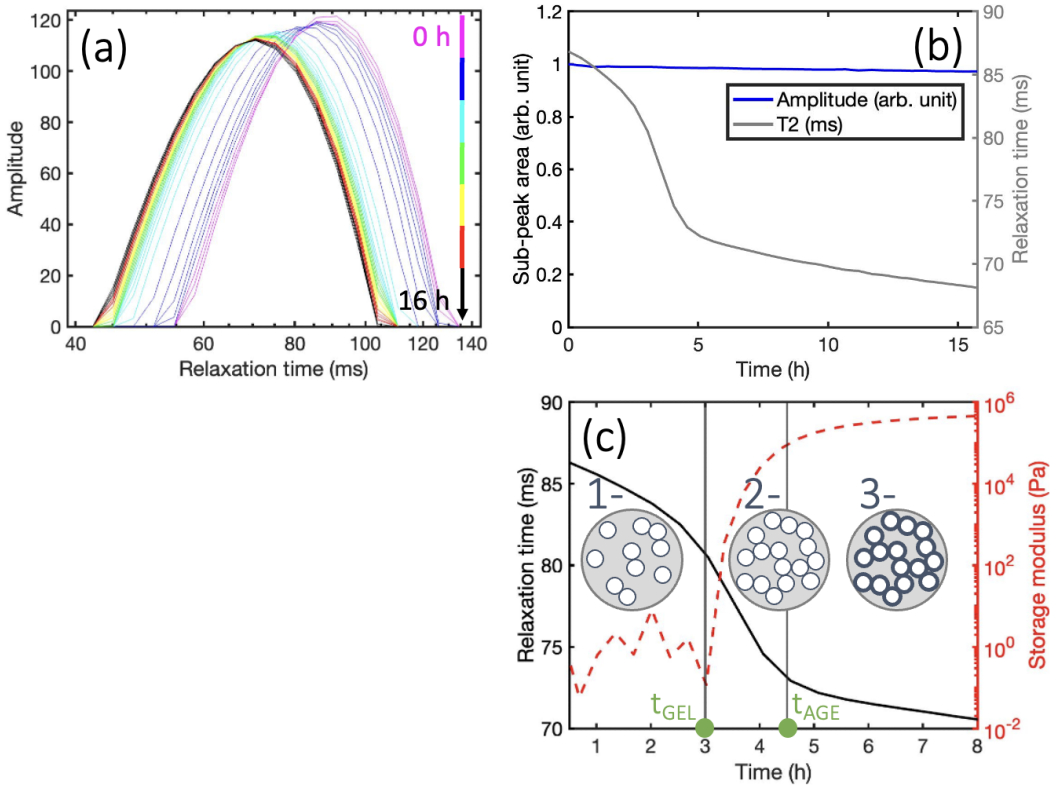

Figure 5.3: (a) Relaxation time distributions of the gelation process for a gel made of $6\ nm$ silica particles with initial volume fraction of $11.25\ \%$. (b) Evolution of the amplitude (arbitrary unit - blue curve) deduced from the integration of the distributions over the corresponding range of relaxation times and evolution the relaxation time ($T2$ in ms -grey curve) corresponding to the most representative value of the peak in the probability density function. (c) Comparison of the evolution of the elastic modulus (in Pa) with the relaxation time. The diagrams 1 to 3 are the representations of the stages of gelation of a colloidal gel.

network formation and the decrease of the pore size. Indeed, from Fast Exchange Theory (FET see equation 2.2), we know that $T2 \propto V/S$ with V the water volume and S surface in contact with water. Therefore, the more ramifications there are, the more $T2$ drops because even if S decreases, V decreases relatively faster.

- 3- Ageing: after a certain time $t = t_{AGE}$, the storage modulus follow a slower power law of square root of time $G' \sim \sqrt{t}$ describe by the Johnson Kendall Roberts (JKR) theory [F.Bonacci et al. 2020]. During this last regime, the contact between the particles progressively becomes stiffer but the connectivity stay fix.

5.1.1.2 Variation of the gel composition

We challenge our results by varying the density (from $\phi = 1.875\ \%$ to $\phi = 11.25\ \%$) and particle size (diameter of $d = 6\ nm$ and $d = 22\ nm$) of our gel.

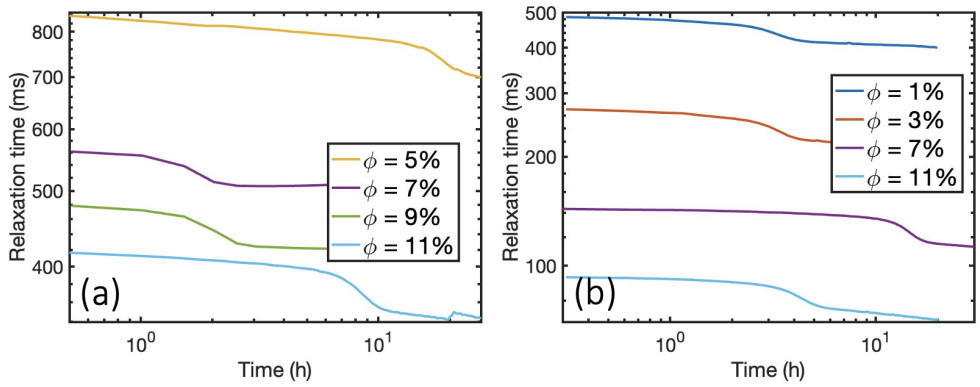

Figure 5.4: Evolution of the relaxation time at different densities during the gelation process for: (a) 22 nm beads and (b) 6 nm beads.

Fig 5.4 represents the evolution of the relaxation time for 22 nm beads and 6 nm at different densities during the gelation process. We observe that the initial and final relaxation time decrease when we increase the particle density. It also decreases when we decrease particle size. Moreover, we notice that the duration of each regime (t_{GEL} and t_{AGE}) is changing between experiment. However, the gelation time (t_{GEL}) depend on the efficiency of the urease. This effectiveness varies according to the quantity introduced but also to the date of use after the opening of the product. It is therefore difficult to obtain comparable timing.

We compare the evolution of the relaxation time during the network formation by calculating the variation of the relaxation time ($\Delta T2$) between t_{GEL} and t_{AGE}. We observe that $\Delta T2$ increases with the decrease of the colloid concentration and with the increase of the particle size.

5.1.1.3 End of gelation

The ageing regime can be prolonged, but the gel can be damaged in the long term. We therefore fix a time where we consider the gel to be ready for the drying test. This time is set to be after the regime of network formation and before one day after his preparation. We notice that during ageing, the relaxation time is changing less and so the differences at $t = t_{AGE}$ and $t > t_{AGE}$ can be negligible.

At the end of the gelation process, we recorded the characteristic relaxation time of each sample (see Fig 5.5). Since the network is totally formed, we can consider the gel to be a porous media. Using the Fast exchange theory (FET see equation 2.2 and section 2.3.3.2), we know that the relaxation time is proportional to V/S in the case of small pores (the case of the 1.875 % concentration is critical):

$$\frac{1}{T_2} = \frac{1}{T_{2\ bulk}} + \eta_2 \frac{S}{V} \tag{5.2}$$

With V the volume of liquid, S the wetted surface corresponding to the number of particles ($n_p = (3\phi W)/(4\pi a^3)$) multiplied by the surface of a particle ($S_p = 4\pi a^2$), W the volume of the sample, ϕ the particle concentration, a the particle radius, η_2 the surface relaxivity of silica

and $T_{2\ bulk} = 2.3\ s$ the relaxation time of bulk water. Equation 5.2 is valid when the diffusion is sufficiently fast to explore the characteristic pore size. In our experiments, the first term is negligible $1/T_{2\ bulk}$ as well as the relaxivity. Therefore, the relaxation time of the liquid in the pore simply scales with the ratio of the volume to the wetted surface: $T2 \propto V/S$ (see equation 5.3).

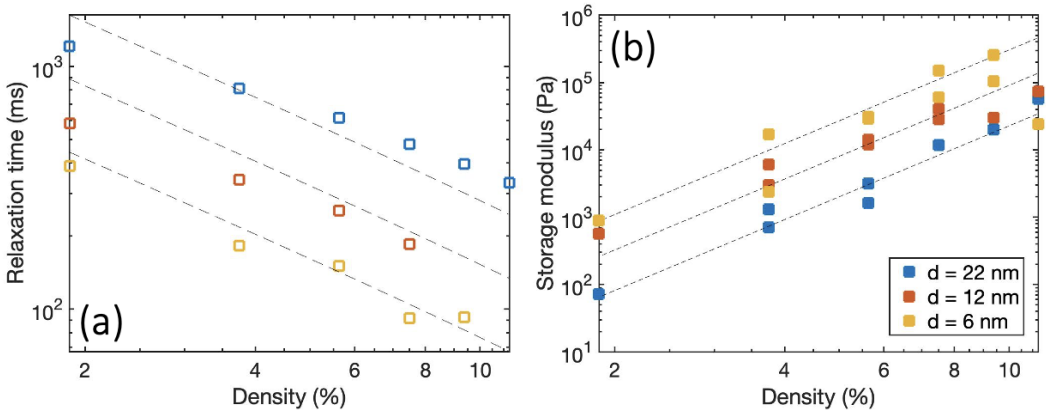

Figure 5.5: (a) Evolution of the relaxation time at the end of the gelation process for different densities and different beads size and (b) its corresponding storage modulus obtained with the rheometer. The dotted lines correspond to the models respectively 5.3 and 5.4.

In Fig 5.5-a, we observe that the relaxation time is dependent on the density and particle size. The relaxation time decreases as the particle density increases and as the particle size decreases. It follows a law depending on both density ϕ and particle diameter $d = 2a$:

$$\begin{aligned} V &= (1-\phi)W \\ S &= \frac{3\phi W}{a} \\ T2 \propto \frac{V}{S} &= \frac{(1-\phi)a}{3\phi} \end{aligned} \tag{5.3}$$

Moreover, from rheological experiments, we obtained the storage modulus for various densities and pore sizes. We see that as the density increases, the storage modulus increases. And as the beads size decreases, the storage modulus increase.s This is inversely proportional to the relaxation time obtained from the ^{1}H NMR analyses. Again, the modulus depends on the gel parameters (ϕ and d):

$$G' \propto \frac{\phi^{3.5}}{d^2} \tag{5.4}$$

5.1.2 Drying process

After characterizing our system, we conducted different drying experiments of samples made of various particle densities (from $\phi = 1.875\ \%$ to $\phi = 11.25\ \%$) and particle sizes (diameter of $d = 6\ nm$, $d = 12\ nm$ and $d = 22\ nm$). The samples are made in a 10 mm diameter NMR tube. We study samples of 1cm height which corresponds to the field of view of 1D profiles.

We follow the evolution of drying with NMR instrument and with an Alvium 1800 U-158 camera ($1456 \times 1088\ pixel$ resolution and $3.45 \times 3.45\ \mu m/pixel$ spatial resolution) described in section 2.2.3. In both set-ups, the drying is controlled by applying a dry air flux at $4\ cm$ from the top of the sample at a flow rate ($q \approx 4l/min$).

5.1.2.1 Drying kinetics of a single layer samples

We follow the drying kinetics of a colloidal silica gel made of the same initial particle density and size. Using ^{1}H NMR technique, we are able to follow the quantity of water within the sample in time. Fig 5.6 shows the results and analysis obtained for a gel made of $6\ nm$ silica particles with initial volume fraction of $7.5\ \%$:

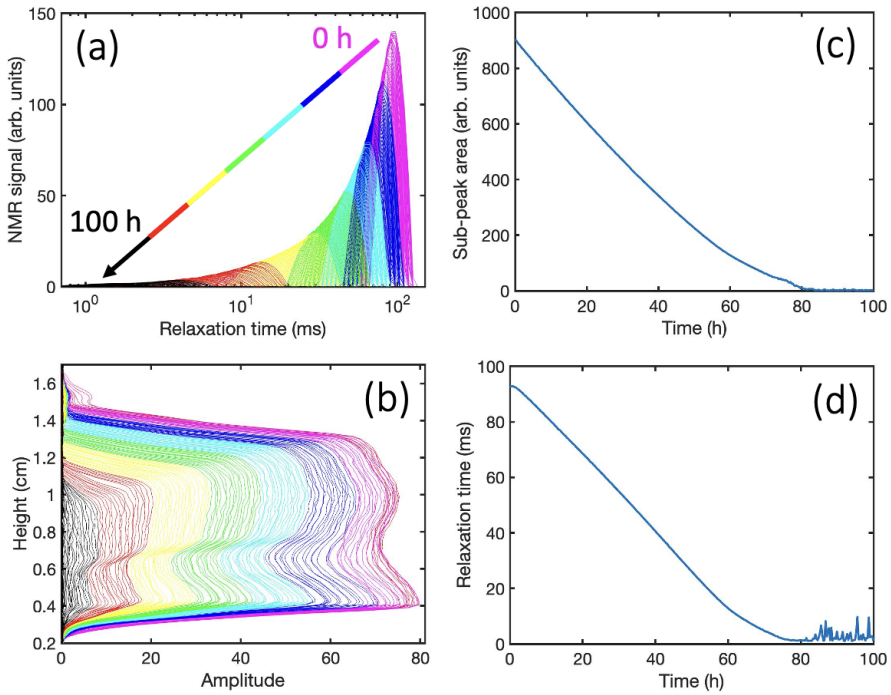

Figure 5.6: Experiment for a colloidal gel of $6\ nm$ silica particles with initial volume fraction of $7.5\ \%$: (a) Probability density function (PDF) distribution representing the amplitude according to the relation time $T2$ in ms according to time (represented by different colors), (b) 1D distribution profiles along the vertical axis showing the distribution of water with time, representation of (c) the amplitude and (d) the relaxation time $T2$.

- Fig 5.6-a show the relaxation time distributions obtained with the Laplace transform of the NMR signal. As we said earlier, in our system, we only detect the water present in the gel structure which results in a distribution around one relaxation time (one peak). We can follow the evolution of this peak during drying. Here each color corresponds to a different time (from pink $t = 0\ h$ to black $t = 100\ h$). The time increment is usually fixed around $18\ min$. Note that our experiments are limited by the sensitivity of the machine to low

relaxation times: the spectrometer used can only reach down to $T2 = 0.1\ ms$. This means that if we have water relaxing bellow this time it won't be visible on the PDF.

- Fig 5.6-b show the 1D profile along the vertical axis of the water concentration of the sample in time. Again, each color corresponds to a different time. We can correlate the profile with the NMR spectrum giving us more information about the evolution of the shape of the sample during drying. In the experiment we alternate CPMG program with 1D profile program. The 1D profile is even more limited in the amount of water detected at a low relaxation time, meaning that by the end of the drying process, water may no longer be visible.

- Fig 5.6-c is a representation of the evolution of the amplitude in time. This value is obtained by calculating the integration of the distribution over the corresponding range of relaxation times. Here the value is arbitrary but proportional to the water quantity. It can be converted in water content m in g:

$$m(t) = \frac{Amp(t) \times m_0}{Amp_0}$$
$$m_0 = (1 - \phi) \times V_0 \times \rho_{water}$$

  With m_0 the initial mass of water, ϕ the particle density $V_0 = S_0 \times h_0 \approx 0.7\ cm^3$ the initial volume of the sample and ρ_{water} the water density.

- Fig 5.6-d is a representation of the evolution of the transversal relaxation time $T2$ in time. This value corresponds to the integration of the relaxation time over the corresponding range of amplitude. The relaxation time is proportional to V/S and following this parameter over time gives us information about the evolution of the pore size.

The first observation shows that the relaxation time $T2$ is shifting, and the amplitude of the signal is decreasing during drying. From the 1D profile, we observe that the sample is gradually shrinking in height (from $h = 1\ cm$ to $h = 0.6\ cm$) during the drying process. It appears that the sample contracts homogeneously with a constant drying rate.

5.1.2.2 Water mass evolution

First, we look at the evolution of the water mass contained in the gel in time while varying the initial particle density: from $\phi = 1.875\ \%$ to $\phi = 11.25\ \%$. We also performed experiments with different beads sizes: $22\ nm$, $12\ nm$ and $6\ nm$. In order to compare experiments, we normalize the water mass $m(t)$ by the initial water mass m_0. Moreover, since for the different tests the initial drying rate is not perfectly controlled, we also normalize the time by the initial drying rate τ:

$$\tau = \frac{m(t) - m_0}{t - t_0}$$

In Fig 5.7, we compare the mass ratio according to time ratio at different volume fractions. We observe for each particle size, a first period of constant drying rate followed by a slow decrease

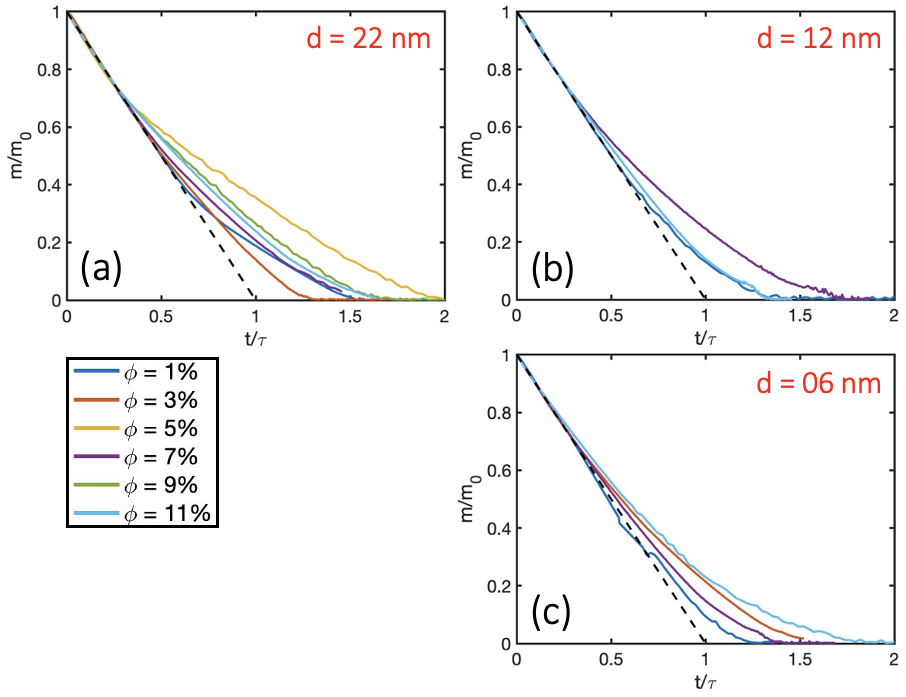

Figure 5.7: Representation of the mass ratio according to time ratio at different colloidal volume fraction for (a) $22\ nm$, (b) $12\ nm$ and (c) $6\ nm$ beads size. The black dotted lines represent a constant drying rate.

of the drying rate over time. Indeed, the mass ratio curve is aligned with the black dotted line (modeling a constant drying rate) at the beginning of the drying. Then, the curve is moving further and further away from this trend. This is similar to typical drying of non-shrinking porous media which is divided into two regimes: a constant drying rate period (CRP) followed by a falling rate period (FRP). However, we observe that for our materials the second regime appears very quickly. Note that the transition appears earlier for the more concentrated solutions. To understand the origin of this change of regime, we must analyze the geometric behavior of our gel.

5.1.2.3 Deformation during drying

Let's have a closer look at the evolution of the structure of our gels during drying to understand these two regimes. In Fig 5.8, we have represented the 1D profiles of different gels. The evolution of the contraction can be followed by the top of the sample. The top of the sample can be identified by the change in slope of the profile (see black dots on Fig 5.8-d). In each case, we observe that the profiles decrease in amplitude over time with a shrinkage in height of the sample. As a first approximation, one could consider a single contraction regime. However, the evolution of the free surface position follows two different slopes (see the two red arrows). We can therefore identify two different contraction regimes. The transition between these two regimes is consistent with the transition point of the two drying regimes (constant drying rate and decreasing drying rate). In addition, we observe a third period (corresponding to the profiles in black) corresponding to a drop

of the gel height.

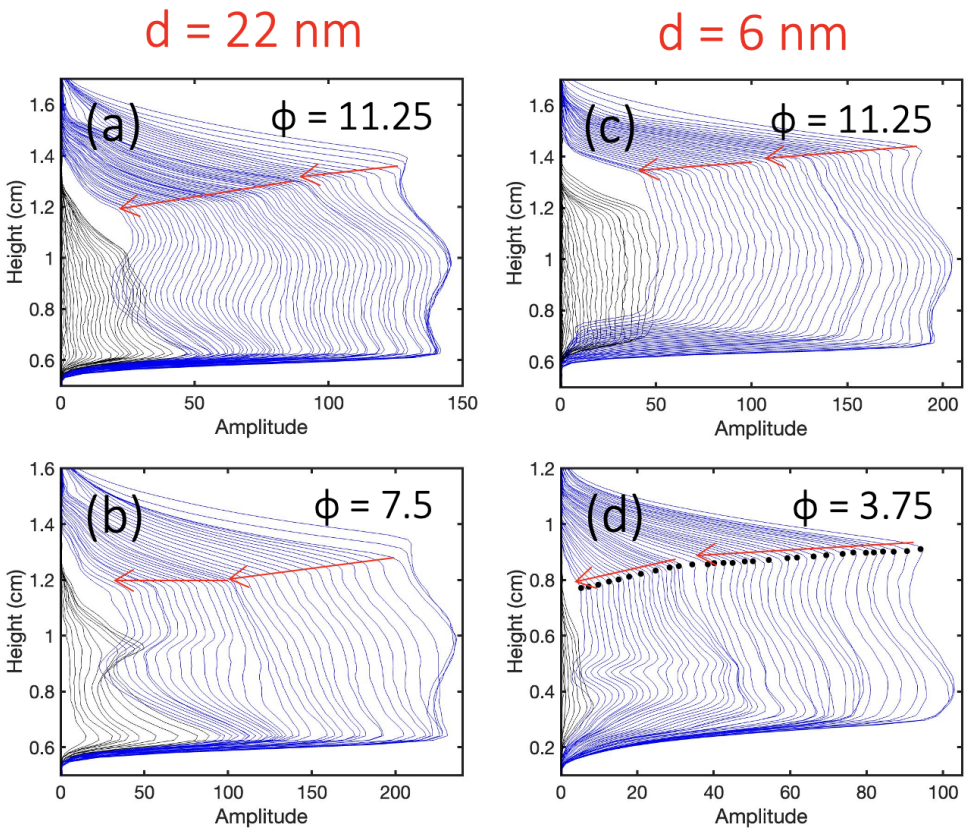

Figure 5.8: NMR profiling measurement along the vertical axis during drying of different gels: made of 22 nm at (a) $\phi = 11.25$ % and (b) $\phi = 7.5$ %, made of 6 nm at (a) $\phi = 11.25$ % and (b) $\phi = 3.75$ %. Red arrows represent the evolution of the sample free surface. The black curves represent the 1D profiles after detachment of the gel from the substrate surface. The black dots are the corresponding position of the sample free surface.

Thanks to the macroscopic observations we can identify the origin of these three regimes (see Fig 5.9). Even if the experiments are reproducible, it should be noted that the macroscopic and NMR methods are performed with different samples. Therefore, the timing of the regime changes is not necessarily identical. Between images 1 and 2, the gel dries at a constant speed corresponding to the first period (see first arrow of the Fig 5.8-c). We can see that the drying surface has not changed. Image 2 corresponds to the moment of regime change from constant drying to decrease of the drying rate. We can observe that the gel is now detached from the right side and the bottom of the substrate. Between 2 and 4, the drying surface is decreasing at the same time as the gel is shrinking. The sides of the gel here are not considered as drying surfaces. Indeed, as shown on the scheme, between the gel and the wall, the air is saturated with vapor which limits the drying surface to the top of the sample. Finally, the gel represented in black (see Fig 5.8) is simply the gel that has detached from the tube wall (see pictures 4 to 5). Thus, the change in regime would be due to the change of the drying surface. The more the drying surface decreases, the more the

drying speed decreases and therefore the slower the contraction.

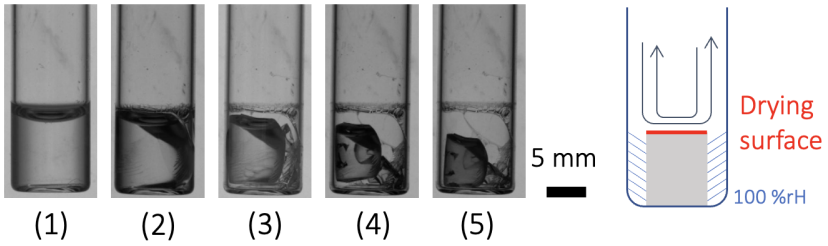

Figure 5.9: Images of the macroscopic evolution of a sample made of $6\ nm$ at $\phi = 11.25\ \%$ at different drying stages: (1) initial state, (2) end of the drying at constant rate, (3) intermediate states, (4) before falling and (5) final state. Scheme for drying a gel with a reduced surface.

To verify that the contraction is proportional to the decrease in the amount of water, we analyze the evolution of the representative relaxation time according to the water concentration. In Fig 5.10, we represented the normalize relaxation time $T2/T2_0$ with the normalize mass m/m_0 for the various bead sizes with $T2_0$ the initial relaxation time and m_0 the initial water mass. This gives use information about the evolution of the structure as the sample is losing water. Indeed, from the fast exchange theory, the relaxation of water in pores is proportional to the pore volume over the wet surface: $T2 \propto V/S$ [Maillet, Sidi-Boulenouar, and Coussot 2022].

We observe a significant decrease of $T2$ which follows a linear trend with respect to the water mass (see black dotted lines). We have a homogeneous shrinkage of the pores with no dewetting of the solid surface S. In Fig 5.10, we represented the relaxation time according to the particle density. The particle density is obtained from the evolution of the water mass considering that the pore volume remains saturated. We compare the evolution for a gel (at $11.25\ \%$ volume fraction using $6\ nm$ beads) with the Fast Exchange theory (see Fig 5.5-a) (see red dots). It is then observed that the two curves are overlapping. We can then expect a similar structure between a sample prepared by gelation at a certain concentration and the same one obtained by drying with pores always saturated.

We have seen that our gels, with a fairly low imposed air flow, shrink isotropically while losing water continuously. The drying speed decreases simultaneously with the drying surface. Now, we will be able to study these gels by overlaying two gels composed of different densities or different particle sizes.

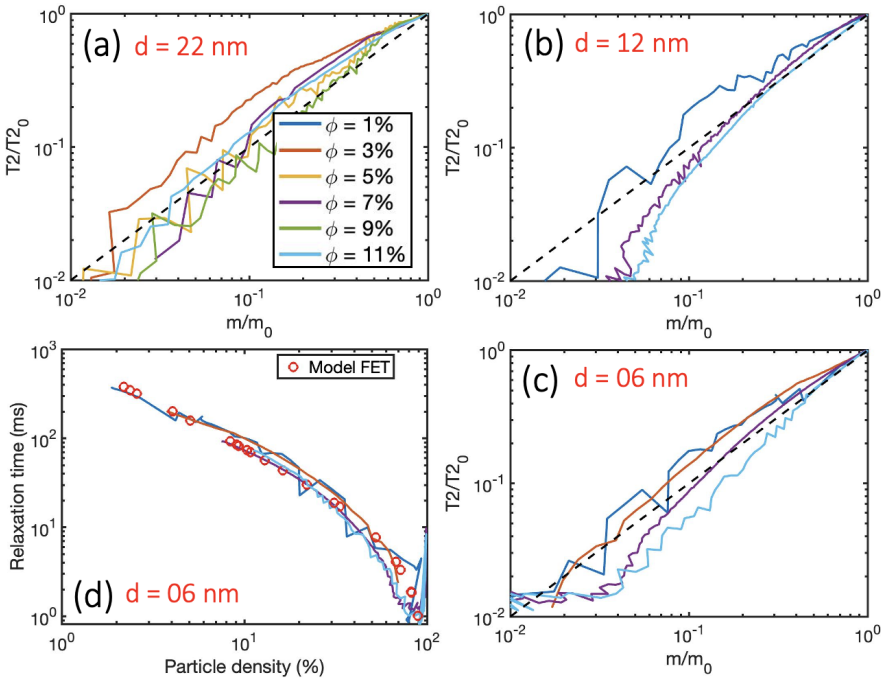

Figure 5.10: Representation of the normalize relaxation time according to the normalize water content at different particle densities for various bead size: (a) $22\ nm$, (b) $12\ nm$ and (c) $6\ nm$. The dotted black lines have a slope of one. (d) Evolution of the representative relaxation time according to the particle density obtained from (red dots) the FET model (equation 5.3) (plain lines) from the water mass evolution.

5.2 Drying bi-layers

Now that we have a better understanding of the drying process of a gel with one pore size, we can challenge our experiment by introducing a second pore size. For this purpose, we studied a gel composed of two layers of gels with either different particle densities or different particle sizes.

5.2.1 Gelation process

The manufacturing process of our gels consists in realizing a first layer of a height of $0.5\ cm$, wait for the gelation process (see Fig 5.11-a), realize a second layer of a height of $0.5\ cm$, wait for the gelation process (see Fig 5.11-b) and then carry out the drying experiment.

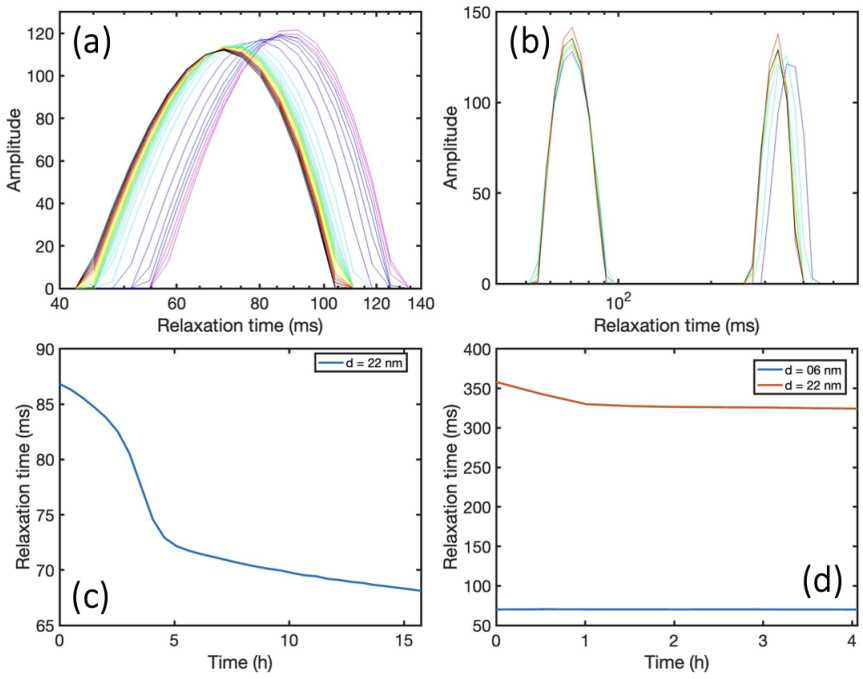

Figure 5.11: (a) Relaxation time distribution of the gelation process of fist layer made of $11.25\ \%$ gel at $6\ nm$ beads size. (b) Relaxation time distribution of the gelation process of the second layer made of $11.25\ \%$ gel at $22\ nm$ beads size. Representation of the evolution of the relaxation time $T2$ in time for (c) the gelation of the first layer and (d) the gelation of the second layer.

As we saw in the first part of this chapter, every particle density and size refers to a different relaxation time. From Fig 5.11-b, we observe that the presence of two different layers implies two different pics. This is true only if the relaxation time of the two layers is sufficiently distributed. Otherwise, it will be too hard to distinguish them. For further studies, we try to take gels with a composition leading to a well-spaced relaxation time.

Note that at the end of the gelation of both layers (see Fig 5.11-d), we obtain a value of relaxation time close to the values obtained for a single layer (see Fig 5.7) respectively around $T2 = 70\ ms$ and $T2 = 320\ ms$.

5.2.2 Bi-layer with different particle densities

We first challenge our experiments by varying the density of the two layers. We used density values as far apart as possible to obtain peaks that can be distinguished: $1.875\ \%$ and $11.25\ \%$. In this experiment, the bead size is fixed. The goal here is to compare the drying dynamics with the lower particle concentration on the top layer and with the higher particle concentration on the top layer. In the following sections, we presented the case for the $22\ nm$ beads size sample. Note that we performed another set of experiments with $6\ nm$ silica particles which exhibit similar results.

5.2.2.1 Top layer at low particle density

The first experiment is made with the top layer composed of the lowest particle density ($1.875\ \%$) and the bottom layer with the highest particle density ($11.25\ \%$) as shown on the scheme in Fig 5.12-a. The relaxation time distribution during the drying experiment is presented Fig 5.12-a. We obtained two peaks corresponding to the water contained in both layers. As seen in Fig 5.11, each peak can be attributed to a pore size which is directly related to the amount of particle introduced: the left peak corresponds to the $11.25\ \%$ layer and the right peak to the $1.875\ \%$ layer (see green and yellow arrows). In Fig 5.12-b, we represented the evolution of the water concentration in time. The water concentration of each population is normalized by the initial total water concentration $A = m(t)/m_{TOT-ini}$. Note that the total sample concentration is the sum of all the water in the sample $m_{TOT} = m_{11.25} + m_{1.875}$. Moreover, concerning the representative relaxation time (see Fig 5.12-c), we have only represented its evolution over time for each population when the two peaks are far enough apart. Indeed, during the drying process, the water populations can no longer be distinguished, and we observe the merging of the peaks. The representative relaxation time has then no more physical meaning.

Let's analyze this case using the evolution of the water concentration (see Fig 5.12-b) and the representative relaxation time for each peak (see Fig 5.12-c). We then identify two different stages:

- First stage (blue curves on the relaxation time distribution): the right peak (top layer) is decreasing and shifting toward lower relaxation time. Indeed, in Fig 5.12-b we observe a fast decrease of the water content of the top layer (green line) during $3\ h$. While the top layer is losing water, it is also shrinking until reaching a relaxation time analogous to that of the bottom layer (see green square in Fig 5.12-c). The drying of the top layer is consistent with homogeneous drying as seen above for a single layer. In the meantime, we observe the increase of the yellow curve (bottom layer). Indeed, as the top layer dries, it reaches relaxation times similar to those of the top layer. The increase of $20\ \%$ corresponds therefore to the amount of water in the upper layer relaxing at the same time as the lower layer. We can conclude that in this regime, it is essentially the upper layer that dries. At the end of the regime, $35\ \%$ of the total water in the upper layer and $100\ \%$ of the total water in the lower layer remains.
- Second stage (black curves on the relaxation time distribution): at this stage it is difficult to

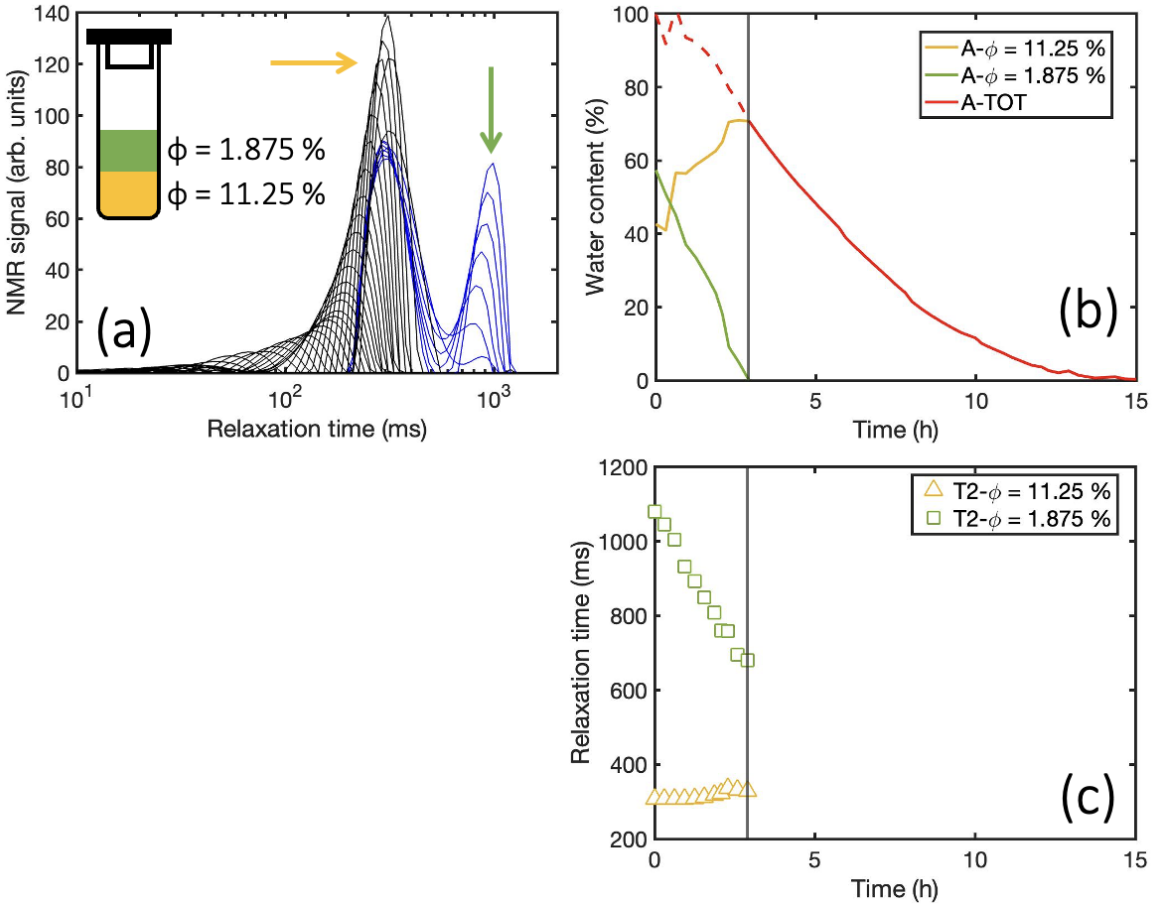

Figure 5.12: Experiment for the $22\ nm$ silica particle with the low particle density on the top. (a) Relaxation time distribution representing the two layers at $11.25\ \%$ (left peak) and $1.875\ \%$ (right peak). The different stages are represented in blue (first one) and black (second one). Scheme of the position of the layers in the NMR tube. (b) Evolution of the water content (in $\%$) in time and (c) evolution of the representative relaxation time (in ms) for: the $11.25\ \%$ layer (yellow), the $1.875\ \%$ layer (green) and the total sample (red). The vertical grey line represents the stage delimitation.

distinguish the two peaks. However, we observe that the peak shift towards low relaxation times without the appearance of a second peak (see Fig 5.12-a). Indeed, if we had only the upper layer drying, we would have the appearance of a peak at the lowest relaxation time without the peak representing the bottom layer having changed from its initial state. We can therefore make the hypothesis that the two layers dry simultaneously after reaching similar relaxation times. Moreover, we observe a progressive decrease in the quantity of water which corresponds to the homogeneous dry model seen previously.

The drying dynamics of a gel composed of two layers with the top layer less concentrated in particles can be explained in two regimes: contraction and drying of the top layer and then quasi-homogeneous drying of the two layers when the top layer has reached a relaxation time similar to the bottom layer. The analysis of the 1D profile of this dynamic is in agreement with these conclusions with a first decrease of the position of the sample free surface (green arrow) without change of the concentration of the bottom of the sample. Then the rest of the sample is shrinking (yellow arrow).

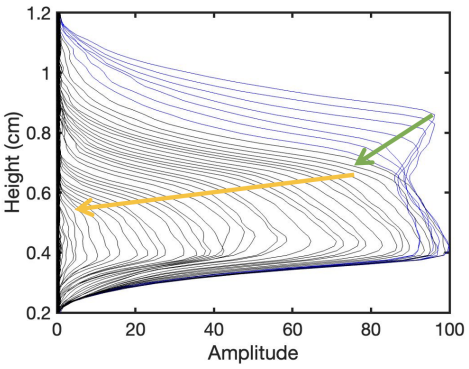

5.2.2.2 Top layer at high particle density

In this experiment, we reversed the two layers (see scheme in Fig 5.13). The relaxation time distribution during the drying experiment is presented Fig 5.13-a. Likewise, we obtained two peaks corresponding to the water contained in both layers: the left peak corresponds to the 11.25 % layer and the right peak to the 1.875 % layer (see green and yellow arrows). We identify two regimes different from the first case:

- First stage (in blue): both layers are simultaneously drying and both peaks are shifting towards smaller relaxation times. We note from Fig 5.13-b that the bottom layer (green curve) is drying faster than the top layer (yellow curve). Likewise, the relaxation time of the bottom layer is shifting faster (see green square in Fig 5.13-c). However, we could explain the difference in drying rate by the increase in the amount of water in the yellow curve as seen in the first step above. During this regime, whatever the drying rate, we observe the drying of both layers simultaneously.
- Second stage (in black): this regime is identical to the previous case with the top layer at low particle density. The peak representing the two layers decreases in amplitude less and less rapidly (as a uniform layer) and shifts to the lowest relaxation times.

The drying dynamics of a gel composed of two layers with the top layer more concentrated in particles can be explained in two regimes: drying of both layers with a higher drying rate for the bottom layer followed by drying of both layers with a higher drying rate for the top layer. Indeed, the analysis of the 1D profile of this dynamic is in agreement with these conclusions with a more important contraction of the bottom layer (green arrow) while observing the drying of the top layer (yellow arrow). It seems that the bottom of the sample loses more water

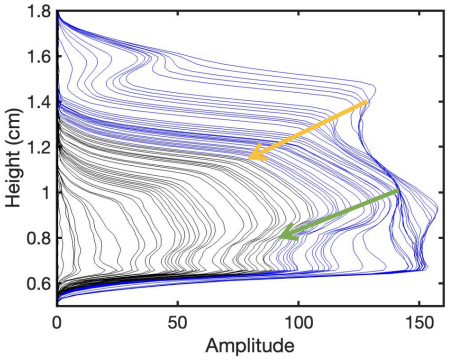

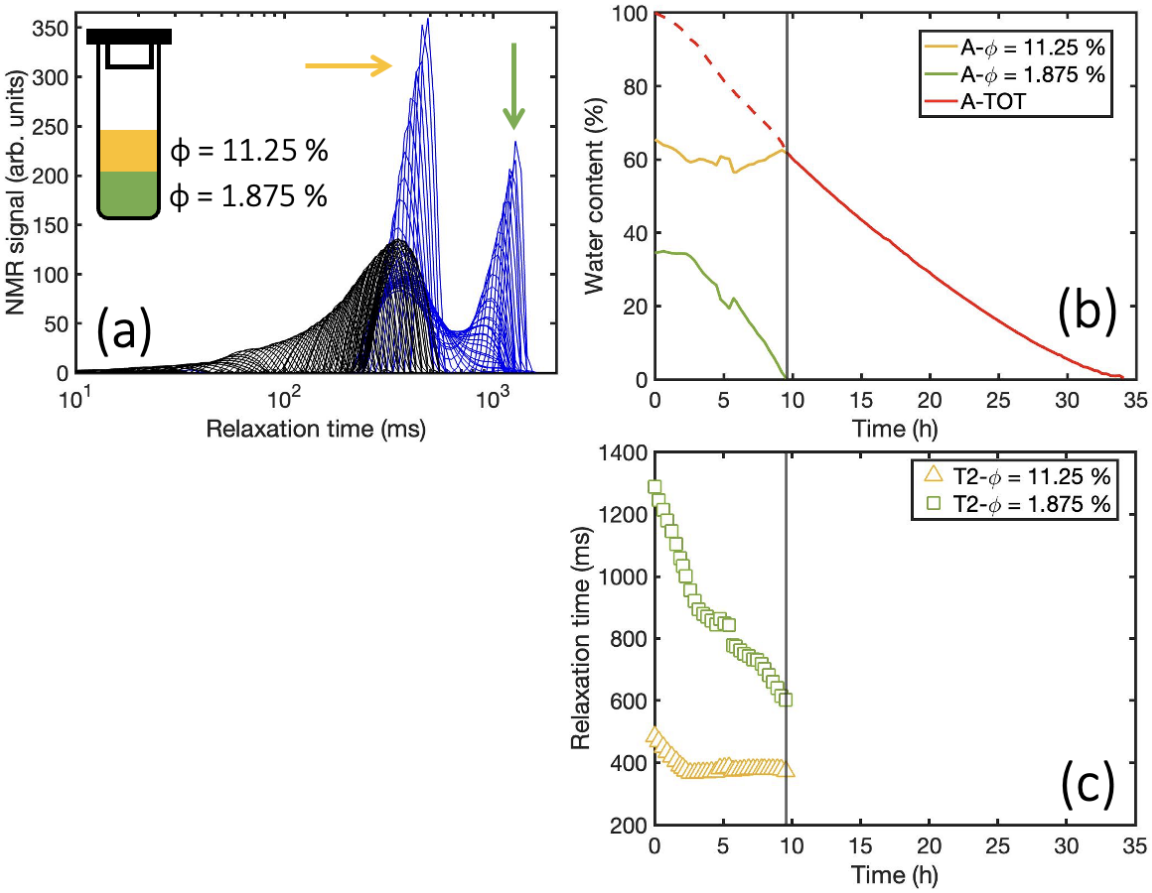

Figure 5.13: Experiment for the $22\ nm$ silica particle with the high particle density on the top. (a) Relaxation time distribution representing the two layers at $11.25\ \%$ (left peak) and $1.875\ \%$ (right peak). The different stages are represented in blue (first one) and black (second one). Scheme of the position of the layers in the NMR tube. (b) Evolution of the water content (in $\%$) in time and (c) evolution of the representative relaxation time (in ms) for: the $11.25\ \%$ layer (yellow), the $1.875\ \%$ layer (green) and the total sample (red). The vertical grey line represents the stage delimitation.

than the top (the amplitude of the profile is lower at the bottom than at the top). Then in the second part of the drying process (black profiles), it seems that both layers reach an identical water concentration (amplitude is homogenized on the whole height of the sample).

For a sample composed of different densities, during the drying process, it is the layer with the lowest particle concentration that will dry first or more quickly if it is at the bottom of the sample. Beyond a certain concentration, both layers will dry simultaneously. The transition between the two regimes here is not well determined. It seems that the change occurs when both layers reach an identical relaxation time. We have seen that this relaxation time is proportional to the particle density, but it is also proportional to the elastic modulus (see Fig 5.5). To see the impact of the

elastic modulus, we will now study gels composed of different sizes of beads. Indeed, with the same particle concentration and different particle sizes, the gels exhibit a different elastic modulus (see Fig 5.5-b).

5.2.3 Bi-layer with different beads sizes

In this part, we keep the same density, and we vary the beads size: $6\ nm$ and $22\ nm$. We performed three sets of experiment at different densities: $3.75\ \%$, $5.625\ \%$ and $11.25\ \%$. As they exhibit the same behavior, we only presented the case with high particle density. The goal here is to compare the drying dynamic with the higher bead size on the top layer and with the lower bead size on the top layer.

5.2.3.1 Top layer with small beads size

Let's first analyze the case of small beads size on the top layer (see scheme on Fig 5.14-a). The relaxation time distribution during the drying experiment is presented Fig 5.14-a. We obtained two peaks corresponding to the water contained in both layers. As seen in Fig 5.11, each peak can be attributed to a pore size which is directly related to the beads size used: the left peak corresponds to the $6\ nm$ layer and the right peak to the $22\ nm$ layer (see green and yellow arrows). Note that the initial amplitude of each is almost identical since it is proportional to the density of each layer. The variations are due to the amount of gel (height) introduced for each solution (about $0.5cm$).

Let's analyze this case using the evolution of the water concentration (see Fig 5.14-b) and the representative relaxation time for each peak (see Fig 5.14-c). We then identify two different stages:

- First stage (blue curves on the relaxation time distribution): the top layer (right peak) is decreasing and shifting toward lower relaxation time. Indeed, we observe a decrease of the water content (green curve in Fig 5.14-b) and a decrease of the representative relaxation time (green square in Fig 5.14-c). In the meantime, the bottom layer is slightly drying (yellow curve). The top layer has lost $65\ \%$ of its total water while the bottom layer has only lost $10\ \%$. During this regime both layers are drying with a top layer drying much faster.
- Second stage (black curves on the relaxation time distribution): both layers dry simultaneously with the bottom layer drying faster (see green and yellow curves in Fig 5.14-b). At the beginning of this regime the top layer has reach a representative relaxation time close to $T2 = 150\ ms$. The upper layer appears to be limited in deformation and the gel will prefer to empty the lower layer.

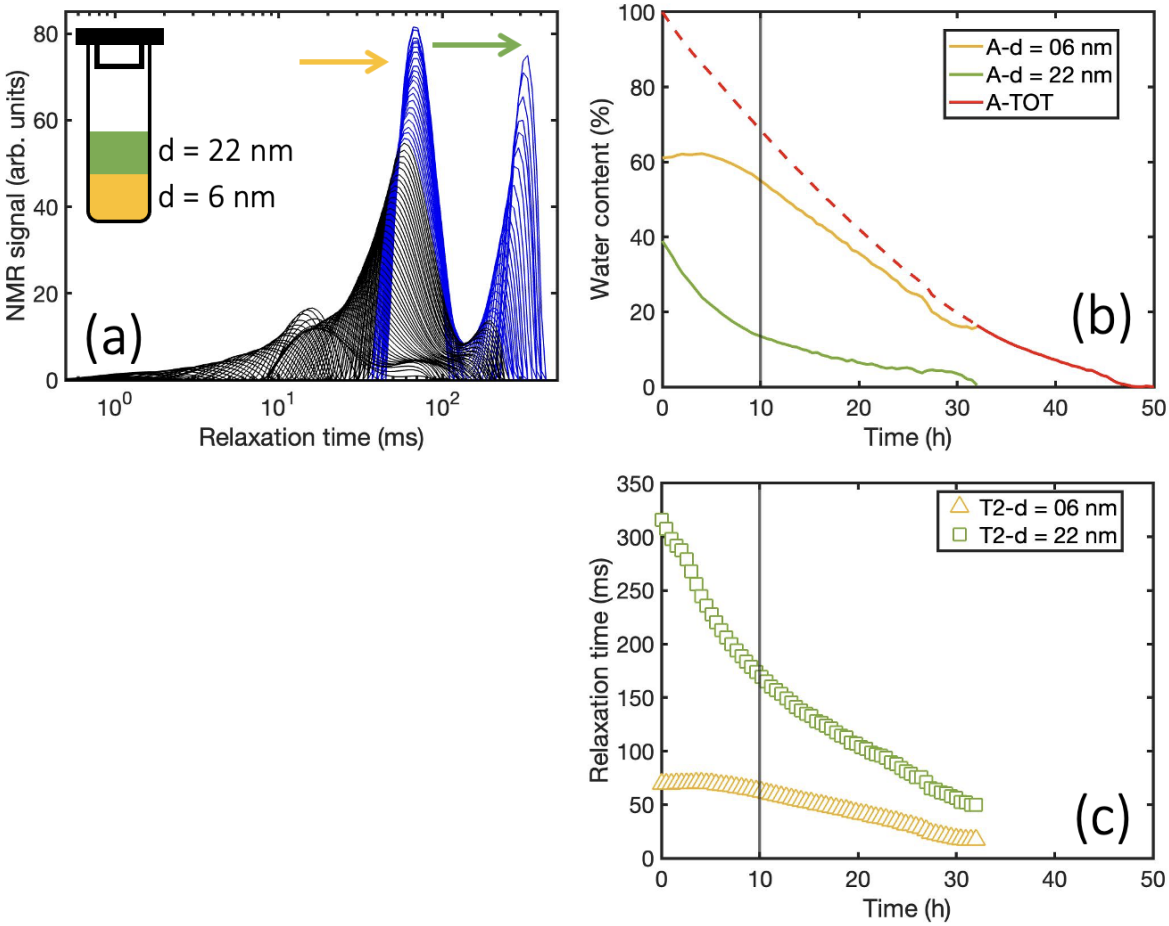

Figure 5.14: Experiment for the $11.25\ \%$ silica particle density with the small bead size on the top. (a) Relaxation time distribution representing the two layers for $6\ nm$ (left peak) and $22\ nm$ (right peak) bead sizes. The different stages are represented in blue (first one) and black (second one). Scheme of the position of the layers in the NMR tube. (b) Evolution of the water content (in $\%$) in time and (c) evolution of the representative relaxation time (in ms) for: the $6\ nm$ layer (yellow), the $22\ nm$ layer (green) and the total sample (red). The vertical grey line represents the stage delimitation.

The drying dynamics of a gel composed of two layers with the top layer made of big beads size can be explained in two regimes: drying of the top layer with a very small decrease of water in the bottom layer and then drying of both layers with a higher drying rate for the bottom layer. The transition of the two regimes occurs when the lower layer is limited in deformation. The analysis of the 1D profile of this dynamic is in agreement with these conclusions with a first decrease of the position of the sample free surface (green arrow) without significant

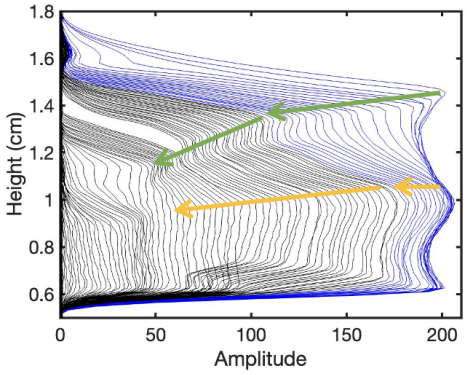

change of the concentration at the bottom of the sample.
Then, we observe that both layers are drying and the
bottom of the sample loses more water than the top (big yellow arrow). It seems that despite different dynamics, both layers shrink isotropically.

5.2.3.2 Top layer with big beads size

In this experiment, we reversed the two layers (see scheme in Fig 5.15). The relaxation time distribution during the drying experiment is presented Fig 5.15-a. Likewise, we obtained two peaks corresponding to the water contained in both layers: the left peak corresponds to the $6\ nm$ layer and the right peak to the $22\ nm$ layer (see green and yellow arrows). We identify two regimes different from the first case:

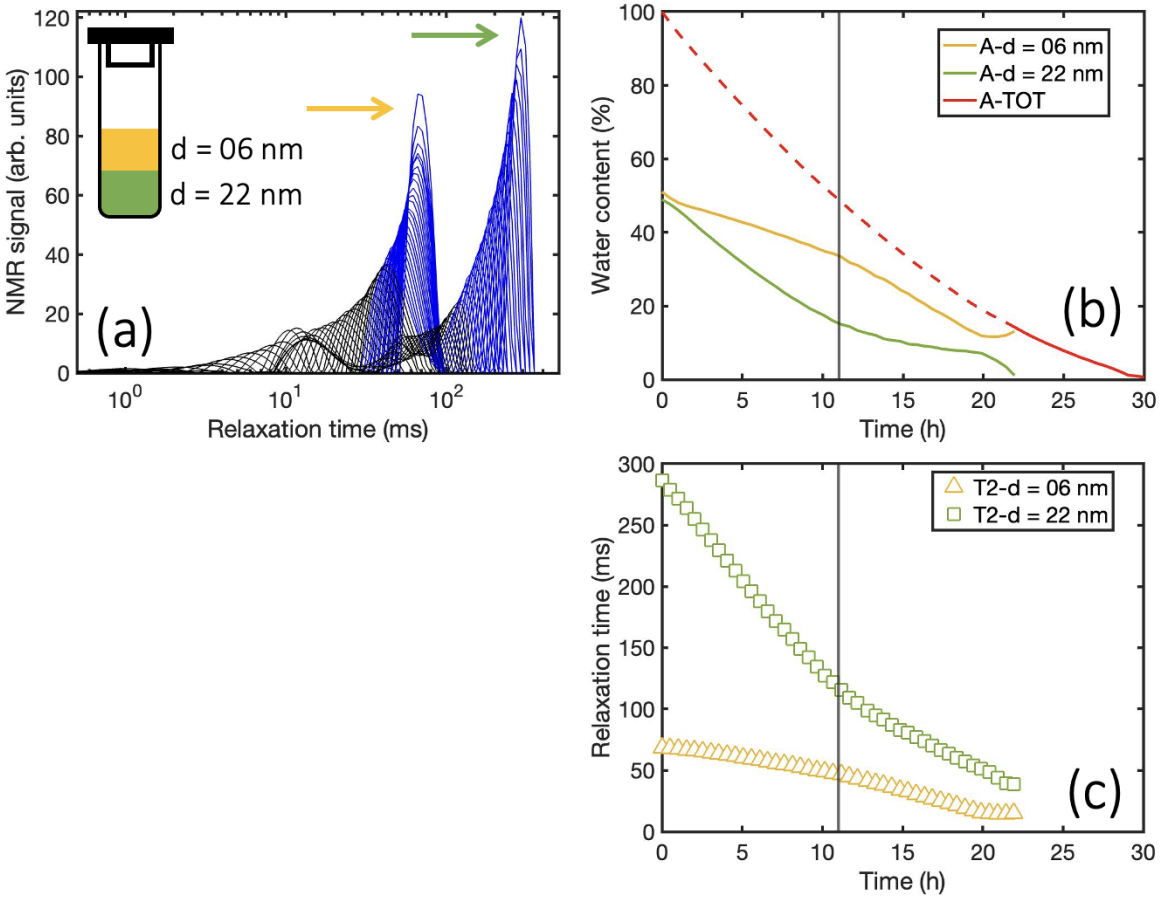

Figure 5.15: Experiment for the $11.25\ \%$ silica particle density with the big bead size on the top. (a) Relaxation time distribution representing the two layers for $6\ nm$ (left peak) and $22\ nm$ (right peak) bead sizes. The different stages are represented in blue (first one) and black (second one). Scheme of the position of the layers in the NMR tube. (b) Evolution of the water content (in $\%$) in time and (c) evolution of the representative relaxation time (in ms) for: the $6\ nm$ layer (yellow), the $22\ nm$ layer (green) and the total sample (red). The vertical grey line represents the stage delimitation.

- First stage (in bleu): both peaks are drying simultaneously and shifting towards smaller relaxation times. We note from Fig 5.15-b (representation of the water content in time) that the bottom layer (green curve) is drying faster that the top layer (yellow curve). Same dynamics are observed on the evolution of the relaxation time (see Fig 5.15-c).
- Second stage (in black): the dynamics of drying is reversed. It is now the top layer that dries faster. We notice that the bottom layer has reached a relaxation time $T2 = 120\ ms$. In the same way as in the previous case, the drying of the layer is limited by its ability to deform.

The drying dynamics of a gel composed of two layers with the bottom layer made of big beads size can be explained in two regimes: the two layers dry simultaneously with the bottom layer drying faster and then the dynamic is reversed. The transition of the two regimes occurs when the lower layer is limited in deformation. The analysis of the 1D profile of this dynamic is in agreement with these conclusions with a large decrease of the water content in the bottom layer (big green arrow) followed by a large decrease of the water content in the top layer (big yellow arrow). It seems that despite different dynamics, both layers shrink isotropically.

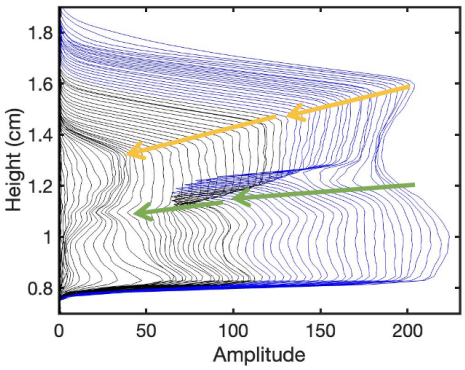

We observe in both experiments identical dynamics: fast drying of the layer with the largest particles. Then this layer is limited in deformation and its drying speed decreases. Meanwhile, the drying speed of the layer with smaller particles increases.

5.2.4 Drying process

Whether we change the particle density or the particle size, we change the pore size. It is then observed that whatever the position of the layers, it is the largest pores which empty first. This is consistent with studies on non-deformable bi-porous materials [Maillet, Sidi-Boulenouar, and Coussot 2022, Lerouge et al. 2020]. Two regimes are observed: after the partial drying of the large pores, the two layers dry simultaneously. In a deformable medium, the transition between the two regimes is limited by the elasticity of the gel. Indeed, the drying mechanism of the gel is therefore controlled by an osmotic pressure (described by the elastic modulus) which tends to balance out over time.

5.3 Conclusion

In this chapter, we studied the drying of colloidal gels. We first characterized our gels using NMR and rheology. We could observe the impact of the particle concentration and the particle size on the elastic modulus of our gels. The use of NMR to study the drying of colloidal gels, allows us to follow the water concentration of our samples over time as well as its distribution over the height of the sample (thanks to the 1D profiles). By coupling this method to a macroscopic study by camera imaging, we concluded that the drying dynamics induced an isotropic contraction of the gel. The study of these gels by layering two gels with different particle concentration or different particle sizes, shows that the drying process occurs in two steps: at first, it is mainly the layer with the largest pores that dries, then after reaching a critical deformation, the two layers dry in parallel.

Chapter 6

Dry crack in colloidal gels

Because of its imbibition and drying cycles, wood can undergo large deformations. This can impact surface treatments, leading for example to paint cracking (see Fig 6.1-b). This phenomenon is called flaking paint and can be found in many hygroscopic materials (soil, skin, blood, coffee). In particular, we can see the formation of regular patterns from desiccation cracking. Crack patterns naturally occur on a wide variety of lengths (see Fig 6.1): from crack networks in soil to cracks in thin films.

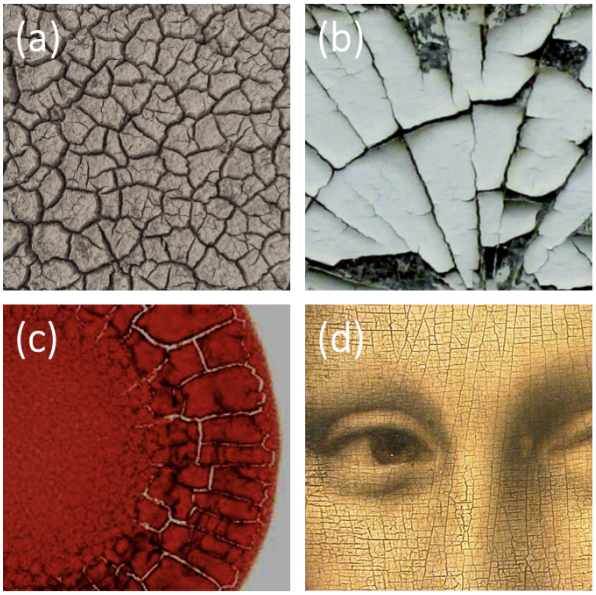

Figure 6.1: Examples of crack networks: (a) Cracks in soil, (b) Paint cracks on a beam, reflecting the growth rings of the underlying wood [Nandakishore and Goehring 2016], (c) Cracks in dried blood droplets [Zeida and Brutin 2013], (d) Craquelure on the painting Mona Lisa by Leonardo da Vinci.

The stress state near the tip of a crack can be described by the stress intensity factor K (usually applied for homogeneous, linear elastic material). The magnitude of K depends on specimen geometry, the size and location of the crack or notch, and the magnitude and the distribution of loads on the specimen. In 1957, G. Irwin discovered that the stresses around a crack are proportional

to the stress intensity factor. Moreover, crack loading can be categorized into three primary modes depending on the type of displacement of the fracture surfaces (see Fig 6.2) : opening (I), in-plane shear (II) or out-of-plane shear (III). Therefore, a crack can be described in a combination of those modes, each related to a stress intensity factor (K_I, K_{II} and K_{III}).

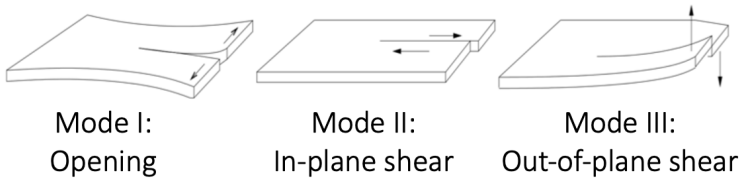

Figure 6.2: The three primary modes of crack loading.

- Mode I: opening mode and involves a tensile stress pulling the crack faces apart. For a plane stress, the fracture occurs when $K_I \geq K_c = \sqrt{\Gamma E}$ with E the Young's modulus and Γ the surface energy.
- Mode II: sliding mode and involves a shear stress that makes the crack faces slide in the direction parallel to the primary crack dimension.
- Mode III: tearing mode and involves a shear stress that makes the crack faces slide in the direction perpendicular to the primary crack dimension.

Fracture propagation in hard, elastic materials has been studied for about one century and is now very well established. A. A. Griffith contributed to the development of fracture mechanics by explaining the failure of brittle materials [Griffith 1921]. Brittle fractures are described with no plastic deformation before fracture. The fracture will happen in the elastic regime. It is a low energy fracture. Griffith's work was motivated by two contradictory facts:

1. Reduction of mechanical energy: If we consider a nominal stress σ applied on a material with a crack of length $2a$ (and with a thickness B and described by its elastic modulus E), the driving force for crack propagation is decrease in mechanical energy (which have two components, strain energy and external work done): $\Delta U_M = -(\pi\sigma^2 a^2 B)/E$.
2. Increase of the energy of the system: as the crack propagate, two new free surfaces are created. This energy is account for the resistance of the crack growth: $\Delta U_S = 4aB\gamma$, with γ the surface energy density.

Therefore, a crack will propagate when the decrease in elastic strain energy is at least equal to the energy required to create the new crack surface.

$$\sigma = \sigma_r = \sqrt{\frac{2E\gamma}{\pi a}}$$

The generalization of fracture propagation to complex, viscoelastic materials is much more recent and less well understood [Knauss 2015]. In ductile fracture, there is a significant plastic

deformation before fracture happens. The material deforms plastically before it cracks, and we can't recover the initial shape. It is a high energy fracture. The energy absorbed in ductile fracture is high.

When a significant region around a crack tip has undergone plastic deformation (the process region), other approaches can be used to determine the possibility of further crack extension and the direction of crack growth and branching. The fracture process takes place in a small region near the crack edge and is subjected to very high loads. Material separation occurs in this region (continuum mechanics does not work in this context). For example, in Fig 6.3-b we observe the crazing of polymer keeping the material together in the process zone [Broberg 1999]. Dugdale 1960 and Barenblatt 1962 introduce the concept of cohesive zone model (CMZ) to explain the gradual phenomenon happening at the crack tip. The Dugdale model describe the plastic zone size w at the front of the crack and the crack tip opening δ in the case where $\sigma << \sigma_y$ and $w << a$, where σ is the nominal stress applied on the material, σ_y the traction along the plastic region corresponding to the yield stress of the material and a the crack of length (see Fig 6.3-a):

$$w = \frac{\pi}{8}(\frac{K_I}{\sigma_y})^2 \tag{6.1}$$

$$\delta = \frac{K^2}{\sigma_y E} \tag{6.2}$$

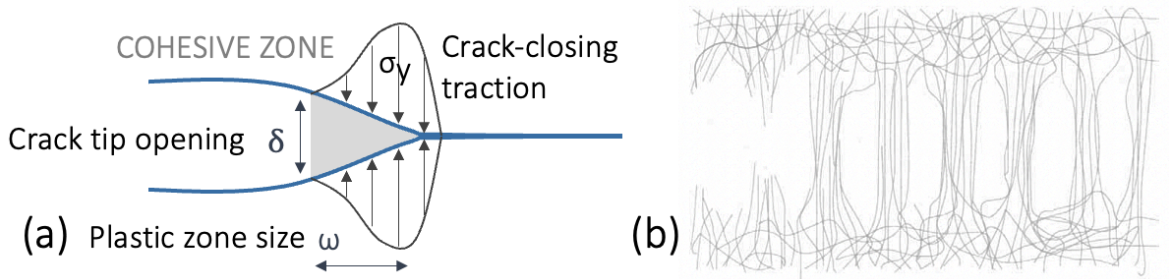

Figure 6.3: (a) Schematic of the cohesive zone fracture model. (b) Schematic view of crazing at the edge of a crack in a polymer. In the plane of the crack, the molecules form fibrils, between which voids appear. The fibrils are broken at the crack (to the left), but intact and load-carrying, apart from some broken molecules, in the process region [Broberg 1999].

Based on fracture mechanics, the material will fail at stress $\sigma_{fail} = K_I/\sqrt{\pi a}$. Moreover, based on plasticity, the material will yield when $\sigma_{fail} = \sigma_y$. These curves intersect when $a = K_I^2/\pi\sigma_y^2$. This value of a is called as transition flaw size a_t and depends on the material properties of the structure. When $a < a_t$, the failure is governed by plastic yielding, and when $a > a_t$ the failure is governed by fracture mechanics.

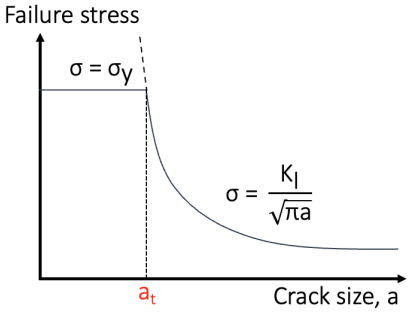

Many studies on fracture in viscoelastic materials have been based on this process zone concept. In particular, Broberg 1999 is a well detailed introduction on this subject. It has also been studied in crack closure where the Laplace pressure is governing the action from capillary forces in moist atmosphere

During the drying process, high mechanical stresses are generated. Cracks formation is a way to optimize stress release all over the system, their patterns reveal some mechanical properties of the matter [Bacchin et al. 2018]. The resulting crack patterns depend on many parameters like: the layer thickness [Lazarusa and Pauchard 2010], the drying rate [Piroird et al. 2016], the permeability of the porous media, the mechanical properties [Boulogne, Giorgiutti-Dauphiné, and Pauchard 2013, Peron et al. 2013], adhesion to the substrate [Thiery et al. 2016].

The propagation of fractures in soft solids impacts our everyday life in a variety of aspects. In this chapter, we want to understand the mechanism leading to these patterns. Using microscopic and rheological analysis, we are understanding more about the macroscopic scale of the propagation of the crack. We explore the impact of water by varying the density and the size of colloidal silica particles.

6.1 Macroscopic scale

To study drying fractures we used colloidal hydrogels (see section 2.1.2.2 for the preparation protocol). They are representative of soft, viscoelastic, and deformable materials. We will see in particular that they present different properties from hard materials and thus, we observe very different fracture behavior. Moreover, they allow us a great variability in density and size of particles. Let us first analyze the formation of macroscopic patterns observed in our system.

6.1.1 Macroscopic characteristics

6.1.1.1 Fracture initiation

We followed the drying of a colloidal gel restrained between two glass slides spaced $1\ mm$ apart. One side of the $7.5 \times 5.0 \times 0.1\ cm^3$ mold is opened in order for the gel to dry (see Fig 6.4-a). We varied the width of this opening from $0.1\ cm$ to $2.0\ cm$. After some drying time, the gel will start to fail under the drying force. Usually, after one to three days according to the opening size, the Urease concentration, and the porosity of the gel (size of the colloidal particles and density). Note that the air flux is not controlled, and the sample is left to dry at ambient air. We filmed the evolution of the sample while drying with a Alvium 1800 U-158 camera ($1456 \times 1088\ pixel$ resolution and $3.45 \times 3.45\ \mu m/pixel$ spatial resolution).

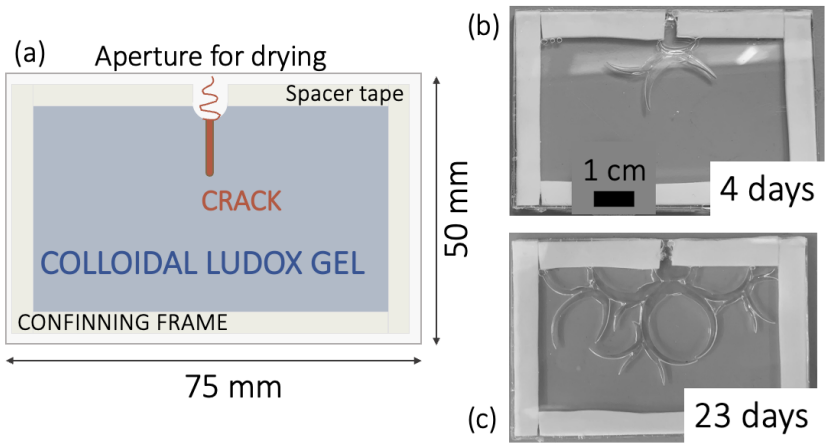

Figure 6.4: (a) Set-up for colloidal cracks. Images of the colloidal gel at a density $1.875\ \%$ and diameter size $6\ nm$ showing the evolution of the fracture (b) after 4 days and (c) after 23 days.

At a macroscopic scale, Fig 6.4 show two images of the evolution of the dry crack. The first image is taken 4 days after the preparation of the gel and the second one after 23 days. The crack nucleates at the drying surface, in this case after one day. The crack then propagates and is splits into several cracks. The cracks are not linear creating curved geometric pattern. The low speed of the fracture propagation (up to $15\ \mu m.mn^{-1}$) allows us to study it in more detail.

6.1.1.2 Crack patterns

We want to investigate furthermore the crack pattern by varying the density of silica particles (from $1.875\ \%$ to $11.25\ \%$) and changing the size of the silica beads ($6\ nm$, $12\ nm$ or $22\ nm$). Fig 6.5-c, shows the curved geometric pattern for different density and different particle diameter ($22\ nm$ and $12\ nm$). At the macroscopic scale, we observe that the crack pattern differs according to the density and the volume fraction of our gels. We observed two dimensions that described the shape of our fracture patterns: the width w_M and the radius of curvature r_M.

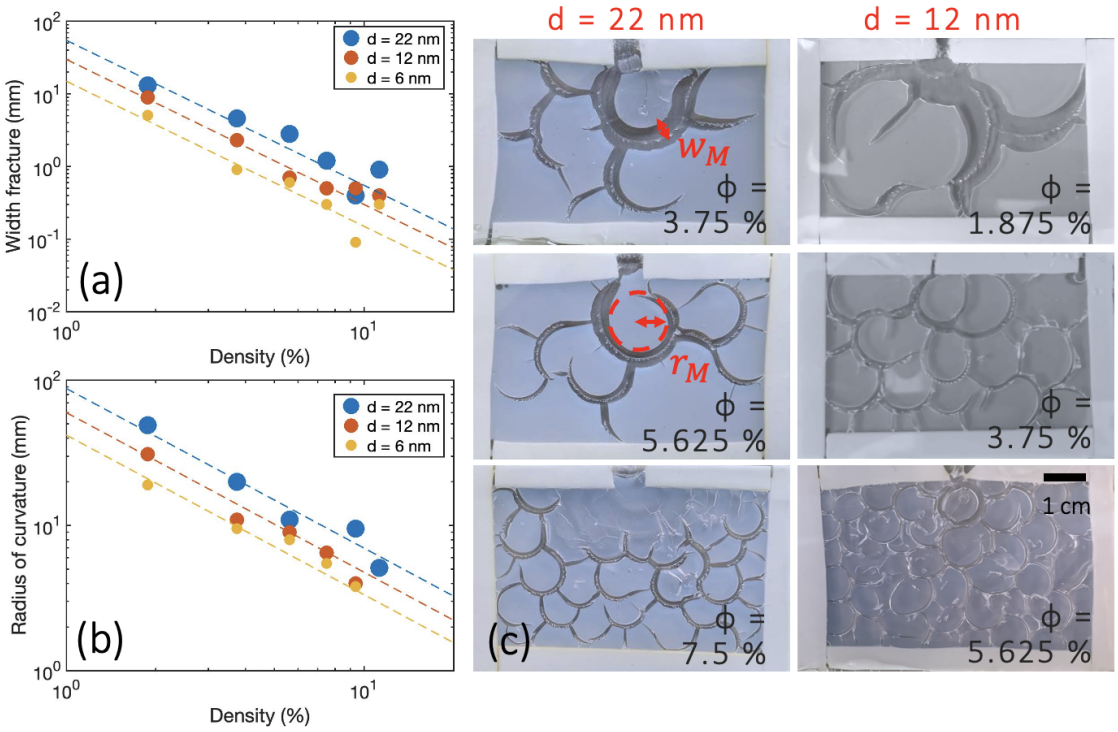

Figure 6.5: (a) Representation of the fracture width in mm and (b) the curvature of the fracture in mm according to different particle concentration for different colloidal size particle. (c) Macroscopic images of the colloidal gel cracks for diameters size $22\ nm$ and $12\ nm$ at different densities.

We reported the fracture width w_M and the macroscopic radius of curvature r_M according to the gel density for different beads size in the Fig 6.5-a-b. Both dimensions decrease with increasing density and decreasing particle size. We find that the characteristic parameters follow a low depending on the particle density (ϕ): $w_M \sim \phi^{-p}$, with $p \approx 2$ and $r_M \sim \phi^{-p}$, with $p \approx 1.1$. Note that the fracture width also varies in time. Indeed, the fracture is getting wider and wider as the gel is drying. Even when the sample is filled of cracks, the gel is still shrinking leading to the widening of the fracture. To compare our experiments with each other, we took the values at comparable timing and used the fractures closest to the opening.

6.1.1.3 Curvature of patterns

We challenged our experiments by changing the thickness of our gels (increasing the spacer tape). Fig 6.6, is the representation of patterns formed by the same gel (at $5.625\ \%$ with $22\ nm$ beads) at different thickness (from $0.8\ mm$ to $3.5\ mm$). We mainly observe a change of curvature. Indeed, the radius of curvature is increasing as the thickness of the gel is increasing (see Table 6.1). There is thus a dependence of the thickness on the shapes of the macroscopic patterns. In the rest of our study, we will use samples of $\sim 1.2\ mm$ thickness. This limits the study to dry crack propagation in a quasi-2D geometry.

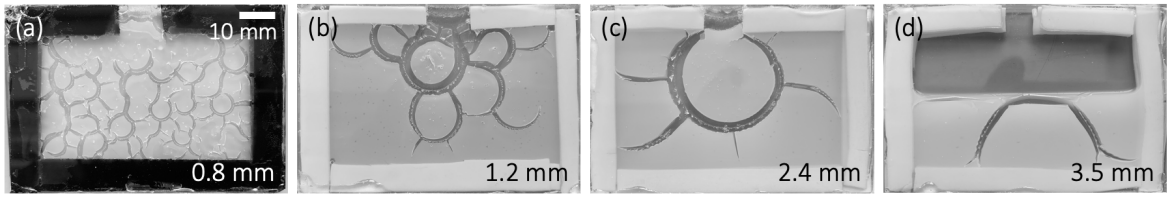

Figure 6.6: Macroscopic images of the colloidal gel cracks made of $22\ nm$ beads at $5.625\ \%$ density for different thickness: (a) $0.8\ nm$, (b) $1.2\ nm$, (c) $2.4\ nm$ and (d) $3.5\ nm$.

Thickness (in mm)	0.8	1.2	2.4	3.5
Radius of curvature (r_M in mm)	2.9	7.7	14.4	17.5

Table 6.1: Macroscopic radius of curvature according to different sample thickness for a gel at $5.625\ \%$ density and $22\ nm$ beads.

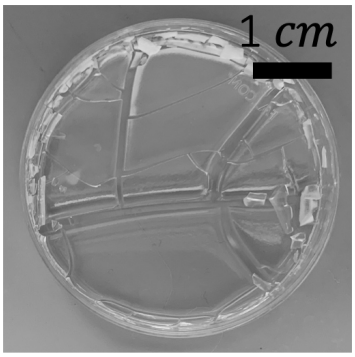

The curved pattern is surprising. The curvature of the cracks might be due to different reasons: a water concentration gradient that would direct the fracture towards the drying surface or by the difference in internal tension of the gel on the broken or unbroken parts. For a better understanding, we tried in vain to obtain straight fractures by changing the size, position, and shape of the opening, imposing an air flow, creating notches to initiate the fracture or creating two drying sources opposite each other to direct the concentration gradient. It seems that the only way to obtain a straight fracture is to have a homogeneous drying which leads to fast crack propagation not visible in our set-up. In the right image, we were able to obtain straight fracture by leaving the all surface of a colloidal sample made of $22\ nm$ silica particles at initial volume fraction of $5.625\ \%$ dry at ambient air. In the latter case we have the gel adhering to the bottom surface and preventing the shrinking of the gel. With a non-adherent surface and a slow drying, we can have a sample that shrinks homogeneously without fractures [Thiery et al. 2016].

6.1.2 Fracture propagation

6.1.2.1 Direction of propagation

From the evolution of the fracture, a first crack is propagating in the sample. At one point, several cracks are created from this first one. From Fig 6.7-b-2, the created cracks seems to be evenly distributed along the original fracture. Further, from the new cracks, other cracks will again appear until the gel is fully dry.

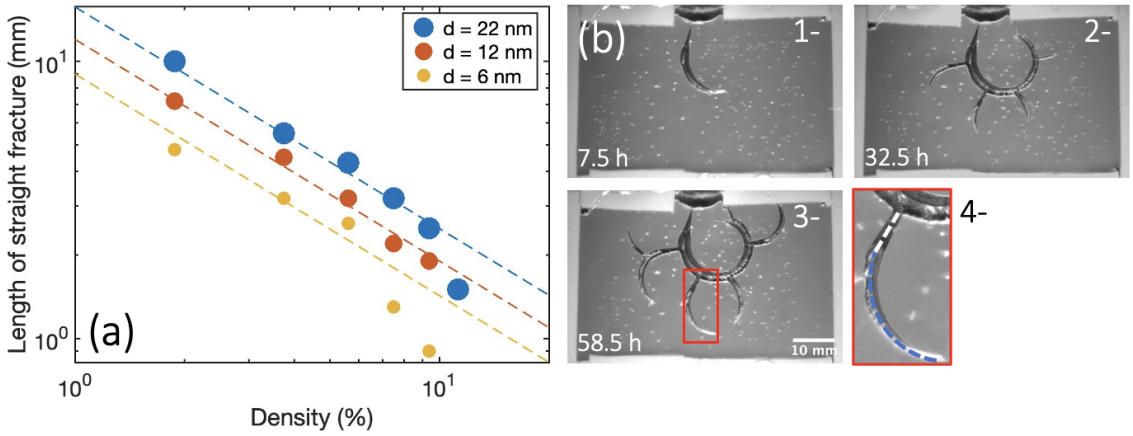

Figure 6.7: (a) Representation of the characteristic length of the straight section of the fracture (in mm) according to the particle density (in $\%$) for different beads sizes. (b) (1-2-3) Images of the colloidal gel at a density 5.625 $\%$ and diameter size 22 nm showing the evolution of the shape of the fracture in time with $t = 0$ h set to be the beginning of the fracture propagation. (4) Representation of the zoom of the fracture shape.

Looking closer at the shape of the fracture, we observe that the fracture propagation undergoes two different stages: a first linear propagation of the fracture (perpendicular to its origin) represented in white in Fig 6.7-b-4 and a second stage where the fracture is curved represented in blue. These two steps are present in all the gels and whatever the timing of creation of the fracture (at the beginning or at the end of the drying). Fig 6.7-a show the evolution of the characteristic length of the straight stage of the fracture for different samples. We find that the length l_M is decreasing with increasing volume fraction as $l_M \sim \phi^{-p}$, with $p \approx 0.8$ and decreasing particle size.

We can detect small white spots in the sample. They represent small bubbles of air trapped in the gel during the gelation process. Indeed, the insertion of air can happen during the injection of the solution into the mold. However, they do not seem to disturb or influence the propagation of the fracture.

6.1.2.2 Propagation velocity

The drying rate here is not controlled as the sample is just left at ambient air. The velocity of the fracture depends mainly on the drying velocity which depends on different parameters: size of

opening, the humidity and the temperature of the environment and the position of the fracture in the sample.

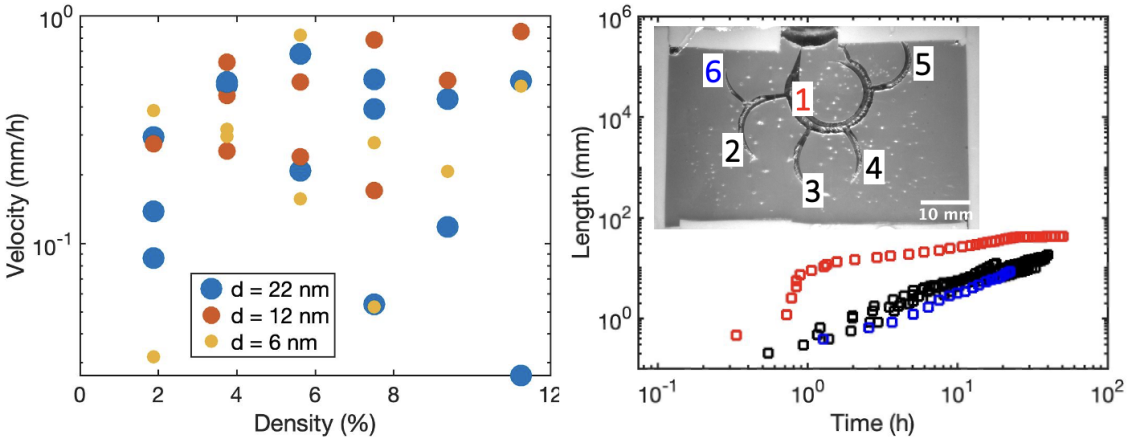

Figure 6.8: (a) Representation of propagation velocity (in $mm.h^{-1}$) according to different particle concentration for different colloidal size particle. (b) Evolution of the fracture length (in mm) in time (in h) for the different fractures present in the sample at a density $5.625\ \%$ and diameter size $22\ nm$. Each number correspond to the order of fracture creation.

From Fig 6.8-a, we see that the values are scattered. We recorded a value of the velocity varying from $0.026\ mm.h^{-1}$ to $0.85\ mm.h^{-1}$. Indeed, we observed that the velocity also varies in time. Fig 6.8-b, we observe the first fracture (red curve) progress faster than the second fracture (black curve) and even faster than the sixth (blue curve). The more the fracture progress in the sample, the slower will be the propagation velocity. Moreover, it seems that the speed during the rectilinear propagation is faster than the curved one (see the beginning of the red curve).

6.2 Microscopic scale

To understand the origin of the macroscopic pattern formed, we investigate the breaking mechanism at the microscale using a confocal microscope. The colloidal gel is transparent, and the fractures studied are slow (range from $0.5\ \mu m.mn^{-1}$ to $15\ \mu m.mn^{-1}$) and therefore justify the use of this instrument.

6.2.1 Fracture investigation

6.2.1.1 Three phases

The first observation of a dry crack (see Fig 6.9) shows some remarkable particularities: a shape that does not correspond to the singular models of fractures and the tip of the fracture filled of a different fluid. The fracture seems to be decomposed into two parts.

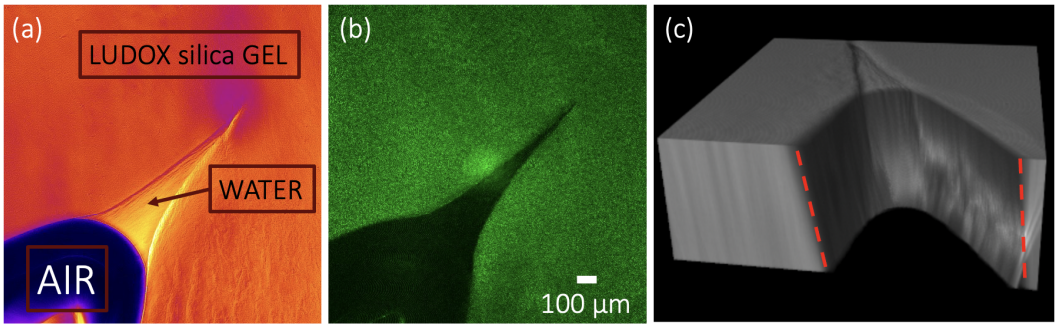

Figure 6.9: (a) Bright-field image and (b) backscattering image of a dry crack in a colloidal gel at a density $1.875\ \%$ and diameter size $12\ nm$. Note that all colors are artificial: the detected signal is an intensity unrelated to the color of the excitation or emission lights. (c) 3D reconstruction of the fracture.

Comparing the bright field image of the confocal with backscattering image, we are able to identify the third phase which is not the air (bright field = black / purple) and not the gel (backscattering = green). It is actually water coming from the colloidal gel. The role of the water will be discussed and reviewed furthermore later on.

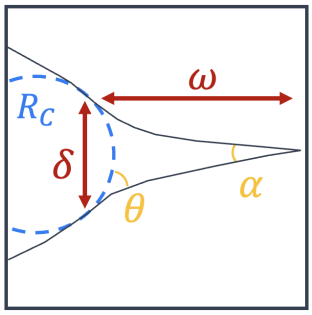

We identify multiple parameters to analyze the shape of the fracture: the radius of curvature at the water-air interface R_c; the water phase describes by a length w and a width δ; the angle at the tip of the fracture α; and the contact angle at the three phases junction θ.

We note that these parameters are valid for the whole height of the fracture. Indeed, the selected thickness allows us to address a 2D problem. It should be noted, however, that the macroscopic curvature is also reflected microscopically by a fracture tilted over the entire height. Observation made from the 3D reconstruction of the fracture (see red dotted lines in Fig 6.9-c).

6.2.1.2 Impact of the gel composition

Let's challenge our experiments by varying the density of silica particles (from $1.875\ \%$ to $11.25\ \%$) and changing the size of the silica beads ($6\ nm$, $12\ nm$ or $22\ nm$). Fig 6.10 reveals the fracture tip shape for the different gels.

For each gel, we observe the same phenomenon where the fracture is composed of two phases: air and water. Note that for a same sample, the different fractures present have the same parameters. Even during its evolution, the parameters remain unchanged. However, the lowest and higher density are limited case:

- On the lower density $1.875\ \%$, the water part of the fracture is not stable and varies in length and width. At this density, the network is composed of weaker bounds leading to bigger deformations but less homogeneous. Moreover, the radius of curvature is larger than the thickness of the gel. By increasing the thickness of the gel, we obtained more reproducible data but the fracture starts to be harder to analyze as it can evolve in a 3D space.
- On the higher density $11.25\ \%$, we are limited on the resolution. The parameters are more challenging to obtain. The fracture is thinner and the delimitation of the two phases is more difficult to see.

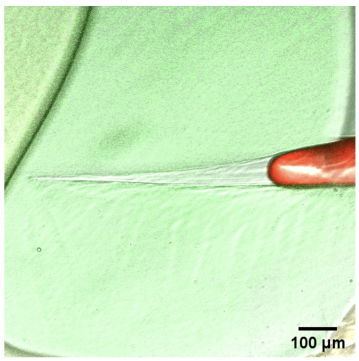

We also challenge our experiment by using a different fluid driving the fracture. The objective is to determine the influence of another fluid on the shape of the fracture. An experiment made by Sijie Sun and Stefano Aime shows the penetration of dichloromethane (in red) in a colloidal gel (in green) at $1.875\ \%$ with the $6\ nm$ particles. And indeed, it was observed that the characteristics describing the fracture varied depending on the fluid used. It remains that we still observe the same features: a fracture composed of two fluids. Those experiments are harder to realize as they are hand pressed crack. It is then impossible to follow the evolution of the fracture as they are not controlled and too fast for our set-up. We analyze the fracture after the propagation, in a stable state, here corresponding to the moment where we release the pressure. Moreover, we obtain scattered values for the parameters describing the fracture. As the pressure is released, the fracture tries to close again.

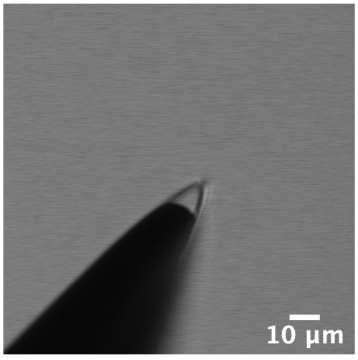

We tried to obtain the same phenomenon with a different material, here PEG hydrogels. Most of the fracture formed in the gel where without water. Drying the sample resulted in either delamination or fast and straight fracture propagation. We eventually observed the water phase some time after the nucleation of the crack itself. However, the parameters describing it were not consistent for a same experiment.

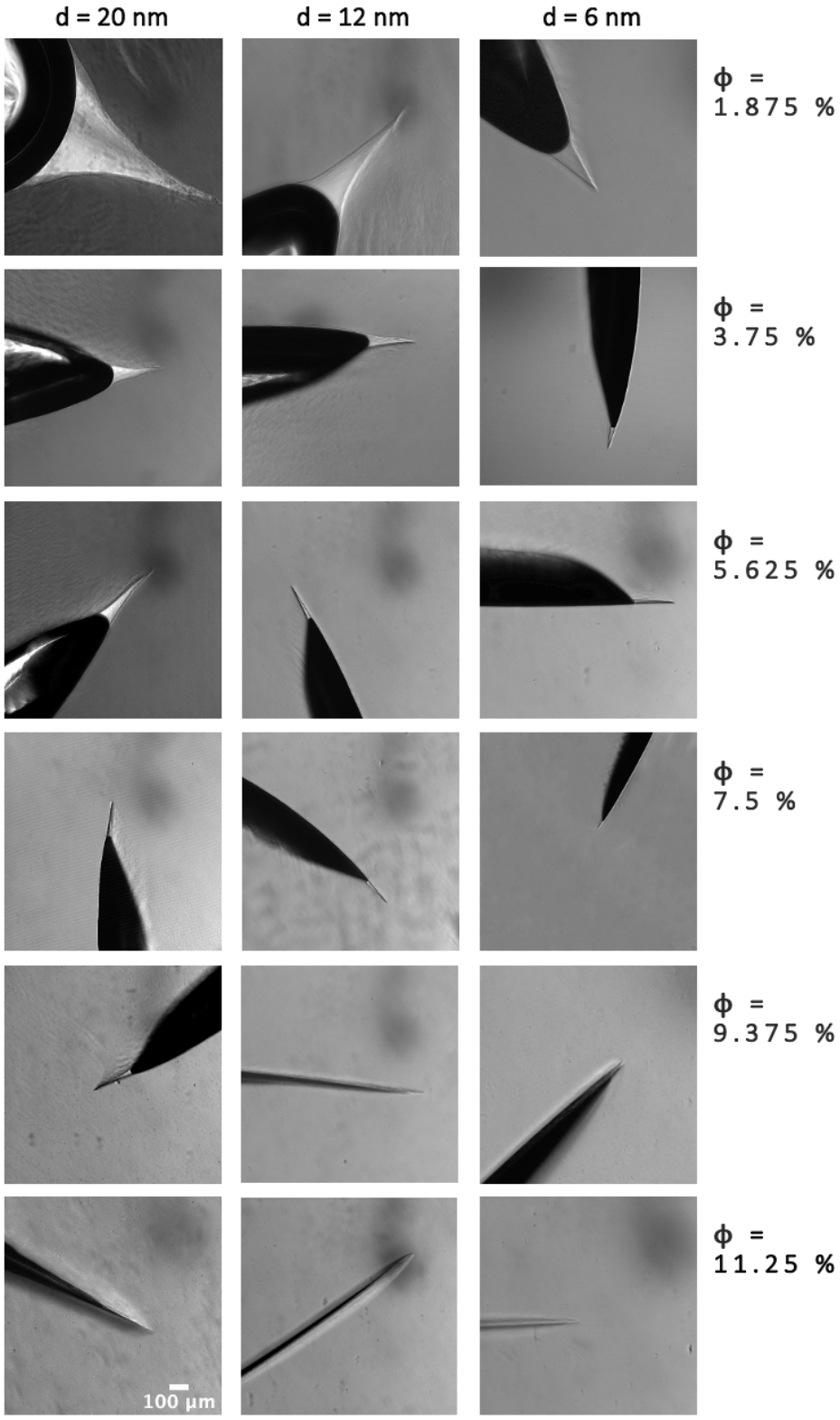

Figure 6.10: Raw images from the confocal microscope showing the shape of the fracture according to the density (from $1.875\ \%$ to $11.25\ \%$) and the beads size ($6\ nm$, $12\ nm$ or $22\ nm$).

6.2.2 Microscopic characteristics

Fig 6.10 we notice that the different parameters describing the shape of the fracture vary according to the gel characteristics. Let's analyze here these microscopic characteristics.

6.2.2.1 Curvature at the interface

The interface between the air-filled and water-filled fracture forms a curved boundary that we defined by R_c, the radius of curvature. From Fig 6.10, we reported the radius of curvature for each density and particle size in Fig 6.11. For a same particle diameter, the radius of curvature decreases as the particle density increase. Also, as the size of the particle diameter decrease, the radius of curvature decrease.

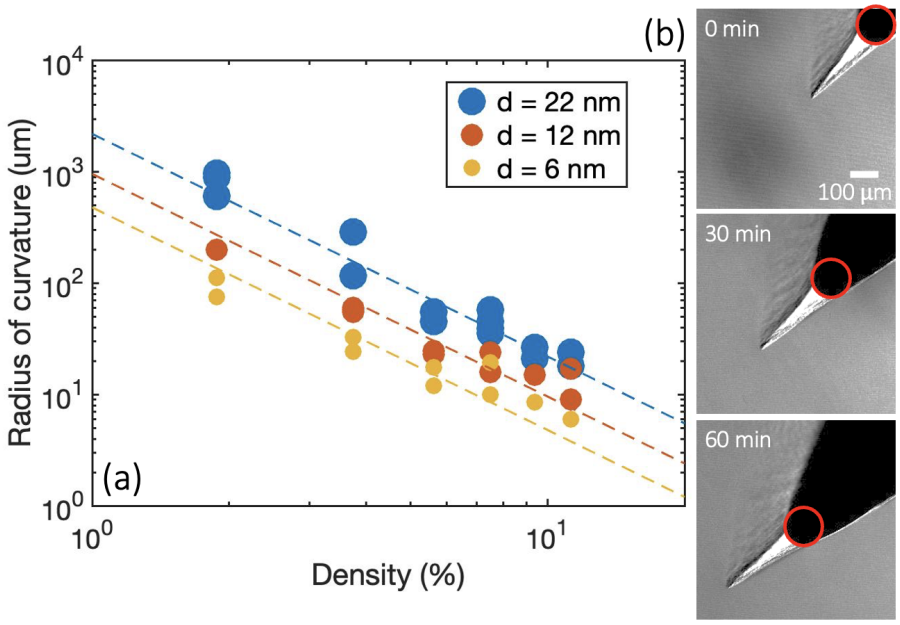

Figure 6.11: (a) Radius of curvature (in μm) according to the density (in $\%$ volumetric) for different size beads d. The dotted lines have a slope in -2. (b) Raw images form the confocal microscope showing the constant evolution of the radius of curvature in time for a colloidal gel at a density 5.625 $\%$ and diameter size 22 nm.

In Fig 6.11, for each beads size, the radius of curvature follows a power law depending on the density ϕ of the colloidal gel and the diameter size d of the colloidal particles: $R_c \sim d/\phi^2$. In the case of intermediate densities, we observe that this parameter remains well defined. Indeed, we see in Fig 6.11-b that during the evolution of a fracture in a gel at a density 5.625 $\%$ and diameter size 22 nm, the curvature represented by a red circle does not change in time. However, for low density, the radius of curvature is really large and can reach up to $R_c = 1000$ μm. In diameter, it is twice the thickness of the sample (at 1 mm). We then conducted the same experiment by increasing the thickness by 2 or 3 and notice that the value of the radius of curvature was more reproducible for diameter higher than the sample thickness. In fact, for the 22 nm particles at $\phi = 1.875$ $\%$, for a

$1\ mm$ thickness, we obtain $R_c = 600\ \mu m$ whereas for a $2\ mm$ thickness, we obtain $R_c = 980\ \mu m$. At $3\ mm$ thickness, the sample start to become cloudy, and the fracture start to propagate in a 3D space. We have seen in Fig 6.6, a thickness dependency on the shape of the macroscopic patterns. It is therefore not surprising to obtain a dependency on parameters at the microscopic scale. For a fix thickness at $1\ mm$, the low density ($\phi = 1.875\ \%$) is defined as the limit since we start to obtain scattered data sets. Note that from $\phi = 9.5\ \%$, the boundary between the two phases starts to be hard to detect. This might explain the deviation of the experimental values from the trend line for small silica particles at high density.

We also reported the angle at the triple line between the air/gel/water. In Fig 6.12, we see that the values are scattered but it seems that as the density of gel increase, the contact angle increase up to $\theta = 80°$.

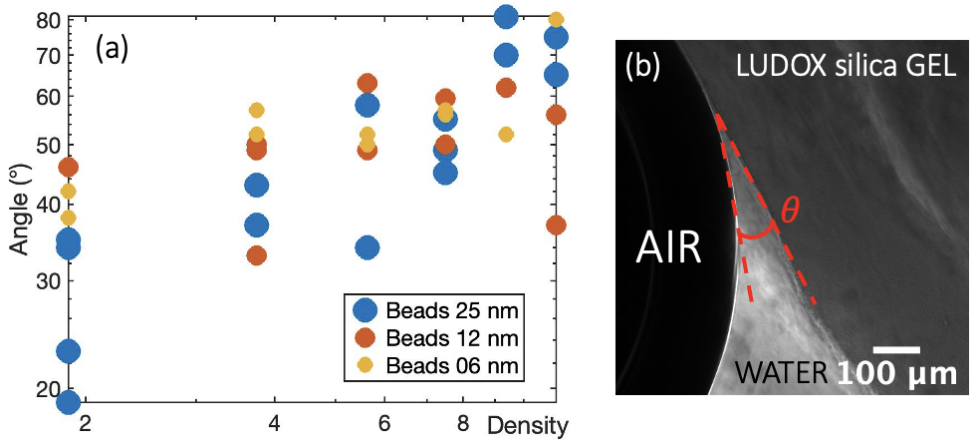

Figure 6.12: (a) Angle at the triple line between the three phases (air/gel/water) according to the density (in % volumetric) for different size beads. (b) Raw image from the confocal of a fracture at the interface air/water for a gel made of $22\ nm$ silica particles with initial volume fraction of $1.875\ \%$.

6.2.2.2 Shape of the water phase

The water phase of the fracture can be described as a triangle with a length w and a width δ. The width of the water phase is defined as chords of the circle describing the interface air/water which connects the two triple points (defined as the point where the three phases coexist). The length is therefore the distance between the center of this chords and the tip of the fracture. Likewise, we investigate these characteristics by varying the beads size and the density of our gel (see Fig 6.13).

The length of the water phase decrease with increasing density and decreasing particle size (see Fig 6.13-a) as well as the width (see Fig 6.13-b). On Fig 6.13-c, we see the evolution of a fracture in gel at $1.875\ \%$ and $22\ nm$ beads size. We notice that even if the radius of curvature does not change in time, the dimensions describing the water phase are changing in this experiment. As

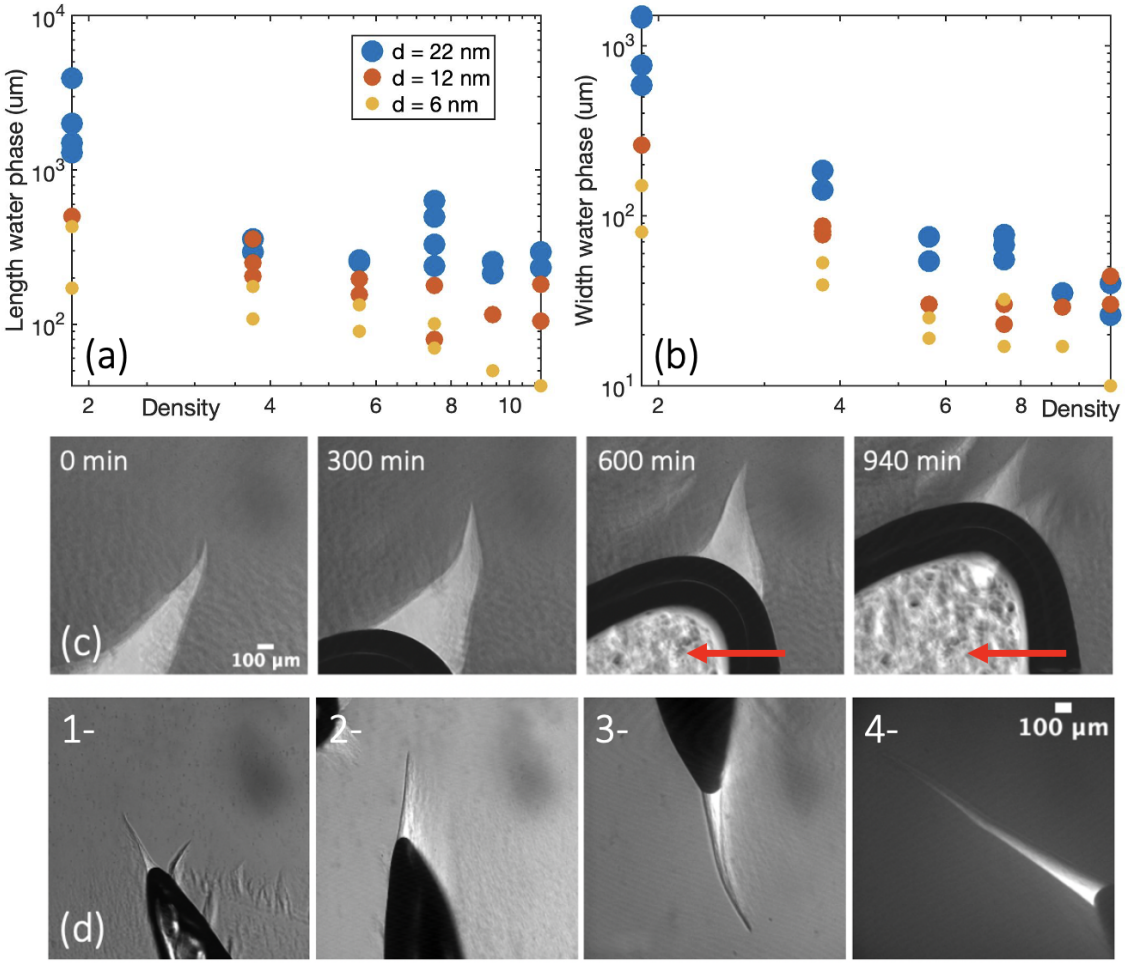

Figure 6.13: (a) Length of the water phase and (b) width of the water phase according to the density (in % volumetric) for different size beads. Raw images from the confocal microscope showing: (c) the evolution in time of the water phase for a 1.875 % gel made of 22 nm beads; (d) fractures in colloidal gels made of 22 nm beads at 5.625 % density for different thickness: (1) 0.8 nm, (2) 1.2 nm, (3) 2.4 nm and (4) 3.5 nm.

said earlier, the low density is an extreme case where network might not be as homogeneous as higher density. At $t = 940$ min, the water phase seems to have split into several water phases. We therefore took for every experiment the largest values for both dimensions corresponding to a limit value. Note that the cloudy part in the air phase (see red arrows) is residual gel stick to the glass slides. Moreover, for high densities, the resolution makes it difficult to detect the water-filled fracture. Note that we observe an increase of the parameters describing this phase when we increase the thickness of the sample. Indeed, in Fig 6.13-c, we observe that as the thickness is increasing, both the length and the width of the water phase are increasing.

We also reported the angle of the fracture tip, which actually correspond to the ratio of half the width over the length: $\alpha = 2\arctan(\delta/2w)$.

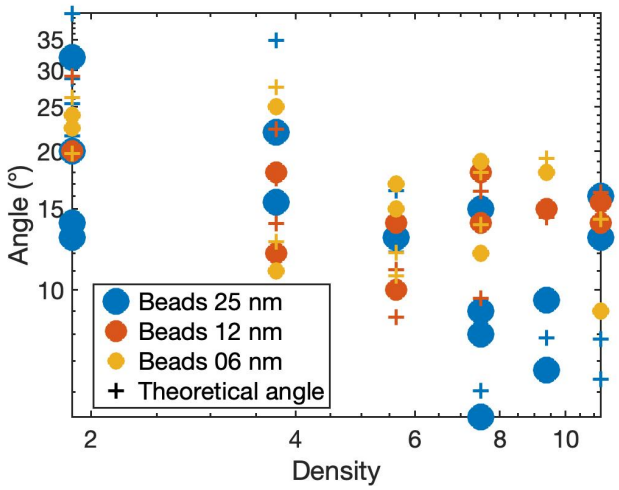

Figure 6.14: Angle at the tip of the water phase according to the density (in % volumetric) for different size beads (circle) and the corresponding theoretical angle calculated from the length ratio (cross).

In Fig 6.14, we see that the reported values of the tip angle (circle) correspond somehow to the values calculated thanks to the two dimensions of lengths (cross). It seems that whatever the beads size, the data points collapse in one trend where the angle decrease as the density increase.

6.3 Rheology: deformation until failure

To have a better understanding of this phenomenon, we conducted some experiment to obtain rheological information about our gels at the time of the failure. In the previous chapter we described the monitoring of the gelation process with a rheometer. Here we use the same gels and the same methodology with a cone-plate geometry (see section 5.1.1 and annex 7.4).

6.3.1 Properties of colloidal gels

6.3.1.1 Elastic modulus

As a reminder, we have seen that the gel undergoes three phases during the gelation process: diluted regime, network formation (at $t = t_{GEL}$) and ageing (at $t = t_{AGE}$) (see Fig 6.15-b). In order to obtain the rheological data at the moment of failure, we follow the evolution of the elastic modulus on a rheometer during the gelation process until we observe the apparition of the fracture on the confocal microscope. We then obtain the same elastic modulus of the gel in the mold and the gel in the rheometer. Indeed, the elastic modulus is still increasing during the aging of the gel, and it is important to have the same gel when we proceed at the rheological analysis to obtain the right values at the observation time. Note that we also followed the internal tension (defined as axial force divided by cone surface) that should increase during the gelation process. This parameter allows us to validate our experiment since if we observe a drop in time, it means that the gel detaches from the surface and the stress recorded is no longer reliable.

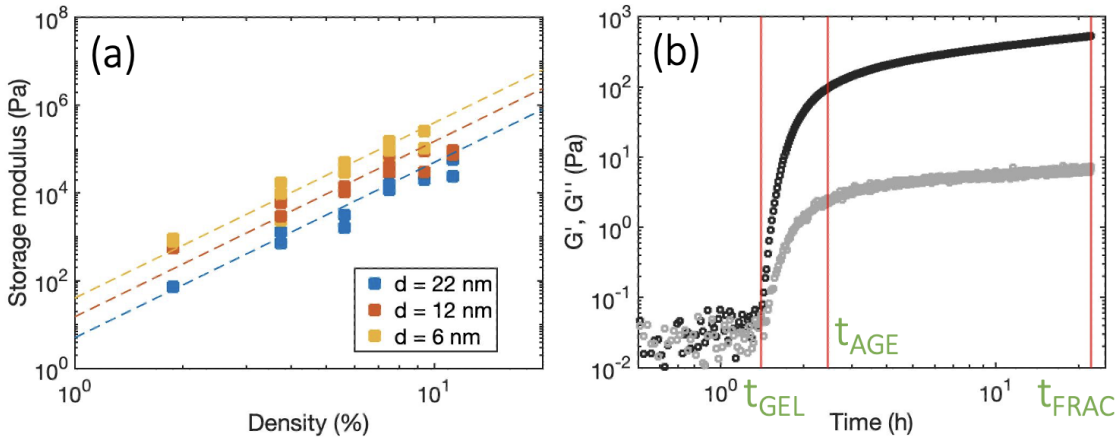

Figure 6.15: (a) Storage modulus according to the density (in % volumetric) for different size beads at the failure time. The dotted line has a slope in 4. (b) Evolution of the storage modulus (black line) and loss modulus (grey line) in time during the gelation process for a colloidal gel of $12\ nm$ silica particles with initial volume fraction of $1.875\ \%$ indicating the delimitation of the different regime during the gelation process.

Fig 6.15-a, we reported the value of the storage modulus (in Pa) at the time of fracture (at $t = t_{FRAC}$) for each beads size and each density. The storage modulus G' increases as the particle

size decrease and increases with particle volume fraction in a power-law fashion and can be fitted to [Shih et al. 1990]:

$$G' \sim \phi^4$$

6.3.1.2 Rheometer

After the gelation process, at $t = t_{FRAC}$, we want to determine the linear viscoelastic regime of our system. We use the protocol describe in section 2.5.2.1 to conduct a strain sweep and obtain the different gel characteristics at the failure of the material. For availability reasons, we realize the experiment with different instruments: in strain controlled (Ares G2) and in stress controlled (TA instrument).

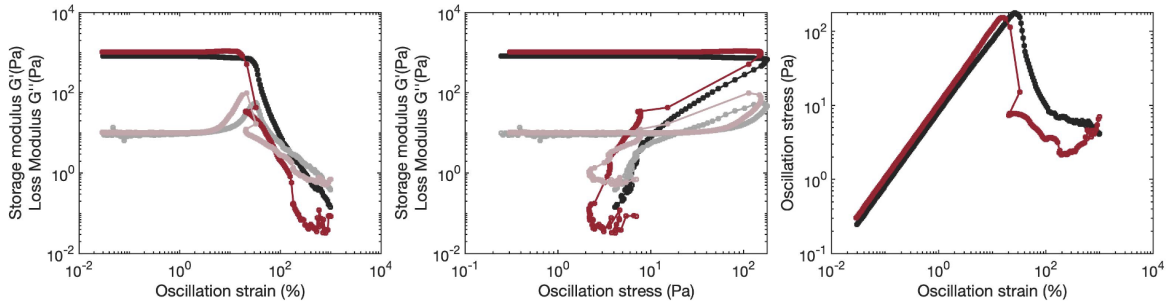

Figure 6.16: Experiment on strain controlled (Ares G2) rheometer in black and grey and on stress controlled (TA instrument) rheometer in red and purple for $22\ nm$ silica particles with initial volume fraction of $3.75\ \%$: (a) Storage modulus and loss modulus according to strain of . (b) Storage modulus and loss modulus according to stress. (c) Stress according to strain.

In Fig 6.16, for the gel ($22\ nm$ beads size and $3.75\ \%$ volume fraction), we observe that we obtain the same data points with both instrument: in strain controlled (in black) and in stress controlled (in red). For further work, we carried out the experiments with the two types of instruments and not having significant differences, the type of instrument used for each experiment will not be specified.

6.3.2 Rheological characteristics at the failure

6.3.2.1 Yield strain

From the strain sweep, we record the evolution of the loss modulus (in Pa) according to the strain (in $\%$) for different densities and beads size (see Fig 6.17). The yield strain corresponds to the maximum value of deformation that the material can support before failing. In Fig 6.17-b, the failing or fracture of the material is manifested by the drop of both curves. We notice that the loss modulus (grey curve) starts to be non-linear before the failing point. The material can deform slightly before failing.

We challenged our experiments by varying the density and the pore size (see Fig 6.17-c-d).

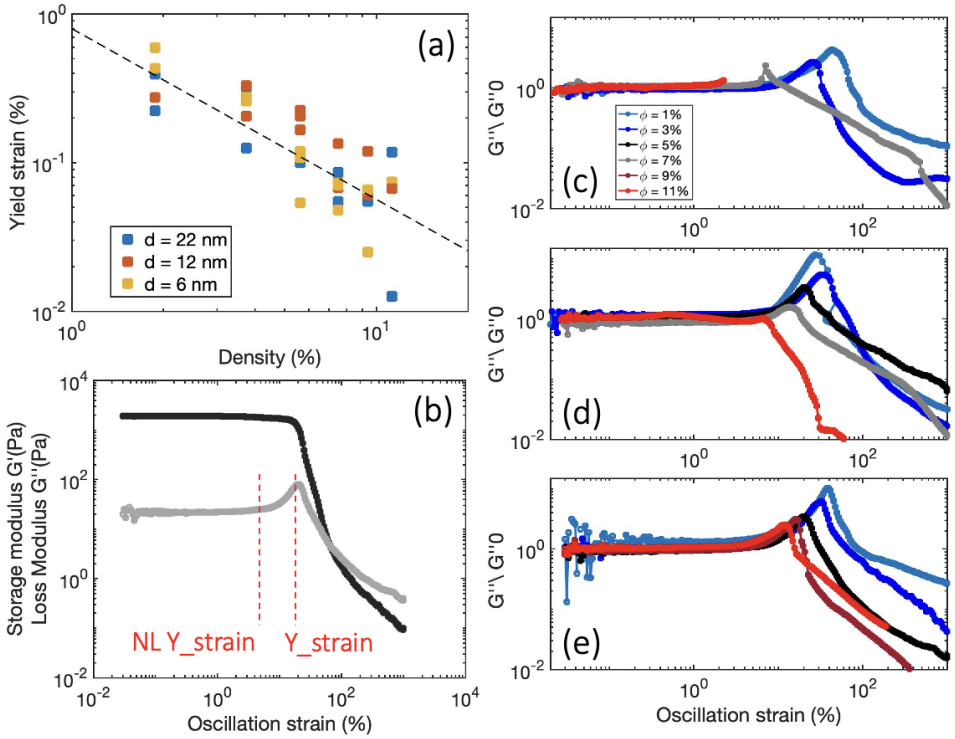

Figure 6.17: (a) Yield strain (in $\%$) according to the density (in % volumetric) for different size beads at the failure time. The dotted line has a slope in -1.15. (b) Storage modulus (black) and loss modulus (grey) according to strain of $22\ nm$ silica particles with initial volume fraction of $5.625\ \%$. Evolution of the loss modulus for different densities: (c) for $6\ nm$ beads, (d) for $12\ nm$ beads and (e) for $22\ nm$ beads.

We observe that the non-linear strain is shorter for higher densities. Indeed, the gel seems to fail catastrophically as soon as the first bonds break whereas for low volume fraction, the non-critical plastic dissipation before complete failure is larger.

In Fig 6.17-a, we reported the values of the yield strain. We observe that data points are collapsing into a single curve that decreases with the volume fraction of the particles and follows a power law:

$$Y_{strain} \sim \frac{1}{\phi^{1.15}}$$

We note that the experiments are more complicated to perform at high density and even more so with small particles. The internal tension of the gel is very high, and the water tends to evaporate which damages the sample even before the experiment is performed.

6.3.2.2 Yield stress

From the previous experiment (strain sweep), we can also obtain the yield stress. The yield stress is the minimum stress at which a solid will undergo permanent deformation. From Fig 6.18-b, we exploit the storage and loss modulus according to the oscillation stress. The yield stress corresponds

here to the maximum stress (before the failure).

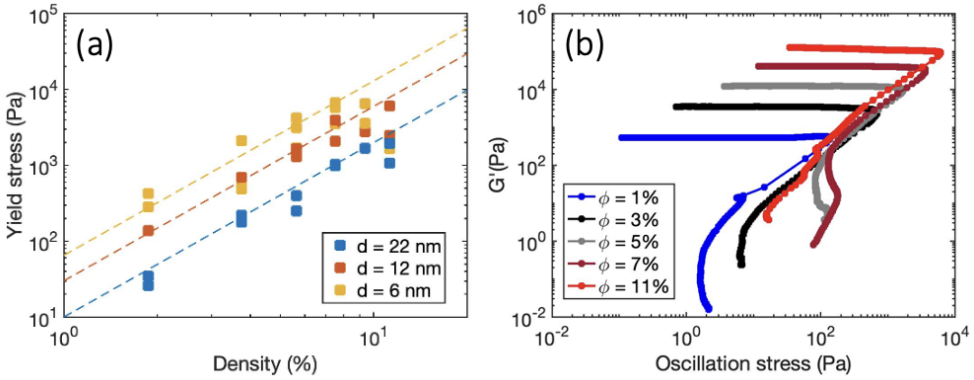

Figure 6.18: (a) Yield stress (in Pa) according to the density (in % volumetric) for different size beads at the failure time. The dotted line has a slope in 2.3. (b) Storage modulus according to stress of $12\ nm$ silica particles with various initial volume fraction.

In Fig 6.18-a, we reported the yield stress for each experiment. We observe that the yield stress increase as the beads size decreases and as the density increases. Moreover, it seems that for high densities, the yield stress starts to decrease again. Note that the yield stress depends on the network connectivity and therefore on the gel density, following a power-law:

$$Y_{stress} \sim \phi^{2.3}$$

6.3.2.3 Young modulus

Finally, we can obtain the Young modulus corresponding to the linear part of the curve of the stress according to the strain.

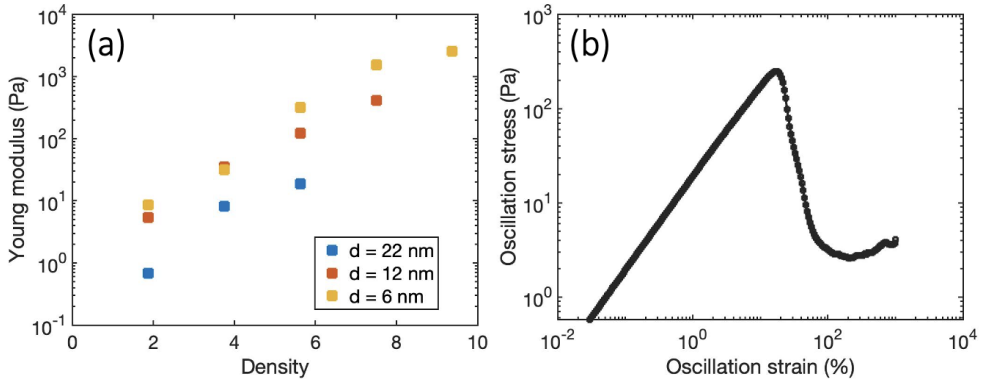

Figure 6.19: (a) Young modulus (in Pa) according to the density (in % volumetric) for different size beads at the failure time. (b) Oscillation stress function of oscillation strain of $22\ nm$ silica particles with initial volume fraction of $5.625\ \%$.

6.4 Characterization from microscopic to macroscopic scale

With the microscopic and rheological studies, we will try to understand the mechanisms leading to the formation of the macroscopic patterns. Thus, we will first try to understand locally the models describing the particular shape of our fracture leading us to a model describing the macroscopic patterns.

6.4.1 Cohesive zone model

In this section, we want to understand the role of the water phase to describe the shape of our fracture. From rheology studies, we have seen that the gel can undergo a non-critical plastic dissipation before complete failure. This regime is called non-linear, and it gets increasingly extended as the density is decreased, just like the length of the aqueous phase. Here, we suggest that this water phase is analogous to a cohesive zone (see Fig 6.3) [Broberg 1999]. This zone is described as a gradual phenomenon where the material is not fully separated. Here the concept of cohesive zone is particular since instead of fibers or polymers which would have the role to maintain the fracture closed (crazing in polymers), we have essentially water.

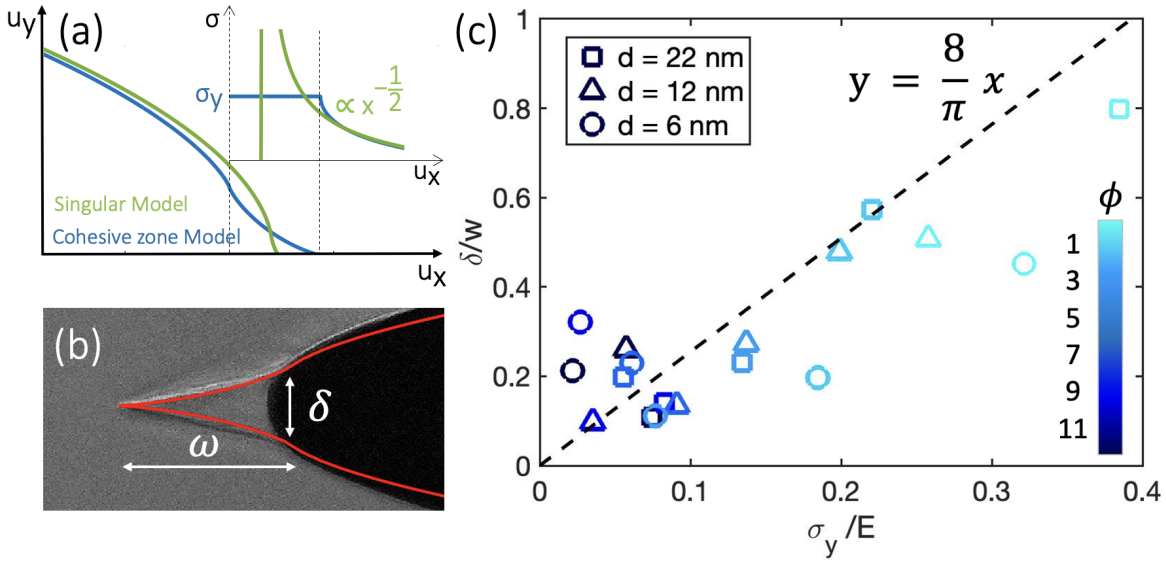

Figure 6.20: (a) Representation of a fracture profile for the singular model (in green) and for the cohesive zone model (in blue). (b) Raw image of a fracture in the confocal microscope from a $1.875\ \%$ colloidal gel made of $6\ nm$ silica particles. (c) Representation of the ratio of the lengths describing the fracture according to the rheological data of the gel for different bead sizes: (circle) $6\ nm$, (triangle) $12\ nm$, and (square) $22\ nm$ at different particle densities (from low - light blue to high - dark blue). The dotted line has a slope $8/\pi$.

The Dugdale model can describe the non-linear process located at the front of the crack. By relating the opening of the process zone δ (equation 6.1) and its length w (equation 6.2) within Mode I crack tips, we can link the geometrical characteristics of the process zone with the

rheological characteristics of the material:

$$\frac{\delta}{w} = \frac{8}{\pi}\frac{\sigma_y}{E} \tag{6.3}$$

Using equation 6.3, we see that the model fit the fracture profile (see Fig 6.20-b). We reported the fracture characteristic of the water phase (δ/w) compared to the rheological data for different densities and particle sizes (see Fig 6.20-c). We observe that the data points collapse in a $8/\pi$ trend corresponding to the model (equation 6.3). Note that we can see scattered data points which is expected as the rheology is not an exact representation of the experiment conditions. This is especially the case for the $6\ nm$ particles since the rheological data are complicated to obtain and therefore more scattered.

We now understand the bonding role of water in the fracture and its shape which is described by the cohesive zone model. In the case of the dry crack in our colloidal gel, the process is so slow that the shape is always in the maximum configuration (before fracture propagation). We now need to understand the process that leads to the expansion of the fracture.

6.4.2 Pressure equilibrium

At the interface air-water, we have a pressure jump that can be described by the Laplace equation:

$$\Delta P = \gamma(\frac{1}{R_1} + \frac{1}{R_2})$$

With $\gamma = 72\ mN.m^{-1}$, the water surface tension; R_1, the radius of curvature of the interface air/water and $R_2 = 0.5\ mm$, the second radius of curvature corresponding to the thickness of the sample.

In Fig 6.21-b, we reported the balance of pressure involved at the fracture tip. In dry crack, $P_1 = P_{atm}$ with $\Delta P = P_1 - P_2$ and $P_3 = P_\infty - \sigma_{yield}$. With P_1, the pressure of the air phase, P_2 the pressure of the water phase and P_3 the pressure of the gel at the tip of the fracture describes in Fig 6.20-a. As the fracture is quasi-static and from the cohesive zone model:

$$\begin{aligned} P_2 &= P_3 \\ P_1 - \Delta P &= P_\infty - \sigma_{yield} \\ \Delta P &= \sigma_{yield} \end{aligned} \tag{6.4}$$

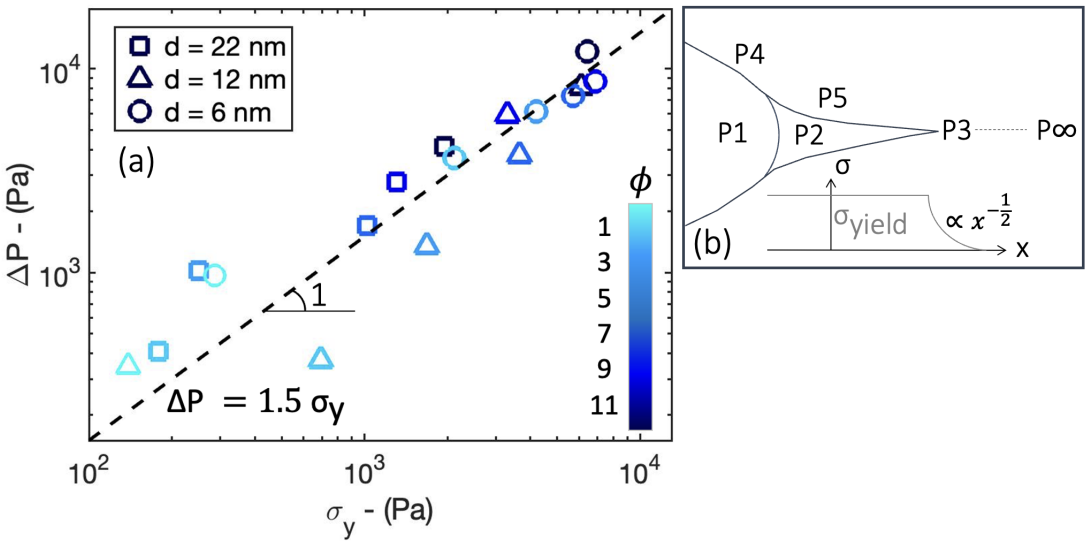

Figure 6.21: (a) Representation of the Laplace pressure according to the yield stress for different bead sizes: (circle) $6\ nm$, (triangle) $12\ nm$, and (square) $22\ nm$ at different particle densities (from low - light blue to high - dark blue). (b) Scheme of the different pressure involved in the system at the fracture tip.

Comparing the rheological data (yield stress represented by solid lines) with the microscopic data (Laplace pressure represented by empty squares), we observe that the data are almost identical (see Fig 6.21-a). A factor of 1.5 seems to separate the two data sets. This factor is not surprising since, again, it is questionable to directly compare the properties obtained in oscillation with the properties obtained from a fracture under normal tensile stress. Note that we also obtained a match of the equation 6.4 for Sijie Sun and Stefano Aime experiments using a different fluid (dichloromethane) with a surface tension of $\gamma = 28\ mN.m^{-1}$.

One can wonder if the fluid at the tip is essentially composed of water and therefore question the value of the surface tension. Using a tensiometer, we were able to calculate the surface tension of water while adding the different fluids used in the solution. We obtained: for water $\gamma = 72\ mN.m^{-1}$, for water from the sink $\gamma = 67\ mN.m^{-1}$, for water plus Urease $\gamma = 65\ mN.m^{-1}$ and for water plus Urea plus Ludox $\gamma = 61\ mN.m^{-1}$. It is not possible to directly calculate the surface tension of the liquid present at the tip of the fracture but it remains likely that it is not pure water.

6.4.3 Driving mechanism

We have seen that the fracture has a characteristic shape related to the rheological properties of the gel. It seems that there is a competition between air breaking the material and water preventing the fracture to propagate. As water is drying from the colloidal gel, the crack propagates. Let's try to understand the process of the fracture:

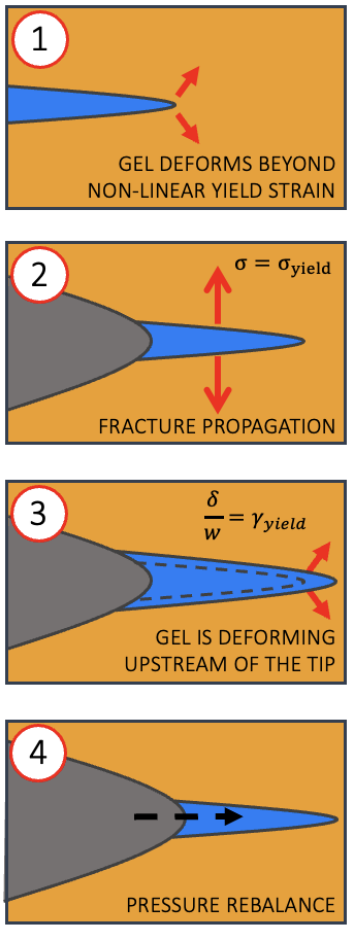

- When the gel dries (orange area), the gel deforms and increases its internal tension. When the deformation reaches the non-linear strain, some connections are broken and we observe the appearance of the cohesive zone (blue area).
- When the tension reaches the value of the yield stress, a fracture propagates (grey area) and releases the internal tension of the gel.
- While the gel continues to dry, the bonds upstream of the fracture continue to be weakened, which means that the cohesive zone increases. As the model predicted a constant δ/w ratio, both width and length are increasing
- As the cohesive zone has increased, the pressure P_2 decrease. This implies an increase of the Laplace pressure and therefore a value higher than the yield stress: $\Delta P > \sigma_{yield}$. Leading to the propagation of the fracture. As our fracture is quasi-static, we are always in the extreme case and the equilibrium is done instantly with the front of the air-water interface advancing at the same time as that of the tip: steps 3 and 4 are simultaneous.

6.4.4 Pattern formation

After understanding the mechanisms at the microscopic scale, we are now interested in the macroscopic scale and in understanding the mechanisms involved in the formation of patterns.

In porous media, the water concentration equilibrium is ensured by Darcy law (6.5). During drying, the sample is losing water. The volume rate (6.6) of the amount of lost water is describe as a drying area A multiply by the drying velocity v. Here, we assume that the drying speed corresponds to the speed of the fracture.

$$q = \frac{Q}{A} = -\frac{k}{\mu L}\Delta p \tag{6.5}$$

$$\dot{V} = Av \tag{6.6}$$

With k the permeability, $\mu = 1\ mPa.s$ the water viscosity and L the length.

To obtain a straight fracture, a sample should remain homogeneous in both sides: $P4 = P4' = P5 = P5'$ (see Fig 6.22-b). As long as Darcy flow Q is higher than the volume rate $\dot{V}$ of water that evaporates, the equilibrium should be assured. This statement is no longer valid at a certain length L_{lim} (6.7), at $Q = \dot{V}$:

$$L_{lim} = \frac{k\Delta p}{\mu v} \tag{6.7}$$

$$k = \frac{(1-\phi)^3}{45\phi^2}a^2 \tag{6.8}$$

Here, we defined the permeability from the monodisperse packing sphere formula with radius a as a function of the density ϕ, through Kozeny-Carman's expression (6.8).

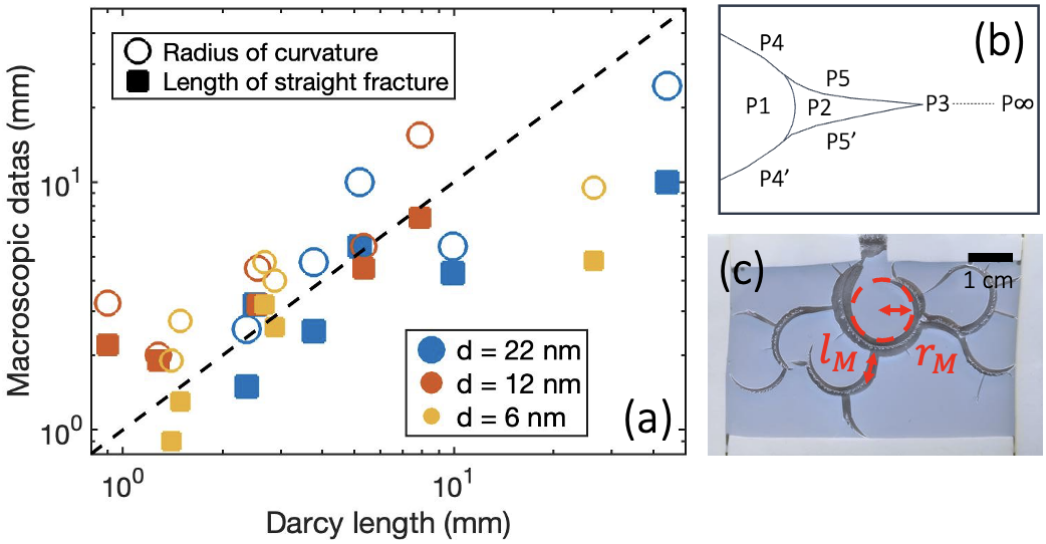

Figure 6.22: (a) Evolution of the macroscopic radius of curvature (empty dots) and the length of the straight section of the fracture (filled square) according to the limit length L_{lim} for different size beads and different densities. (b) Scheme of the different pressure involved in the system. (c) Macroscopic image of the colloidal gel cracks for diameters size $22\ nm$ at $5.625\ \%$ volume fraction.

We represented in Fig 6.22-a, the macroscopic radius of curvature (empty dots) and the length of the straight section of the fracture (filled square) according to the limit length L_{lim}. We observe that the data points collapse in a linear trend corresponding to the model (equation 6.7). The macroscopic pattern of our fracture is explained by Darcy law and the capacity of the material to homogenize. This theory does not take into account the thickness of the sample. We have seen that the patterns differ according to this parameter. If we consider that the sample dries essentially through the opening, we can therefore consider that the velocity v is not constant for different thickness. Thus, the parameter is taken into account in the velocity. Note that in this model we should also take into account the internal tension of the gel which might also depend on the thickness of the gel.

6.5 Conclusion

Through microscopic and rheological studies, we were able to understand the formation of macroscopic patterns. Fracturing during drying in soft colloidal gels are profoundly different from what typically found in hard materials: in addition to the cracking gel and the invading air-filled crack, we observe a third, wedge-shaped region filled with pure water, ahead of the crack tip. Indeed, we show that in these gels fracture energy is set by the water-air interface, while the gel mechanical properties determine the fracture morphology. The propagation of fractures in soft solids is set by the equilibrium between the Darcy flow and the drying velocity.

Conclusion & Perspectives

In this thesis, we have addressed various issues concerning the hygroscopy of wood such as structural modifications or changes in fluid transfer physics related to the sensitivity of wood to moisture. Throughout this work, we have used various materials: different wood species and hygroscopic materials that can mimic the hygroscopic character of wood. Thanks to different techniques that allowed us a multi-scale study, we were able to develop an understanding of the physical phenomena of hygroscopic materials:

The implementation of a new method for a non-invasive and non-destructive study of fluid transport inside wood, allowed us to obtain a direct measurement of the diffusion coefficient of bound water in wood. The use of NMR during the imbibition of a wood sample, allowed us to study the different populations of water found in hardwood (bound water, free water in vessels and in fibers). Thus, by using paint to isolate the imbibition plane and oil to prevent water from penetrating the wood by capillarity, we obtained by Fick's second law a diffusion coefficient of bound water in the three directions of the wood (tangential, radial, and longitudinal). The variability of the diffusion rate according to the direction of study is explained by the orientation of the cellulose microfibrils with respect to the axis of the cells (also at the origin of the phenomenon of anisotropy of the shrinkage and swelling of wood). The diffusion of water molecules is therefore faster in the longitudinal direction and slower in the tangential direction. The NMR study of water transfer during imbibition also allowed us to identify the source of water allowing the filling of the fibers and to propose a mechanism of the imbibition dynamics in the longitudinal direction. We identified that the filling of the fibers with water is done by recondensation of the bound water and that the air contained in the fibers is emptied thanks to the pits which create an air path towards the outside of the sample. The tortuosity of the wood, different in its three directions, impacts the filling speed of the fibers. We propose the following explanation: the filling speed of the fibers is controlled by the diffusion speed of the bound water as well as by the evacuation speed of the air. To complete this study, it would be interesting to perform the same experiments at the Synchrotron (Soleil) to obtain a direct visualization of the phenomena. For the future, this technique could be applied to different wood species and a work on the different parts of the wood (earlywood or latewood) could be done.

Then we studied the impact of the water concentration on the wetting properties of wood. We first show a general property: the contact angle of a water drop placed on the wood surface is

initially very large ($> 90°$), then the drop slowly spreads at a speed several orders of magnitude lower than the one expected by the balance between gravity and/or surface tension and viscous effects. From an analysis of the phenomenon and further tests with a model hygroscopic material (a hydrogel), we show that this effect is associated with the diffusion of water in the solid and the resulting swelling and deformation around the contact line. This deformation ensures a real (local) contact angle close to zero. The spreading then results from the progressive diffusion of water at farther distance and successive perturbations of the line of contact when the drop enters in contact with small liquid droplets dispersed along the surface (residues of the chemical reaction during gel preparation). It is suggested that a similar effect occurs for the water drop over a wood surface and explains the large initial contact angle and slow spreading: the line of contact is initially pinned thanks to a wood surface deformation resulting from wood surface swelling due to water absorption, thus leading to a large contact angle, but will unpin when the local conditions (deformation of the wood surface roughness) have changed as a result of water diffusion at further distance, allowing for a small displacement up to the next pinning point and so on. To go even further in this study, the objective would be to obtain a visualization of the deformation at a very small scale. The use of a confocal microscope combined with the use of tracing particles within the gel could allow us to follow the evolution of the gel at the contact line.

To understand the impact of hygroscopic deformations during drying of porous media, we studied colloidal gel. The use of NMR allowed us to monitor the water composition of our samples to understand the drying mechanisms. For monolayers, two main drying phases can be observed: a constant drying rate and then a decrease in the drying rate. This difference is explained by the decrease of the drying surface over time. Indeed, the study of the 1D profiles and the macroscopic observations by camera allowed us to identify an isotropic contraction of the sample. The decrease of the drying rate also impacts the contraction of the material since we find two dynamics of contraction which correspond to the two drying phases. Subsequently, the study of bilayer (whether by changing the concentration of particles or the size of particles used) showed us that after the partial drying of large pores, both layers dry simultaneously. In a deformable medium, the transition between the two regimes is limited by the elasticity of the gel. The drying mechanism of the gel is therefore controlled by an osmotic pressure (described by the elastic modulus) which tends to balance out over time. To go further in the study, an additional experiment should be performed by changing both the size of the particles and their concentrations which would allow us to obtain different structures with similar initial elastic moduli.

Finally, we studied drying-induced fracturing in colloidal silica gels. At the microscopic scale, we are able to characterize the fracture shape and compare it to the rheology of the material. The particularity of the fracture is that the upstream is filled with water. Using the cohesive zone model, we show that water plays a role here in keeping the fracture closed. Furthermore, in these gels, the fracture energy is determined by the water-air interface, while the mechanical properties of the gel determine the fracture morphology. On a macroscopic scale, the drying fracture splits into several cracks forming a regular pattern. The explanation brought here would be the equilibration of the

water concentration during drying is effective according to Darcy's law over a certain distance which would imply the curvature of the fractures from this distance. In our study, the adhesion of the gel to the substrate is not taken into account. To develop this aspect, an interesting direction of study would be to complete the experiments by varying the thickness of the gels. Moreover, the use of different materials as substrate could bring new elements to the understanding of these patterns.

Bibliography

[1] A.W. Adamson and A.P. Gast. *Physical Chemistry of Surfaces*. Sixth Edition, 1997. ISBN: 9780471148739 (cit. on p. 84).

[2] E. Agoua, S. Zohoun, and P. Perré. "Utilisation d'une double enceinte pour déterminer le coefficient de diffusion d'eau liée dans le bois en régime transitoire: recours à la simulation numérique pour valider la méthode d'identification: A double climatic chamber used to measure the diffusion coefficient of water in wood in unsteady-state conditions: determination of the best fitting method by numerical simulation". In: *International Journal of Heat and Mass Transfer* (2001). DOI: https://doi.org/10.1016/S0017-9310(01)00022-9 (cit. on p. 55).

[3] S. Aime et al. "A stress-controlled shear cell for small-angle light scattering and microscopy". In: *Review of Scientific Instruments* (2016). DOI: https://doi.org/10.1063/1.4972253 (cit. on p. 46).

[4] D.M. Anderson. "Imbibition of a liquid droplet on a deformable porous substrate". In: *Physics of fluids* (2004). DOI: 10.1063/1.2000247 (cit. on p. 87).

[5] J.D. Andrade et al. "Contact Angles at the Solid-Water Interface". In: *Journal of Colloid and Interface Science* (1979). DOI: https://doi.org/10.1016/0021-9797(79)90350-3 (cit. on pp. 85, 96).

[6] C.D. Araujo et al. "Proton magnetic resonance techniques for characterization of water in wood: application to white spruce". In: *Wood Science and Technology* (1992). DOI: 10.1007/BF00194466 (cit. on p. 58).

[7] B.Derjaguin and L. Landau. "Theory of the stability of strongly charged lyophobic sols and of the adhesion of strongly charged particles in solutions of electrolytes". In: *Academy of Sciences of the USSR* (1941). DOI: 10.1016/0079-6816(93)90013-L (cit. on p. 29).

[8] P. Bacchin et al. "Drying colloidal systems: Laboratory models for a wide range of applications". In: *European Physical Journal* (2018). DOI: http://dx.doi.org/10.1140/epje/i2018-11712-x (cit. on p. 144).

[9] A.K. Bajpai et al. "Responsive polymers in controlled drug delivery". In: *Progress in Polymer Science* (2008). DOI: 10.1016/j.progpolymsci.2008.07.005 (cit. on p. 36).

[10] G.I. Barenblatt. "The Mathematical Theory of Equilibrium Cracks in Brittle Fracture". In: *Advances in Applied Mechanics* (1962). DOI: https://doi.org/10.1016/S0065-2156(08)70121-2 (cit. on p. 143).

[11] J.C. Berg. *Wettability*. Marcel Dekker, Inc, 1993. ISBN: 0824790464 (cit. on p. 84).

[12] T. Bertrand et al. "Dynamics of swelling and drying in a spherical gel". In: *Physical Review Applied* (2016). DOI: 10.1103/PhysRevApplied.6.064010 (cit. on p. 36).

[13] C. Boehem and G. Hora. "Water Absorption and Contact Angle Measurement of Native European, North American and Tropical Wood Species to Predict Gluing Properties". In: *Walter de Gruyter* (1996). DOI: https://doi.org/10.1515/hfsg.1996.50.3.269 (cit. on p. 85).

[14] M. Bonnet et al. "NMR determination of sorption isotherms in earlywood and latewood of Douglas fir. Identification of bound water components related to their local environment". In: *Holzforschung* (2017). DOI: doi.org/10.1515/hf-2016-0152 (cit. on p. 58).

[15] F. Boulogne, F. Giorgiutti-Dauphiné, and L. Pauchard. "How to Reduce the Crack Density in Drying Colloidal Material?" In: *IFP Energies nouvelles* (2013). DOI: 10.2516/ogst/2013119 (cit. on p. 144).

[16] F. Boulogne, F. Ingremeau, et al. "Tuning the Receding Contact Angle on Hydrogels by Addition of Particles". In: *Langmuir* (2016). DOI: 10.1021/acs.langmuir.6b01209 (cit. on p. 87).

[17] K. Broberg. *Cracks and Fracture*. Academic Press, 1999. ISBN: 9780121341305 (cit. on pp. 143, 144, 161).

[18] K.R. Brownstein and C.E. Tarr. "Spin-Lattice Relaxation in a System Governed by Diffusion". In: *Journal of Magnetic Resonance* (1976). DOI: https://doi.org/10.1016/0022-2364(77)90230-X (cit. on p. 42).

[19] H.Y. Carr and E.M. Purcell. "Effects of diffusion on free precession in nuclear magnetic resonance experiments." In: *Physical review* (1954). DOI: https://doi.org/10.1103/PhysRev.94.630 (cit. on p. 40).

[20] A. Carré, J.C. Gastel, and M.E.R. Shanahan. "Viscoelastic effects in the spreading of liquids". In: *Nature* (1996). DOI: 10.1038/379432a0 (cit. on p. 108).

[21] M. Cocusse et al. "Two-step diffusion in cellular hygroscopic (vascular plant-like) materials". In: *Science advances* (2022). DOI: 10.1126/sciadv.abm7830 (cit. on pp. 19, 24, 41, 54).

[22] P. Coussot. *Rheophysics: Matter in all its States*. Savoir actuels, 2012. ISBN: 978-2759807598 (cit. on pp. 29, 47).

[23] P. Coussot. "Scaling approach of the convective drying of a porous medium". In: *The European Physical Journal* (2000). DOI: https://doi.org/10.1007/s100510051160 (cit. on p. 119).

[24] J. Crank. *The Mathematics of Diffusion*. Oxford university press, 1975. ISBN: 0198533446 (cit. on pp. 54, 72).

[25] D.S. Dugdale. "Yielding of steel sheets containing slits". In: *Journal of the Mechanics and Physics of Solids* (1960). DOI: https://doi.org/10.1016/0022-5096(60)90013-2 (cit. on p. 143).

[26] S.V. Dvinskikh et al. "NMR imaging study and multi-Fickian numerical simulation of moisture transfer in Norway spruce samples". In: *Engineering Structures* (2011). DOI: https://doi.org/10.1016/j.engstruct.2011.04.011 (cit. on p. 58).

[27] F.Bonacci et al. "Contact and macroscopic ageing in colloidal suspensions". In: *Nature Materials* (2020). DOI: https://doi.org/10.1038/s41563-020-0624-9 (cit. on p. 121).

[28] P.F. Faure and S. Rodts. "Proton NMR relaxation as a probe for setting cement pastes". In: *Science direct* (2008). DOI: 10.1016/j.mri.2008.01.026 (cit. on pp. 43, 61).

[29] P.G. de Gennes, F. Brochard-Wyart, and D. Quéré. *Capillarity and wetting phenomena: Drops, bubbles, pearls, waves*. Springer-Verlag New York, 2004. ISBN: 9781441918338 (cit. on pp. 83, 88, 98).

[30] J. Gérard et al. *Atlas des bois tropicaux*. Quae, 2016. ISBN: 9782759225521 (cit. on p. 25).

[31] O. Gezici-Koç et al. "Bound and free water distribution in wood during water uptake and drying as measured by 1D magnetic resonance imaging". In: *Cellulose* (2017). DOI: https://doi.org/10.1007/s10570-016-1173-x (cit. on p. 52).

[32] R.J. Good. "Contact angle, wetting, and adhesion: a critical review". In: *Journal of adhesion science and technology* (2012). DOI: https://doi.org/10.1163/156856192X00629 (cit. on p. 85).

[33] A.A. Griffith. "The Phenomena of Rupture and Flow in Solids". In: *Royal Society* (1921). DOI: https://doi.org/10.1098/rsta.1921.0006 (cit. on p. 142).

[34] M. Guvendiren, J.A. Burdick, and S. Yang. "Kinetic study of swelling-induced surface pattern formation and ordering in hydrogel films with depth-wise crosslinking gradient". In: *Soft Matter* (2010). DOI: https://doi.org/10.1039/B927374C (cit. on p. 105).

[35] M. Guvendiren, S. Yang, and J.A. Burdick. "Swelling-Induced Surface Patterns in Hydrogels with Gradient Crosslinking Density". In: *Advanced functional materials* (2009). DOI: 10.1002/adfm.200900622 (cit. on p. 106).

[36] P.J. Hore. *Nuclear Magnetic Resonance*. Oxford university press, 2015. ISBN: 0198703414 (cit. on p. 38).

[37] A. Jamaaoui. "Durabilité et comportement hygroscopique du Douglas en relation avec son patrimoine génétique". In: *Phd thesis* (2017). DOI: http://www.theses.fr/2017LIMO0068 (cit. on p. 55).

[38] J. Johansson and J-G Salin. "Application of percolation modelling on end-grain water absorption in aspen (Populus tremula L.)" In: *Wood Material Science & Engineering* (2011). DOI: https://doi.org/10.1080/17480272.2010.537768 (cit. on p. 52).

[39] T. Kajiya, P. Brunet, et al. "A liquid contact line receding on a soft gel surface: dip-coating geometry investigation". In: *Soft Matter* (2014). DOI: https://doi.org/10.1039/C4SM01609B (cit. on pp. 87, 102).

[40] T. Kajiya, A. Daerr, et al. "Dynamics of the contact line in wetting and diffusing processes of water droplets on hydrogel (PAMPS-PAAM) substrates". In: *Soft Matter* (2011). DOI: https://doi.org/10.1039/C1SM05944K (cit. on p. 87).

[41] H. Kim. "Experimental Thermo and Fluid Engineering: Particle Image Velocimetry". In: *Department of Mechanical Engineering* (2022) (cit. on p. 46).

[42] J. Kim. "Morphological Analysis of Crease Patterns Formed on Surface-Attached Hydrogel with a Gradient in Thickness". In: *Journal of Applied polymer science* (2014). DOI: DOI: 10.1002/app.40482 (cit. on p. 105).

[43] W.G. Knauss. "A review of fracture in viscoelastic materials". In: *International Journal of Fracture* (2015). DOI: 10.1007/s10704-015-0058-6 (cit. on p. 142).

[44] M. Kobayashi et al. "Aggregation and Charging of Colloidal Silica Particles: Effect of Particle Size". In: *Langmuir* (2005). DOI: 10.1021/la046829z (cit. on p. 30).

[45] P-S de Laplace. *Traité de Mécanique Céleste*. 1805 (cit. on p. 87).

[46] A. Laskowska and P. Kozakiewicz. "Surface Wettability of Wood Species from Tropical and Temperate Zones by Polar and Dispersive Liquids". In: *Drvna Industrija* (2017). DOI: 10.5552/drind.2017.1704 (cit. on p. 86).

[47] V. Lazarusa and L. Pauchard. "From craquelures to spiral crack patterns: influence of layer thickness on the crack patterns induced by desiccation". In: *Soft Matter* (2010). DOI: 10.1039/c0sm00900h (cit. on p. 144).

[48] B. Leboucher. "Fabriquer en bois massif : anticiper les variations". In: *Le Bouvet* () (cit. on pp. 20, 61).

[49] T. Lerouge et al. "Drying of a Compressible Biporous Material". In: *Physical Review Applied* (2020). DOI: 10.1103/PhysRevApplied.13.044061 (cit. on pp. 119, 138).

[50] A. Lesaine et al. "Role of particle aggregation in the structure of dried colloidal silica layers". In: *Royal Society of Chemistry* (2020). DOI: 10.1039/d0sm00723d (cit. on pp. 31, 117).

[51] C. Liaw, J. Pereyra, and M. Guvendiren. "Chapter 9: Wrinkling on Covalently Anchored Hydrogels". In: *Springer Nature Switzerland* (2019). DOI: https://doi.org/10.1007/978-3-030-05123-5_9 (cit. on p. 104).

[52] E. Liptáková and J. Kúdela. "Analysis of the Wood-Wetting Process". In: *Holzforschung* (1994). DOI: 10.1515/hfsg.1994.48.2.139 (cit. on p. 86).

[53] B. Maillet, R. Sidi-Boulenouar, and P. Coussot. "Dynamic NMR Relaxometry as a Simple Tool for Measuring Liquid Transfers and Characterizing Surface and Structure Evolution in Porous Media". In: *Langmuir* (2022). DOI: 10.1021/acs.langmuir.2c01918 (cit. on pp. 43, 128, 138).

[54] D. Mannes et al. "Non-destructive determination and quantification of diffusion processes in wood by means of neutron imaging". In: *Holzforschung* (2009). DOI: 10.1515/HF.2009.100 (cit. on p. 56).

[55] M. McCully et al. "Some properties of the walls of metaxylem vessels of maize roots, including tests of the wettability of their lumenal wall surfaces". In: *Annals of Botany* (2014). DOI: https://doi.org/10.1093/aob/mcu020 (cit. on p. 67).

[56] S. Meiboom and D. Gill. "Modified spin-echo method for measuring nuclear relaxation times". In: *The Review of Scientific Instruments* (1958). DOI: https://doi.org/10.1063/1.1716296 (cit. on p. 40).

[57] R.S. Menon et al. "An NMR Determination of the Physiological Water Distribution in Wood during Drying". In: *Journal of Applied polymer science* (1987). DOI: https://doi.org/10.1002/app.1987.070330408 (cit. on p. 58).

[58] M. Morra, E. Occhiello, and F.Garbassi. "Knowledge about polymer surfaces from contact angle measurements". In: *Advances in Colloid and Interface Science* 32 (1990), pp. 79–116. DOI: https://doi.org/10.1016/0001-8686(90)80012-O (cit. on pp. 84, 85, 98).

[59] P. Nandakishore and L. Goehring. "Crack patterns over uneven substrates". In: *Soft Matter* (2016). DOI: https://doi.org/10.1039/C5SM02389K (cit. on p. 141).

[60] A.W. Neumann. "Contact angles and their temperature dependence thermodynamic status, measurement, interpretation and application". In: *Advances in Colloid and Interface Science* (1974). DOI: https://doi.org/10.1016/0001-8686(74)85001-3 (cit. on p. 84).

[61] D.M. Nguyen et al. "Mechanisms of liquid imbibition in Douglas-fir inferred from 1H nuclear magnetic resonance methods". In: *De Gruyter* (2020). DOI: https://doi.org/10.1515/hf-2020-0051 (cit. on p. 52).

[62] T.A. Nguyen. "Approches expérimentales et numériques pour l'étude des transferts hygroscopiques dans le bois". In: *Phd thesis* (2014). DOI: https://tel.archives-ouvertes.fr/tel-01130828/document (cit. on p. 55).

[63] W. Olek. "Analysis of the cup method application for determination of the bound water diffusion coefficient in wood". In: *Folia forestalia polonica* (2003). DOI: 10.1515/HF.2005.007 (cit. on p. 56).

[64] W. Olek, P. Perre, and J. Weres. "Inverse analysis of the transient bound water diffusion in wood". In: *Holzforschung* (2005). DOI: 10.1515/HF.2005.007 (cit. on pp. 56, 73).

[65] F. Heger P. Navi. *Comportement thermo-hydromécanique du bois*. Presses Polytechniques et Universitaires Romandes, 2005. ISBN: 9782880746209 (cit. on p. 19).

[66] R. Passas. *Handbook of Natural Fibres*. Woodhead Publishing Limited, 2012. ISBN: 9780857095510 (cit. on p. 15).

[67] H. Penvern et al. "How Bound Water Regulates Wood Drying". In: *Physical review applied* (2020). DOI: 10.1103/PhysRevApplied.14.054051 (cit. on pp. 19, 54, 55, 85).

[68] P. Peralta. "Sorption of Moisture by Wood Within A Limited Range of Relative Humidities". In: *Wood and Fiber Science* (1994). DOI: 10.1515/HF.2010.061 (cit. on p. 18).

[69] H. Peron et al. "Formation of drying crack patterns in soils: a deterministic approach". In: *Geotechnica* (2013). DOI: 10.1007/s11440-012-0184-5 (cit. on p. 144).

[70] C. Piao, J.E. Winandy, and T.F. Shupe. "From Hydrophilicity to Hydrophobicity: A Critical Review: Part I. Wettability and Surface Behavior". In: *dWood and Fiber science* (2010) (cit. on pp. 85, 86).

[71] K. Piroird et al. "Role of evaporation rate on the particle organization and crack patterns obtained by drying a colloidal layer". In: *EPL Journal* (2016). DOI: 10.1209/0295-5075/113/38002 (cit. on p. 144).

[72] S.W. Provencher. "A constrained regularization method for inverting data represented by linear algebraic or integral equations". In: *Computer Physics Communications* (1982). DOI: https://doi.org/10.1016/0010-4655(82)90173-4 (cit. on pp. 42, 43).

[73] P.L. Ritger and N.A. Peppas. "Transport of penetrants in the macromolecular structure of coals: 4. Models for analysis of dynamic penetrant transport". In: *Fuel* (1987). DOI: https://doi.org/10.1016/0016-2361(87)90130-X (cit. on p. 36).

[74] H.N. Rosen. "Exponential dependency of moisture diffusion coefficient". In: *Wood Science* (1976) (cit. on p. 56).

[75] L. Rostom, S. Caré, and D. Courtier-Murias. "Analysis of water content in wood material through 1D and 2D 1H NMR relaxometry: Application to the determination of the dry mass of wood". In: *Magnetic Resonance in Chemestry* (2020). DOI: https://doi.org/10.1002/mrc.5125 (cit. on p. 18).

[76] M. Scheikl and M. Dunky. "Measurement of Dynamic and Staue Contact Angles on Wood for the Determination of its Surface Tension and the Penetration of Liquids into the Wood Surface". In: *Holzforschung* (1998). DOI: https://doi.org/10.1515/hfsg.1998.52.1.89 (cit. on p. 86).

[77] M. Sedighi-Gilani et al. "Erratum to: Liquid uptake in Scots pine sapwood and heartwood visualized and quantified by neutron radiography". In: *Materials and Structures* (2014). DOI: https://doi.org/10.1617/s11527-013-0136-z (cit. on p. 52).

[78] M.E.R. Shanahan. "The influence of solid micro-deformation on contact angle equilibrium". In: *Journal of Physics* (1987). DOI: 10.1088/0022-3727/20/7/018 (cit. on p. 108).

[79] W-H. Shih et al. "Scaling behavior of the elastic properties of colloidal gels". In: *The American Physical Society* (1990). DOI: 10.1103/physreva.42.4772 (cit. on p. 158).

[80] J.F. Siau. *Transport Processes in Wood*. Springer Series in Wood Science, 1984. ISBN: 9783642692130 (cit. on pp. 17, 56, 73).

[81] C. Skaar. *Wood-Water Relations*. Springer Series in Wood Science, 2012. ISBN: 9783642736858 (cit. on p. 19).

[82] R.W. Style, R. Boltyanskiy, et al. "Universal Deformation of Soft Substrates Near a Contact Line and the direct Measurement of Solid Surface Stresses". In: *Physical review letters* (2013). DOI: 10.1103/PhysRevLett.110.066103 (cit. on p. 108).

[83] R.W. Style, C. Hyland, et al. "Elastocapillarity: Surface Tension and the Mechanics of Soft Solids". In: *Review in Advance* (2017). DOI: https://doi.org/10.1146/annurev-conmatphys-031016-025326 (cit. on p. 108).

[84] R.W. Style, C. Hyland, et al. "Surface tension and contact with soft elastic solids". In: *Nature Communications* (2013). DOI: 10.1038/ncomms3728 (cit. on p. 108).

[85] J. Suard. "Etude du séchage de matériaux bi-poreux composites par relaxométrie RMN". In: *Stage* (2022) (cit. on p. 119).

[86] J. Thiery et al. "Drying kinetics of deformable and cracking nano-porous gels". In: *The European Physical journal* (2016). DOI: 10.1140/epje/i2016-16117-3 (cit. on pp. 144, 147).

[87] E.E. Thybring, M. Kymalainen, and L. Rautkari. "Experimental techniques for characterising water in wood covering the range from dry to fully water-saturated". In: *Springer* (2017). DOI: https://doi.org/10.1007/s00226-017-0977-7 (cit. on p. 181).

[88] H.D. Tiemann. *Effect of moisture upon the strength and stiffness of wood*. U.S. Department of Agriculture, Forest Service, 1906. ISBN: 1361992263 (cit. on p. 17).

[89] M.-C. Trouy. *MOOC Anatomie du bois*. URL: https://lms.fun-mooc.fr/courses/course-v1:lorraine+30003+session04/info (cit. on p. 14).

[90] V. Trujillo, J. Kim, and R.C. Hayward. "Creasing instability of surface-attached hydrogels". In: *Soft Matter* (2008). DOI: DOI:10.1039/b713263h (cit. on p. 104).

[91] I. Vazquez-Cooz and R. W. Meyer. "Distribution of libriform fibers and presence of spiral thickenings in fifteen species of acer". In: *IAWA Journal* 27 (2006), pp. 173–182. DOI: https://doi.org/10.1163/22941932-90000146 (cit. on p. 16).

[92] E. J. W. Verwey and J. T. G.Overbeek. "Theory of the Stability of Lyophobic Colloids". In: *Elsevier* (1949). DOI: https://doi.org/10.1002/pol.1949.120040321 (cit. on p. 29).

[93] L. Wadsö. "A critical review on anomalous or non-Frickian vapor sorption". In: *Division of Building Materials Lund University* (1992) (cit. on p. 36).

[94] M.E.P Wålinder and C. Ström. "Measurement of Wood Wettability by the Wilhelmy Method: Part 2. Determination of Apparent Contact Angles". In: *Walter de Gruyter* (2001). DOI: https://doi.org/10.1515/HF.2001.006 (cit. on p. 85).

[95] W. Wang et al. "Correlation between dynamic wetting behavior and chemical components of thermally modified wood". In: *Applide Surface Science* (2014). DOI: https://doi.org/10.1016/j.apsusc.2014.10.139 (cit. on p. 85).

[96] N. Wells and R.E. Moon. "Wood Swelling: Pressures Exerted from Saturated Wood Materials". In: *Seventh Congress on Forensic Engineering* (2015). DOI: 10.1061/9780784479711.021 (cit. on p. 65).

[97] R N. Wenzel. "Resistance of solid surfaces to wetting by water". In: *Industrial and Engineering Chemistry* (1936). DOI: 10.1021/ie50320a024 (cit. on p. 85).

[98] W. B. Zeida and D. Brutin. "Influence of relative humidity on spreading, pattern formation and adhesion of a drying drop of whole blood". In: *Colloids and Surfaces* (2013). DOI: 10.1016/J.COLSURFA.2013.03.019 (cit. on p. 141).

[99] M. Zhou, S. Caré, A.King, et al. "Wetting enhanced by water adsorption in hygroscopic plant like materials". In: *Physical review research* (2019). DOI: 10.1103/PhysRevResearch.1.033190 (cit. on pp. 19, 24, 26, 52–54, 56, 59, 67, 79, 86, 90).

[100] M. Zhou, S. Caré, D. Courtier-Murias, et al. "Magnetic resonance imaging evidences of the impact of water sorption on hardwood capillary imbibition dynamics". In: *Wood Sci Technol* (2018). DOI: https://doi.org/10.1007/s00226-018-1017-y (cit. on pp. 52, 88).

Chapter 7

Appendices

7.1 Formulation of the different PEG hydrogels

Percentage of PEG-MA (%)	dH2O (g)	PEG-MA (g)	PEG-DA (g)	APS (μL)	TEMED (μL)
0	6.18	2.17	0	100	100
25	6.18	1.50	0.67	100	100
50	6.18	1.09	1.09	100	100
75	6.18	0.67	1.50	100	100
92	6.18	2.00	0.17	100	100
100	6.18	0	2.17	100	100

Table 7.1: Hydrogel components and quantities at different polymer concentrations.

The Table 7.1 presents a summary of the compositions of the different hydrogels used in this work.

7.2 Formulation of the different colloidal gels

ϕ (% v/v)	V_{sol2}	LUDOX TM 50		LUDOX HS 40		LUDOX SM 30	
		V_{sol1}	V_{sol3}	V_{sol1}	V_{sol3}	V_{sol1}	V_{sol3}
1.875	1.250	0.625	8.125	0.852	7.898	1.284	7.466
3.75	1.250	1.250	7.500	1.705	7.045	2.568	6.182
5.625	1.250	1.875	6.875	2.557	6.193	3.853	4.897
7.5	1.250	2.500	6.250	3.409	5.341	5.137	3.613
9.375	1.250	3.125	5.625	4.261	4.489	6.421	2.329
11.25	1.250	3.750	5.000	5.114	3.636	7.705	1.045

Table 7.2: Volumes of each solutions (V_{sol1}, V_{sol2} and V_{sol3} in (in ml)) for obtaining colloidal gels at different concentrations (from $\phi = 1.875$ % to $\phi = 11.25$ %) and for three particles size ($d_{TM\ 50} = 22\ nm$, $d_{HS\ 40} = 12\ nm$ and $d_{SM\ 30} = 6\ nm$).

The Table 7.2 is used to obtain a total volume: $V_{TOT} = 10\ ml$ with $M_{urease} = 0.03\ g$ dissolved in the water solution (V_{sol3}).

7.3 Diffusion of bound water in softwood

In chapter 3, we studied the fluid exchanges in the hardwood during the imbibition. In particular, we succeeded in obtaining a diffusion coefficient for bound water. Thus, we wanted to perform preliminary experiments to compare the results obtained in hardwood species with softwood species. Here we used Douglas fir.

Water distribution

Fig 7.1 shows the relaxation time distribution (T_2) of a fir sample after imbibition. As for hardwood, we immerse a $10 \times 10 \times 10\ mm^3$ sample in the NMR tube filled with water. Softwood are different from hardwood in terms of structure (see section 1.1.2). We find mainly tracheids which compose $90\ \%$ of the cells. In softwood, we also differentiate three peaks corresponding to water in different states [Thybring, Kymalainen, and Rautkari 2017]:

- Bound water present in the cell wall of the wood via hydrogen bonds. This population relaxes the same as for hardwood with T_2 smaller than $10\ ms$.
- Free water in tracheids at a representative $T_2 = 50\ ms$. This peak is quite large since it reflects a certain dispersion in the pore size. Indeed the biggest peak is representative of the tracheids (from $20\ \mu m$ to $50\ \mu m$ for Douglas) and the small peak is representative of wood ray (from $5\ \mu m$ to $10\ \mu m$), pits and small cavities. We have no means to strictly distinguish the water amount in rays and tracheids. In the following discussion, we will simply consider these two peaks as a whole and refer to them as the free water.
- The last peak at a representative $T_2 = 300\ ms$ does not represent water in wood but surface water on the specimen.

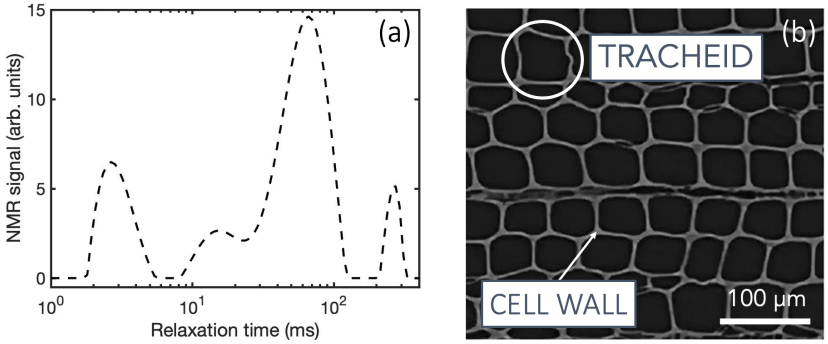

Figure 7.1: (a) T_2 relaxation time distribution of a Douglas fir sample saturated in water. (b) Representation of the microstructure of a softwood sample in TR section from an optical microscope.

Water evolution

We can follow the evolution of the different water population during imbibition with fir sample. We also have the peak of the bulk water represented around $T_2 = 1800\ ms$ (see Fig 7.2). The calculation of the sub-peak area for each water population in times allows to define different dynamics:

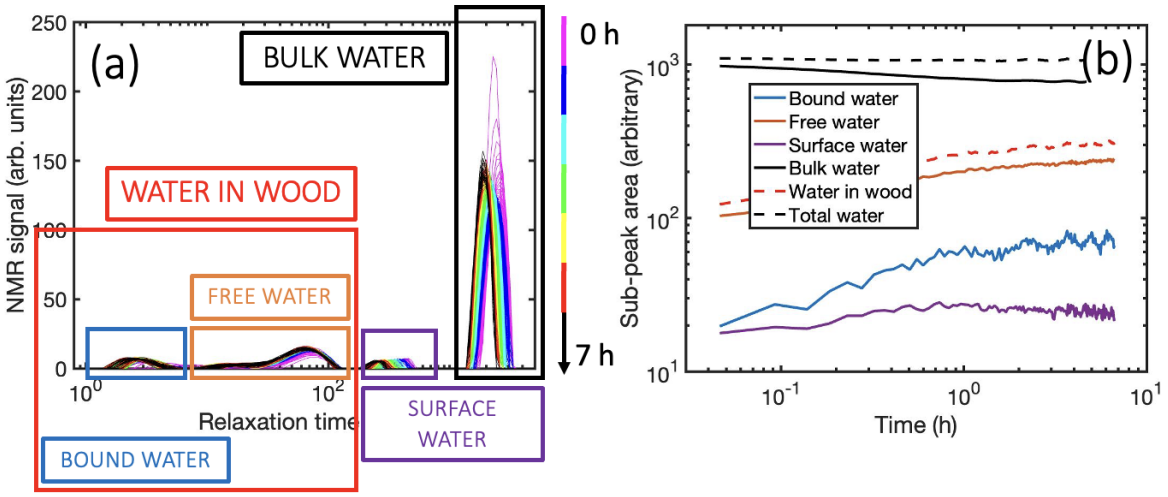

Figure 7.2: (a) Evolution of the T_2 relaxation time distribution over time from $0\ h$ in pink to $5\ h$ in black for a fir sample. Each peak correspond to a different water population: bound water (blue), water in pores (orange), water at the surface (purple) and bulk water (black). (b) Representation of the sub-peak area according to time for the different populations and for the total water in wood (red dotted line) and the total water (black dotted line).

- Total water (dotted black line) remains constant over time.
- Bulk water (black line) is decreasing over time while the water in wood (dotted red line) is increasing in time. In the case of softwood, they are not proportional since we don't consider the surface water (purple line) to be part of the water in the wood.
- Surface water (purple line) remains approximately constant over time which is not surprising as the imbibition plane does not change over time.
- Free water (orange line) increases in time. We notice that the first point does not start from 0 implying that a part of the sample can imbibe faster than the experiment time. A fast dynamic like water in the vessels.
- Bound water (blue line) increases faster than free water. We also note a shift of the peak towards the lower T_2. In this chapter we will not interpret the T_2 shifts which are potentially due to wood deformations but too subtle to determine a physical trend. Moreover, one might think that we are loosing some information in the low T_2 but as the total signal stay constant, we will assume that all the water is observed.

Diffusion process

For softwood, we use in the radial and tangential directions, the paint in five faces. In the longitudinal direction, we use silicone oil 50 as it allows us to distinguish water in tracheids and to neglect surface water which will be integrated to the oil peak. In Fig 7.3, we represent the evolution of the height reached by the bound water as a function of time in the three wood directions.

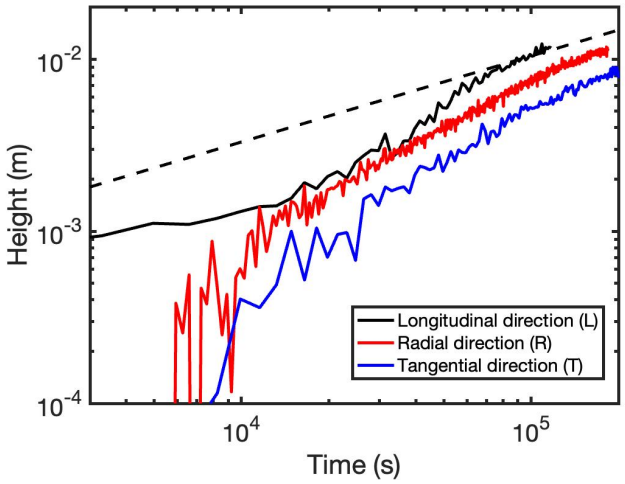

Figure 7.3: Evolution of the height (in m) reached by the bound water over time (in s) for the three fir directions: longitudinal direction (red line), radial direction (grey line) and tangential direction (blue line). The dotted lines have a slope in $1/2$.

For softwood, we did not obtain an evolution of bound water in square root of time. This may be due to the presence of water vapor in the system. Indeed, for softwoods, the presence of areolated pits allow a better circulation of vapor in all directions. Thus, as predicted by the literature, we have less difference in the evolution of the bound water front in the three directions. We still have a faster dynamic in the longitudinal direction and slower in the tangential direction.

7.4 Results on the properties of colloidal gels

Fig 7.4, 7.5 and 7.6 are the results obtained by rheometry on the follow-up of the gelation and the analysis of the rheological characteristics at the end of the gelation for gels with different concentrations (from $\phi = 1.875$ % to $\phi = 11.25$ %) and different sizes ($22\ nm$, $12\ nm$ and $6\ nm$) of particles. For each figure: the dark red curves represent the evolution of the storage modulus (G'), the light red represent the evolution of the loss modulus (G'') and the green one represent the axial force.

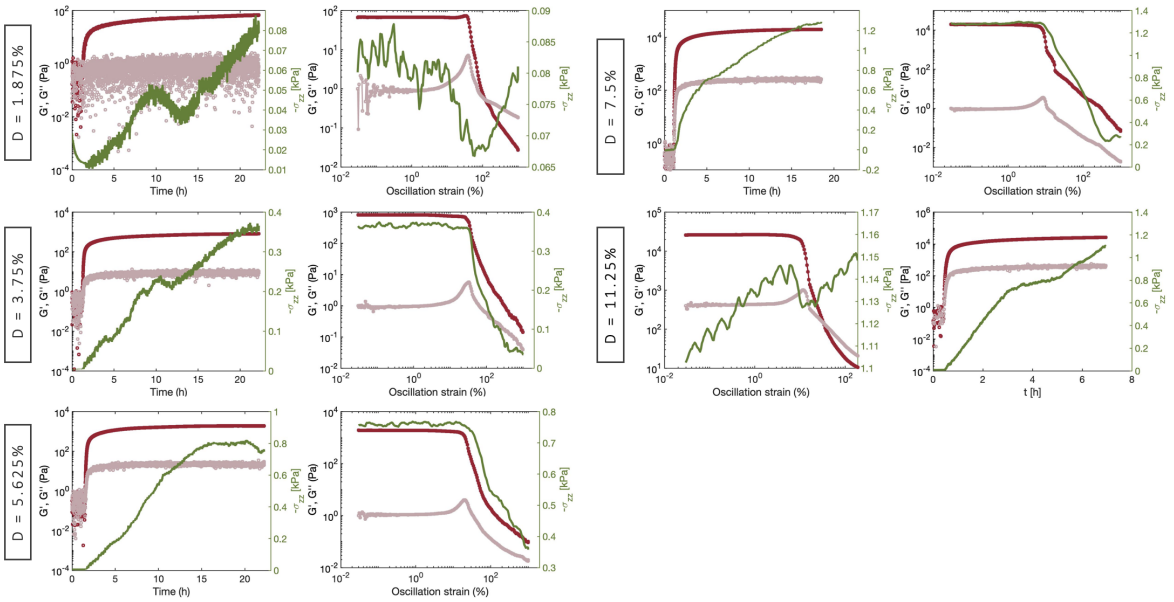

Figure 7.4: Evolution of the storage modulus (G'), the loss modulus (G'') and the axial force for the $22\ nm$ beads at different particle concentrations: (left) during the gelation process (time sweep) and (right) at the end of the gelation process (strain sweep).

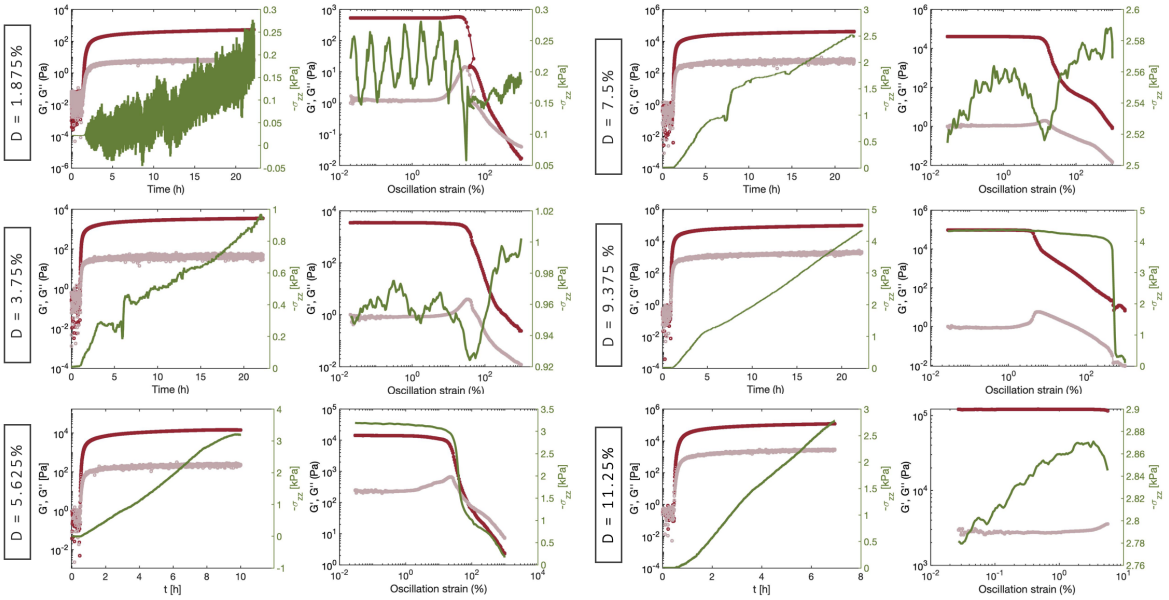

Figure 7.5: Evolution of the storage modulus (G'), the loss modulus (G'') and the axial force for the $12\ nm$ beads at different particle concentrations: (left) during the gelation process (time sweep) and (right) at the end of the gelation process (strain sweep).

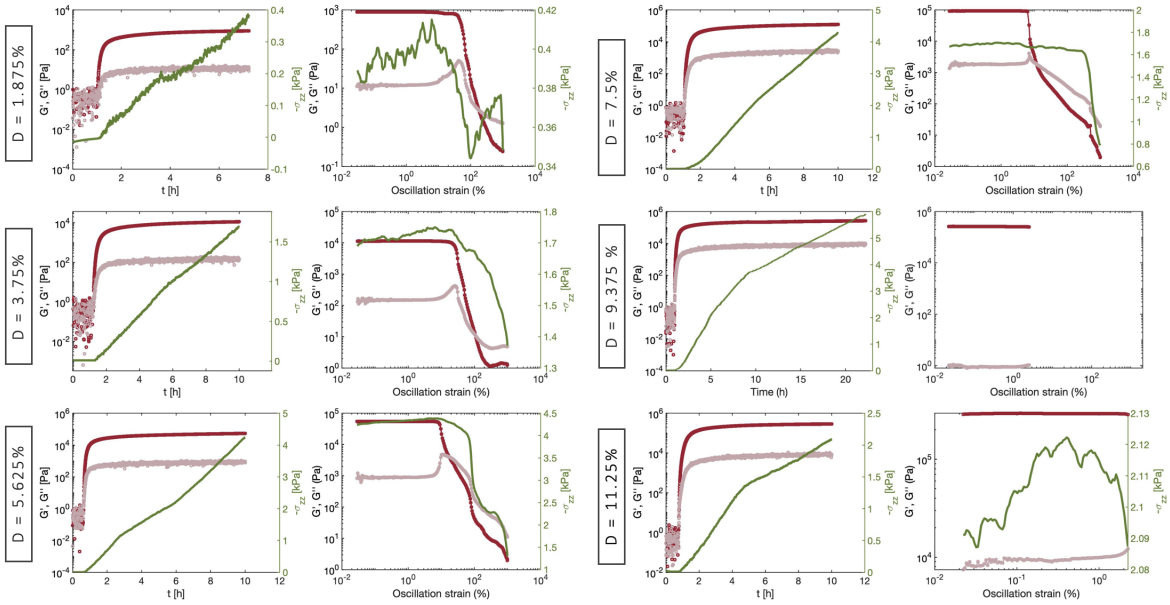

Figure 7.6: Evolution of the storage modulus (G'), the loss modulus (G'') and the axial force for the $06\ nm$ beads at different particle concentrations: (left) during the gelation process (time sweep) and (right) at the end of the gelation process (strain sweep).